DISSERTATION
SUBMITTED TO THE
COMBINED FACULTY OF
NATURAL SCIENCES AND MATHEMATICS
OF THE
RUPERTO-CAROLA-UNIVERSITY OF HEIDELBERG,
GERMANY
FOR THE DEGREE OF
DOCTOR OF NATURAL SCIENCES

PUT FORWARD BY

M. SC. KATHARINA MARGARETHA JOHANNA
WOLLENBERG
BORN IN: BAYREUTH, GERMANY

ORAL EXAMINATION: JANUARY 16TH, 2019

DIVERSITY OF POPULATION III STAR FORMATION

INFLUENCE OF ROTATION, TURBULENCE, AND MAGNETIC FIELDS ON THE FRAGMENTATION BEHAVIOR OF POPULATION III PROTOSTELLAR DISKS AND IMPLICATIONS FOR THE LATER EVOLUTION OF THE STAR-FORMING ENVIRONMENT

REFEREES:

APL. PROF. DR. SIMON C. O. GLOVER
PRIV. DOZ. DR. ANDREAS KOCH

For those who stayed with me
when everything turned dark.
And for those who have experienced the same.

Amicus certus in re incerta cernitur.
- *Cicero*

Man muss noch Chaos in sich haben,
um einen tanzenden Stern gebären zu können.

- Friedrich Nietzsche, Also sprach Zarathustra

Abstract

The aim of this thesis is to improve our understanding of the fragmentation behavior of Population III protostellar disks under the influence of rotation, turbulence, and magnetic fields. We further evaluate consequences that may be inferred for the later evolution of the star-forming halo and its surroundings with respect to protostellar ejections and in terms of the impact of radiative feedback on later chemical enrichment of neighboring halos.

In the main part of this thesis, we follow the collapse of a primordial gas cloud until the formation of the first protostar and the creation of a highly gravitationally unstable protostellar disk system. We find that turbulence promotes the fragmentation of the protostellar disk and both rotation and magnetic fields can provide some stabilization against it. While the total mass growth of the collection of protostars is only mildly affected by rotation and turbulence, magnetic fields can have such a strong impact on the dynamical evolution of the disk system that accretion onto the protostars is highly disturbed and their mass growth is significantly reduced. In spite of all the differences, the disk generally breaks up into a protostellar cluster that develops a top-heavy mass function. Interactions between protostars in the cluster are highly dynamical and lead to a considerable number of protostellar ejections. We demonstrate that some of these ejected Population III protostars, even if they continue to accrete for some longer period after they have left the disk environment, continue to have masses of $M \lesssim 0.8\,\mathrm{M}_{\odot}$. Hence, they have lifetimes longer than the current age of the Universe and thus describe Population III candidates that could still be observable today.

In another project, we assess the role of photoevaporation of a pristine halo by a near-by Population III star prior to the supernova explosion of that star. We demonstrate that it is crucial for realistic simulations of metal enrichment to account for the photoevaporation as the radiation ablates and thins out the outer halo layers and thus makes the halo more susceptible to mixing with the metals from the supernova ejecta.

In this thesis, we use both analytical estimations and numerical simulations. Further tests are conducted to investigate the performance of our numerical methods and the sensitivity of our results to the numerical resolution. We demonstrate that general trends, in particular when effects of turbulence are examined, cannot be reliably deduced from only a single numerical run. Instead a statistical analysis of an ensemble of realizations based on the same initial conditions needs to be considered.

Zusammenfassung

Das Ziel dieser Dissertation ist es, unser Verständnis von Fragmentationsverhalten Population III protostellarer Scheiben unter dem Einfluss von Rotation, Turbulenz und Magnetfeldern zu verbessern. Weiterhin untersuchen wir dieses Thema auf mögliche Konsequenzen für die spätere Entwicklung des Halos, in dem sich das Scheibensystem befindet, und seine Umgebung im Hinblick auf Protosterne, die aus ihrem Entstehungssystem hinausgeschleudert wurden, oder bezüglich des Einflusses von Strahlungsfeedback auf die chemische Anreicherung benachbarter Halos.

Im Hauptteil dieser Arbeit folgen wir dem Kollaps einer primordialen Gaswolke bis zur Entstehung des ersten Protosterns und der Bildung einer protostellaren Scheibe. Diese ist hochinstabil aufgrund starker Eigengravitation. Wir finden, dass Turbulenz die Fragmentation der Scheibe begünstigt und sowohl Rotation als auch Magnetfelder stabilisierend auf die Scheibe wirken. Während der Gesamtmassenzuwachs der Protosterne innerhalb der Scheibe nur gering von Turbulenz oder Rotation beeinflusst wird, können Magnetfelder die dynamische Entwicklung der Scheibe so beeinträchtigen, dass die Akkretion der Protosterne extrem gestört und damit ihr weiteres Massenwachstum signifikant eingeschränkt wird. Trotz all dieser Unterschiede bildet sich durch Fragmentation der Scheibe ein Cluster von Population III Protosternen heraus, dessen Massenfunktion durch schwere Sterne mehrerer Sonnenmassen dominiert ist (*top-heavy mass function*). Interaktionen zwischen den Protosternen im Cluster sind hochdynamisch und führen dazu, dass eine beträchtliche Anzahl der Protosterne aus dem Scheibensystem, in dem sie entstanden sind, hinausgeschleudert wird. Wir verfolgen deren weitere Entwicklung auf ihrem Weg an den Rand des Halos und zeigen, dass der Großteil von ihnen trotz fortgeführter Akkretion eine Masse kleiner als $M \lesssim 0.8\,\mathrm{M}_\odot$ beibehält. Population III Sterne dieser Masse haben eine Lebenszeit, die das gegenwärtige Alter des Universums übersteigt, und könnten daher bis heute überlebt haben und damit noch beobachtbar sein.

In einem weiteren Projekt betrachten wir die Photoevaporation eines Halos durch einen externen Population III Stern in seiner Nachbarschaft. Wir analysieren, welche Bedeutung dieser Prozess für die weitere Entwicklung des Halos hat, wenn dieser durch die anschließende Supernova des Population III Sterns mit Metallen angereichert wird. Wir zeigen, dass die Modellierung der Photoevaporation von Wichtigkeit ist, da durch diesen Prozess die Gasschichten innerhalb des Halos von außen nach innen ausgedünnt werden und dadurch Metalle der Supernova tiefer in den Halo eindringen und sich besser mit dem Gas im Halo vermischen können.

In dieser Doktorarbeit werden sowohl analytische Abschätzungen als auch numerische Simulationen verwendet. Weiterhin überprüfen wir die Qualität unserer numerischen Methoden und wir testen die Empfindlichkeit unserer physikalischen Ergebnisse auf Änderungen der numerischen Auflösung. Wir zeigen, dass keine verlässlichen allgemeinen Trends aus einer einzigen Simulation gefolgert werden können, besonders wenn Effekte von Turbulenz in die Simulation einfließen. Stattdessen sollte eine statistische Analyse eines Ensembles aus Simulationen gleicher Anfangsbedingung herangezogen werden.

Contents

List of Figures

List of Tables

CHAPTER

1 Introduction

1.1 Motivation

The appearance of the first luminous objects, the so-called Population III (Pop III) stars ended the dark ages of the Universe and heralded a new era of structure formation leading to the formation of further generations of metal-enriched stars and the first galaxies. Population III stars are assumed to have formed from primordial gas, consisting mainly of hydrogen and helium, in so-called minihalos of mass $M \sim 10^5 - 10^6\,\mathrm{M}_\odot$ at redshift $z \sim 20 - 50$ (e.g. Tegmark et al., 1997; Abel et al., 2002; Bromm & Larson, 2004; Yoshida et al., 2003, 2006). Minihalos were the first dark matter halos to have reached masses that allowed sufficient baryonic matter to fall into their potential wells, virialize, and produce large enough amounts of molecular hydrogen, the main coolant at that time (Saslaw & Zipoy, 1967; Palla et al., 1983; Galli & Palla, 1998), to efficiently cool to a minimum temperature of $T \sim 200\,\mathrm{K}$, where first star formation was triggered (Tegmark et al., 1997; Barkana & Loeb, 2001; Yoshida et al., 2003; Glover, 2013).

Compared to present-day star formation, temperatures in primordial gas were considerably higher implying that both the Jeans mass ($M_\mathrm{J} \propto T^{3/2}\rho^{-1/2}$) and accretion rates ($\dot{M} \propto T^{3/2}$) were large in Population III star formation (Omukai & Nishi, 1998; Omukai & Palla, 2001, 2003). While the first numerical studies yielded single, very massive stars with $M \gtrsim 100\,\mathrm{M}_\odot$ (see e.g. Abel et al., 2002; Bromm et al., 2002; Bromm & Larson, 2004), this picture has changed over the last decade. Simulations have found that in more realistic environments the star-forming cloud contains some non-zero angular momentum which leads to the formation of a protostellar disk. As the mass flow onto the disk is generally higher than the accretion onto the protostar, the disk becomes highly self-gravitating and breaks up into a cluster of several protostellar fragments (e.g. Clark et al., 2008; Turk et al., 2009; Greif et al., 2011; Clark et al., 2011b,a; Smith et al., 2011; Stacy & Bromm, 2013). The further evolution of the Population III protostars within the protostellar disk system is considerable influenced by their dynamical interactions. Accretion onto individual protostars is highly variable and may even be terminated, in a process called fragmentation-induced starvation (from present-day star formation Peters et al., 2010), as the protostars compete for their common mass reservoir (Greif et al., 2011; Greif et al., 2012; Girichidis et al., 2012; Smith et al., 2012; Hosokawa et al., 2016). Close encounters between protostars may lead to mergers (Greif et al., 2011; Greif et al., 2012; Stacy et al., 2016) or ejections (Greif et al., 2011; Stacy & Bromm, 2013; Stacy et al., 2016). The inferred initial mass function (IMF) of Pop III protostellar clusters is a top-heavy distribution ranging from subsolar values to over a hundred solar masses (Greif et al., 2011; Clark et al., 2011a; Stacy & Bromm, 2013; Susa, 2013; Hirano et al., 2014; Stacy et al., 2016) and has a large deficit of low mass stars compared to mass functions by Salpeter (1955) or Kroupa (2001). Determining the shape of the Pop III IMF has become an important aspect as it is essential for estimating the impact of these stars on their environment.

At about the time when the formation of Population III protostellar clusters were first studied in numerical simulations, research also began with exploring the role of primordial magnetic fields in the Pop III star-forming process in more detail (e.g. Machida et al., 2008a; Schleicher et al., 2010; Sur et al., 2010, 2012; Schober et al., 2012; Machida & Doi, 2013; Peters et al., 2014). The first magnetic fields were possibly created during inflation (Turner & Widrow, 1988), early Universe phase transitions (Sigl et al., 1997) or the Biermann battery mechanism (Biermann, 1950; Xu et al., 2008). Initially, they had field strengths of only $B = 10^{-30} - 10^{-18}\,\mathrm{G}$ and for a long time it was not sure whether such weak seed would be dynamically important during first star formation at all. By investigating the amplification mechanism of the turbulent small-scale dynamo (SSD) (Kazantsev, 1968; Kulsrud et al., 1997), it was shown that the weak seed fields can be amplified to small-scale, tangled field configurations of about $\sim 10^{-5}\,\mathrm{G}$ (Schleicher et al., 2010; Sur et al., 2012; Peters et al., 2012; Turk et al., 2012; Schober et al., 2012; Schleicher et al., 2013). Turbulence that occurs during virialization (Wise & Abel, 2007; Greif et al., 2008) or during prestellar gas collapse (e.g. Sur et al., 2010; Clark et al., 2011b; Turk et al., 2012) can drive the SSD procedure of random stretching, twisting and folding of magnetic field lines which converts kinetic into magnetic energy. How these magnetic fields further evolve, for example when and how they transition into a coherent, large-scale structure is not yet fully understood, although mechanisms such as an α-Ω dynamo acting in differentially rotating disk might present a possible pathway (e.g. Steenbeck & Krause, 1966; Vainshtein & Ruzmaikin, 1971; Arshakian et al., 2009). It is expected and has been demonstrated in a few studies that magnetic fields may affect the Population III star formation in similar ways to present-day star formation. They can drive jets and outflows (Machida et al., 2006, 2008a; Machida & Doi, 2013; Latif & Schleicher, 2016) and stabilize protostellar disks against fragmentation by magnetic pressure (Peters et al., 2014) or through efficient magnetic braking (Machida & Doi, 2013). Overall, however, this field of research is still in its infancy.

Having high surface temperatures of the order of $\gtrsim 10^5\,\mathrm{K}$, Population III stars are expected to have affected their near and far environment significantly through radiative feedback in the ultraviolet (UV) spectrum (Bromm et al., 2001b; Omukai & Palla, 2001; Schaerer, 2002; Hosokawa et al., 2011; Stacy et al., 2012). They likely have also contributed to the reionization of Universe (e.g. Shapiro et al., 1994; Haiman et al., 1997; Barkana & Loeb, 2001; Kitayama et al., 2004; Alvarez et al., 2006). Of particular importance are Lyman-Werner photons with energies of $11.2 - 13.6\,\mathrm{eV}$ because they can destroy molecular hydrogen (Field et al., 1966; Stecher & Williams, 1967) and can travel freely over large distances as hydrogen and helium is optically thin to this kind of radiation. Mass growth may eventually be stopped as the accretion reservoir is photoevaporated (Hosokawa et al., 2011; Stacy et al., 2012; Susa, 2013; Susa et al., 2014; Stacy et al., 2016). Neighboring halos may be ionized (Whalen et al., 2004; Kitayama et al., 2004; Alvarez et al., 2006; Abel et al., 2007; Johnson et al., 2007) and become promising sites either for zero-metallicity star formation in pre-ionized gas, termed Population III.2 star formation (McKee & Tan, 2008; Clark et al., 2011a; Greif et al., 2011; Hosokawa et al., 2012; Hirano et al., 2014), or for the formation of supermassive black holes (see e.g. Oh & Haiman, 2002; Volonteri & Rees, 2005; Volonteri, 2012) when pre-existing molecular hydrogen is largely destroyed and only atomic hydrogen cooling is possible.

At the end of their lives, it is assumed that Pop III stars with masses $M \lesssim 40\,\mathrm{M}_\odot$ explode in a core-collapse supernova (CCSN), those with $140 \lesssim M \lesssim 260\,\mathrm{M}_\odot$ in a pair-instability supernova (PISN), and those with masses $40 \lesssim M \lesssim 140\,\mathrm{M}_\odot$ and $M \gtrsim 260\,\mathrm{M}_\odot$ collapse directly into a black hole (e.g. Heger & Woosley, 2002). Metals, which are ejected into the interstellar and intergalactic medium by CCSN and PISN explosions, are taken up into the first generation of metal-enriched stars, the so-called Population II stars. Stellar archaeology, in which these metal-enriched but still metal-poor stars, for example extremely metal-poor stars (EMP) (Beers & Christlieb, 2005; Frebel & Norris, 2015) or ultra metal-poor stars (UMP) (Karlsson et al., 2013), are observed and their metal constituents are analyzed, can therefore provide constraints on the mass range of Population III stars. Direct observation of Pop III stars so far may only be possible for those with masses below $0.8\,\mathrm{M}_\odot$ that could have survived until today (Yoshida et al., 2006; Greif et al., 2011; Kippenhahn et al., 2012), because otherwise Population III stars are too distant in space and time to be observable with current and near-future telescopes (Zackrisson et al., 2011; Rydberg et al., 2013).

Population III stars shaped their environment and influenced the subsequent evolution of the Universe until today. It is therefore an important and exciting task to examine them. The main questions that arise are

- How do Population III stars form?
- What is the shape of their initial mass function?
- How do they influence their environment?

In this thesis we are going to address aspects of all three questions. We will mainly focus on parts of the star-forming process and will investigate how differing initial conditions affect the general outcome and what they imply for the answers to the other two questions. Here in the beginning, we note that we investigate the very first stars, Population III.1., that form in minihalos in which molecular hydrogen is the dominant coolant in contrast to Population III.2 stars for which hydrogen deuteride (HD) is another major contributor to the cooling efficiency of the primordial gas. In following, we will therefore write Population III for simplicity but actually mean Population III.1. Population III.2 will be mentioned specifically when needed.

1.2 Outline of this thesis

The goal of this thesis is to improve our understanding of the fragmentation behavior of Population III protostellar disks under the influence of rotation, turbulence, and magnetic fields. We are interested in effects with respect to the resulting number of protostars and their mass evolution and which consequences may be inferred for later times in the evolution of the star-forming halo and its surrounding in terms of protostellar ejections and in terms of the impact of radiative feedback on later chemical enrichment of a neighboring halo. Both analytical and numerical methods will be applied in order to examine these topics. The structure of this thesis and the main questions addressed in it are as follows:

Chapter 2: In this chapter, important stages in the physical and chemical history of our Universe until the onset of first star formation are reviewed. Then, the current understanding of different stages of Population III star formation and evolution is presented.

Chapter 3: The two numerical codes used for this thesis, AREPO and ZEUS-MP, are described. Regarding AREPO, updates in the primordial chemistry network and two new implementations, the variable adiabatic index and the sink accretion luminosity, are introduced. Finally, the generation of the initial conditions used in the studies with AREPO are explained.

Chapter 4: ***How does photoevaporation of a pristine halo by a near-by Population III star prior to the star's supernova explosion affect the outcome of chemical enrichment of this halo?*** A set of 2D ZEUS-MP simulations is performed. It is studied how the shape of the halo is affected by the stellar ionizing radiation during the photoevaporation until the death of the star as a supernova. It is discussed how this outcome will influence the efficiency of chemical enrichment through the supernova ejecta wave.

Chapter 5: ***How do different levels of rotation and subsonic turbulence affect the fragmentation behavior of a Population III protostellar disk in terms of number of protostellar fragments and total mass accreted by them? Which mass functions arise? Are merger events and protostellar ejections observed and how often do they occur?*** The collapse of a primordial Bonnor-Ebert sphere with different initial levels of rotation and subsonic turbulence is followed beyond the formation of the first protostar to investigate the fragmentation behavior of the protostellar disk and the evolution of the protostellar cluster. Nine different combinations of rotation and turbulence are considered. For each combination five realizations are run that differ either in terms of the random seed chosen to initialize the turbulent velocity field or, for the runs without turbulence, in terms of the random mesh cell positions used to setup the Bonnor-Ebert sphere initial conditions. It is evaluate whether this approach is preferable compared to a single realization per setup. The studies are performed in 3D with the Voronoi moving-mesh code AREPO. The sink particle method is used to represent Population III protostars. The relevance of sink particle merging is assessed.

Chapter 6: ***How sensitive are the results of Chapter 5 to the choice of the values applied for the two resolution constraints: the sink particle accretion radius and the number of cells per Jeans length?*** In this chapter, three test series are performed to investigate the sensitivity of the results presented in Chapter 5 to changes in the size of the sink accretion radius or in the number of cells per Jeans length. The initial setups resemble those in Chapter 5. The simulations are conducted again with AREPO.

Chapter 7: ***Can small-scale, tangled magnetic fields stabilize Population III protostellar disks?*** In an analytical approach, an expression of the Toomre criterion which accounts for effects due to magnetic pressure is re-formulated in terms of the saturation magnetic field strength as gained through small-scale, turbulent dynamo action. This formula is then applied to exemplary unstable Population III protostellar disks extracted from previous studies and from our own simulations in Chapter 5.

Chapter 8: ***How does the outcome from Chapter 5 change in presence of a large-scale uniform magnetic field?*** A purely rotational and a purely turbulent realization from Chapter 5 is re-run with an initial large-scale, coherent magnetic field. The simulations are carried out with AREPO assuming ideal magnetohydrodynamics. Possible effects on the number of fragments, their mass growth and the stabilization of the protostellar disk system are analyzed.

Chapter 9: In this final chapter, the main results of this thesis are summarized and prospects of follow-up studies are given.

CHAPTER 2

Theory

This chapter summarizes important stages in the physical and chemical history of the Universe until the appearance of the first stars, the Population III (Pop III) stars. It focusses then on describing the current understanding of different stages in the formation and evolution of Pop III stars and provides a thematic background for the studies presented in Chapter 4 to 8 of this thesis. In Sections 2.1, 2.2, and 2.3, we briefly recap the cosmological description of the expansion of the Universe, its early thermal and chemical evolution, and the formation of the first structures. The chemistry of the primordial gas leading to the formation of the first stars is discussed in Section 2.4. Section 2.5 then covers several important aspects of Population III star formation from the birth of the star until its aftermath.

This chapter is written in my own words. It generally follows the structure of the lecture *Dark Ages of the Universe* by S. C. O. Glover given at Heidelberg University, Winter Term 2014/2015. The content, however, was extended, specified, and updated where needed. This is in particular the case for the Section 2.4 and 2.5 where the origin of additional material is indicated by the references. Section 2.1, 2.2, and 2.3, contain typical topics covered in lectures and books about cosmology. Especially the book *"The First Galaxies in the Universe"* by A. Loeb and S. R. Furlanetto (Loeb & Furlanetto, 2013), the lectures series *"Cosmology"* and *"Early Universe"* by Anthony Lewis at University of Sussex, Winter/Spring Term 2012/2013 and the book *"Cosmological Physics"* by J. A. Peacock (Peacock, 1999) were additional general references for me while writing these three subsections.

2.1 Cosmology

The currently most favored cosmological theory of our Universe is the so-called ΛCDM model, i.e. a Universe containing cold dark matter (CDM) and a cosmological constant, Λ, that is usually associated with dark energy. This model is based on the two assumptions that

1. the Universe is isotropic on sufficiently large scales, and
2. our location in the Universe is not particularly preferred to any other place in the Universe (*Copernican principle*).

Both can be summarized in the cosmological principle saying that the Universe is homogeneous and isotropic on large-scales. Observations such as the close to isotropic nature of the cosmic microwave background (CMB), see Fig. 2.1, and the homogeneous large-scale distribution of galaxies (e.g. Scrimgeour et al., 2012), support the

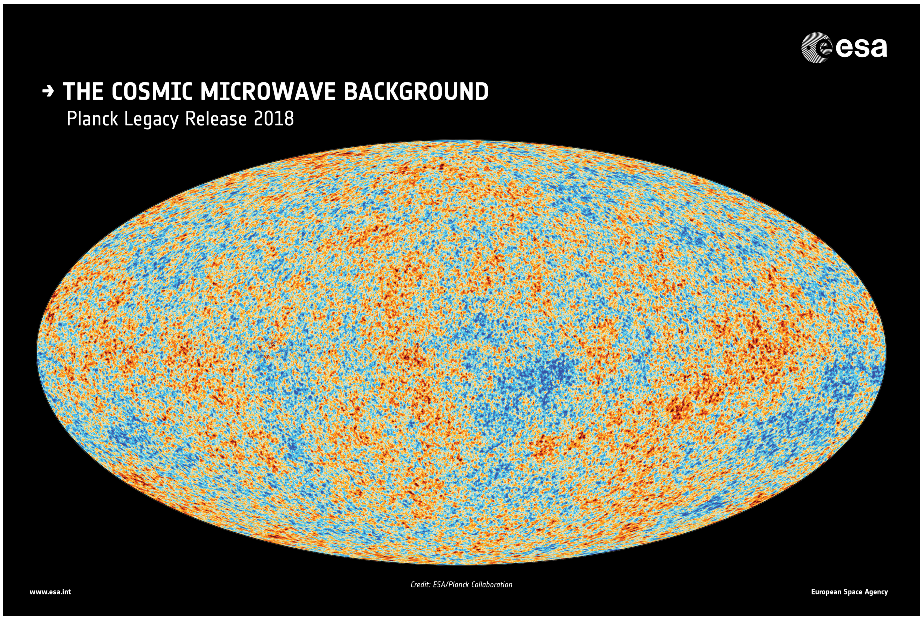

Figure 2.1: The cosmic microwave background as observed by the Planck satellite. The structures seen in the map are temperature fluctuations of the order of $\Delta T/T \simeq 10^{-5}\,\mathrm{K}$. Except for these tiny fluctuations corresponding to density inhomogeneities that are the seeds of later structures in the Universe, the radiation from the CMB is isotropic. See Section 2.2 and 2.3 for more details. Image credit: ESA/Planck Collaboration, Planck Legacy Release, July 2018; see also (Planck Collaboration et al., 2018a). Image source: `http://sci.esa.int/science-e-media/img/55/ESA_Planck_CMB2018.jpg`.

ΛCDM cosmology. Furthermore, the accelerated expansion of the Universe can be explained by means of dark energy.

The ΛCDM model uses Albert Einstein's General Relativity Theory (GRT) to describe large-scale gravitational interaction between objects within the Universe. A key result of GRT is that the geometrical structure of Universe is a four-dimensional spacetime. Under the assumption of the cosmological principle, it can be described by the Friedmann-Lemaître-Robertson-Walker metric (FLRW) which in spherical coordinates (r, θ, ϕ) is given by

$$ds^2 = c^2\,dt^2 - a(t)^2\left(dr^2 + f_{\mathrm{K}}^2(r)\,[d\theta^2 + \sin^2\theta\, d\phi^2]\right) \ . \tag{2.1}$$

Here, c is the speed of light and $f_{\mathrm{K}}(r)$ includes a description of the curvature, denoted by K, where

$$f_K(r) = \begin{cases} \sqrt{K}\,\sin(\sqrt{K}\,r) & K > 0, \text{ i.e. closed, spherical curvature,} \\ r & K = 0, \text{ i.e. flat, no curvature,} \\ \sqrt{|K|}\,\sinh(\sqrt{K}\,r) & K < 0, \text{ i.e. open, hyperbolic curvature.} \end{cases} \tag{2.2}$$

The time-dependent scale factor, $a(t)$, describes the relative size of the Universe. Its present-day value is defined to be $a_{\mathrm{today}} = a_0 = 1$. An expanding Universe is characterized by $\dot{a} > 0$. Instead of $a(t)$, we often refer to the redshift, z, which follows

$$1 + z = \frac{1}{a} \ , \tag{2.3}$$

when we talk about the timeline or the expansion state of the Universe. Present-day is $z = 0$. The redshift per se describes the relative difference between the wavelength of light when it is observed, λ_{obs}, and its original wavelength at time of emission, λ_{em}:

$$z = \frac{\lambda_{\mathrm{obs}} - \lambda_{\mathrm{em}}}{\lambda_{\mathrm{em}}} \ . \tag{2.4}$$

Due to the expansion of the Universe, light of a source that moves relative to the observer is shifted in its wavelength. If it moves away from (toward) the observer it is shifted to longer (shorter) wavelengths, i.e. into a redder (bluer) spectrum.

The dynamical evolution of the scale factor and with it of our Universe is described by the Friedmann equations

$$\left(\frac{\dot{a}}{a}\right) = \frac{\kappa}{3}\rho - \frac{Kc^2}{a^2} + \frac{\Lambda}{3} \ , \tag{2.5}$$

$$\frac{\ddot{a}}{a} = -\frac{\kappa}{6}\left(\rho + \frac{3P}{c^2}\right) + \frac{\Lambda}{3} \ , \tag{2.6}$$

which combined lead to a third equation

$$\frac{d}{dt}\left(a^3 \rho c^2\right) + P\frac{d}{dt}\left(a^3\right) = 0 \ . \tag{2.7}$$

Here, c is again the speed of light, $\kappa = 8\pi G$ with the gravitational constant G, K denotes the curvature, and Λ is the dimensionless cosmological constant. Furthermore, it is assumed that the Universe is filled with a perfect fluid of energy density $\rho(t)$ and pressure $P(t)$ that follows the equation of state

$$P = w\rho c^2 \quad \begin{cases} w = 0 & \text{(pressureless matter; non-relativistic particles)} \\ w = 1/3 & \text{(radiation; relativistic particles)} \\ w = -1 & \text{(dark energy/ cosmological constant)} \quad . \end{cases} \tag{2.8}$$

By inserting the three cases of Eq. (2.8) individually in Eq. (2.7), we can derive how the energy densities of different species evolve with the expansion of the Universe. The energy density of pressureless particles (subscript "m") evolves in a simple fashion due to the expansion in the volume of the Universe:

$$\rho_{\mathrm{m}}(t) = \rho_{\mathrm{m},0}\, a^{-3} \ . \tag{2.9}$$

In the expression for the radiation energy density (subscript "r")

$$\rho_{\mathrm{r}}(t) = \rho_{\mathrm{r},0}\, a^{-4} \tag{2.10}$$

in addition to the effect of the spatial expansion, there is an additional effect due to the fact that the energy per photon declines as a^{-1}. Subscript "0" denotes present-day values corresponding to $a_0 = a_{\mathrm{today}} = 1$. The history of the expansion of the Universe is also a history of its thermal evolution. According to the Stefan-Boltzmann law the radiation density scales with the temperature as $\rho_{\mathrm{r}} \propto T^4$ and combined with how the radiation temperature evolves with the scale factor $\rho_{\mathrm{r}} \propto a^{-4}$, we see that

$$T_{\mathrm{r}} \propto a^{-1} \tag{2.11}$$

Therefore, the Universe was hotter in the past.

The Hubble parameter is defined as $H = \dot{a}/a$. Its present-day value $H_0 = 100\,h\,\mathrm{km\,s^{-1}\,Mpc^{-1}}$, where $h \simeq 0.674$ (Planck Collaboration et al., 2018b) is known as the Hubble constant. For each component of the Universe a density parameter $\Omega \equiv \rho/\rho_{\mathrm{crit}}$ with the critical energy density

$$\rho_{\mathrm{crit}} \equiv \frac{3H^2}{\kappa} \tag{2.12}$$

can be defined so that for radiation and matter it is $\Omega_{\mathrm{r}} \equiv \rho_{\mathrm{r}}/\rho_{\mathrm{crit}}$ and $\Omega_{\mathrm{m}} \equiv \rho_{\mathrm{m}}/\rho_{\mathrm{crit}}$ respectively, $\Omega_\Lambda \equiv \Lambda/(3H_0^2)$ for the cosmological constant Λ, and $\Omega_{\mathrm{K}} \equiv -Kc^2/H_0^2$ for the curvature. They obey

$$1 = \Omega_{\mathrm{r}} + \Omega_{\mathrm{m}} + \Omega_\Lambda + \Omega_{\mathrm{K}} \ . \tag{2.13}$$

The first Friedmann equation, Eq. (2.6), can then be rewritten as

$$H^2 = H_0^2 \left[\frac{\Omega_{\mathrm{r}}}{a^4} + \frac{\Omega_{\mathrm{m}}}{a^3} + \frac{\Omega_{\mathrm{K}}}{a^2} + \Omega_\Lambda \right] \ . \tag{2.14}$$

Due to the dependence on the scale parameter, one can see from Eq. (2.14) that the expansion of the Universe was dominated by different energy parameters, i.e. energy densities, at different times. More detailed calculations find that the early Universe was dominated by the radiation energy density until the time of matter-radiation equality ($z \sim 3300$). During this era the scale factor scaled as $a(t) \propto t^{1/2}$. Between $3300 \gtrsim z \gtrsim 0.4$, the Universe was matter-dominated and the scale factor followed $a(t) \propto t^{2/3}$. Since $z \sim 0.4$ until today, the Universe is dominated by a cosmological constant which we associate with dark energy. It is now in a state of accelerated expansion $a(t) \propto \exp(t)$. The Planck satellite and its predecessors have performed detailed measurements of the cosmic microwave background and derived the values of several cosmological parameters. The current results suggest that the Universe is flat ($\Omega_{\mathrm{K}} \sim 0$, i.e. $K \sim 0$) with $\Omega_\Lambda = 0.689$, $\Omega_{\mathrm{m}} = 0.311$ (both baryonic and dark matter), and $\Omega_{\mathrm{b}} = 0.049$ for baryonic matter (Planck Collaboration et al., 2018b). Until today it is not clear what dark energy and dark matter really consist of. We experience their influence only indirectly via the expansion of the Universe (dark energy) and on the formation and evolution of large-scale structure (dark matter). We will discuss the role of dark matter a bit more in Section 2.3 but because both components are of lesser immediate relevance for the physics studied in this thesis, we refrain from going into more details here.

2.2 Early thermal and chemical evolution

The Cosmic Microwave Background (CMB) is the farthest we can look into the history of our Universe. It emerges at around $z \sim 1100$ when the early Universe transitions from being fully ionized into transparency. Photons which initially were tightly bound to matter through Compton scattering from free electrons, were then able to pass freely as the free electron density declined when the ionized primordial species recombined. Before we give some more details on the time of recombination, we briefly recap the current understanding of the thermal and chemical evolution of the Universe before the emergence of the CMB. For a general overview of different stages in the history of the Universe, see Fig. 2.2.

Within the first seconds after the Big Bang, the fundamental forces (gravity, and the strong, weak and electromagnetic force) emerged from the extremely hot ($k_{\mathrm{B}}T \gtrsim$

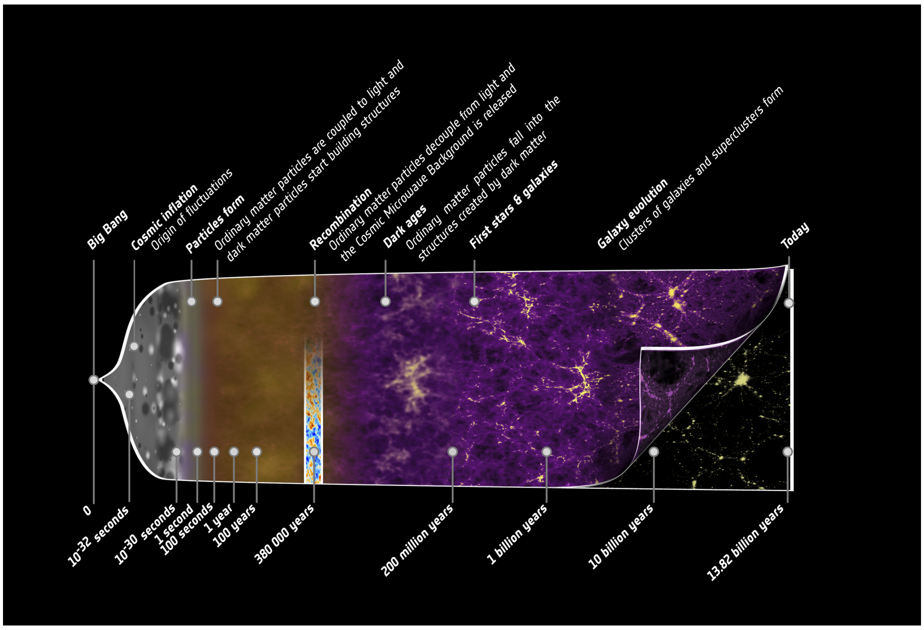

Figure 2.2: Graphical illustration of the expansion history of the Universe. Image credit: ESA - Christophe Carreau. Image source: `http://www.esa.int/spaceinimages/Images/2013/03/Planck_history_of_Universe_zoom`.

10^{15} GeV) and dense initial state of the Universe. After a short period of inflationary expansion of the Universe, the first elementary particles (quarks, leptons, gauge bosons and the Higgs boson) started to form. In the beginning, they were still unconfined in the so-called quark-gluon plasma. The first elementary particles and their composites formed as particle/anti-particle pair due to the high temperatures in the plasma. However, most of these pairs annihilated each other while Universe continues to cool. Neutrinos ν (and $\bar{\nu}$ is an antineutrino) were the first elementary particles to decouple from the plasma. Within minutes after the Big Bang, the Universe cooled to $k_\mathrm{B}T \simeq 1\,\mathrm{GeV}$ and the first composite subatomic particles, protons, p, and neutrons, n, condensed out of the plasma. Initially their abundance was kept in equilibrium via the reactions

$$\mathrm{p} + \mathrm{e}^- \leftrightarrow \mathrm{n} + \nu \tag{2.15}$$

$$\mathrm{p} + \bar{\nu} \leftrightarrow \mathrm{n} + \mathrm{e}^+ \ , \tag{2.16}$$

where e^+ is a positron, but at $k_\mathrm{B}T \simeq 800\,\mathrm{keV}$ a neutron-to-proton number density ratio of

$$\frac{n_\mathrm{n}}{n_\mathrm{p}} = e^{-\Delta mc^2/k_\mathrm{B}T} \simeq \frac{1}{6} \tag{2.17}$$

with the mass difference between protons and neutrons $\Delta mc^2 \simeq 1.4\,\mathrm{MeV}$, and the Boltzmann constant k_B, freezed out with the overall temperature decline as the reactions became too slow and thermal equilibrium could no longer be maintained. As some neutrons transformed into protons via β^- decay, the ratio declined further to

$$\frac{n_\mathrm{n}}{n_\mathrm{p}} \simeq \frac{1}{7} \ . \tag{2.18}$$

The creation of heavier nuclei by fusion of protons and neutrons was initially prevented by the large number of high energy photons in the hot matter-radiation plasma that were able to disintegrate such nuclei. About three minutes after the Big Bang, when $k_\mathrm{B}T \simeq 80\,\mathrm{keV}$, however, nuclear fusion of protons and neutrons to some heavier elements became possible. The resulting primordial gas had a composition of $\sim 75\%$ ionized hydrogen (^{1}H), $\sim 25\%$ ionized helium (mostly ^{4}He, some ^{3}He) and some traces of deuterium (^{2}D; D/H $= 2.5 \times 10^{-5}$) and lithium (^{7}Li, ^{6}Li; Li/H $\simeq 5 \times 10^{-10}$) (Cyburt et al., 2008). Elements heavier than Lithium only occurred in negligible abundance as nuclei with 5 or 8 nucleons to which the first elements could further fuse are not stable and thus quickly decayed again.

As the Universe cooled further down, recombination reactions, through which the ionized species turned neutral, became efficient. At $z > 2000$ already helium started to recombine. A larger impact on the state of the Universe, however, came from the recombination of hydrogen via

$$\mathrm{H}^+ + \mathrm{e}^- \rightarrow \mathrm{H} + \gamma \tag{2.19}$$

where γ denotes photon emission. The substantial decline in the free electron fraction due to this reaction allowed photons that were still strongly coupled to the ionized plasma through Compton scattering, to travel freely. The plasma and with it the Universe turned transparent. This happened at $z \sim 1100$, the Universe had cooled to a temperature $T \lesssim 4000\,\mathrm{K}$ ($k_\mathrm{B}T < 0.4\,\mathrm{eV}$). The photons from this epoch of "last scattering" make up the cosmic microwave background. The ionization fraction of the primordial gas finally froze out at $z \sim 700 - 800$ to a value of $x \sim 2 \times 10^4$ because the recombination reaction became too slow to considerably alter the ionization fraction any further (e.g. Schleicher et al., 2008). With the end of recombination we entered the epoch of the Dark Ages of the Universe that ended with the formation of the first stars. The Universe remained mainly neutral until it was reionized through radiation emitted from the first stars, galaxies and quasars.

2.3 Structure formation

Within ΛCDM cosmology, structure formed hierarchically from small scales to larger scales. It is assumed that during the short epoch of inflationary expansion of the Universe immediately after the Big Bang, quantum fluctuations were strongly magnified and manifested themselves as ripples in spacetime. These materialized themselves later as perturbations in the mass density of the radiation-matter fluid that filled the early Universe. As we have discussed above, these density fluctuations correspond to the tiny temperature variations observed in the cosmic microwave background.

As dark matter interacts only gravitationally and its interaction with ordinary (baryonic) matter is weak, it is expected to have frozen out from the common particle-radiation fluid very soon after the Big Bang. Perturbations in the dark matter density that were larger than the cosmic background density started to grow further until they eventually decoupled from the evolution of their cosmic environment and collapsed to form the first dark matter halos. Baryonic matter on the other hand was strongly coupled to radiation through Compton scattering before $z \sim 1100$. Small-scale fluctuations in the baryonic matter density were smoothed out through the common diffusion of the matter-radiation fluid as the photon number density is kept in equilibrium, a process termed "Silk damping". Only perturbations larger than the diffusion radius of the matter-radiation fluid, i.e. the distance the fluid could move within a particular time, were able to survive and manifested themselves as so-called "baryonic acoustic oscillations" in the cosmic microwave background. After the baryonic matter decoupled from the radiation, perturbations within its matter density could grow unhindered. Already established dark matter halos attracted baryonic gas which fell into the halo potential wells, accumulated there and condensed to form the first gas clouds.

In some sufficiently massive halos, primordial gas evolved to produce large enough amounts of molecular hydrogen, the prime coolant at that time, to cool to temperatures $T \sim 200\,\mathrm{K}$ and trigger gas collapse to form the first protostars. Before we discuss the evolution of primordial chemistry within the dark matter halos is more detail in Section 2.4, we first recap some important concepts in the context of structure formation, starting with a description of the condensation of the first small density fluctuations into overdense regions in Section 2.3.1 and then estimating how massive the dark matter needed to be in order to attract sufficient amounts of baryonic gas in Section 2.3.2.

2.3.1 Growth of initial density fluctuations

The initial evolution of small density fluctuations can be examined analytically in the linear regime, while the non-linear evolution during the actual collapse of the overdense structure needs to be modeled numerically. For the linear approach only small density perturbations, i.e. $|\delta| << 1$ where $\delta = \delta\rho/\rho_0$ is the density contrast, on top of a uniform background density ρ_0 are considered[1]. The latter solely changes with the expansion of the Universe, $\rho_0(t) = \rho_0(t)(1+z)^3$; see also Eq. (2.9) above[2]. How the tiny fluctuations evolve can be studied with linear perturbation theory. For that, one formulates the continuity equation, the momentum equation and the Poisson equation

$$\frac{\partial\rho}{\partial t} + \nabla\cdot(\rho\mathbf{v}) = 0 \tag{2.20}$$

$$\frac{\partial\mathbf{v}}{\partial t} + (\mathbf{v}\cdot\nabla)\,\mathbf{v} = -\frac{\nabla P}{\rho} + \nabla\Phi \tag{2.21}$$

$$\nabla^2\Phi = 4\pi G\rho \tag{2.22}$$

with a slightly disturbed density and velocity, $\rho(\mathbf{x},t) = \rho_0(t) + \delta\rho(\mathbf{x},t)$ and $v(\mathbf{x},t) = v_0(t) + \delta v(\mathbf{x},t)$. Here, $v_0(t) = H\mathbf{r}$ is the velocity field of the Hubble flow, and $\mathbf{x}$ denotes comoving spatial coordinates. To first order in the perturbed quantities, we find

$$\ddot{\delta} + 2H\dot{\delta} = \left(4\pi G\rho_0\delta + \frac{c_\mathrm{s}^2\nabla^2\delta}{a^2}\right) \tag{2.23}$$

where pressure in the momentum equation (2.21) is substituted by an isothermal equation of state $p = \rho c_\mathrm{s}^2$. We can solve this with a plane wave ansatz

$$\delta(\mathbf{x},T) = \int \frac{d^3k}{(2\pi)^3}\hat{\delta}(\mathbf{k},t)e^{-i\mathbf{k}\cdot\mathbf{x}} \tag{2.24}$$

and get

$$\ddot{\hat{\delta}} + 2H\dot{\hat{\delta}} = \hat{\delta}\left(4\pi G\rho_0 + \frac{c_\mathrm{s}^2k^2}{a^2}\right)\ . \tag{2.25}$$

The first term on the right-hand-side of Eq. (2.26) describes gravity, the second one thermal pressure. The pressure is written in terms of an isothermal equation of state here: $P = \rho c_\mathrm{s}^2$. In our discussion, we distinguish between baryonic and dark matter.

---

[1] This approach breaks down when $|\delta| \gtrsim 1$, which is then treated in non-linear computations.

[2] We omit the subscript "m" for matter here.

Baryonic matter: $P = \rho c_\mathrm{s}^2$

On large spatial scales, $k \rightarrow 0$ or $\lambda = 2\pi/k \rightarrow \infty$, the gravity overcomes thermal pressure forces. Thus, Eq. (2.26) can be simplified to

$$\ddot{\hat{\delta}} + 2H\dot{\hat{\delta}} = 4\pi G\rho_0\hat{\delta} \ . \tag{2.26}$$

This has a decaying-mode solution $\hat{\delta} \propto t^{-1}$ and a growing-mode solution $\hat{\delta} \propto t^{2/3}$; both are scale-independent.

Towards smaller spatial scales, $k \rightarrow \infty$ or $\lambda \rightarrow 0$, where pressure cannot be neglected anymore, we can derive an expression for the scale at which pressure and gravity forces become comparable. We equate the two terms on the right-hand-side of Eq. (2.26) to get the so-called Jeans scale

$$k_\mathrm{J} \equiv \frac{2\sqrt{\pi G\rho_0}}{c_\mathrm{s}} \tag{2.27}$$

above which gravity dominates over thermal pressure and density perturbations can grow. For smaller perturbations the pressure gradient that arises will tend to smooth out the fluctuation. In real space, we can derive the Jeans length for $\lambda = 2\pi/k$,

$$\lambda_\mathrm{J} \equiv c_\mathrm{s}\sqrt{\frac{\pi}{G\rho_0}} \ . \tag{2.28}$$

and formulate an expression for the mass belonging to the perturbation:

$$M_\mathrm{J} = \frac{4\pi}{3}\rho_0\left(\frac{\lambda_\mathrm{J}}{2}\right)^3 \tag{2.29}$$

$$= \frac{1}{6}\pi^{-1/2}G^{-3/2}\frac{c_\mathrm{s}^3}{\rho_0^{1/2}} \ . \tag{2.30}$$

We note that the Jeans mass M_J just gives a rough guidance for the actual critical mass for collapse as we have derived this expression under simplified assumptions, e.g. we assumed that the overdense region has a uniform density.

Dark matter: $P = 0$

As dark matter is pressureless (see also Eq. (2.8)), Eq. (2.25) reduces to Eq. (2.26) on all scales, i.e. dark matter perturbations grow in a mostly scale-independent fashion. They initially follow $\delta \propto t^{2/3}$ until they enter the non-linear growth regime. However, similar to the effects of thermal pressure on baryonic matter fluctuations, dark matter has a small but non-zero velocity dispersion which leads to suppression of the growth of perturbation on small scales comparable to the size of the Earth.

2.3.2 Dark matter halos and baryonic gas

Numerical simulations show that dark matter halos are ellipsoid-shaped objects in the intersections of large-scale filamentary structure, the so-called the cosmic web; see also Fig. 2.3 for an illustration. The halos steadily continue to grow through accretion and through merging with other halos from their close environment.

After decoupling from the radiation, baryonic gas will flow into dark matter halos that have grown massive enough to gravitationally attract it. The critical mass scale of

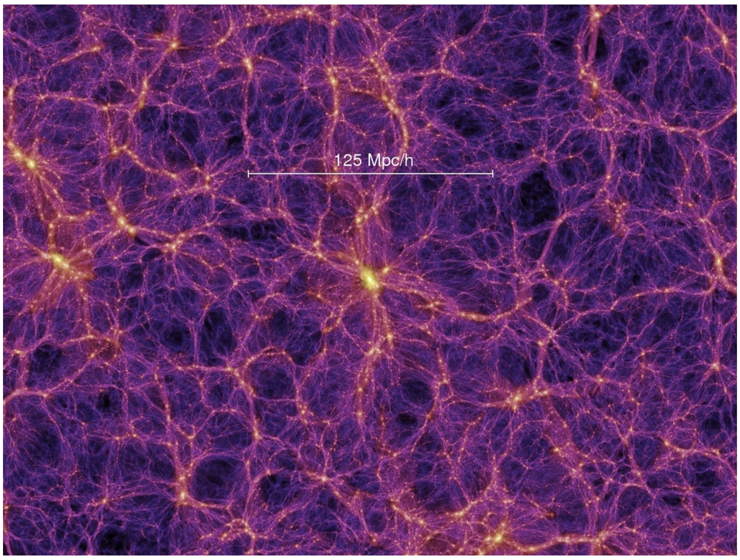

Figure 2.3: The dark matter distribution of the cosmic web at $z = 1.4$. Dark matter halos form at intersections of the large-scale filamentary structure. They have ellipsoidal shape. Image credit: Volker Springel, Millennium Simulation, 2005; see also Springel et al. (2005). Image source: `http://wwwmpa.mpa-garching.mpg.de/galform/virgo/millennium/seqF_037a_half.jpg`.

dark matter halos in this case can be estimated with the Jeans mass. From Eq. (2.30), we see that $M_{\mathrm{J}} \propto c_{\mathrm{s}}^3 \rho^{-1/2} \propto T^{3/2} \rho^{-1/2}$. At redshift $z >> 100$, the coupling between baryons and radiation is still tight so that both have a common temperature evolution of $T \propto (1 + z)$; see Eq. (2.11). Since matter evolves as $\rho \propto \rho_0 a^{-3} \propto \rho_0 (1 + z)^3$, the Jeans mass is constant and given by (Barkana & Loeb, 2001):

$$M_{\mathrm{J}} = 1.35 \times 10^5 \left(\frac{\Omega_m h^2}{0.15} \right)^{-1/2} \mathrm{M}_\odot \ . \tag{2.31}$$

The mass of the dark matter halos is still smaller than that for $z >> 100$. At $z < 100$, the baryonic gas temperature evolves independently from the radiation temperature and follows $T \propto (1+z)^2$ yielding a time-dependent Jeans mass expression given by (Glover, 2013)

$$M_{\mathrm{J}} = 5.18 \times 10^3 \left(\frac{\Omega_m h^2}{0.15} \right)^{-1/2} \left(\frac{\Omega_b h^2}{0.026} \right)^{-3/5} \left(\frac{1+z}{10} \right)^{3/2} \mathrm{M}_\odot \ . \tag{2.32}$$

The time-dependence of the Jeans mass at $z < 100$, makes it difficult to derive a general minimum mass scale for dark matter halos. However, one can use the so-called filter mass (Gnedin & Hui, 1998) which is an appropriately time-averaged version of the Jeans mass:

$$M_{\mathrm{F}} = \frac{4\pi}{3} \rho_0 \left(\frac{\lambda_{\mathrm{F}}}{2} \right)^3 \tag{2.33}$$

with the filter wavelength (Gnedin, 2000)

$$\lambda_{\mathrm{F}}^2 = \frac{3}{1+z} \int_z^\infty \lambda_{\mathrm{J}}^2 \left[1 - \left(\frac{1+z}{1+z'} \right)^{1/2} \right] dz' \ . \tag{2.34}$$

The masses of first dark matter halos that become comparable to the filter mass are $M \gtrsim 2 \times 10^4\,\mathrm{M}_\odot$ at $z \simeq 30 - 40$ (Naoz & Barkana, 2007). The minimum mass is, however, further increased to $M > 2 \times 10^5\,\mathrm{M}_\odot$ at $z \sim 30$ due to streaming velocities of baryonic matter relative to the dark matter (Tseliakhovich & Hirata, 2010). Prior to decoupling, the baryonic-matter-radiation fluid has a sound speed that is almost half the speed of light. Although, the sound speed of the baryonic component drops to the value of the adiabatic sound speed $c_\mathrm{s} = \sqrt{\gamma k_\mathrm{B} T/(\mu m_\mathrm{p})}$, where γ is the adiabatic index and m_p the proton mass, it continues to have a velocity of $\sim 30\,\mathrm{km\,s^{-1}}$ relative to the dark matter. While at $z \simeq 30 - 40$ the size of the relative streaming velocity has declined to a few $\mathrm{km\,s^{-1}}$, it is still supersonic and as such the relative streaming velocities have a considerable impact similar to an effectively increased sound speed. As a consequence the infall of baryonic gas into dark matter halos is delayed to lower redshift and with it the onset of first star formation (Tseliakhovich et al., 2011; Fialkov et al., 2012).

The first dark matter halos that fulfill the minimum mass criterion are called "minihalos" and have typical masses of a few $10^5 - 10^7\,\mathrm{M}_\odot$ at $z \sim 20 - 30$ (e.g. Tegmark et al., 1997; Yoshida et al., 2003). Only from this mass range on, enough baryonic gas falls into the halo and may form a sufficiently high fractional abundance of molecular hydrogen so that the gas can cool to $T \sim 200 - 300\,\mathrm{K}$ and trigger collapse and first star formation. We will discuss this constraint in more details in the next section.

2.4 Primordial chemistry

We briefly recap the chemical composition of the primordial gas at the end of the recombination era ($z \sim 800$); for further details see also Section 2.2. The gas consists in total mass mainly of neutral hydrogen, (H; $\sim 75\%$) and neutral atomic helium (He; $\sim 25\%$). Further constituents in significantly smaller abundances are deuterium (D; $\mathrm{D/H} \simeq 2.5 \times 10^{-5}$) and lithium (Li; $\mathrm{Li/H} \simeq 5 \times 10^{-10}$ - most of this in the form of singly ionized lithium rather than neutral atoms) (Cyburt et al., 2008). Since the helium recombined at much higher redshift than hydrogen, there are almost no helium ions remaining at that time, whereas the ionized hydrogen fraction is still $\mathrm{H^+/H} \simeq \mathrm{D^+/D} \simeq 2.5 \times 10^{-3}$ (Wong et al., 2008; Cyburt et al., 2008). For all other molecular or ionized species fractional abundances were much lower ($< 10^{-12}$) (Alizadeh & Hirata, 2011), and heavier elements still need to be first produced in the first and second generations of stars and their supernovae.

Due to this simple chemical composition lacking metal species and dust, which are very efficient gas coolants in later stages of the universe, molecular hydrogen, $\mathrm{H_2}$, is the most important coolant within the primordial gas (e.g. Saslaw & Zipoy, 1967). $\mathrm{H_2}$ has quantized rotational, vibrational and electronic states, of which the smallest energy difference is given by the transition between the second and zeroth rotational level with $E_{20}/k \approx 512\,\mathrm{K}$ [3]. Therefore, this transition together with vibrational transitions allows the gas to cool down to $T \sim 150 - 200\,\mathrm{K}$ depending on the fractional abundance of $\mathrm{H_2}$ and the gas density.

While the gas flows into the dark matter potential wells, it is heated to roughly the

---

[3] The transition between the first and zeroth rotational level is highly forbidden as $\mathrm{H_2}$ has no permanent dipole moment.

virial temperature of the minihalo[4]

$$T_{\mathrm{vir}} \simeq 2000 \left(\frac{M_{\mathrm{halo}}}{10^6\,\mathrm{M}_\odot} \right)^{2/3} \left(\frac{1+z_{\mathrm{vir}}}{20} \right) \mathrm{K} \ . \tag{2.35}$$

by adiabatic compression and through shocks. In order to trigger collapse and star formation, the gas within the minihalo must be able to proceed efficient cooling and radiate away the accumulated thermal energy (Hoyle, 1953; Rees, 1976; Rees & Ostriker, 1977). A fractional abundance of $x_{\mathrm{H}_2} \sim 10^{-3}$ enables enough cooling (Tegmark et al., 1997; Glover, 2013). Both the amount of molecular hydrogen that forms (see more details below) as well as the H_2 cooling rate strongly increase with the gas temperature (e.g. Glover & Abel, 2008; Glover, 2013). It is found that the actual amount of molecular hydrogen needed for efficient cooling becomes smaller with higher temperature. Thus, a critical temperature value can be derived above which the gas will be able to form enough H_2 for the gas within a minihalo to cool to temperatures where collapse and star formation is triggered. For $x_{\mathrm{H}_2} \sim 10^{-3}$ the critical temperature is $T_{\mathrm{crit}} \sim 1000\,\mathrm{K}$ and it is insensitive to the redshift (Tegmark et al., 1997; Glover, 2013). Using this temperature in Eq. (2.35) and solving for the halo mass we receive $M_{\mathrm{halo}} \sim 4 \times 10^5\,\mathrm{M}_\odot$ as representative value for a minihalo that is massive enough to attract baryonic gas so that it can form sufficient H_2 to cool and promote star formation.

There are three main processes that govern the formation of molecular hydrogen in the primordial gas in the minihalo prior to the formation of the first protostar: H_2 formation via the H^- and the H_2^+ channel, which lead to a molecular hydrogen fraction of $x_{\mathrm{H}_2} \sim 10^{-3}$ during the initial low density evolution of the gas within the minihalo and the initial stages of gas collapse ($n < 10^8\,\mathrm{cm}^{-3}$), and three-body H_2 formation yielding to about fully molecular gas during gas collapse for number densities of $n \gtrsim 10^8\,\mathrm{cm}^{-3}$. The direct formation of H_2 via

$$\mathrm{H} + \mathrm{H} \rightarrow \mathrm{H}_2 + \mathrm{e}^- \tag{2.36}$$

is forbidden as H_2 has no dipole moment and happens at negligible rate (Gould & Salpeter, 1963). Both the H^- channel,

$$\mathrm{H} + \mathrm{e}^- \rightarrow \mathrm{H}^- + \mathrm{h}\nu \tag{2.37}$$

$$\mathrm{H}^- + \mathrm{H} \rightarrow \mathrm{H}_2 + \mathrm{e}^- \ , \tag{2.38}$$

and the H_2^+ channel,

$$\mathrm{H} + \mathrm{H}^+ \rightarrow \mathrm{H}_2^+ + \mathrm{h}\nu \tag{2.39}$$

$$\mathrm{H}_2^+ + \mathrm{H} \rightarrow \mathrm{H}_2 + \mathrm{H}^+ \ , \tag{2.40}$$

where some photons of energy $h\nu$ are emitted, rely on the presence of either free electrons or protons (or ionized atomic hydrogen) in order to catalyze their reactions. These originate from the residual ionization abundance from the recombination era or through ionization during shocks while the gas streams into the minihalo potentials. The former is $x \sim 2 \times 10^{-4}$ in the IGM prior to first star formation (Schleicher et al., 2008). The latter is generally negligible for the minihalos that host the very first stars and becomes

---

[4] Equation (2.35) is taken from Bromm (2013) and assumes that the gas consists mainly of neutral hydrogen with a mean molecular weight of $\mu \approx 1.2$. See for a more elaborate expression e.g. Barkana & Loeb (2001). The definition of T_{vir} in Eq. (2.35) should be seen as an approximate estimate. Formulae in the literature may differ depending on the assumptions made for their derivation.

relevant only later in time when the radiation of the first stars can affect gas in their host halos or in neighboring halos by ionizing radiative feedback (see also Section 2.5.4 below), or when more massive halos have formed within which significant amounts of gas can be collisionally ionized while falling into the halo. For a ionization fraction of $x = n_{\mathrm{H}^+}/n_{\mathrm{H}} \gtrsim 0.03$ the number of mutual neutralizations,

$$\mathrm{H}^- + \mathrm{H}^+ \rightarrow \mathrm{H} + \mathrm{H} \ , \tag{2.41}$$

strongly increases and reduces the available amount of H^- and thus of H_2 formed via the H^- channel (Glover, 2005). For the studies presented in this thesis, however, mutual neutralizations are negligible.

H^- and H_2^+ are sensitive to being photodissociated by photons from the cosmic microwave background. This is important at high redshift, but becomes less important as the redshift decreases and the CMB cools. For this reason, molecular hydrogen can start forming via the H_2^+ channel only after $z \sim 330$. Due to the lower binding energy of H^-, it takes until $z \sim 100$ for the H^- pathway to become effective. Before primordial chemistry that leads to first star formation begins in the minihalos, only a fractional abundance of $x_{\mathrm{H}_2} \sim 2 \times 10^{-6}$ is created via the two pathways. For $z < 100$, the efficiency of the H_2^+ channel declines with the decreasing temperature in the Universe. In the primordial gas in minihalos, formation of molecular hydrogen via the H^- channel thus makes up $\sim 80 - 90\,\%$ of the total amount of H_2 formed.

While the actual formation of H_2 in the associative detachment reaction in the bottom lines of the reaction pairs (2.37) and (2.39) happens fast, the amount of molecular hydrogen depends strongly on the rates at which H^- and H_2^+ are created, i.e. the radiative attachment in the top lines of the two reactions chains. Under the assumption that radiative recombination of electrons and hydrogen ions is the only other process that affects the amounts of e^- and H^+, one finds that the H_2 fraction is strongly temperature dependent and scales as $x_{\mathrm{H}_2} = k_{\mathrm{ra}}/k_{\mathrm{rec}} \ln(1 + t/t_{\mathrm{rec}})$, where k_{ra} and k_{rec} are the rate coefficients for the radiative attachment and the recombination and t_{rec} is the recombination time. As we can see the evolution of the molecular hydrogen fraction is logarithmic: most of the molecular hydrogen is created within a few recombination times but then further H_2 formation stagnates due to the loss of electrons and hydrogen ions to the recombinations. The ratio of the rate coefficients is therefore the dominant factor that determines the amount of molecular hydrogen. It is strongly temperature dependent with $k_{\mathrm{ra}}/k_{\mathrm{rec}} \simeq 10^{-8}\,T^{1.5}$ and yields a molecular hydrogen fraction of $x_{\mathrm{H}_2} \sim 10^{-3}$ for the typical temperatures of a few thousand Kelvin in the gas (see e.g. Glover, 2013).

During gas collapse, three-body H_2 formation becomes effective for densities $n \gtrsim 10^8\,\mathrm{cm}^{-3}$:

$$\mathrm{H} + \mathrm{H} + \mathrm{H} \rightarrow \mathrm{H}_2 + \mathrm{H} \tag{2.42}$$

$$\mathrm{H} + \mathrm{H} + \mathrm{H}_2 \rightarrow \mathrm{H}_2 + \mathrm{H}_2 \tag{2.43}$$

and

$$\mathrm{H} + \mathrm{H} + \mathrm{He} \rightarrow \mathrm{H}_2 + \mathrm{He} \ . \tag{2.44}$$

Since its formation rate is highly density dependent ($\propto n^3$), most of the hydrogen is converted quickly into its molecular form during ongoing collapse, i.e. $x_{\mathrm{H}_2} \sim 1$ (Palla et al., 1983) [5]. Each formation of a hydrogen molecule deposits the binding energy of 4.48eV almost completely in form of thermal energy into the gas. Although the H_2 fraction increases strongly, the cooling is not efficient enough to counteract the overall temperature increase of the gas due to this formation heating. The heating due to three-body H_2 formation is the major energy input into the gas at these densities and may also affect the further dynamical evolution of the gas. The two other main cooling processes in the primordial gas beside H_2 line cooling are H_2 collision-induced emission (CIE) cooling ($n \sim 10^{14}$–$10^{16}\,\mathrm{cm}^{-3}$) and H_2 collisional dissociation cooling ($n \gtrsim 10^{16}\,\mathrm{cm}^{-3}$). For more details of the chemistry during primordial gas collapse see Section 2.5.1 and for a more numerical perspective Section 3.2.3.

Finally, H_2 molecules are mainly destroyed through two processes. The first is collisional dissociation

$$\mathrm{H_2 + H \rightarrow H + H + H} \tag{2.45}$$

$$\mathrm{H_2 + H_2 \rightarrow H + H + H_2} \tag{2.46}$$

which however is only important in gas with a few thousand Kelvin (for $z < 1000$). This becomes relevant in the Population III star-forming process for $n \gtrsim 10^{16}\,\mathrm{cm}^{-3}$ (see also Section 2.5.1 below) and acts as a cooling process, as for each dissociation an energy of 4.48 eV is subtracted from the gas.

The second H_2 destruction process is photodissociation of molecular hydrogen by UV Lyman-Werner (LW) photons with energies between 11.2 eV (energy of from H2 ground state to the Lyman state) and 13.6 eV. It is a two-step process, called the Solomon process,

$$\mathrm{H_2 + h\nu \rightarrow H_2^* \rightarrow H + H} \tag{2.47}$$

based on an excitation of H_2 to the second of third electronic state by the LW photons, a subsequent decay of $\sim 15\%$ of the molecules to the vibrational continuum, and finally the dissociation of those (Field et al., 1966; Stecher & Williams, 1967). This process has a strong influence on the environment of the radiating star; see also Section 2.5.4. Further destruction processes that depend on stellar radiation are photonionization for photon energies above 13.6 eV, or excitation to the vibrational continuum from an excited state[6]. However, although such processes are important in principle (e.g. Hosokawa et al., 2011; Stacy et al., 2012; Susa et al., 2014; Stacy et al., 2016), they do not play a role in most of the situations studied in this thesis.

2.5 Population III stars

2.5.1 Protostellar collapse

First star formation can be triggered in primordial gas in minihalos that is able to produce molecular hydrogen fractional abundances of $x_{\mathrm{H_2}} \sim 10^{-3}$. This allows the gas to cool down to $T \sim 200\,\mathrm{K}$. As we have already seen in Section 2.3 from Eq. (2.30), the Jeans mass, a measure of the balance between gas self-gravity and thermal pressure,

---

[5] At these densities, reaction (2.42) is the dominant one. However, its exact rate coefficient value is currently still under debate (Glover, 2008; Turk et al., 2011). The choice of the values affects the morphology of the gas, its velocity structure and its temperature profile (Turk et al., 2011). See also Section 3.2.3 for the choice in our numerical method.

[6] Direct excitation to the vibrational continuum from the ground state is strongly forbidden (Glover & Brand, 2001).

scales as $M_\mathrm{J} \propto c_\mathrm{s}^3 \rho^{-1/2} \propto T^{3/2} \rho^{-1/2}$. With declining temperatures, the self-gravity of a particular gas cloud overweighs its internal thermal pressure at some point and the cloud begins to collapse and condenses further.

If a Jeans-unstable gas cloud has sufficient rotational energy, it may in some cases fragment into two Jeans-unstable clouds that subsequently evolve independently from each other (Machida et al., 2005, 2008b; Turk et al., 2009; de Souza et al., 2013). Turbulent flows which arise during the virialization process of the gas within the dark matter halo (see e.g. Wise & Abel, 2007; Greif et al., 2008), are even more efficient in breaking up the unstable gas within minihalos. In this way clouds of masses $\sim 100 - 1000\,\mathrm{M}_\odot$ form which continue to collapse and evolve into star-forming systems (Abel et al., 2002). For the following description, see also Fig. 2.4.

At a density of $n \sim 10^4\,\mathrm{cm}^{-3}$, the gas enters the so-called "loitering phase" (Bromm et al., 2002) where the collapse is slowed down. Even though more material falls in and accumulates in the center of the minihalo, the gas density only grows slowly. $n = 10^4\,\mathrm{cm}^{-3}$ is often termed the *critical density* n_crit. At this point the rotational and vibrational level populations of H_2 are close to their local thermodynamic equilibrium (LTE) values. This means that for $n > 10^4\,\mathrm{cm}^{-3}$, the cooling rate per unit volume (Λ) of molecular hydrogen scales like $\Lambda_{\mathrm{H}_2} \propto n$ compared to its lower density behaviour of $\Lambda_{\mathrm{H}_2} \propto n^2$, i.e. cooling becomes less effective. In addition, heating processes such as compressional heating start to dominate over cooling processes and consequently the gas begins to heat up.

The collapse decouples locally, meaning that it detaches form the large-scale behavior of the gas, and speeds up again, when it reaches the local Bonnor-Ebert mass (Ebert, 1955; Bonnor, 1956). For the value of the critical density at a temperature of $T \sim 200\,\mathrm{K}$ this mass limit is $M_\mathrm{BE} \sim 1000\,\mathrm{M}_\odot$.

The next important evolutionary step of the gas collapse sets in when the gas density is of the order of $n \sim 10^8\,\mathrm{cm}^{-3}$ and three-body H_2 formation sets in leading to a almost fully molecular gas (Palla et al., 1983). The increased cooling efficiency due to the larger amount of molecular hydrogen, is, however not completely able to counteract the significant H_2 formation heating. At $n \sim 10^9\,\mathrm{cm}^{-3}$ the collapse even stalls. Although the strong increase of the main coolant molecular hydrogen, can trigger some local chemothermal instabilities within the gas, their perturbations do not have enough time to grow significantly to induce fragmentation as the collapse proceeds in about the same timescale ($t_\mathrm{growth} \sim t_\mathrm{collapse}$) (Yoshida et al., 2006).

At $n \sim 10^{10}\,\mathrm{cm}^{-3}$, the main rotational and vibrational lines of H_2 start to become optically thick. Cooling becomes ineffective, but is not suppressed completely: there is still some dissipation of energy possible through the wings of the H_2 emission lines which can escape through low continuum opacity regions of the gas which has been shown in several 1D- and 3D-simulations (e.g. Omukai & Nishi, 1998; Omukai et al., 1998; Ripamonti et al., 2002; Ripamonti & Abel, 2004; Yoshida et al., 2006; Turk et al., 2009; Clark et al., 2011a). Therefore, the gas temperature does not increase too much and collapse is able to proceed.

At $n \sim 10^{14}\,\mathrm{cm}^{-3}$, collision-induced emission (CIE) of H_2 becomes important as coolant (Ripamonti & Abel, 2004). At such high densities, it is likely for two colliding H_2 molecules to form a combined, complex intermediate state (super-molecule) that has a non-zero dipole moment and can emit a photon via dipole transitions. The lifetime of the collision state is only of the size of $\delta t < 10^{-12}\,\mathrm{s}$ and thus makes this reaction

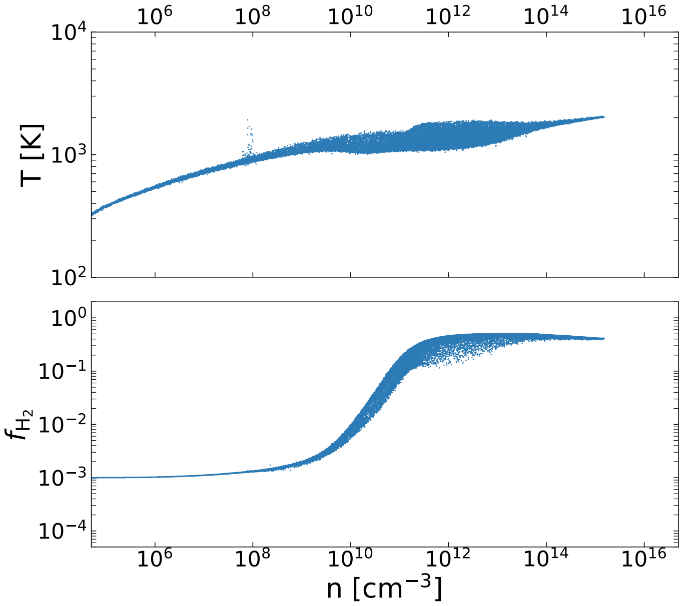

Figure 2.4: Gas temperature and molecular fraction, $x_{\mathrm{H}_2} = f_{\mathrm{H}_2}$ as function of number density. We show the distribution of the gas cells in run β001-1 from Chapter 5 just before the formation of the first protostar. The simulation started from a primordial gas cloud with Bonnor-Ebert density profile and rigid rotation described by a β parameter of $\beta = 0.01$, see also Section 3.2.5. Image credit: myself.

unlikely to happen at lower densities. Following Heisenberg's Uncertainty principle,

$$\Delta E \Delta t \geq \frac{\hbar}{2} \, , \tag{2.48}$$

due to the short lifetime of the super-molecule state, there will be a large spread in the photon energies of the dipole transition. The individual emission lines of the dipole transition will further broaden and eventually merge into a continuum that allows the gas to further emit sufficient energy and cool (Omukai & Nishi, 1998; Ripamonti et al., 2002; Ripamonti & Abel, 2004).

However, at $n \sim 10^{16}\,\mathrm{cm}^{-3}$, the gas finally becomes optically thick also in the continuum and thus CIE becomes ineffective and gas cooling is strongly suppressed (Omukai & Nishi, 1998; Ripamonti & Abel, 2004). Radiative cooling is no longer effective. In the further collapse evolution, the gas heats therefore up until at $T \sim 2000\,\mathrm{K}$, molecular hydrogen starts dissociating. The dissociation behaves as a thermostat since the energy gained through the collapse is converted into the energy needed to dissociate a hydrogen molecule, and thus the temperature does not change much. Once the H_2 abundance is exhausted, the temperature continues to increase during this further adiabatic collapse until around $T \sim 10000\,\mathrm{K}$. At this point atomic hydrogen starts ionizing and acts again as a thermostat until all gas is ionized. At a density of $n \sim 10^{20}\,\mathrm{cm}^{-3}$, the temperature has grown such that the thermal pressure within the gas core of size $\sim 0.1\,\mathrm{AU}$ and with a mass of $\sim 0.01\,\mathrm{M}_\odot$ is able to counteract further collapse and it is bound by a strong accretion shock (Yoshida et al., 2008). The Population III protostar is born.

2.5.2 Accretion

Population III accretion rates are generally higher than those found in present-day star-forming environments because of the limited cooling ability of the primordial gas yielding temperatures $T \sim 200 - 300\,\mathrm{K}$ compared to $T \sim 10\,\mathrm{K}$ in present-day star-forming cores. As a first estimate of the accretion rate, one can consider the gas inflow from the collapsing envelope toward the cloud center. This rate is given through the ratio of the Jeans mass, $M_\mathrm{J}(R) \propto c_\mathrm{s}^3/\sqrt{G^3\rho} \propto T^{3/2}/\rho^{1/2}$, within radius R, and the free-fall time at this radius, $t_\mathrm{ff} = \sqrt{3\pi/(32G\rho)} \propto (G\rho)^{-1/2}$, where ρ is the mean density of the cloud. Here, we assume that a gravitational unstable cloud of radius R, described via the Jeans mass and the mean gas density, has a characteristic collapse time which is the free-fall time:

$$\dot{M} \sim \frac{M_\mathrm{J}(R)}{t_\mathrm{ff}(R)} \sim \frac{c_\mathrm{s}^3}{G} \propto T^{3/2} \ . \tag{2.49}$$

The main dependency lies on the sound speed and correspondingly the gas temperature in the star-forming cloud (Larson, 1969; Shu, 1977) leading to about a two orders of magnitude higher accretion rate in primordial gas ($\dot{M} \sim 10^{-3} - 10^{-2}\,\mathrm{M_\odot\,yr^{-1}}$) compared to present-day gas. We note that this is only a simple order of magnitude estimate as in reality the gas collapse proceeds more slowly than with t_ff due to e.g, thermal pressure support within the gas, and the density structure is non-uniform.

Furthermore in reality, the collapsing gas cloud has some non-negligible angular momentum. After an initial adiabatic, spherical accretion phase (roughly until the mass of the protostar is $M \sim 0.1\,\mathrm{M_\odot}$; see e.g. Hosokawa & Omukai (2009) and Hosokawa et al. (2010)), during which the accreted material accumulates around the protostar without significant cooling, the gas angular momentum leads to the formation of a rotationally supported disk around the densest point and thus the protostar. The inflow rate discussed above then illustrates the mass flux from the envelope onto the disk. The disk expands rapidly in an inside-out fashion. Viscous transport leads to a redistribution of angular momentum in order to maintain angular momentum conservation. Material moving inwards gives angular momentum to disk material which consequently needs to move further out (so-called viscous disk spreading, see e.g. Lynden-Bell & Pringle, 1974). In this way, the disk funnels gas toward the central parts where the protostellar core grows via accretion.

A common description of the mass flux through disks is given by the Shakura & Sunyaev (1973) model

$$\dot{M}(R) \simeq 2\pi\,\nu(R)\,\Sigma(R) \tag{2.50}$$

where $\Sigma(R)$ is the surface density of the disk and ν is the turbulent, kinematic viscosity of the gas of the form

$$\nu_{vis}(R) \simeq \alpha\,c_\mathrm{s}(R)\,H_\mathrm{p}(R) = \alpha\,\frac{c_\mathrm{s}^2(R)}{\Omega(R)} \ . \tag{2.51}$$

with the sound speed $c_\mathrm{s}(R)$, the pressure scale height of the disk $H(R)$, and the angular frequency Ω of the disk. The mass flow through the disk crucially depends on the origin and corresponding strength of effective viscosity of the disk gas. The viscosity is responsible for shear forces and torques which account for the powerful and effective mass and angular momentum transport through the disk. The value of the Shakura–Sunyaev parameter, α, can for example be derived by magnetorotational instability (MRI) (Balbus & Hawley, 1991) giving values of $\alpha \sim 0.01$, or by gravitational instabilities even leading to $\alpha \sim 1$ (see e.g. Clark et al., 2011a). The exact origin and

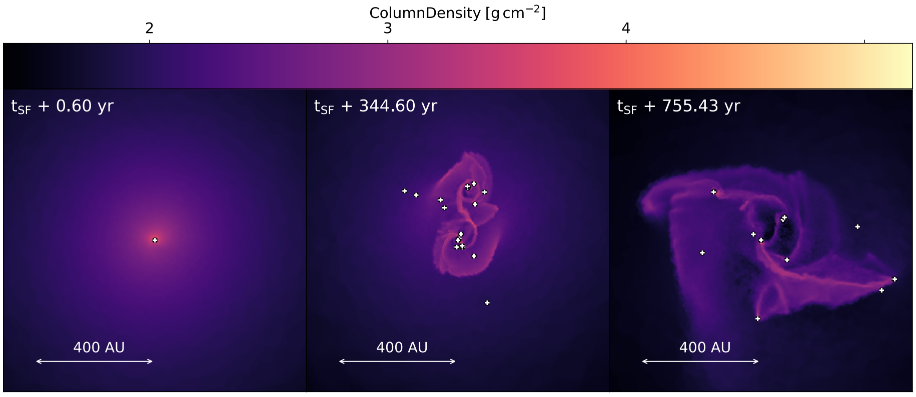

Figure 2.5: Column density projections of the evolution of the protostellar disk system in run β001-1 from Chapter 5. Times are with respect to the time of the formation of the first protostar. Over time, the disk develops spiral-arm features and fragments. Some of the fragments become new protostars. The protostars are denote by the white circles. The simulation started from a primordial gas cloud with Bonnor-Ebert density profile and rigid rotation described by a β parameter of $\beta = 0.01$, see also Section 3.2.5. The projection has a thickness of 1000 AU. Image credit: myself.

value of this parameter is still under discussion. Under the assumption of $\alpha \approx 1$, using $R = 10\,\mathrm{AU}$, $\Sigma(R) \sim 4 \cdot 10^3\,\mathrm{g\,cm^{-2}}$, $c_\mathrm{s}(R) \sim 2\,\mathrm{km\,s^{-1}}$ and $\Omega(R) \sim v_\mathrm{Kep}(R) \sim 9\,\mathrm{km\,s^{-1}}$ (values taken from Fig. 2, black-dashed line, and Fig. 16 in Clark et al., 2011a), one estimates the disk scale height via a relation for a non-self-gravitating, Keplerian disks (see e.g. Lodato, 2007) as

$$H(R) = \frac{c_\mathrm{s}(R)}{\Omega_\mathrm{K}(R)} = \frac{c_\mathrm{s}(R)R}{v_\mathrm{K}(R)} \sim 2\,\mathrm{AU}\ . \tag{2.52}$$

and with equation (2.50) and (2.51)

$$\dot{M}(R) \approx 4 \cdot 10^{-3}\,\mathrm{M_\odot\,yr^{-1}}\ . \tag{2.53}$$

Again we note that this is just an order of magnitude estimate. The Shakura-Sunyaev model is strictly speaking only valid for thin accretion disks with $H/R << 1$ whereas here $H/R \sim 0.2 < 1$. Nevertheless, this gives us a first idea of accretion rates in the Population III disk context. More advanced analytical approaches and detailed numerical simulations have found that typical Population III accretion rates vary over time and have values of $\dot{M}_\mathrm{acc} \sim 10^{-4} - 10^{-1}\,\mathrm{M_\odot\,yr^{-1}}$, with higher rates in the beginning which steadily decline over a few hundred to a few thousand years (e.g. Omukai & Palla, 2001; Abel et al., 2002; Omukai & Palla, 2003; Yoshida et al., 2008; Clark et al., 2011b,a; Greif et al., 2011; Smith et al., 2012; Greif et al., 2012; Hirano et al., 2014; Stacy et al., 2016). It also has been found that inflow rates onto the disk are generally higher than the mass flux through the disk leading to thick accretion disks that are strongly self-gravitating and that eventually become gravitationally unstable and prone to fragmentation (e.g. Turk et al., 2009; Stacy et al., 2010; Clark et al., 2011b,a; Greif et al., 2011; Smith et al., 2012; Greif et al., 2012; Latif & Schleicher, 2015; Stacy et al., 2016; Hosokawa et al., 2016). See also Fig. 2.5.

New protostars can be formed in locally unstable disk gas, when the gas is able to cool faster than its collapse timescale (Rees & Ostriker, 1977) and when the collapse proceeds on times shorter compared to the shear motions within the rotating disk (Gammie, 2001). For a first analysis of the disk stability the *Toomre criterion* (Toomre, 1964) can be used. The Toomre parameter

$$Q(R) = \frac{\kappa(R)\, c_{\mathrm{s}}(R)}{\pi G \Sigma(R)} \tag{2.54}$$

compares disk self-gravity, denoted by the surface density $\Sigma(R)$, to thermal pressure and rotation within the disk. The latter two are indicated by the sound speed $c_s(R)$ and the epicyclic frequency $\kappa(R)$ respectively, and act to stabilize the disk against perturbations induced by self-gravity. In case of a Keplerian disk, the epicyclic frequency equals the angular velocity, $\kappa(R) = \Omega(R) = \sqrt{GM(R)/R^3}$. The parameters defining the Toomre-Q vary with the radius in the disk. A disk is said to be stable for $Q > 1$ and unstable for $Q < 1$. When $Q \sim 1$ the disk is strongly self-gravitating and is about to become unstable. Non-axisymmetric perturbations within the disk can grow and may lead to the development of spiral arms in order to redistribute the excess material and its angular momentum efficiently. Gravitational torques arising from the spiral arms facilitate the outward transfer of angular momentum (e.g. Clark et al., 2011a; Greif et al., 2012; Stacy et al., 2016; Hosokawa et al., 2016).

Fragmentation may not be a necessary result of $Q < 1$. However, it is promoted with the simultaneous fulfillment of the *Gammie criterion* (Gammie, 2001),

$$t_{\mathrm{thermal}} \leq 3\Omega^{-1} \equiv \frac{3}{2\pi}\, t_{\mathrm{orbital}}, \tag{2.55}$$

which compares cooling and orbital timescales. Here, $t_{\mathrm{thermal}} = e/\Lambda$ with e is the internal energy density and Λ is the volumetric cooling (or heating) rate, and $t_{\mathrm{orbital}} = 2\pi/\Omega$. Clark et al. (2011a) and Greif et al. (2012) for example found both criteria to be fulfilled over a wide radius range and note their strong dependence on the disk thermodynamics. Due to a thermostat effect, that is balancing thermal feedback from the protostar and heating from compressional dissociation of H_2 with cooling from H_2–line and collision-induced emission or from collisional dissociation, the disk temperature stays roughly constant between $1000 - 3000\,\mathrm{K}$.

If the disk eventually breaks up, new protostars may arise in locally dense enough regions and a Pop III protostellar cluster builds up. The evolution of an individual protostar depends on its interactions with the surrounding gas and the other objects in the cluster. The protostars compete for their common mass reservoir, yielding highly variable accretion rates Greif et al. (2011); Greif et al. (2012); Smith et al. (2012); Hosokawa et al. (2016). Some protostars might even stop accreting completely if their gas supply is removed by fragmentation or accretion onto neighboring protostellar companions, a process termed fragmentation-induced starvation in the context of present-day star formation (Peters et al., 2010). Furthermore, during close encounters protostars might get disrupted or even merge (Greif et al., 2011; Greif et al., 2012; Stacy et al., 2016; Hosokawa et al., 2016). In addition, the complicated multiple-body dynamics during close interactions can lead to ejection of individual protostars from the protostellar disk or even from the halo. Indeed simulations find an ejection rate of $\sim 30\%$ (Greif et al., 2011; Stacy & Bromm, 2013; Stacy et al., 2016). The physics of this process and its dependence on the properties of the initial gas cloud are studied in detail in Chapters 5, 6, and 8.

2.5.3 Evolution of the protostellar structure

Different stages of the evolution of the protostellar structure can be described through the interplay of two timescales. First, there is the accretion timescale

$$t_{\mathrm{acc}} = \frac{M_\star}{\dot{M}_\star} \tag{2.56}$$

which characterizes the time over which the protostar grows in mass through accretion. Here, $M_\star$ is the protostellar mass and $\dot{M}_\star$ the accretion rate. And second, there is the Kelvin-Helmholtz contraction time

$$t_{\mathrm{KH}} = \frac{GM_\star^2}{R_\star L_\star} \tag{2.57}$$

which quantifies the time over which the protostar radiates accumulated energy away. G is the gravitational constant and $M_\star$, $R_\star$, $\dot{M}_\star$ and $L_\star$ are the mass, radius, accretion rate and luminosity of the protostar respectively. The luminosity here is the interior protostellar[7] luminosity due to the release of thermal energy,

$$L_\star = 4\pi R_\star^2 \sigma_{\mathrm{SB}} T_\star^4 \ , \tag{2.58}$$

where σ_{SB} is the Stefan-Boltzmann constant and $T_\star$ the effective temperature. Together with the accretion luminosity

$$L_{\mathrm{acc}} = \frac{GM_\star \dot{M}_\star}{R_\star} \ , \tag{2.59}$$

$L_\star$ makes up the total protostellar luminosity $L_\star + L_{\mathrm{acc}} = L_{\mathrm{tot}}$. L_{acc} describes the energy release at the accretion shock where the accreting material enters the protostellar surface. In the beginning of the protostellar evolution L_{acc} is the dominant source of luminosity. $L_\star$ gradually increases when the protostar becomes able to radiate away excess entropy that is both taken up through the accretion process from the incoming material and produced internally once nuclear burning begins.

Initially $t_{\mathrm{acc}} << t_{\mathrm{KH}}$ and the star grows via accretion while its interior luminosity is still very small. As we have described in Section 2.5.2 above, typical Population III accretion rates of $\dot{M}_{\mathrm{acc}} \sim 10^{-4} - 10^{-2}\,\mathrm{M}_\odot\,\mathrm{yr}^{-1}$ have been found in previous studies (e.g. Omukai & Palla, 2001; Abel et al., 2002; Omukai & Palla, 2003; Yoshida et al., 2008; Clark et al., 2011a; Greif et al., 2011; Greif et al., 2012; Hirano et al., 2014; Stacy et al., 2016). Due to these high rates, significant amounts of entropy are brought into the the stellar interior and can accumulate there. Accretion is termed either "hot" or "cold" depending on whether high or low amounts of entropy are carried along. The net value of entropy that is actually accumulated within the protostar depends on how much of the incoming entropy of the accreted material is already radiated away before entering the stellar surface. The main part of entropy that is taken up into the protostar is produced at the accretion shock where the accretion inflow enters the protostellar surface. In the context of disk accretion where the accreting flow only touches part of the stellar surface, the accretion shock is small. The main entropy source here arises through viscous dissipation within the disk and is mostly already radiated away at the disk surface. Thus, the entropy increase of the protostar through disk accretion is

---

[7] We note that these luminosity relations are still valid and applicable when the star has entered the main sequence.

low compared to spherical accretion where the accretion shock surrounds basically the whole protostellar surface and only little entropy is being radiated away before entering the protostar (Hosokawa & Omukai, 2009; Hosokawa et al., 2010).

Nevertheless, in both kinds of accretion, the protostar takes up new material and with it additional entropy, and because in this first phase of protostellar growth (*convection or adiabatic accretion phase* for $M_\star \lesssim 5-6\,\mathrm{M}_\odot$), the protostellar opacity is high due to bound-free and free-free absorptions (*Kramer's law*: $\kappa \propto \rho T^{-3.5}$), radiative loss of additional entropy is minimal. The core continues to contract, leading to a temperature increase in the central regions which is enough for the opacity there to drop. In this way, the protostar becomes more and more radiative from inward-out which allows it to redistributes its interior entropy and transport it toward its outer layers (*a luminosity wave*; Stahler et al. 1986). An inverted entropy profile arises within the protostar. While the entropy is low in the central parts, it accumulates more and more at the surface originating from both the stellar interior and accretion from the outside. The protostar reacts to excess amounts of entropy by bloating up in radius in order to stay in hydrostatic equilibrium (*swelling phase*). It expands to radii exceeding $100\,\mathrm{R}_\odot$ at a protostellar mass of $5-10\,\mathrm{M}_\odot$: the protostar becomes puffed-up or "fluffy" (Stahler et al., 1986; Omukai & Palla, 2001, 2003; Hosokawa & Omukai, 2009; Hosokawa et al., 2010; Smith et al., 2012; Maeder & Meynet, 2012).

The interior luminosity increases significantly, becomes dominant and consequently $t_{\mathrm{acc}} > t_{\mathrm{KH}}$, when the luminosity wave arrives at the protostellar surface. Excess entropy is now radiated away efficiently, and when more entropy is radiated away than newly taken up, the protostar enters the *Kelvin-Helmholtz contraction phase* ($M_\star \lesssim 10-40\,\mathrm{M}_\odot$). The *Zero-Age Main Sequence* (ZAMS) is reached once the interior luminosity arising from hydrogen burning counteracts further contraction (Omukai & Palla, 2001, 2003; Hosokawa & Omukai, 2009; Hosokawa et al., 2010).

Indeed, nuclear burning in Population III (proto)stars already starts with deuterium burning at core temperatures of $T_c \gtrsim 10^6\,\mathrm{K}$ even before ZAMS and partially contributes to the interior entropy that moves outwards via the luminosity wave (Hosokawa & Omukai, 2009; Hosokawa et al., 2010). Once core temperatures of $T_c \gtrsim 10^8\,\mathrm{K}$ are reached, carbon can be produced via the triple-α process and consequently the CNO cycle can start as well.

2.5.4 Radiative feedback

Due to their puffed-up protostellar structure that leads to low effective temperatures of $T_\star \sim 5000\,\mathrm{K}$, Population III protostars influence their environment mainly through optical and near-infrared radiation that heats up their surroundings but does not further interfere with the accretion, the protostellar mass growth and the disk evolution. The same is true for contributions from the accretion luminosity. Previous studies have shown that accretion luminosity heating is not strong enough to completely stabilize the protostellar disk against fragmentation (Clark et al., 2011a; Smith et al., 2011; Stacy et al., 2016).

Population III stars on the main sequence (typically once $> 10\,\mathrm{M}_\odot$) can have surface temperatures of $T \gtrsim 10^5\,\mathrm{K}$ and thus produce significant ultraviolet (UV) radiation with H_2 photodissociating and photoionizing radiation, i.e. photons with energy $h\nu > 11.2\,\mathrm{eV}$ which affect the accretion process (Bromm et al., 2001b; Omukai & Palla, 2001; Schaerer, 2002; Hosokawa et al., 2011; Stacy et al., 2012). The high surface temperatures are a consequence of higher core temperatures, which occur because the core must become hotter during Kelvin-Helmholtz contraction in order for the triple-α process to become effective and the CNO cycle to start.

A significant effect on the efficiency of accretion arises through thermal pressure due to an increase in gas temperature. This is able to unbind gas and drive it through lower dense regions out of protostellar system, i.e. to photoevaporate them and quench accretion due to the lack of accreting material. Lyman–Werner radiation ($11.2 \leq h\nu \leq 13.6\,\mathrm{eV}$) dissociates H_2 molecules in the surrounding gas envelope, and thus reduces the cooling effect of the gas (e.g. Omukai & Nishi, 1998; Glover & Brand, 2001). Although dense H_2 gas is able to generate some self-shielding against this radiation, it was found that photodissociation heating can greatly slow down accretion but not stop it completely (McKee & Tan, 2008; Stacy et al., 2012; Susa, 2013; Susa et al., 2014; Stacy et al., 2016). In case of photoionization, the energy of electrons freed by the process heats the gas. Temperatures in the HII regions behind the front of ionizing radiation are high enough ($T > 10^4\,\mathrm{K}$) for gas to reach sound speeds that are larger than typical escape velocities from the protostellar system and the entire minihalo (Whalen et al., 2004, 2008). The analytic study by McKee & Tan (2008) followed Hollenbach et al. (1994) and proposed that photoevaporation will stop accretion from about $140\,\mathrm{M}_\odot$ on. More recent 2D simulations by Hosokawa et al. (2011) see the accretion stop already at about $43\,\mathrm{M}_\odot$. In their 3D simulation, Stacy et al. (2016) found that accretion is significantly reduced by thermal pressure generated through both photodissociating and photoionizing radiation. Their simulation run only for $\sim 5000\,\mathrm{yr}$ after the formation of the first protostar so that no definite answer about the final Population III masses can be made in this case.

The efficiency of radiative feedback depends on the three-dimensional structure of the gas surrounding the star. First, chemical self-shielding in high density regions, such as the disk, reduces effects of radiative feedback, (see e.g. Schauer et al., 2015, in the context of H_2 self-shielding and Lyman–Werner escape fractions from primordial minihaloes). Second, low-column-density regions, such as the zones along the polar direction of the protostar–disk system or leaks through a fragmented protostellar disk or the Strömgren sphere of an HII regions generated by ionization front instabilities, make it easier for radiation to escape. The typical density profiles of Pop III star-forming cores, $\rho \propto r^{-2.2}$ found in cosmological simulations (e.g. Abel et al., 2002; Bromm et al., 2002; Yoshida et al., 2008) allows ionizing radiation together with their HII regions to break out of the star-forming core and even the minihalo and to also affect neighboring minihalos radiatively (see e.g. Whalen et al., 2008, 2010; Smith et al., 2015).

When the total protostellar luminosity approaches the Eddington luminosity[8], radiation pressure is able to counterbalance the gravitational infall of material onto the star. The expression of the Eddington limit, however, is mainly valid for spherical symmetry. In realistic simulations, radiation pressure is directed along regions with low column densities and does not affect accretion strongly (e.g. in the context of present-day massive star formation, see Krumholz et al., 2005, 2009; Kuiper et al., 2010, 2011; Kuiper & Yorke, 2013; Kuiper et al., 2015; Klassen et al., 2016). Something similar is true for radiation pressure in Pop III context, e.g. Lyman α radiation pressure has been found to be ineffective in influencing accretion (McKee & Tan, 2008; Stacy et al., 2012). On the other hand, photoionization pressure, as long as it is not diluted through tunnels created by ionization front instabilities yet, might counterbalance the inward ram pressure (e.g.

---

[8] The luminosity of a star is equal to the Eddington luminosity when the outward-directed radiative force is in balance with the inward-directed gravitational force, i.e. above this luminosity, the stellar radiation is able to counteract gravitational infall or accretion onto the star.

Haehnelt, 1995; McKee & Tan, 2008; Stacy et al., 2012). In particular, this might be possible during the early states of a ionization front and a corresponding HII region for $\lesssim 100\,\mathrm{AU}$ distance from the protostar, as motivated in an estimation by Stacy et al. (2012).

2.5.5 Deuterium chemistry and Population III.2 stars

The gas in minihalos can be more strongly ionized through the ionizing radiation of a nearby or progenitor Pop III star (e.g. Oh & Haiman, 2002; Nagakura & Omukai, 2005; Yoshida et al., 2008), through X-rays from Pop III supernova remnants, X-ray binaries, or quasars (e.g. Glover & Brand, 2003; Hummel et al., 2015), or through cosmic rays (Hummel et al., 2016). In massive halos the gas falling into the potential well may also be more strongly shocked and collisionally ionized. Strongly ionized minihalos can be termed *pre-ionized minihalos* in contrary to the above *quiescent minihalos* that have not been affected through radiation before.

In such environments, the gas is able to produce a higher fraction of molecular hydrogen which in turn is able to cool the gas to $T \sim 150\,\mathrm{K}$ or below compared to the otherwise typical $T \sim 200\,\mathrm{K}$. At these temperatures the formation of deuterated hydrogen, HD, is facilitated and since its formation reaction is exotherm while its inverse reaction is endotherm it easily forms from $\mathrm{H_2}$ via

$$\mathrm{H_2} + \mathrm{D^+} \rightarrow \mathrm{HD} + \mathrm{H^+} \ , \tag{2.60}$$

and its abundance may become even larger than the cosmic ratio of D/H (see Section 2.4 above) (Bromm et al., 2002; Johnson & Bromm, 2006; Glover & Abel, 2008). HD has a weak dipole moment that allows a rotational transition between the first excited state and the ground state with a transition energy of $E_{10}^{\mathrm{HD}}/k = 128\,\mathrm{K}$. Thus temperatures down to the temperature of the cosmic microwave background $T_{\mathrm{CMB}} = (1+z)\,2.725\,\mathrm{K}$ ($\sim 57\,\mathrm{K}$ at $z = 20$) are possible (Nagakura & Omukai, 2005; Johnson & Bromm, 2006; Yoshida et al., 2008). HD becomes the dominant cooling at $T \lesssim 200\,\mathrm{K}$[9].

Star formation dominated by HD chemistry is termed Population III.2 in contrast to the one described above in Section 2.5.1 dominated by $\mathrm{H_2}$ which are defined as Population III.1 stars (McKee & Tan, 2008). For a gas collapse proceeding under HD cooling, the critical density is $n_{\mathrm{crit}} \sim 10^6\,\mathrm{cm^{-3}}$, i.e. higher than in the low-ionization case. The corresponding Bonnor-Ebert mass is smaller $M_{\mathrm{BE}} \sim 40\,\mathrm{M_\odot}$ for $T \sim 100\,\mathrm{K}$. The further evolution of the gas and the final mass of Population III.2 is still under debate. Studies by Greif et al. (2011); Hosokawa et al. (2012) and Hirano et al. (2014) suggest smaller final masses compared to Pop III.1 stars in quiescent minihalos because of smaller initial Jeans masses and/or lower accretion rate due to efficient HD cooling. In the simulations by Clark et al. (2011b), on the other hand, cooling by $\mathrm{H_2}$ and HD became inefficient in collapsing gas within pre-ionized minihaloes at some point. Consequently, the gas continued to evolve adiabatically, its temperature rose, and the gas was supported against further gravitational instability. The collapse slows down and turbulent gas motions within the cloud are given enough time to decay. This resulted in that star-forming clouds in their Pop III.2 minihaloes showed a much smaller degree and widespread of fragmentation and thus remained more massive than their Pop III.1 counterparts.

---

[9] Other possible coolants at these low temperature, such as LiH or $\mathrm{H_2^+}$ and $\mathrm{H_3^+}$ have been shown to be unimportant (Mizusawa et al., 2005; Glover & Savin, 2009).

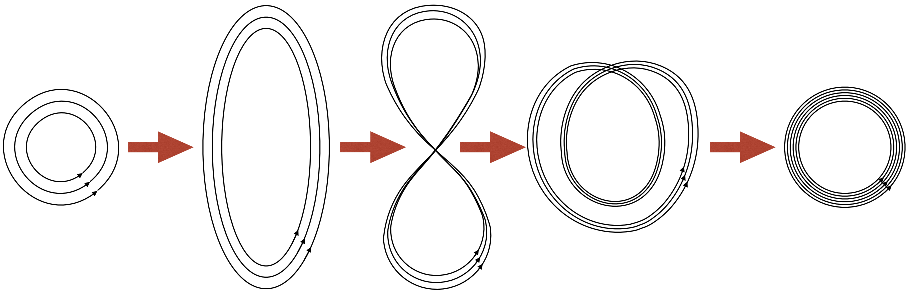

Figure 2.6: Schematic sketch of the small-scale dynamo action. In a procedure of random stretching, twisting and folding of magnetic field lines in a turbulently moving plasma converts kinetic into magnetic energy. Image credit: myself following Jennifer Schober.

2.5.6 Primordial magnetic fields and Population III star formation

Due to their so far unknown nature and impact, examining the formation of Population III stars under the influence of primordial magnetic fields has received increasing attention only recently (e.g. Tan & Blackman, 2004; Maki & Susa, 2004; Silk & Langer, 2006; Machida et al., 2006; Maki & Susa, 2007; Schleicher et al., 2010; Sur et al., 2010; Federrath et al., 2011b; Sur et al., 2012; Turk et al., 2012; Latif & Schleicher, 2016). The following summary will therefore often refer to results in present-day star formation and thus we will specifically denote results in the context of primordial star formation.

The evolution of primordial magnetic fields starts with magnetic seed fields of the order of $B = 10^{-30} - 10^{-18}\,\mathrm{G}$ which may have been created during inflation (Turner & Widrow, 1988), early Universe phase transitions (Sigl et al., 1997) or the Biermann battery mechanism (Biermann, 1950; Xu et al., 2008). This is very small compared to typical field strengths of up to $10^{-6}\,\mathrm{G}$ measured in the interstellar medium today (e.g. Crutcher, 2009).

The small-scale or turbulent dynamo (Kazantsev, 1968; Kulsrud et al., 1997) describes a possible way how weak seed fields are further amplified. Its mechanism is illustrated in Fig. 2.6. Through random stretching, twisting and folding of magnetic field lines in a turbulently moving plasma kinetic energy is converted into magnetic energy. Turbulence that is generated for example as gas falls into dark matter halos (Wise & Abel, 2007; Greif et al., 2008), as gas is accreted into the center of the halo (e.g. Klessen & Hennebelle, 2010; Elmegreen & Burkert, 2010; Federrath et al., 2011b), or as it condenses to form the first stars, the so-called Population III (Pop III) stars (e.g. Sur et al., 2010; Clark et al., 2011b; Turk et al., 2012) can efficiently drive a small-scale dynamo (SSD) (Kazantsev, 1968; Kulsrud et al., 1997). The magnetic field strength is increased exponentially within a free-fall time (Subramanian, 1997; Brandenburg & Subramanian, 2005). The magnetic field first saturates on small scales, more exactly on the viscous scale below which the turbulence is dissipated. In a cascade-like fashion the magnetic energy is transported to larger scales until it also saturates on the turbulent forcing scale, i.e. the scale at which turbulence is pumped into the system (Schekochihin et al., 2002). In this way a primordial tangled magnetic field of up to $B \sim 10^{-5}\,\mathrm{G}$ is generated (Schleicher et al., 2010; Sur et al., 2012; Peters et al., 2012; Turk et al., 2012; Schober et al., 2012; Schleicher et al., 2013; Susa et al., 2015). Schober et al. (2012) have found the magnetic field saturates already within a small density increase during pre-stellar collapse of primordial star formation. Any further amplification during collapse only happens through compression of the magnetic field lines, which scales as $B \propto \rho^{3/2}$ for a spherical collapse of gas with density ρ. Non-ideal magnetohydrodynamical effects such as ohmic resistivity and ambipolar diffusion which lead to a diffusion and consequently reduction of the magnetic field do not hinder the action of the small-scale dynamo significantly (e.g. Schober et al., 2012).

The exact transition between a small-scale tangled field to a large-scale coherent field is not completely understood yet. But it has been found that a mechanism such as the α-Ω dynamo that operates in differentially rotating disks may order small-scale tangled field into a coherent, large-scale structure and further amplify it (e.g. Steenbeck & Krause 1966; Vainshtein & Ruzmaikin 1971; Arshakian et al. 2009; and in particular in primordial context Pudritz & Silk 1989; Tan & Blackman 2004).

There are several ways in which magnetic fields affect star formation. One important effect is that magnetic field can suppress fragmentation of protostellar disks. A process that is also studied in this thesis is disk stabilization through magnetic pressure support (Lynden-Bell, 1966). This can be qualitatively described through an extended Toomre criterion (Kim & Ostriker, 2001)

$$Q_{\mathrm{mag}} = \frac{\kappa\,(c_{\mathrm{s}}^2 + v_{\mathrm{A}}^2)^{1/2}}{\pi\,G\,\Sigma} \tag{2.61}$$

where $v_{\mathrm{A}} = B/\sqrt{4\pi\,\rho}$ is the Alfvén velocity that describes how fast changes in the magnetic field configuration, denoted by the field strength B, propagate through a plasma of density ρ. Furthermore, c_{s} is the speed of sound, G the gravitational constant, Σ the disk surface density, and κ the epicyclic frequency. The magnetic pressure basically extends the stabilizing effects of the thermal gas pressure by a magnetic field component. This effect has been observed in previous ideal MHD studies of present-day star formation (e.g. Hosking & Whitworth, 2004; Hennebelle & Teyssier, 2008; Peters et al., 2011; Seifried et al., 2011). It was also found in Population III star formation by Peters et al. (2014) who studied the influence of a small-scale, turbulent magnetic field on the collapse of a rapidly rotating gas cloud. We study the impact of magnetic fields in Population III protostellar disk stabilization through magnetic pressure in Chapter 7 & 8 in this thesis. For our projects we consider ideal magnetohydrodynamics. This means that there is perfect coupling between the electrons, ions, and neutral species in the examined plasma and the magnetic field lines follow the density distribution, i.e. flux freezing.

Other ways to increase the stability of circumstellar disk that are not examined in this thesis include for example angular momentum redistribution either via magnetic braking (e.g. Mouschovias & Paleologou 1979; Mellon & Li 2008; Mellon & Li 2009; Hennebelle & Ciardi 2009, Hennebelle et al. 2011; and in the context of Pop III star formation e.g. Machida & Doi 2013), or through jets (e.g. Blandford & Payne 1982; Konigl & Pudritz 2000; Banerjee & Pudritz 2006; ;Seifried et al. 2012; and in the context of Pop III star formation Machida et al. 2006; Machida et al. 2008a; Machida & Doi 2013).

2.5.7 Initial mass function and the high-mass end

The earliest numerical studies suggested that Population III stars form in an isolated fashion and grow to very large masses of $\gtrsim 100\,\mathrm{M}_\odot$ (Abel et al., 2002; Bromm et al., 2002; Bromm & Larson, 2004). More advanced numerical simulations within the last decade now study Population III star formation far beyond the formation of the first protostar. They find that a protostellar cluster is created through fragmentation of the highly self-gravitating disk that forms due to non-negligible angular momentum within the collapsing gas cloud (Clark et al., 2008; Turk et al., 2009; Stacy et al., 2010; Clark et al., 2011b; Greif et al., 2011; Clark et al., 2011a; Smith et al., 2011; Stacy & Bromm, 2013). Examinations of these protostellar clusters indicate that the initial mass function of Population III stars follows a top-heavy distribution with masses ranging from subsolar to over a hundred solar masses, with the majority of the masses lying at a few ten solar (Greif et al., 2011; Clark et al., 2011a; Stacy & Bromm, 2013; Susa, 2013; Stacy et al., 2016).

Population III stars accrete as long as their is enough gas supply and the accretion process is not terminated through radiative feedback or interactions with stellar companions, i.e. through fragmentation-induced starvation or ejections. This means they can continue to grow in mass while being already on the ZAMS or the main sequence. Studying ways in which Pop III may grow significantly in mass and reach values of several hundred or even thousands of solar masses, is a very active field in current research. One possibility may be through constantly or at least in regular episodes recurring high accretion rates above some critical value (of the order of $4 \times 10^{-3}\,\mathrm{M_\odot\,yr^{-1}}$ see e.g. Omukai & Palla (2003), Hosokawa & Omukai (2009) and Hosokawa et al. (2010)) that lead to long-lasting fluffy protostars thereby reducing any accretion-limiting radiation (see e.g. Hirano et al., 2014; Hosokawa et al., 2016; Sakurai et al., 2016; Haemmerlé et al., 2018). Similarly, frequent merging between protostars in the Pop III cluster may promote higher mass Pop III star formation (see e.g. Hosokawa et al. (2016) or in the context of present-day star formation Baumgardt & Klessen (2011) and Moeckel & Clarke (2011)). Also magnetic fields might be able to provide favorable conditions by stabilizing protostellar accretion disks against fragmentation and thus reducing effects due to fragmentation-induced starvation within Pop III clusters (in the context of present-day star formation, see Price & Bate (2007), Hennebelle & Teyssier (2008)) or by removing angular momentum in the direct surrounding of the star so efficiently that no disk forms. Therefore no fragmentation occurs and a single protostar can accrete material directly (spherically) and undisturbed (e.g. Machida & Doi, 2013). In Fig. 2.7, we give a schematic overview of Population III star formation in particular stressing high-mass star formation promoting (positive) and limiting (negative) feedback processes.

2.5.8 Fate of Population III stars and observational signatures

The final fate of Population III stars depends mainly on their mass (e.g. Heger & Woosley, 2002):

- $M_\star < 8-10\,\mathrm{M_\odot}$: planetary nebula and white dwarf
- $10 \lesssim M_\star \lesssim 40\,\mathrm{M_\odot}$: core-collapse supernova (CCSN; type II supernova with a neutron star remnant or, when $M_\star \gtrsim 20\,\mathrm{M_\odot}$, black hole remnant)
- $40 \lesssim M_\star \lesssim 140\,\mathrm{M_\odot}$: supernova explosion followed by black hole
- $140 \lesssim M_\star \lesssim 260\,\mathrm{M_\odot}$: pair-instability supernova (PISN); no remnant. Rotating Pop III stars may explode as PISN already from a mass of $\sim 65\,\mathrm{M_\odot}$ onwards (Chatzopoulos & Wheeler, 2012). In a pair-instability supernova, the enormous energy of the explosion destroys the star completely without leaving a remnant.

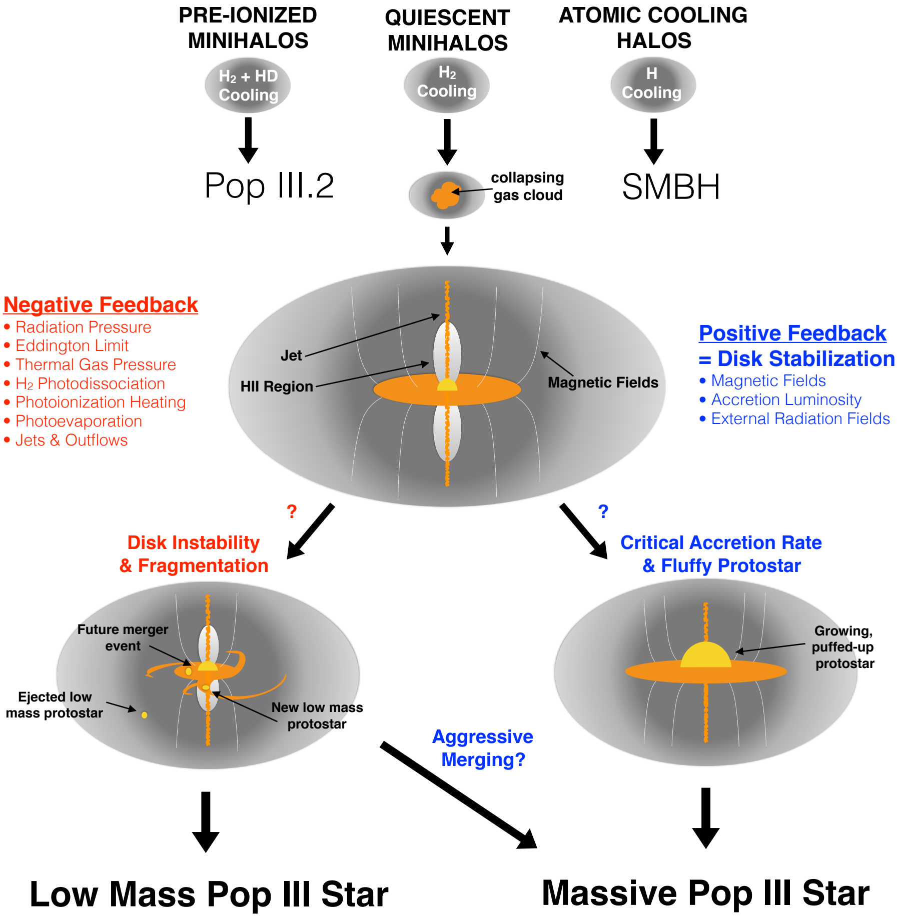

Figure 2.7: Scheme of Population III star formation: Intermediate mass stars ($\lesssim 10\,\mathrm{M}_\odot$; e.g. Pop III.2 stars) evolve in pre-ionized minihalos and supermassive stars ($\gtrsim 10^5\,\mathrm{M}_\odot$; e.g. supermassive black hole (SMBH) seeds) in atomic cooling halos. Pop III.1 stars form in quiescent minihalos which are unaffected by external feedback. Red: Negative feedback processes of the protostar–disk system and disk instability will limit mass growth of the protostar to a few ten $\mathrm{M}_\odot$. Whereas - denoted in blue - disk stabilizing mechanisms through magnetic fields and external heating, high accretion rates (> a few $10^{-3}\,\mathrm{M}_\odot\,\mathrm{yr}^{-1}$) or aggressive merger events can boost formation of very massive Pop III.1 stars ($\gtrsim 10^3\,\mathrm{M}_\odot$). Image credit: myself.

The core of a PISN progenitor star is able to become hot enough for the production of electron-positron pairs out of photons. The removal of these photons leads to a reduction of the radiation pressure that counteracts gravity within the star. Thus, the star is able to contract further, which again accelerates burning processes and pair production and repeats the cycle. An instability in the stellar interior develops that promotes a runaway collapse of the star until the energy within the star has grown to large enough values to completely disrupt it.

- $M_\star \gtrsim 260\,\mathrm{M}_\odot$: direct collapse into a black hole.

Since observational signals from Population III stars play only a minor role in the situations studied in this thesis, we refrain from going into too much detail here but give a general overview. We will give some more explanations in later chapters where appropriate. Population III stars are not expected to be observable with current and upcoming technologies as they are too distant in space and time (e.g. Zackrisson et al., 2011; Rydberg et al., 2013). An exception may be low-mass Pop III survivors with masses below $M \sim 0.8\,\mathrm{M}_\odot$. Their lifetimes are long enough for them to have survived until today (Yoshida et al., 2006; Greif et al., 2011; Kippenhahn et al., 2012). Their low brightness, however, makes them difficult to detect. So far, no such star has been discovered. To increase the chance of finding them, an extension of current surveys may be needed (Hartwig et al., 2015a; Ishiyama et al., 2016), for example also to cover low-mass satellites of the Milky Way as they may have a higher fraction of low mass Pop III survivors compared to the Milky Way and thus could be promising regions for the search for them (Magg et al., 2018).

Signatures of more massive Population III stars may be observed indirectly through analyzing the metal constituents of extremely metal-poor stars (EMP) (Beers & Christlieb, 2005; Frebel & Norris, 2015) or ultra metal-poor stars (UMP) (Karlsson et al., 2013). Population III core-collapse supernovae and pair-instability supernovae enriched their host halo, the intergalactic medium (e.g. Madau et al., 2001; Bromm et al., 2003; Greif et al., 2007; Wise & Abel, 2008), and even neighboring halos (e.g. Smith et al., 2015; Chen et al., 2017) with their metals that then were taken up in the generation of the first metal-enriched stars, the so-called Population II stars (e.g Bromm et al., 2001b; Mackey et al., 2003). By comparing the observed metal content in metal-poor stars with numerical predictions of Pop III supernova yields, one can estimate the Pop III progenitor that enriched the gas from which the metal-poor star was formed. Mostly, features of CCSN supernovae of $15 - 40\,\mathrm{M}_\odot$ Pop III stars were found (e.g. Beers & Christlieb, 2005; Frebel et al., 2005, 2008; Karlsson et al., 2008; Joggerst et al., 2010). Pop III PISN signatures have not been conclusively detected yet (Aoki et al., 2014). Currently, results from both numerical simulations (see Section 2.5.7) and observations suggest that Population III PISNe were a rare phenomenon. If they existed, their explosions may be directly observable, e.g. with the *James Webb Space Telescope*, due to their large luminosities (Whalen et al., 2013c). Other indirect constraints on Population III stars may be gained through the observation of gamma-ray bursts (e.g. Bromm & Loeb, 2006; Wang et al., 2012) or gravitational waves (e.g. Hartwig et al., 2016; Belczynski et al., 2017; Pacucci et al., 2017; Schneider et al., 2017).

CHAPTER

3 Numerical methods

For the first part of the studies described in Chapter 4, we use the Eulerian grid code ZEUS-MP (Norman, 2000; Hayes et al., 2006). The simulations presented in Chapter 5, 6 and 8 are performed using the moving-mesh code AREPO (Springel, 2010). Below, I briefly introduce the two codes, paying special attention to code features that are of particular importance to our numerical studies. Here, I especially describe new features implemented by us or changes introduced by us within already existing modules. In the first part of this chapter, in Section 3.1, I give details of the code ZEUS-MP. Section 3.2 concentrates completely on the numerical details of our studies with the AREPO code. After giving a general overview of the code, I explain further details of the code modules that are important for our studies: the sink particle module (3.2.1), the sink accretion luminosity calculation (3.2.2), the primordial chemistry network (3.2.3), and the variable adiabatic index (3.2.4). The accretion luminosity computation was newly implemented and tested by me. The variable adiabatic index was coupled to the primordial chemistry network by Simon Glover and and tested by me. Finally, in the last subsection (3.2.5), I describe how we set up our initial conditions for the simulations in Chapter 5, 6, and 8, i.e. the Bonnor-Ebert sphere and the turbulent velocity field.

3.1 ZEUS-MP

For our study presented in Chapter 4, we use the massively-parallel, (magneto-) hydrodynamical [1], multiphysics Eulerian grid code ZEUS-MP (Norman, 2000; Hayes et al., 2006). In this code, hydrodynamics is evolved on a structured mesh using a staggered-grid finite-difference scheme with a second-order accurate, monotonic advection scheme (Norman, 1980; Norman & Winkler, 1986; Leer, 1977). The gas self-gravity is updated at every hydrodynamical time step through a conjugate gradient solver that solves Poisson's equation. Simulations can be performed 1D, 2D and 3D on a spherical, cylindrical or Cartesian grid. Our simulations use a 2D cylindrical grid. We also employ a primordial chemistry network with nine species (H, H^+, He, He^+, He^{2+}, H^-, H_2^+, H_2, and e^-), each having its own continuity and non-equilibrium rate equations (Anninos et al., 1997). As the chemical species share a common velocity field with the hydrodynamical fluids, their advection terms are included in the hydrodynamical cycle whereas the rate equations are advanced separately. Charge conservation and conservation of the mass of the individual elements is enforced at every update of the chemical network as it is not guaranteed otherwise. The code accounts for important heating (see further Whalen & Norman, 2008a) and cooling processes (e.g. Galli &

---

[1] For our purposes, we employ hydrodynamics only.

Palla, 1998) in the primordial environment, such as H_2 line cooling, collisional ionization and excitation of H and He, recombinations of H^+ and He^+, inverse Compton scattering from the CMB and bremsstrahlung emission. For a complete list see Whalen & Norman (2006). The gas energy density is affected by these processes and is updated at every update of the chemical network.

We use a specific version of the code which includes a multifrequency photon-conserving raytracing UV transport scheme (Whalen & Norman, 2008a,b). Radiation is treated as a plane wave together with a $1/r^2$ attenuation of the flux intensity in order to account for geometrical dilution effects. The stellar spectra consist of blackbody emission rates which are discretized into 40 uniform bins covering 0.755 eV to 13.6 eV, and 80 logarithmic bins stretching from 13.6 eV to 90 eV. Time-averaged Population III ionizing photon rates and stellar surface temperatures are taken from Tables 3 and 4 of Schaerer (2002). The values of the ionizing photon rates fix the normalization of the stellar spectral-energy density (SED), allowing the emission rates in the other bins to be derived. Furthermore, the code treats H_2 photodissociation through Lyman-Werner photons ($11.2-13.6\,\mathrm{eV}$) separately via the self-shielding functions of Draine & Bertoldi (1996). A summary of the radiative reactions is given in Table 1 in Whalen & Norman (2008a). In this way, this version of the code is able to follow the propagation of photodissociating and ionizing radiation from point sources, i.e. the evolution of cosmological ionization fronts (Whalen & Norman, 2008a,b).

3.2 AREPO

AREPO has an unstructured moving-mesh based on the so-called Voronoi tessellation. Its mesh-generating points follow a quasi-Lagrangian behavior by being advected with the underlying fluid velocity. In this way AREPO is able to combine advantageous properties of both adaptive mesh refinement (AMR) and smoothed-particle hydrodynamic (SPH) codes while simultaneously alleviating or even eliminating several of their error-inducing disadvantages. For example, AREPO remains the accuracy of mesh-based hydrodynamics (e.g. reduction of errors from artificial viscosity or from noise of kernel estimates as encountered in SPH codes) but avoids the introduction of preferred directions as in Cartesian grids. Furthermore, AREPO's Lagrangian nature allows the moving mesh to follow and adapt continuously in resolution to the way density fluctuations evolve under their own self-gravity. This make AREPO an ideal code to study gas collapse.

The Voronoi grid is initialized with the help of the so-called Delaunay tessellation that divides space into a mesh of triangles (2D) or tetrahedra (3D) via triangulation. The vertices of the Delaunay cells are the mesh-generating points for the Voronoi cells while mid-points of circumcircles/spheres around each Delaunay cell (i.e. center of the circle or sphere around such a cell) form the vertices of the Voronoi cells. The Voronoi cells have a polygonal (2D) or polyhedral (3D) shape. For more details on grid properties and the technique used to generate the grid, see section 2 of Springel (2010).

In our simulations, the local Jeans length continuously decreases while the gas collapses to ever smaller scales. We therefore employ a Jeans refinement criterion based on the Truelove criterion (Truelove et al., 1997) that makes sure to resolve the local Jeans length by a minimum number of cells to avoid artificial fragmentation. In the original case of isothermal gas the minimum number is four cells, while for a variable equation of state a minimum number of eight cells is used (e.g. Turk et al., 2012). Depending on the type of physical process that is numerically modeled, higher numbers may need to be used. For example to resolve turbulent motions arising in the gas while it is gravitationally collapsing one needs to employ at least 32 cells per Jeans length (e.g. Federrath et al., 2011b; Greif et al., 2012). A cell in AREPO that fulfills the refinement criterion is split into two cells. To guarantee conservation of mass, momentum and energy, their values in the original cell are now weighted by the volumes of the two newly-established cells and then distributed accordingly. This leaves the density, pressure and velocity of the original cell unchanged. The mesh-generating point of the new cell only has a tiny offset from the location of the mesh-generating point of the original cell. Over the course of a few time-steps, a mesh regularization procedure draws the two points away from each other and toward the center of masses of the two newly established cells. This regularization procedure produces roundish cells and a honeycomb-like structure of the mesh that optimizes the computational efficiency of the code. Another useful application is the de-refinement strategy for regions that are unaffected by gas collapse. As in the refinement procedure, after the mesh-generating point of a cell is removed, the content of the former cell is distributed to the neighboring cells in a conservative and volume-weighted fashion (i.e. depending on which volume fraction of the original cell they receive). Then, the mesh regularization procedure smooths the grid again. For the studies presented in this thesis a recent version of the code is used that includes updates to reduce mesh noise and deviations from mesh regularity during the regularization process (Mocz et al., 2015).

AREPO solves the hydrodynamical Euler equations through a finite-volume strategy using a hybrid approach between the Godunov method based MUSCL-Hancock scheme (van Leer, 1984; Toro, 1997; van Leer, 2006) and a Runge-Kutta time integration scheme (Pakmor et al., 2016) together with a Riemann solver. In this approach the system's volume is discretized into a finite number of disjoint cells, represented by the Voronoi grid cells. After the fluid states, described by the conserved quantities mass, momentum and energy, have been obtained at each side of the cell interfaces with the help of the time integration scheme, a flux vector of the fluid exchange between cells is computed using the Riemann solver. This approach described in section 3 of Springel (2010) (with updates on the convergence behavior in Pakmor et al. (2016), further makes sure to retain the Galilean invariance of the numerical system.

For ideal magnetohydrodynamical (MHD) simulations, a similar finite-volume strategy is followed by employing again a Godunov approach including the method by Darwish & Moukalled (2003) for the spatial extrapolation of the fluid states across neighboring cells, the time-prediction scheme as described in the original AREPO paper by Springel (2010), and a Riemann solver. For both the hydrodynamical the studies presented in Chapter 5 as well as the ideal MHD study described in Chapter 8, we use the HLLD Riemann solver (Miyoshi & Kusano, 2005).

The challenge in numerical MHD computations is to preserve $\nabla \cdot \mathbf{B} = 0$. While it is conserved analytically, this is generally not true anymore for discretized version of the MHD equations. Instead, non-zero values of $\nabla \cdot \mathbf{B}$ occur and tend to increase quickly in non-trivial MHD flows leading to unphysical behavior of the MHD flow such as sudden locally strongly amplified magnetic field values.

In order to avoid this, there are on the one hand schemes that conserve $\nabla \cdot \mathbf{B} = 0$ by construction (e.g. Evans & Hawley, 1988), and on the other hand schemes that simply try to sufficiently minimize spurious $\nabla \cdot \mathbf{B}$ values (e.g. Powell et al., 1999; Dedner et al., 2002). AREPO applies the Powell divergence cleaning scheme (Powell et al., 1999; Pakmor & Springel, 2013). Here, additional $\nabla \cdot \mathbf{B}$ source terms are added to the momentum, energy and induction equation, which introduce a passive advection of $\nabla \cdot \mathbf{B}$ with the fluid flow that tries to diffuse it away once it occurs and in this way counteracts its further growth. This method has been shown to be very stable and advantageous allowing it to be performed in the same step as the computation of the local magnetohydrodynamical fluxes. In addition, for some of our MHD computations, we use a recently added MHD refinement criterion that tests whether the non-zero $\nabla \cdot \mathbf{B}$ value has become sizable. If $2R\nabla \cdot \mathbf{B}/B > C$, where R is the radius of a cell, $\nabla \cdot \mathbf{B}$ the local divergence of the magnetic field, and B the value of the magnetic field strength in this cell, and $C = 0.1$, then we refine the grid. In this way the cell radius and $\nabla \cdot \mathbf{B}$ are reduced while the magnetic field strength stays the same.

For our simulations for which gas self-gravity needs to be computed, we use a tree-based approach with the TreePM method (Springel & Hernquist, 2002) that is implemented in AREPO and that is combined with the Lagrangian hydrodynamical computations. In this way, the gravitational resolution automatically and continuously follows and accurately matches that of the hydrodynamical flow (e.g. Bate & Burkert, 1997). The gravitational force between the different cells of the mesh is derived via the tree algorithm under the assumption that each cell is a point mass with some gravitational softening length. The volume computed form this mass and softening length is slightly larger than the cell's real volume .

AREPO comes with a variety of different modules ranging from radiative transfer methods to black hole physics. Two modules that are of particular importance for this thesis are the sink particle module and the primordial chemistry module. These are described together with our new additions in Sections 3.2.1 - 3.2.4 below.

3.2.1 Sink particle module

Sink particles were invented by Bate et al. (1995) to replace gravitational collapsing and unambiguously gravitationally bound gas structures with a collisionless, non-gaseous particle of the same mass that can continue to grow in mass via accretion but otherwise interacts only gravitationally with its surrounding. The method was developed in order to improve the numerical feasibility and simulating the long-term evolution and interaction of small-scale collapsing gas fragments with their large-scale surroundings. When gas fragments condense toward protostellar densities, the hydrodynamical time steps of the involved cells become rapidly many orders of magnitude smaller (e.g. order of seconds and below) than that of the overall global evolution of the host cloud (e.g. orders of thousands of years). This large dynamical range poses an enormous challenge for current numerical and computational systems. The sink particle implementation we use in our simulations was developed by Paul Clark and include a more stringent set of sink particle formation criteria than the original Bate et al. (1995) design. For a sink particle to form from one of the cells in a set of candidate gas cells that form a control volume, several conditions must be fulfilled. First of all, the sink candidate must have a density higher than the threshold density for sink formation. This value is predefined and usually motivated through the density at which the Jeans length of the gas is only just resolved. Second, it is checked that the sink candidate is not inside the accretion radius of another existing sink. If it is, it could instead be accreted by this sink, see below for more information on that. Third, the sink candidate must be the densest possible potential minimum, i.e. it must be the minimum of the local gravitational potential created by the cells in the control volume. In the fourth criterion, the energy balance within the control volume is tested. The mass within the control volume must exceed the local Jeans mass. For this to be, $|E_{\mathrm{grav}}| > 2\,E_{\mathrm{therm}}$ must hold. Furthermore, the region within the control volume must be bound, i.e. its total energy must be negative. In the sixth and final condition, $\nabla \cdot \mathbf{v} < 0$ and $\nabla \cdot \mathbf{a} < 0$, where $\mathbf{v}$ and $\mathbf{a}$ are the velocity and acceleration vector of the gas within the control volume, must hold to make sure that the gas really converges and is not otherwise involved in tidal interactions or disrupted.

These six criteria ensure that no spurious sink is formed in regions of sudden density increase e.g. in shocks, unless the gas is actually gravitationally bound and collapsing. If a gas particle fulfills all these criteria, it is replaced a sink particle with the same mass and momentum. In AREPO, the sink particle is assigned a gravitational softening length of one third of the accretion radius to avoid artificial fragmentation.

For a gas cell to be accreted by an existing sink particle, first the cell must be within the accretion radius of the sink and be bound and moving toward the sink. The latter can be tested by checking that the radial velocity of the gas particle in the reference frame of the sink is negative. For it to be bound to the sink, its kinetic energy must be smaller than its binding energy with the sink. If the gas cell is in the area of influence of several sink particles, it is accreted by the sink to which it is most strongly bound. If these criteria are satisfied, the mass and momentum of the gas cell are added to that of sink particle. For our studies, we use a refined accretion criterion called *accretion skim cell mass* in which instead of a whole gas cell being accreted and thus destroyed at once by the accretion procedure, only $\sim 90\,\%$ of the cell's mass is *skimmed* and accreted onto the sink while the gas cell is preserved.

3.2.2 Accretion luminosity

The sink particles in the simulations presented in Chapter 5, 6, and 8 represent individual protostars. As gas accretes onto these protostars, it releases a significant amount of energy. We account for this by computing the accretion luminosity[2] for each accreting protostar

$$L_{\mathrm{acc}} = \frac{GM_{\star}\dot{M}}{R_{\star}}, \tag{3.1}$$

and the corresponding volumetric heating rate

$$\Gamma_{\mathrm{acc}} = \rho\kappa_{\mathrm{P}}\left(\frac{L_{\mathrm{acc}}}{4\pi r^2}\right)\mathrm{erg\,s^{-1}\,cm^{-3}}. \tag{3.2}$$

Here, G is the gravitational constant, $\dot{M}$ is the protostellar accretion rate (which we take to be equal to the instantaneous accretion rate onto the sink), $M_{\star}$ and $R_{\star}$ are the mass and radius of the protostar, ρ is the gas density, κ_{P} is the Planck mean opacity, and r is the distance between the accreting sink and the cell in which we are computing the heating rate. Equation 3.2 assumes that the gas is optically thin to the radiation from the accreting protostar, but this is a good approximation in primordial gas (Smith et al., 2011).

To compute the value of $R_{\star}$, we follow the same approach as in Smith et al. (2011) and adopt the analytical prescriptions given by Omukai & Palla (2003):

$$R_{\star} \propto \begin{cases} 26M_{\star}^{0.27}(\dot{M}/10^{-3})^{0.41} & M_{\star} \leq p_1, \\ A_1 M_{\star}^{3} & p_1 \leq M_{\star} < p_2, \\ A_2 M_{\star}^{-2} & p_2 \leq M_{\star}\,\&\, R < R_{\mathrm{ms}}, \end{cases} \tag{3.3}$$

where $R_{\star}$, $M_{\star}$ and $\dot{M}$ are expressed in units of $\mathrm{R}_{\odot}$, $\mathrm{M}_{\odot}$ and $\mathrm{M}_{\odot}\,\mathrm{yr}^{-1}$, respectively, and where the transition points p_1 and p_2 are given by

$$p_1 = 5(\dot{M}/10^{-3})^{0.27}\,\mathrm{M}_{\odot}, \tag{3.4}$$

$$p_2 = 7(\dot{M}/10^{-3})^{0.27}\,\mathrm{M}_{\odot}. \tag{3.5}$$

Finally, the main sequence radius R_{ms} is given by

$$R_{\mathrm{ms}} = 0.28M_{\star}^{0.61}\mathrm{M}_{\odot}. \tag{3.6}$$

Our approach assumes a quasi-spherical accretion onto the sink. We cannot say whether at radii smaller than our accretion radius, $r_{\mathrm{acc}} = 2\,\mathrm{AU}$, a thin inner disk forms and how thermally efficient the flow from disk onto the protostellar surface is (Hosokawa et al., 2010) but in our studies we generally find thick disks down to our assumed accretion radius (see also Clark et al., 2011b, for similar findings), in which the sink is embedded, and thus our approximation is reasonable.

The other assumption made here is that the sink radius responds instantly to changes in the accretion rate. In reality, the characteristic time-scale of the protostellar radial

---

[2] This section will be partially included in Wollenberg, K. M. J., Glover, S. C. O., Clark, P. C., Klessen, R. S., *"The Fragmentation Behavior of Population III Protostellar Disks - Part I"*, MNRAS 2019 (*in prep.*). K. M. J. Wollenberg implemented and successfully tested this feature first in the FLASH code. It was later ported to AREPO by S. C. O. Glover and again tested by K. M. J. Wollenberg. The test consisted of placing a sink particle within a uniformly dense environment and follow its mass growth for some time. The sink accretion rate, its mass and the parameters below are printed out from the code and their values are checked by simple analytic computation.

evolution is of the order of $10^3\,\mathrm{yr}$. For the early protostellar evolution dominated by mass growth ($M \lesssim 10\,\mathrm{M}_\odot$), this is governed by the accretion time-scale, while later stages follow the Kelvin-Helmholtz contraction time-scale, that is the time over which the star can redistribute the entropy, which it has taken-up through accretion, internally. The studies by Smith et al. (2011, 2012) showed that a highly variable accretion rate does not introduce an enormous error in the computation of the radial evolution. Strong variation in the computation of the accretion luminosity due to varying accretion rate and radius are partially smoothed out as $L_{\mathrm{acc}} \propto \dot{M}_{\mathrm{acc}}/R_\star$. Although the overall course of the accretion luminosity still has variations, this is unlikely to impact our results significantly. Clark et al. (2011b) and Smith et al. (2011) showed that although accretion luminosity may reduce fragmentation in the surrounding of the sink, it cannot stop fragmentation of the protostellar disk.

To compute the Planck mean opacity, we again follow Smith et al. (2011) and make use of the values tabulated as a function of density and temperature by Mayer & Duschl (2005). One simplification made in that work was the assumption that the gas and radiation temperatures were equal. This does not lead to a large error for gas temperatures of a few thousand degrees, as these are comparable to the actual photospheric temperatures of the accreting protostars. However, it leads to an unrealistically high value for κ_{P} and Γ_{acc} in gas with $T \sim 10^4$ K or higher. To avoid this problem, we compute κ_{P} using a temperature given by

$$T_\kappa = \min(T, 6000\,\mathrm{K}), \tag{3.7}$$

where T is the actual gas temperature.

3.2.3 Primordial chemical network

Our chemical network mostly follows the network of 45 reactions between the twelve species H, H^+, H^-, H_2^+, H_2, He, He^+, He^{++}, D, D^+, HD and free electrons as presented in table 1 of Clark et al. (2011a), which is based in turn on Glover & Jappsen (2007) and Glover & Abel (2008). Some parts of the deuterium chemistry are different, namely reactions including D^-, HD^+ or D_2 are excluded as those are not significant for controlling the HD abundance. Besides, we study Population III.1 star formation for which the role of HD cooling is minor. Furthermore, our treatment of chemistry and cooling contains several recent improvements in the form of updated rate coefficients compared to the Clark et al. (2011a) model, as summarized in Schauer et al. (2017). The most important change is that we now use a new rate coefficient for the three-body H_2 formation reaction. This and other new chemistry features included for our studies are presented in detail in the following list[3]:

- The reaction rate coefficient for the three-body H_2 formation,

$$\mathrm{H} + \mathrm{H} + \mathrm{H} \rightarrow \mathrm{H}_2 + \mathrm{H}\ , \tag{3.8}$$

  is highly uncertain (Glover, 2008; Turk et al., 2011). In the literature, the slowest rate can be found in Abel et al. (2002) and the fastest in Flower & Harris (2007). Clark et al. (2011a) use an intermediate value suggested by Glover (2008). Previous studies have shown that the behaviour of primordial gas at

---

[3] This list will be partially included in Wollenberg, K. M. J., Glover, S. C. O., Clark, P. C., Klessen, R. S., *"The Fragmentation Behavior of Population III Protostellar Disks - Part I"*, MNRAS 2019 (*in prep.*).

densities $n > 10^8\,\mathrm{cm}^{-3}$ is highly sensitive to the treatment of three-body H_2 formation (Turk et al., 2011; Bovino et al., 2014) and so it is important to model this process as accurately as possible. We now use the rate coefficient computed by Forrey (2013). This yields a more reliable rate coefficient at low gas temperatures than one obtains by applying detailed balance to the collisional dissociation reaction (see e.g. Palla et al., 1983; Flower & Harris, 2007)

$$\mathrm{H_2 + H \rightarrow H + H + H}, \tag{3.9}$$

as in the latter case, one is forced to extrapolate the collisional dissociation rate to a temperature range far below that for which reliable experimental values have been measured.

- In the course of carrying out our simulations, we found that it became extremely computationally expensive to track the non-equilibrium deuterium chemistry in gas with $n \gg 10^8\,\mathrm{cm}^{-3}$, owing to the short chemical timescales involved. Since the HD/H_2 ratio in this regime largely just tracks the cosmological ratio of D to H, and the HD molecules are not important coolants at these densities (Glover & Savin, 2009), we dealt with this problem by switching off explicit tracking of the deuterium chemistry at densities $n > 10^8\,\mathrm{cm}^{-3}$. Instead, we assume that in this regime the ratio of the fractional abundances of HD and H_2, $x_{\mathrm{HD}}/x_{\mathrm{H_2}}$, is given by the cosmological D to H ratio, $x_{\mathrm{D,tot}} = 2.6 \times 10^{-5}$. We do not expect this computational simplification to have any impact on our results.

- Finally, in our simulations, we account for the fact that in warm gas with a high molecular fraction, the adiabatic index of the gas is not necessarily equal to the value for a monatomic gas, $\gamma = 5/3$, but instead depends on the chemical composition and temperature of the gas. AREPO already supports the use of a variable adiabatic index in its HLLD Riemann solver, so our main modification here was to provide routines to compute γ as a function of chemical composition and T for a primordial gas. This is carried out along the same lines as in Clark et al. (2011a). More details and description of a test of this new implementation is given below in Section 3.2.4.

As we have explained in Section 2.4, the most important coolant in primordial gas is molecular hydrogen. In our study of the fragmentation behavior of Pop III protostellar disks the most important processes are

- H_2 rotational and vibrational line cooling (for details on the cooling function see Glover & Abel, 2008)
- H_2 collision-induced emission (CIE) cooling (Ripamonti et al., 2002; Ripamonti & Abel, 2004; Clark et al., 2011b)
- H_2 collisional dissociation cooling (for details regarding the cooling term see Clark et al., 2011b), and
- Three-body H_2 formation heating (for details regarding the heating term see Clark et al., 2011b).

Further relevant processes include effects of cooling due to H_2 destruction by charge transfer, due to collisional ionization of H, He and He^+, or due to recombination of H^+ or He^+, Compton cooling, and bremsstrahlung emission. Further details about the treatment in the code are given in Glover & Jappsen (2007) and Glover & Abel (2008).

In the optical thick regime above densities of $n \gtrsim 10^9\,\mathrm{cm}^{-3}$ (see also Section 2.5.1), we model H_2 cooling using the Sobolev approximation (Yoshida et al., 2006) and Clark et al. (2011a). Although not as accurate as methods involving the solution of the full non-LTE radiative transfer equation (Greif, 2014) or computation of the H_2 column density distribution (Hartwig et al., 2015b), it has a much lower computational cost, which is an important benefit in our current study given the number of simulations that we run. The net cooling rate is

$$\Lambda_{\mathrm{H_2,thick}}(T) = \sum_{\mathrm{u,l}} \beta_{\mathrm{esc,ul}}\, \Delta E_{\mathrm{ul}}\, A_{\mathrm{ul}}\, n_{\mathrm{u}} \ , \tag{3.10}$$

$\Delta E_{\mathrm{ul}} = h\nu_{\mathrm{ul}}$ is the energy difference between the upper (u) and lower (l) energy level, A_{ul} is the Einstein coefficient for spontaneous radiative transition between the two energy levels, and n_{u} is the population density of molecular hydrogen in the upper energy level. The probability that an emitted photon with frequency ν_{ul} can escape from the parcel of gas in question is given by

$$\beta_{\mathrm{esc,ul}} = \frac{1 - \exp(-\tau_{\mathrm{ul}})}{\tau_{\mathrm{ul}}} \tag{3.11}$$

with the optical depth τ_{ul} for which the approximation

$$\tau_{\mathrm{ul}} \simeq \alpha_{\mathrm{ul}}\, L_{\mathrm{s}} = \frac{\alpha_{\mathrm{ul}}}{n_{\mathrm{H_2}}}\, N_{\mathrm{H_2,eff}} \tag{3.12}$$

is used. Here, $\alpha_{\mathrm{ul}} \propto n_{\mathrm{H_2}}$ is the line absorption coefficient and L_{s} is the Sobolev length which is related to the effective H_2 column density by $N_{\mathrm{H_2,eff}} \equiv n_{\mathrm{H_2}}\, L_{\mathrm{s}}$ [4]. The Sobolev length in one dimension is defined as ratio of the thermal velocity, v_{th}, and the absolute of radial velocity gradient dv_{r}/dr:

$$L_{\mathrm{s}} = \frac{v_{\mathrm{th}}}{|dv_{\mathrm{r}}/dr|} \ . \tag{3.13}$$

For a three-dimensional flow, this can be generalized (Neufeld & Kaufman, 1993) to

$$L_{\mathrm{s}} = \frac{v_{\mathrm{th}}}{|\nabla \cdot \mathbf{v}|} \ . \tag{3.14}$$

For a small velocity dispersion in the gas, the Sobolev length can become very large. In order to avoid artificially small values of the H_2 cooling rate, one uses smallest Sobolev length and the local Jeans length in the expression for the optical depth in Eq. 3.12. This is justified as for length scales above the local Jeans length strong density gradients are present and we expect that the contribution to the molecular hydrogen line absorption mostly stems from material within only a few local Jeans lengths (Clark et al., 2011b).

---

[4] The ratio $\alpha_{\mathrm{ul}}/n_{\mathrm{H_2}}$ varies with temperature only. For the treatment of the Sobolev method in our simulation, we can derive cooling rate values through interpolation of a pre-generated table of the cooling rate per hydrogen molecule in the optically thick regime as function first of gas temperature and second of effective molecular hydrogen column density (see also Clark et al., 2011a).

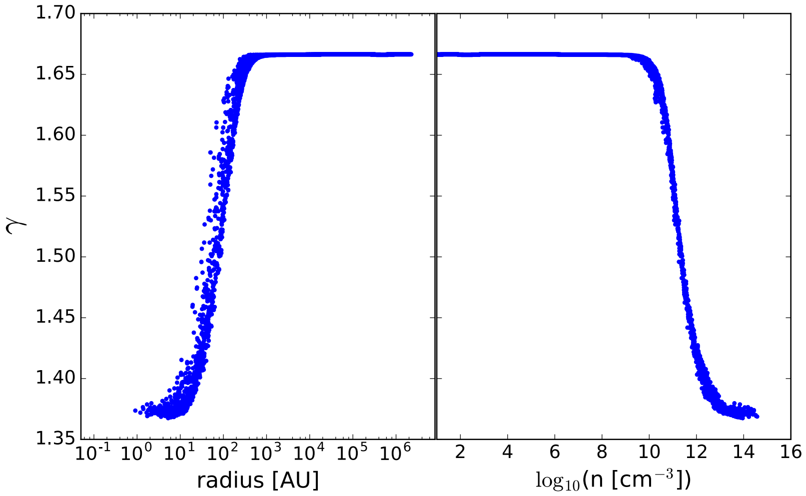

Figure 3.1: Cell distribution for the relation between the adiabatic index γ and the radius (left) as well as γ vs. number density (right) when using the option for variable γ. This test was performed with the Riemann HLLD solver.

For disk densities $n > 10^{14}\,\mathrm{cm}^{-3}$, we use the approximation for the reduction of the CIE cooling rate by continuum absorption from Clark et al. (2011b) and apply the cooling rate

$$\Lambda_{\mathrm{CIE,thick}}(T) = \Lambda_{\mathrm{CIE,thin}} \times \min\left(\frac{1-\exp(-\tau_{\mathrm{CIE}})}{\tau_{\mathrm{CIE}}}, 1\right) \,, \tag{3.15}$$

with the CIE optical depth

$$\tau_{\mathrm{CIE}} = \left(\frac{n_{\mathrm{H_2}}}{7\times10^{15}\,\mathrm{cm}^{-3}}\right)^{2.8} \,. \tag{3.16}$$

This approximate rate agrees within a factor of a few to actual rate measured prior to first protostar formation in Yoshida et al. (2008). Clark et al. (2011b) furthermore tested the quality of this approximation in an accretion disk environment. They find that the effects of the continuum opacity only become important once the gas undergoes runaway gravitational collapse while for disk densities of $n \sim 10^{13} - 10^{15}\,\mathrm{cm}^{-3}$ the gas is still optically thin to CIE cooling. Since we set our sink creation density threshold to $n_{\mathrm{thresh}} \sim 10^{15}\,\mathrm{cm}^{-3}$, it is unlikely that this approximation significantly influences our results.

3.2.4 Variable adiabatic index

In numerical simulations that include primordial chemistry often only a fixed adiabatic index $\gamma = 5/3$ is employed. However, the adiabatic index actually varies between $\gamma = 5/3$ (atomic gas) and $\gamma \leq 7/5$ (warm, highly molecular gas)[5]. In Fig. 3.1, we plot

---

[5] For molecular hydrogen $\gamma = 7/5$ when only the rotational energy levels are populated. With increasing temperature, also H_2 vibrational levels get populated which leads to values of $\gamma < 7/5$.

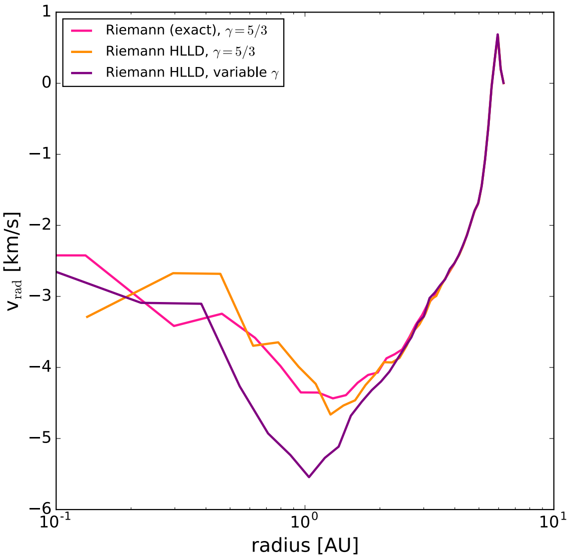

Figure 3.2: Comparison of the radial velocity profiles between the three test runs. The *pink* line is given by the exact Riemann solver at a time of 1.38 yr before the first sink forms (t_{SF}). The *orange* line of the Riemann HLLD with fixed adiabatic index is derived at a time $t_{SF} - 2.14$ yr and the *purple* line for the variable γ run at $t_{SF} - 1.47$ yr.

for all cells in our test simulation the relation between γ and radius (left) as well as γ and number density (right).

AREPO supports the use of a variable adiabatic index within its Riemann HLLD solver (Miyoshi & Kusano, 2005). Therefore, we added routines to compute γ as a function of chemical composition and temperature within our primordial chemistry network.

We performed three test runs: first with the AREPO exact Riemann solver (Toro, 1997) and a fixed adiabatic index of $\gamma = 5/3$, second with the HLLD Riemann solver and $\gamma = 5/3$, and third with the HLLD Riemann solver and the variable γ. Our test setup was a Bonnor-Ebert (BE) sphere collapse with a resolution of 8 cells per Jeans length. Sink particles were included for which we chose an accretion radius of r_{acc} = 4 AU and a threshold density of $n_{thresh} \approx 5 \times 10^{14}\,\mathrm{cm}^{-3}$.

We found that the run with variable γ proceeded faster than the other two: the first sink particle was formed at $t = 1.21887$ Myr compared to $t = 1.21911$ Myr (+240 yr, HLLD solver, fixed γ) and $t = 1.219$ Myr (+130 yr, exact Riemann). In Fig. 3.2, we plot the profiles of the radial velocity of the three different runs at times between one and two years before the first sink formation. We see clearly that the gas infall proceeds with larger velocities in case of the variable γ run.

From Fig. 3.3 and 3.4, we can see that the overall temperature and density profiles stay about the same for all three runs. The data were taken from snapshots at the same times just before first sink formation as in Fig. 3.2. We plot again the distributions of all cells and indicate the mass-weighted mean profiles of distributions by lines.

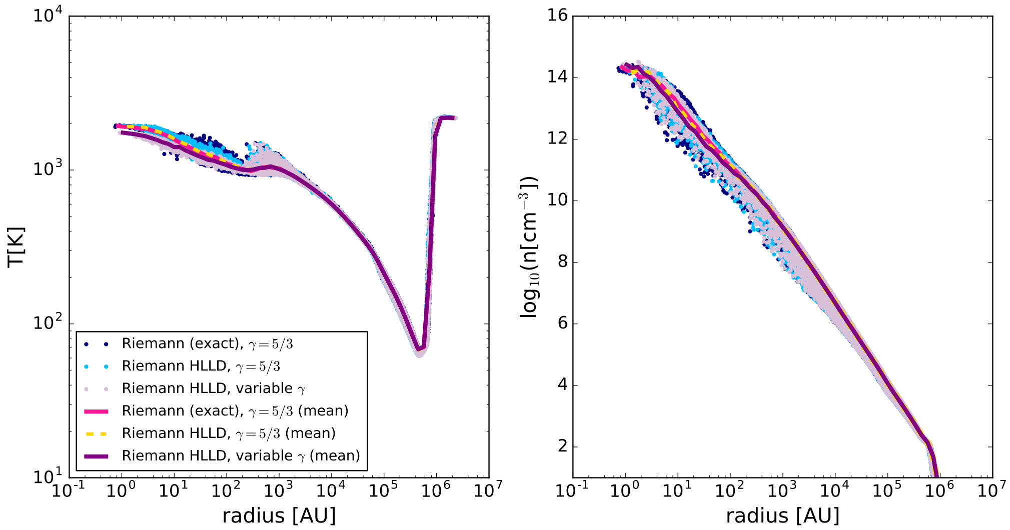

Figure 3.3: Comparison of temperature-radius (left) and number density-radius profiles of the cell distributions within our three test runs. Further indicated by lines are the mass-weighted mean radial profiles.

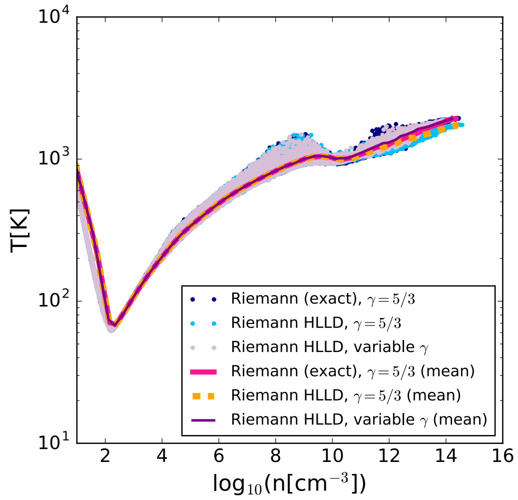

Figure 3.4: Comparison of temperature-number density profile of the cell distributions within our three test runs. Further indicated by lines is the mass-weighted mean.

3.2.5 Generating the initial conditions

Setting up a Bonnor-Ebert sphere density distribution

For the study about the influence of turbulence and rotation on the formation of Population III accretion disks and the creation of Pop III stellar clusters through disk fragmentation presented in Chapter 5, we use an unstable gas cloud with a Bonnor-Ebert (BE) sphere density distribution (Ebert, 1955; Bonnor, 1956) as our initial condition. A BE sphere is a self-gravitating isothermal sphere in hydrostatic equilibrium. The density profile is formally derived as a solution of the so-called dimensionless Lane-Emden equation (Lane, 1870; Emden, 1907). Since the BE profile reproduces density distributions within real (present-day) molecular cloud cores found in observations (e.g. Alves et al., 2001; André et al., 2004; Lada et al., 2007) and since it also well-represents density profiles of primordial gas clouds self-consistently derived in cosmological simulations (e.g. Abel et al., 2002; Bromm et al., 2002; Yoshida et al., 2008), it is frequently used as an initial condition in small-scale simulations of star formation in order to perform studies within an controlled simulation setup. For examples of its use in simulations of present-day star formation see e.g. Banerjee et al. (2004) and Walch et al. (2009) and for primordial star formation see e.g. Machida et al. (2008a), Sur et al. (2010, 2012), and Clark et al. (2011a). For the derivation of the Lane-Emden equation, we start with the equations of an isothermal, spherically symmetric, self-gravitating gas sphere in hydrostatic equilibrium:

Equation of hydrostatic equilibrium:

$$-\frac{1}{\rho}\nabla P - \nabla\Phi = 0 \tag{3.17}$$

$$-\frac{1}{\rho(r)}\frac{P(r)}{dr} - \frac{d\Phi(r)}{dr} = 0 \tag{3.18}$$

Poisson equation:

$$\nabla^2\phi = 4\pi G\rho \tag{3.19}$$

$$\frac{1}{r^2}\frac{d}{dr}\left(r^2\frac{d\Phi(r)}{dr}\right) = 4\pi G\rho(r) \tag{3.20}$$

Equation of state:

$$P = \rho c_{\mathrm{s}}^2 \tag{3.21}$$

$$P(r) = \rho(r) c_{\mathrm{s}}^2 \tag{3.22}$$

where in the second line of each equation the form in spherical coordinates is given. In the equations above, r is the radius of the sphere and ρ, P and Φ are the local density, pressure and gravitational potential of the sphere and G is the gravitational constant. The isothermal sound speed is $c_{\mathrm{s}} = \sqrt{k_{\mathrm{B}}T/(\mu m_{\mathrm{p}})}$ where k_{B} is the Boltzmann constant, T the temperature inside the sphere, μ is the mean molecular weight and m_{p} the proton mass. Combining equations (3.18) and (3.22) and rearranging leads to

$$-\frac{d\ln\rho(r)}{dr} = \frac{d}{dr}\left(\frac{\Phi(r)}{c_{\mathrm{s}}^2}\right) \tag{3.23}$$

of which the solution under condition $\Phi(r=0)=0$ is

$$\rho(r) = \rho_0 \exp\left(-\frac{\Phi(r)}{c_{\mathrm{s}}^2}\right) \ . \tag{3.24}$$

Using this solution with (3.20) leads

$$\frac{1}{r^2}\frac{d}{dr}\left(r^2\frac{d\Phi(r)}{dr}\right) = 4\pi G\rho_0 \exp\left(-\frac{\Phi(r)}{c_{\mathrm{s}}^2}\right) \ . \tag{3.25}$$

With the substitutions

$$\Psi \equiv \frac{\Phi(r)}{c_s^2} \tag{3.26}$$

$$\xi \equiv r\left(\frac{4\pi G\rho_0}{c_s^2}\right)^{1/2} = \frac{r}{r_0} \tag{3.27}$$

we finally arrive the Lane-Emden equation

$$\frac{1}{\xi^2}\frac{d}{d\xi}\left(\xi^2\frac{d\Psi}{d\xi}\right) = \exp(-\Psi)\ . \tag{3.28}$$

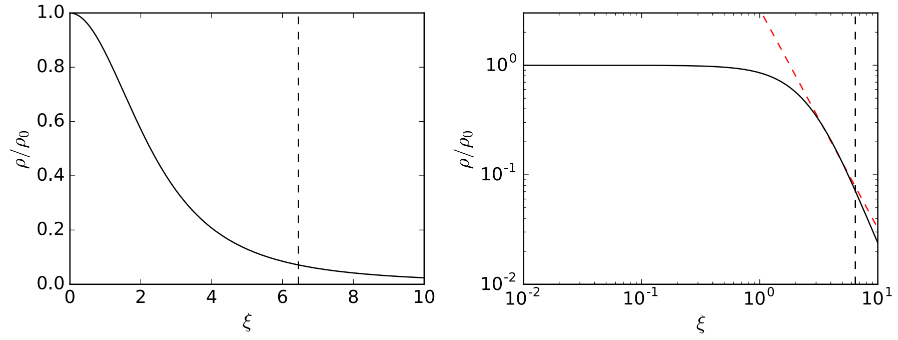

Figure 3.5: Linear (left) and logarithmic (right) plots of Bonnor-Ebert sphere density profiles. Here, the dimensionless parameters ξ and ρ/ρ_0 are plotted. The *black dashed* line indicates the critical (dimensionless) radius $\xi_{\text{crit}} \approx 6.451$. The *red dashed* line in the right plot describes a $\propto \xi^{-2}$ slope which is typical for the BE sphere density profile, and because of its similarity, the BE sphere is a popular description for real molecular clouds.

Under the assumption of the mixed boundary conditions (von Neumann & Cauchy)

$$\Psi(\xi = 0) = 0 \quad \text{and} \quad \left.\frac{d\Psi(\xi)}{d\xi}\right|_{\xi=0} = 0\ , \tag{3.29}$$

the Lane-Emden equation can be integrated numerically. Figure 3.5 shows the resulting Bonnor-Ebert density profile in linear and logarithmic scaling. The dimensionless coordinate ξ includes the characteristic radius $r_0 = c_s/\sqrt{4\pi G\rho_0}$ and the central density of the Bonnor-Ebert sphere ρ_0. When the central density, the internal temperature (via the sound speed c_s) and the radius of the Bonnor-Ebert sphere $R_{BE} = \xi r_0$ is given, the BE sphere is fully described.

The mass of a sphere with a given density profile can be expressed as

$$M = \int_0^r 4\pi r'^2\rho(r')dr'\ . \tag{3.30}$$

Together with (3.24), (3.27) and the Lane-Emden equation (3.28), the BE sphere mass is derived as

$$M_{BE} = 4\pi\rho_0\left(\frac{c_s^2}{4\pi G\rho_0}\right)^{3/2}\xi^2\frac{d\Psi(\xi)}{d\xi}\ . \tag{3.31}$$

By introducing the dimensionless mass

$$m = \frac{1}{\sqrt{4\pi}} \left(\frac{\rho(r)}{\rho_0} \right) \xi^2 \frac{d\Psi(\xi)}{d\xi} \tag{3.32}$$

and together with Eq. 3.21, we arrive at the expression

$$M_{BE} = \frac{m c_s^4}{P^{1/2} G^{3/2}} \ . \tag{3.33}$$

Applying linear stability analysis, Ebert (1955) and Bonnor (1956) found a critical value for the dimensionless radius $\xi_{\rm crit} = 6.451$, which divides stable and unstable solutions of BE sphere. The sphere is stable for $\xi < \xi_{\rm crit}$, it is marginally stable at $\xi = \xi_{\rm crit}$, and unstable for $\xi > \xi_{\rm crit}$. Collapse of a Bonnor-Ebert sphere can be induced by increasing its mass or the external pressure so that the mass of the given sphere becomes larger than the original BE mass. The BE sphere then collapses in the 'classical' outside-in fashion.

Comparison to Jeans criterion

The Jeans length

$$\lambda_J = \sqrt{\frac{\pi c_s^2}{G\rho_0}} \tag{3.34}$$

and the corresponding Jeans mass (a sphere with radius $\lambda_J/2$)

$$M_J = \frac{4\pi}{3} \rho_0 \left(\frac{\lambda_J}{2} \right)^2 = \frac{\pi^{5/2}}{6G^{3/2}} \frac{c_s^3}{\rho_0^{1/2}} \tag{3.35}$$

give a first, simple approach to analyze the stability of self-gravitating gas clouds (Jeans, 1902). These relations are derived through linear perturbation analysis of a homogeneous, isothermal, non-viscous medium in hydrostatic equilibrium. The cloud becomes unstable for $\lambda > \lambda_J$ or $M > M_J$. Thus, collapse sets in when the cloud self-gravity overcomes the balancing support by thermal gas pressure.

When we compare the Jeans length with the critical Bonnor-Ebert sphere radius ($\xi_{\rm crit} = 6.451$), we find

$$\lambda_J = \sqrt{\frac{\pi c_s^2}{G\rho_0}} \approx 1.77 \sqrt{\frac{c_s^2}{G\rho_0}} \quad \text{and} \quad r_{\rm BE,crit} = \left(\frac{c_s^2}{4\pi G\rho_0} \right)^{1/2} \xi_{\rm crit} \approx 1.82 \sqrt{\frac{c_s^2}{G\rho_0}} \ . \tag{3.36}$$

Interestingly, both ansatzes lead to similar values regarding the critical size of a gravitationally unstable sphere although the Jeans criterion was derived for a constant density profile while the BE ansatz considered a non-uniform density distribution.

Collapse timescales

A homogeneously dense, isothermal sphere in hydrostatic equilibrium (no pressure forces, zero initial velocities) collapses within the so-called free-fall time

$$t_{\rm ff} = \sqrt{\frac{3\pi}{32G\rho_0}} \tag{3.37}$$

The free-fall time only depends on the initial density, not on the temperature. Hence, all points of the sphere have the same density at a given time and arrive at the center simultaneously. The collapse is called homologous.

The Bonnor-Ebert sphere is has a non-homogeneous density profile and collapses outside-in, i.e. non-homologously. Therefore, a better expression of the collapse timescale of a BE sphere is (Banerjee et al., 2004)

$$t_0 = \frac{1}{\sqrt{4\pi G\rho_0}} \approx 0.52\, t_{\rm ff} \ . \tag{3.38}$$

Energy balance

The Bonnor-Ebert sphere collapses when its total energy

$$E_{\rm tot} = E_{\rm therm} + E_{\rm rot} + E_{\rm turb} + E_{\rm mag} + E_{\rm grav} \tag{3.39}$$

is negative.

$E_{\rm grav}$ is the gravitational potential energy of the sphere. While for a homogeneous sphere it is

$$E_{\rm grav} = -\frac{3}{5}\frac{GM^2}{R} \ , \tag{3.40}$$

it is for a Bonnor-Ebert sphere

$$E_{\rm grav,BE} = -\frac{3}{\xi_B\Psi_B'}\left\{1 - \frac{\xi_B\exp(-\Psi_B)}{3\Psi_B'}\right\}\frac{GM^2}{R} \ , \tag{3.41}$$

where $\Psi_B \equiv \Psi(\xi_B)$ and $\Psi_B' \equiv \Psi'(\xi_B)$ is the isothermal function as in (3.26) and its derivative both evaluate at the specific dimensionless radius ξ_B (Ebert, 1955; Bonnor, 1956).

The thermal energy of a cloud of mass M at temperature T consisting of gas with mean molecular weight μ is

$$E_{\rm therm} = \frac{3}{2}\frac{k_{\rm B}T}{\mu m_{\rm p}}M \tag{3.42}$$

where $k_{\rm B}$ is the Boltzmann constant and $m_{\rm p}$ the proton mass. The term $k_{\rm B}T/\mu m_{\rm p}$ is the expression for the isothermal sound speed.

The rotational energy is

$$E_{\rm rot} = \frac{1}{2}I\Omega^2 \tag{3.43}$$

with I being the moment of inertia and Ω the rotational frequency. For a Bonnor-Ebert sphere the moment of inertia reads $I = 0.28\,M_{\rm BE}R_{\rm BE}^2$ with $M_{\rm BE}$ and $R_{\rm BE}$ being the mass and radius of the BE sphere[6].

The turbulent energy of the gas within cloud is given by

$$E_{\rm turb} = \frac{1}{2}\sum_i m_i v_{\rm rms}^2 \ . \tag{3.44}$$

---

[6] We derive the pre-factor '0.28' by computing $I = \sum_i m_i r_{\perp,i}$ through summing up over all gas cells within our BE sphere, where m_i is the mass of gas cell i and $r_{\perp,i}$ its distance to the rotation axis of the sphere. As a reference where this factor is also applied see Walch et al. (2009)

where v_{rms} root-mean square velocity and m_i is the mass of gas cell i [7].

In our BE collapse studies, we scale the thermal, turbulent and rotational energies in terms of the gravitational energy, and therefore describe the energy content with the following parameters:

$$\alpha_{\mathrm{therm}} = \frac{E_{\mathrm{therm}}}{|E_{\mathrm{grav}}|} \ , \tag{3.45}$$

$$\alpha = \frac{E_{\mathrm{turb}}}{|E_{\mathrm{grav}}|} \ , \tag{3.46}$$

$$\beta = \frac{E_{\mathrm{rot}}}{|E_{\mathrm{grav}}|} \ . \tag{3.47}$$

To quantify the importance of the magnetic field compared to gravity, we can use the normalized mass-to-flux ratio

$$\mu = \frac{M}{\Phi} \Bigg/ \left(\frac{M}{\Phi}\right)_{\mathrm{crit}} \ . \tag{3.48}$$

Here, $\Phi = \int_A B\,dA$ is the flux of a magnetic field with initial field strength B_0 through the cross section of our cloud of mass M and radius R, and

$$\left(\frac{M}{\Phi}\right)_{\mathrm{crit}} = \frac{c_1}{3\pi}\sqrt{\frac{5}{G}} \tag{3.49}$$

is the critical mass-to-flux ratio with $\mathrm{c}_1 = 0.53$ (Strittmatter, 1966; Mouschovias & Spitzer, 1976) for a uniform sphere, where G is the gravitational constant. For $\mu > 1$ the gravitational force is strong enough to overcome magnetic forces and the cloud can collapse. A cloud with $\mu > 1$ is termed *supercritical* compared to the case where $\mu < 1$ which is called *subcritical*. One can define a parameter as above with

$$\gamma = \frac{E_{\mathrm{mag}}}{|E_{\mathrm{grav}}|} \tag{3.50}$$

which may be approximately estimated with $\gamma \approx \mu^{-2}$. For equality a pre-factor of μ^{-2} has to be derived which depends on the exact gravitational and magnetic energy of the cloud. Computing the energy of the magnetic field can become difficult as one has to consider both the field inside and outside the cloud (see e.g. Lequeux, 2005). Since such a detailed computation is beyond the scope of the studies presented in this thesis, we will refrain from going into further detail here.

Initializing the Bonnor-Ebert sphere initial conditions within AREPO

For generating an AREPO initial condition file having a grid with a particular number of cells, we first construct a file with a 3D uniform distribution of the desired number of cells, e.g. in our case 128^3. In order to gain the Voronoi cell structure, we use the AREPO feature *Mesh Relax*, i.e. running only the mesh regularization procedure, that allows us to evolve the initially uniform grid with AREPO for several time steps without following any physics or grid refinement. When the relaxed Voronoi mesh

---

[7] The thermal, rotational and turbulent energy belong to the kinetic energy: $E_{\mathrm{kin}} = E_{\mathrm{therm}} + E_{\mathrm{macro}}$ where the macroscopic motions of the gas, such as rotation or turbulent gas motions are summed up in the energy term E_{macro}.

structure is established in our initial condition file, we can set up the Bonnor-Ebert sphere density profile. The analytical solution of the Lane-Emden equation gives a table of dimensionless radii ξ and corresponding density distribution values ρ/ρ_0. We choose a desired central density value ρ_0 together with temperature of the gas at this density. The physical radius of the BE sphere can be derived via the characteristic radius

$$r_0 = \frac{c_\mathrm{s}}{\sqrt{4\pi G\rho_0}} \tag{3.51}$$

an the relation

$$R_\mathrm{BE} = \xi_\mathrm{B}\, r_0 \ . \tag{3.52}$$

For the BE sphere to be unstable, we take a value $\xi_\mathrm{B} > \xi_\mathrm{crit} = 6.451$. The choice of the central density may be further influenced by the the energy balance within our sphere. For collapse to happen, the total energy balance of our sphere must be negative, i.e.

$$0 > E_\mathrm{therm} + E_\mathrm{rot} + E_\mathrm{turb} + E_\mathrm{grav} \tag{3.53}$$

$$0 > (\alpha_\mathrm{therm} + \beta + \alpha - 1)|E_\mathrm{grav}| \ . \tag{3.54}$$

Due to the high temperatures in the primordial gas, α_therm is rather high of the order ~ 0.8, for a typical primordial Bonnor-Ebert sphere setup with $\xi_\mathrm{B} = 6.5$. This might cause trouble when choosing high turbulent α and/or rotational β values of the order of a few ten percent as they are motivated from observed star-forming environments or self-consistent cosmological simulations (e.g. Bromm et al., 2002; Goodwin et al., 2004a,b; Yoshida et al., 2006). Consequently, the total energy balance can become positive and possible collapse is very much slowed down or even suppressed completely. To prevent such a scenario and still be able to study effects of different levels of turbulence and rotation on the collapsing sphere, one may re-scale the central density and thus the mass of the Bonnor-Ebert sphere to a higher value. Thereby $|E_\mathrm{grav}|$ increases, α_therm takes on a smaller value, and the total energy balance can be kept negative when all other property values stay the same. We will refer to this procedure again, if it is applied, when we describe the specific initial conditions of our runs.

In order to apply the BE density profile to our prepared AREPO initial condition file, we compute radius vectors, r_i with $i = 1, ..., 128^3$, centered on the geometrical center of our simulation box for all cells. We parametrize the radius vectors to achieve a relation for the dimensionless radius ξ by $r_\mathrm{i}/R_\mathrm{BE} = \xi$. By interpolation from our BE sphere solution table, we assign all cells with $r_\mathrm{i}/R_\mathrm{BE} = \xi < \xi_\mathrm{B}$, a value ρ/ρ_0 of the density profile and multiply this value with our chosen central density ρ_0 value to receive the actual physical density. The cells outside the sphere get the same density value as those cells at the edge of the sphere. Since we do not apply a density contrast at the edge of the sphere, the temperature inside and outside of the sphere is the same.

After setting up the BE density profile in the simulation box of our initial condition file, we can further assign to the cells within the BE sphere some velocity field, e.g. to describe some rotation and/or turbulence. We consider BE spheres that rigidly rotate around the z-axis and therefore assign the cells

$$v_\mathrm{x,j} = \Omega\, y_\mathrm{j} \tag{3.55}$$

$$v_\mathrm{y,j} = -\Omega\, x_\mathrm{j} \tag{3.56}$$

where the rotation frequency is derived from $\beta = E_\mathrm{rot}/|E_\mathrm{grav}|$ with Eq. (3.41) and (3.43) as

$$\Omega = \sqrt{\frac{\beta\, G M_\mathrm{BE}}{0.192\, R_\mathrm{BE}}} \ , \tag{3.57}$$

and x_j, y_j, $v_\mathrm{x,j}$ and $v_\mathrm{y,j}$ are the x and y component of coordinate and velocity of a cell j where index j refers to cells within the BE sphere only.

Since the final AREPO initial condition file only includes cell masses, internal energies, and velocities, cell densities and temperatures finally need to be transformed to masses and internal energies[8].

Initializing the turbulent velocity field

For the study about the influence of turbulence and rotation on the formation of Population III accretion disks and the creation of Pop III stellar clusters through disk fragmentation presented in Chapter 5, we use as initial condition a Bonnor-Ebert sphere for which we vary its initial level of rotational and turbulent energy. The rotation is defined as rigid rotation around the geometrical z-axis. Turbulence is included by superimposing a homogeneous, isotropic Gaussian random field onto our BE sphere. We do not drive the turbulence but let it freely decay over the course of the simulation. The Gaussian random field is constructed by a combination of randomly distributed phases together with an amplitude following a Rayleigh distribution (Bardeen et al., 1986). The power spectrum of the velocity field is chosen to be $P(k) \propto k^{-4}$. The negative exponent (the exponent is generally named spectral index here) illustrates that more power lies at low frequencies k (also called a red spectrum compared to the blue spectrum with positive exponents and power at high frequencies and a white spectrum with n=0 meaning that the power is equally distributed at all frequencies). The choice of $n = -4$ is a standard choice The slope is motivated e.g. by the study of Clark et al. (2011a). This power spectrum mimics that due to the compressibility of the gas, the real power spectrum will be steeper than the standard Kolmogorov description (Kolmogorov, 1941) for incompressibile flows. We construct the field in Fourier space, transform it into real space and only use its real parts. We use a mixed mode spectrum. After deriving the root-mean square value of this field, we invert this value and use it to rescale the velocity of our turbulent field as desired. We perform runs with two different values of the turbulent α: a low turbulence case with $\alpha = 0.05$ and a high turbulence case with $\alpha = 0.25$. Our choice of the values here is motivated by the studies from Goodwin et al. (2004a,b).

Now, we give some more details about the motivation of a homogeneous, isotropic Gaussian random field for the construction of the turbulent velocity field [9].

A random process is described by a collection of random variables. Random variables can be seen as functions which map the outcomes of the process. In general definitions and definitions referring to random processes where the random variables are indexed by integers or real numbers, one usually uses the symbol X. On the other hand, when talking about random fields for which the random variables are indexed by real-valued vectors of some dimension d, one often employs the expression $f(\mathbf{r})$, where $\mathbf{r}$ is some kind of '"location" vector and is also vector-values of dimension d. A (N, d) random field is spanned by a set of N random variables, $f(\mathbf{r_1}),...,f(\mathbf{r_N})$, of which each represents one of the points in N-dimensional real space[10]. According to

---

[8] $E_\mathrm{int} = k_\mathrm{B}T/((\gamma-1)\mu m_\mathrm{p})$ where $\gamma = 5/3$ and $\mu = 1.22$ initially.

[9] The theoretical descriptions and the notations used in this section are motivated from Bardeen et al. (1986), "Stats352 - Spatial Statistics", Prof. J. Taylor, 2009, Stanford University, USA, and "Astro 635 - Elements of Astrophysics, Chapter 3: Random Fields", Nick Kaiser, Institute for Astronomy, University of Hawaii.

[10] For general definitions of probability or cumulative distribution functions, we are going to use the expression X. For formulas directly referring to random fields we use $f(\mathbf{r})$.

the *Kolmogorov Existence theorem* the distributional properties of such a random field are determined by its finite-dimensional distributions. For that we use

$$p(f(\mathbf{r_1}),...,f(\mathbf{r_N}))df(\mathbf{r_1})...df(\mathbf{r_N}) \tag{3.58}$$

which give the probability to observe the field value, i.e. the value of the random variable, $f(\mathbf{r_1}) = f_1$, ..., $f(\mathbf{r_N}) = f_N$ at $1,...,N$ positions $\mathbf{r_1},...,\mathbf{r_N}$; here $p(f(\mathbf{r_1}),...,f(\mathbf{r_N}))$ are the probability distributions of the field at positions $\mathbf{r_1},...,\mathbf{r_N}$. If these probability distributions are multivariate Gaussians, i.e. each random variable follows a Gaussian (also normal) distribution with a probability density function[11]

$$p(x) = \frac{1}{2\pi\sigma^2}\exp\left(-\frac{x-\mu)^2}{2\sigma^2}\right) \tag{3.59}$$

where μ is the mean value, σ is the standard deviation and σ^2 the variance, the random field is called a Gaussian random field[12].

Gaussian fields are often used to describe random fields whose real distributions are not known. This approach is valid as the *Central Limit Theorem* (CLM) states that the sum of a large number of independent random variables tends to be normally distributed, i.e. they follow a Gaussian distribution. Another advantage of Gaussian random field is that their hierarchy of distribution functions can be reduced to joint 2-point correlation functions, that is integrals over the distribution functions connecting two points, e.g.

$$\xi(\mathbf{r_1},\mathbf{r_2}) = \langle f(\mathbf{r_1})f(\mathbf{r_2})\rangle = \int df(\mathbf{r_1})\int df(\mathbf{r_2})\, f(\mathbf{r_1})f(\mathbf{r_2})\, p(f(\mathbf{r_1}),f(\mathbf{r_1}))\ . \tag{3.60}$$

The Fourier transform of the 2-point correlation function is the power spectrum (*Wiener-Khinchin theorem*):

$$P(\mathbf{k}) = \int d^d r\, \xi(\mathbf{r}')\, \exp(i\,\mathbf{k}\,\mathbf{r}') \tag{3.61}$$

where $\mathbf{r}' = \mathbf{r_1} - \mathbf{r_2}$, and

$$P(\mathbf{k}) \propto \langle|\widetilde{f}(\mathbf{k})|^2\rangle \tag{3.62}$$

with

$$\widetilde{f}(\mathbf{k}) = \int d^d r\, f(\mathbf{r})\, \exp(i\,\mathbf{k}\,\mathbf{r}) \tag{3.63}$$

is the Fourier transform of the random field value, i.e. the value of the random variable at position $\mathbf{r}$. To ensure the reality of $f(\mathbf{r})$, it is $\widetilde{f}(\mathbf{k}) = \widetilde{f}^*(-\mathbf{k})$.

In a homogeneous and isotropic Gaussian random field, the 2-point correlation function is a function of the distance only, i.e. of modulus of the separation $|\mathbf{r_1} - \mathbf{r_2}|$, and correspondingly $P(\mathbf{k}) = P(k)$.

To construct a homogeneous and isotropic Gaussian random field numerically, we follow the CLT and represent it by a sum of independent random variables via a Fourier synthesis

$$f(r) = \sum_k \widetilde{f}(k)\, \exp(ikr) \tag{3.64}$$

---

[11] Probability density functions describe the probability that the random variable X has the value x.

[12] σ is called a scale parameter which determines the dispersion of a probability distribution while μ is a location parameter that defines the shift or the location of the peak of the distribution.

where the spatial Fourier modes $\widetilde{f}(k) = \widetilde{f_k} = |\widetilde{f_k}| \exp(i\theta_k)$. Due to the reality of $f(r)$, we focus on the upper half of k-space, and thus the phase angle obeys $\theta_{-k} = -\theta_k$. From Bardeen et al. (1986), we know that for such a field, the various spatial Fourier modes, $\widetilde{f_k}$ must have phases, which are randomly distributed in the interval $[0, 2\pi]$, and amplitudes, $|\widetilde{f_k}|$, which follow a Rayleigh distribution.

The phases are then

$$\exp(i\theta_k) \sim \exp(2\pi i\, u) \tag{3.65}$$

where u is a random number generated from the standard uniform distribution in the interval $[0, 1]$.

A Rayleigh distribution is a continuous probability distribution for positive-valued random variables x whose cumulative distribution function is

$$\mathrm{CDF}(x; \sigma) = 1 - \exp\left(-\frac{x^2}{2\sigma^2}\right) \tag{3.66}$$

with the scale parameter σ. For our purpose, the scale parameter is $\sigma = \sqrt{P(k)}$. For the amplitude, $|\widetilde{f_k}| \propto \sqrt{P(k)}$, to follow a Rayleigh distribution, we apply the *Inverse Transform Sampling method.* In this method, one first derives the inverse of the cumulative distribution function (CDF)[13] of the desired distribution. The scale variable of the distribution is our amplitude. Then, one use the inverse CDF and computes it for random number u which similarly to above is taken from the standard uniform distribution in the interval $[0, 1]$. The result of this computation is the newly generated amplitude that follows the desired distribution:

$$|\widetilde{f'_k}| \sim \sqrt{-2\ln(u)P(k)} \tag{3.67}$$

where again u is a random number generated from the standard uniform distribution in the interval $[0, 1]$.

The whole new expression of the Fourier synthesis then reads

$$f(r) = \sum_k \sqrt{-2\ln(u)P(k)}\ \exp(2\pi i\, u)\ \exp(ikr) \tag{3.68}$$

and describes a homogeneous, isotropic Gaussian random field.

---

[13] The CDF gives the probability that the random variable X takes a value less than or equal to x.

CHAPTER 4

How the first stars regulated star formation: enrichment by nearby supernovae

Parts of this Chapter were published in Chen et al. (2017). I performed the 2D ZEUS-MP simulations of halo photoevaporation by nearby Population III stars and provided the text of Section 2.1. and Figure 2 to the publication[1]. I was an active participant in the discussions that lead to Section 3.1 and parts of the Discussion/Conclusion Section, although the actual text of these sections in the publication were written by my co-authors. In Sections 4.3.2, 4.4 and 4.5, some of the points mentioned in these parts of the paper, are presented in my own words.

The focus in this Chapter generally lies at the analysis of my 2D ZEUS-MP runs. Compared to what is presented in the publication, I present here more details on the physics of halo photoevaporation and illustrate my findings with additional figures. I took two figures from the paper which where produced by Ke-Jung Chen in order to stress the importance and consequences of my 2D ZEUS-MP simulations for the rest of the study presented Chen et al. (2017) [2]

4.1 Introduction

Since the formation of the first stellar objects in the universe, stars have affected their environment by radiative and supernova feedback and influenced the evolution of later stellar generations (e.g. Ciardi & Ferrara, 2005; Greif et al., 2007; Yoshida et al., 2007; Wise & Abel, 2008; Wise et al., 2012; Pawlik et al., 2013; Hirano et al., 2015). Of particular interest is the transition between the metal-free first stars, the so-called Population III (Pop III) stars, and the metal-enriched second generation stars, the so-called Population II (Pop II) stars (e.g. Bromm et al., 2001a; Yoshida et al., 2004). Examining this transition helps us to get a better understanding both of metal enrichment of the early universe per se as well as of the role of radiative feedback in shaping the early universe (e.g. Greif et al., 2007; Smith & Sigurdsson, 2007; Smith et al., 2009; Ritter et al., 2012; Chiaki et al., 2013; Safranek-Shrader et al., 2014) and possible observational signals in terms of supernovae (SNe) (e.g. Whalen et al., 2013b,a) or

---

[1] The mentioned "Section 2.1", "Figure 2", and "Section 3.1" do not refer to sections and a figure in this Chapter but to the original numbers in the publication Chen et al. (2017)

[2] Note that the the name of the halos was changed for the paper. Below the most massive halo is denoted as ’halo 2’ while in the paper it is ’halo 3’. I am going to point out the difference again below where needed.

metal-enriched primordial, low-mass stars (e.g. Beers & Christlieb, 2005; Frebel et al., 2005, 2008).

Numerical models of Population III star formation suggest that they formed in so-called minihalos of mass $\sim 10^5 - 10^7\,\mathrm{M}_\odot$ at redshift $z \sim 20 - 30$ (e.g. Haiman et al., 1996; Tegmark et al., 1997). Depending on the formation scenario, Population III stars might have had masses of up to several hundred $\mathrm{M}_\odot$, when forming in isolation (e.g. Bromm et al., 2002; Abel et al., 2002; Yoshida et al., 2003), or mainly subsolar to a few ten $\mathrm{M}_\odot$ and only sporadically a few hundred $\mathrm{M}_\odot$ when arising in protostellar clusters through fragmentation of protostellar accretion disks (e.g. Greif et al., 2011; Susa et al., 2014; Stacy et al., 2016). With surface temperatures of $\gtrsim 10^5\,\mathrm{K}$, they produced significant ultraviolet (UV) radiation (Bromm et al., 2001b; Omukai & Palla, 2001; Schaerer, 2002; Hosokawa et al., 2011; Stacy et al., 2012). Next to ionizing UV feedback, Lyman-Werner (LW) UV radiation in the energy range of $11.18 - 13.6\,\mathrm{eV}$ is of particular importance as such photons are able to dissociate molecular hydrogen, H_2, the main coolant in primordial gas. Thus, this feedback has direct influence on the efficiency of gas collapse and new star formation both close and far from the Pop III star. Indeed, according to numerical simulations, Pop III HII regions were up to several kiloparsec large and due to the transparency of neutral H and He to the LW radiation, LW photons were able to travel even beyond the edge of the Pop III HII regions. In this way Pop III stars were able to strongly affect their host halos (Whalen et al., 2004; Kitayama et al., 2004; Alvarez et al., 2006; Abel et al., 2007; Johnson et al., 2007) but also neighboring halos by ionizing and photoevaporating them (Whalen et al., 2008, 2010; Smith et al., 2015). Studies have shown that ionizing UV radiation from nearby Pop III stars can ablate the outer layers of the halo in supersonic flows and expose its interior to the IGM (O'Shea et al., 2005; Susa & Umemura, 2006; Susa, 2007; Whalen et al., 2008, 2010; Wise & Abel, 2008; Hasegawa et al., 2009; Susa et al., 2009).

The questions arising here are: what impact does photoevaporation of a halo by a nearby Pop III star have for a subsequent metal-enrichment of that halo by the supernova ejecta of the Pop III star? Can second generation stars promptly form in the debris of the photoevaporated neighboring halo? The earlier study by Cen & Riquelme (2008) simulated enrichment of a $10^6 - 10^7\,\mathrm{M}_\odot$ halo by a nearby Pop III star. They did not consider halo photoevaporation prior to the supernova. They only find mild mixing of metals with the halo gas in the outermost halo layers due to shear instabilities. Metals were not able to penetrate in the halo interior. Some other studies (Gray & Scannapieco, 2011; Richardson et al., 2013) propose that additional turbulent gas motions within the halo might facilitate the taking-up of metals in the halo interior. The study by Smith et al. (2015) then accounted for halo photoevaporation prior to the core-collapse supernova of a $40\,\mathrm{M}_\odot$ Pop III star at $200\,\mathrm{pc}$ distance and found that the photoevaporation and its impact on the halo in stripping of some halo layers made it possible for the supernova ejecta to penetrate into the halo interior.

In our study here, we extend this parameter space and examine the impact of pre-supernova halo photoevaporation on the efficiency of mixing and metal enrichment by the supernova ejecta by considering the effects of $25\,\mathrm{M}_\odot$ and $200\,\mathrm{M}_\odot$ stars at distances larger than Smith et al. (2015). The $25\,\mathrm{M}_\odot$ star dies in a core-collapse supernova (CCSN) whereas the $200\,\mathrm{M}_\odot$ star explodes as a pair-instability supernova (PISN) (Heger & Woosley, 2002).

This chapter is structured as follows: in Section 4.2 we present our general numerical approach for the whole study and in particular for the 2D ZEUS-MP halo photoevaporation simulations together with the corresponding initial conditons. In Section 4.3.1 and 4.3.2, we describe the evolution of our halos during the photoevaporation by a nearby star and after the death of the star. While looking at the results from the subsequent modeling of chemical mixing and enrichment with the CASTRO done by Ke-Jung Chen, we discuss the influence of the halo photoevaporation on the efficiency of metal mixing in Section 4.3.3. We mention some shortcomings of our study in Section 4.4. In Section 4.5, we conclude this chapter with a discussion of our results and the conclusions as well as with giving some prospects for future studies.

4.2 Method

4.2.1 Numerical approach

The numerical approach of entire project presented in Chen et al. (2017) consists of three steps divided over two different numerical codes. The different stages are presented in Fig. 4.1. In the first step, a halo is photoevaporated by UV radiation from a nearby Population III star for the whole lifetime of the star. After the star has died, the simulation is continued for the time the supernova (SN) ejecta needs to reach the border of the simulation box to ensure that the subsequent mixing calculation starts from a more realistic halo setup. The halo photoevaporation is simulated in 2D with the radiation hydrodynamic code ZEUS-MP. In the second step, ZEUS-MP is again used, this time in 1D, to simulate first the expansion of the stellar HII region within the host halo during the lifetime of the star and then the supernova explosion and the consequent propagation of the supernova ejecta to the box boundary. In the third step, the final state of the photoevaporated halo together together with the inflowing SN ejecta from the previous two steps are mapped onto a 3D Cartesian grid of the AMR radiation hydrodynamics code CASTRO (Almgren et al., 2010; Zhang et al., 2011) where now the mixing of the SN ejecta with the photoevaporated halo is modeled. In contrast to detailed primordial chemistry in the ZEUS-MP simulations, in CASTRO only three species (hydrogen, helium, and metals - the individual species of H and He from the ZEUS-MP calculations are summed for the use in CASTRO) are advected with the hydrodynamical flow and only a simple cooling function (Gnedin & Hollon, 2012) is used. With the help of nested grid a maximum resolution of $0.015\,\mathrm{pc} = 3000\,\mathrm{AU}$ is reached. In the following descriptions, we concentrate on the results of the 2D halo photoevaporation simulations. For more details about the numerical method and the result description of the second and third step, please see Chen et al. (2017).

ZEUS-MP

ZEUS-MP is a massively-parallel radiation hydrodynamics code that evolves astrophysical fluid flows self-consistently with nonequilibrium nine-species primordial gas chemistry and multifrequency photon-conserving raytracing UV transport to evolve cosmological ionization fronts (I-fronts; Whalen & Norman, 2006; Whalen & Norman, 2008a,b). More details of the code are provided in Section 3.1.

4.2.2 Initial conditions

We consider 25 and $200\,\mathrm{M}_\odot$ stars at a distance of 250 pc to 6.9×10^5, 2.1×10^6, and $1.2 \times 10^7\,\mathrm{M}_\odot$ halos. In addition, we run a setup with the $200\,\mathrm{M}_\odot$ star at a distance of 500 pc from the halo centers. These halos bracket the range in mass in which Pop III stars form via H_2 cooling and are extracted from cosmological simulations performed

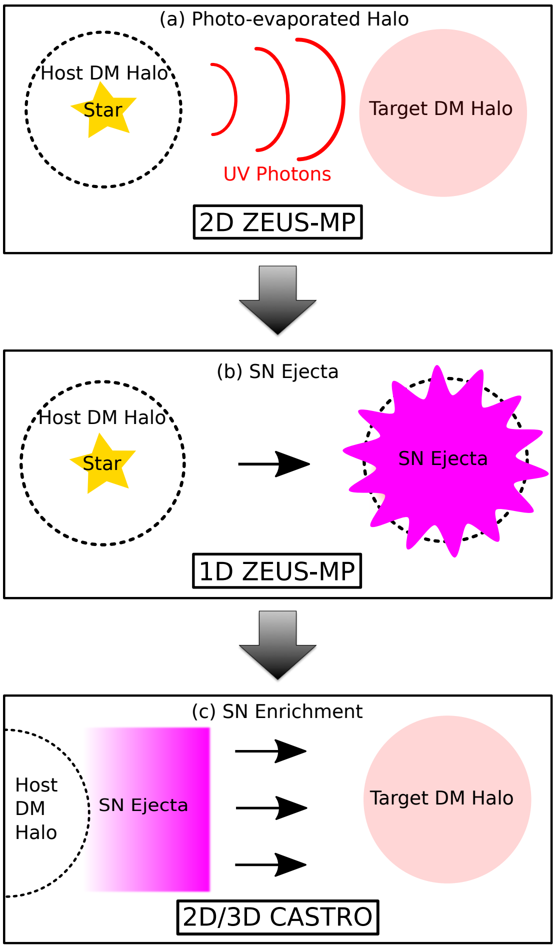

Figure 4.1: Numerical approach of the Chen et al. (2017) project. (a) Photoevaporation of a halo by a nearby Population III star until the end of the star's lifetime, modeled in 2D with ZEUS-MP. (b) 1D ZEUS-MP simulation to model the propagation of supernova (SN) ejecta before they reach the boundary of the simulation box in CASTRO. (c) Multidimensional modeling of SN ejecta mixing with the photoevaporated halo. Image credit: Ke-Jung Chen

Table 4.1: Target halos, supernovae and distance between star from halo center. $R_{200} = R(\rho = 200\,\Omega_{b,0}\,\rho_{crit})$. Note the different labelling of halo 2 and 3 compared to Chen et al. (2017). Furthermore, compared to publication, I have run an additional model of halo photoevaporation: h*sn200-2, where the star stands for 1, 2 or 3. In this model, we consider the photoevaporation of halo 1, 2 and 3 by the $200\,M_\odot$ star at a distance of 500 pc. This setup was not continued with the mixing calculations, but we present it here in the context our halo photoevaporation runs as it shows some interesting features; see below.

Model	Halo mass/ $M_\odot$	R_{200}/pc	SN type	r_{sep}/pc
h1sn25	6.9×10^5	249.6	CC	250
h1sn200	6.9×10^5	249.6	PI	250
h1sn200-2	6.9×10^5	249.6	PI	500
h3sn25	2.1×10^6	320.1	CC	250
h3sn200	2.1×10^6	320.1	PI	250
h3sn200-2	2.1×10^6	320.1	PI	500
h2sn25	1.2×10^7	483.1	CC	250
h2sn200	1.2×10^7	483.1	PI	250
h2sn200-2	1.2×10^7	483.1	PI	500

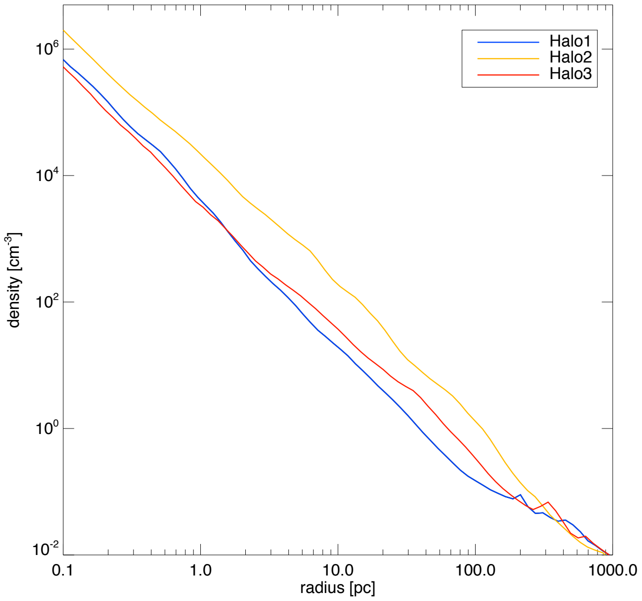

Figure 4.2: Spherically averaged density profiles for the $6.9\times10^5\,M_\odot$ (halo 1), $2.1\times10^6\,M_\odot$ (halo 3), and $1.2\times10^7\,M_\odot$ (halo 2) models.

with the Enzo code (Bryan et al., 2014). We show spherically-averaged density profiles of all three halos prior to illumination in Figure 4.2. As seen from the central densities, they are at intermediate stages of collapse but have not yet formed stars. We present a 2D overview of the halo density structures, the H_2 mass fraction and temperatures in Fig. 10.1 of the Appendix. The densities, gas energies, velocities and species mass fractions of these halos are spherically averaged and mapped onto a two-dimensional (2D) cylindrical coordinate grid in ZEUS-MP. The ionizing UV fluxes and lifetimes of the two stars are taken from Schaerer (2002). Each halo is centered on the z-axis, with only its upper hemisphere residing on the grid. The grid has 1000 zones in z and 500 zones in r for a spatial resolution of 0.25 pc. The boundaries are at -125 pc and 125 pc in z and 0.01 pc and 125 pc in r. Reflecting boundary conditions (BCs) are applied to the inner r boundary and outflow BCs are set on the other three boundaries. All simulations were performed at redshift $z = 20$.

The dark matter potentials of these halos are modeled through computation of a separate potential that cancels out every pressure force on the grid. In this way, the halos are held in hydrostatic equilibrium. The potential is kept fixed for the whole simulation, which is a reasonable approximation as the stars and gas within the halo evolve faster than the potential ($t_{\mathrm{gas}} << t_{\mathrm{merger}}, t_{\mathrm{Hubble}}$).

4.3 Results

In Section 4.3.1, we describe the evolution of halo photoevaporation by a nearby star in general but give specific remarks on differences in the evolution of the three halos. We explain the general evolution of a photoevaporated halo after the death of the nearby star in Section 4.3.2. Finally, in Section 4.3.3, we compare the final structure of our halos at the end of the 2D ZEUS-MP simulations with the levels of mixing observed in the CASTRO simulations.

4.3.1 Halo photoevaporation

At $t = 0\,\mathrm{yr}$, the ionization front (I-front) from the star enters the box from the left. In the beginning, it is R-type and its shape is planar. The latter is a good approximation for the radiation coming from some distant star as considered in our models (Whalen & Norman, 2006; Whalen & Norman, 2008a,b). The density structure of the halo does not change yet as the I-front is still supersonic (see second panel on the left, top row in Fig. 4.3). On the other hand, the molecular hydrogen content of the box is already affected strongly. This is because ahead of the I-front, Lyman-Werner (LW) photons begin to photodissociate the H_2 in the box. In the second picture from the left of the middle row of Fig. 4.3 we can see how the initial high molecular hydrogen fraction, indicated by the yellow color, suddenly decreases with the incoming I-front, shown by the change to green and dark blue color. Some of these UV photons penetrate further into the stratified layers of the halo and dissociate molecular hydrogen there (greenish, reddish areas right of the I-front).

As the I-front slows down, it becomes a D-type front. It passes the halo, ablates gas from its outer layers and shapes the halo into a parabolic, partially cometary appearance because it preferentially advances in the more stratified densities above and below the midplane of the halo (see the pictures in the right two columns of Fig. 4.3.

In the second picture from the left in the middle row in Fig. 4.3, we can see a prominent arc of H_2 emerging in the outer layers of the I-front. It forms there because

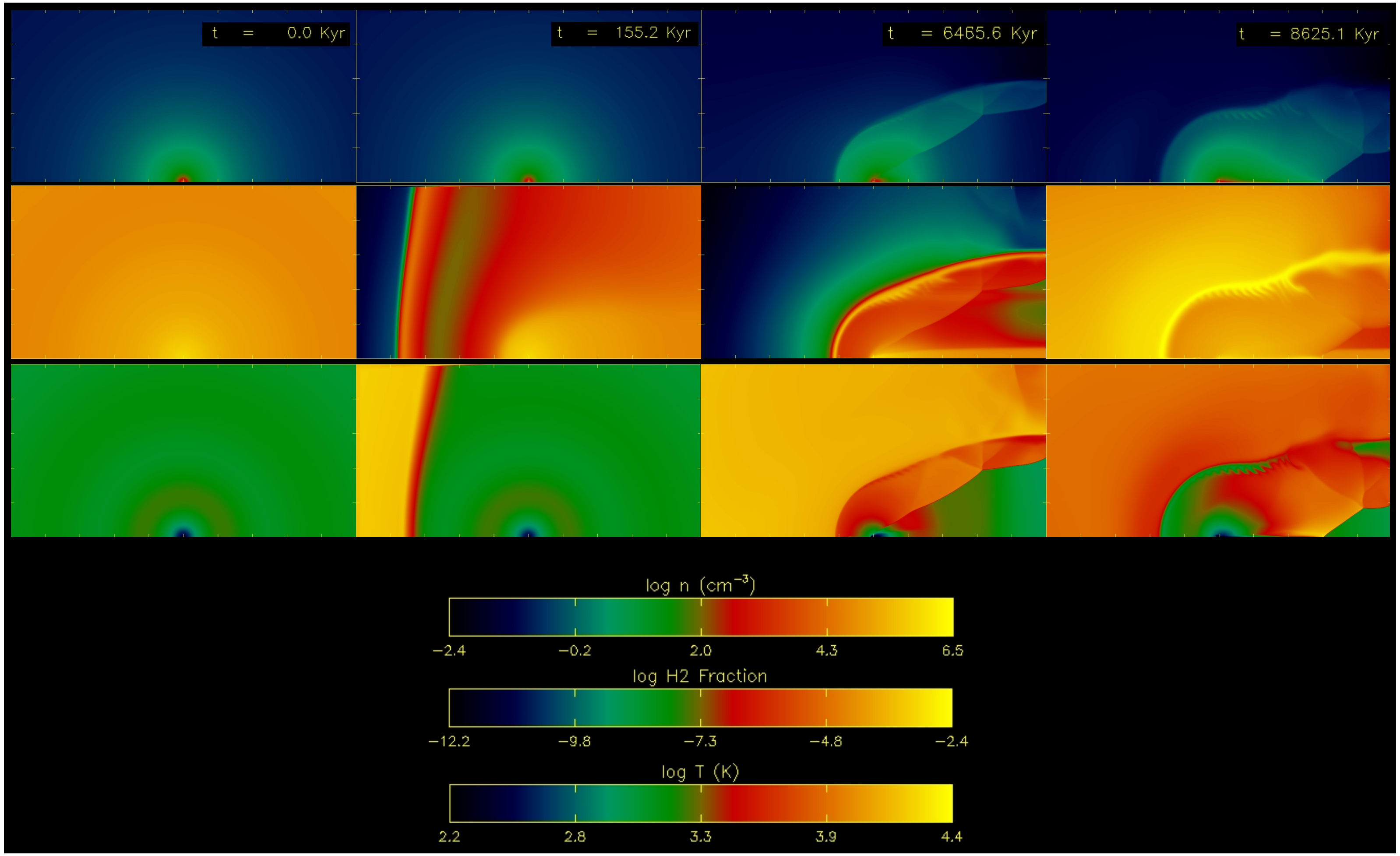

Figure 4.3: Evolution of halo 1 while being photoevaporated by a 25 $M_\odot$ star at 250 pc distance. From top to bottom: halo density structure, H_2 mass fractions and temperatures. The horizontal and vertical axes are z and r, respectively.[a]

---

[a] We have chosen this halo-star combination as representative example for the halo evolution because features that are important for the later discussion can be seen clearly here. In Fig. 10.2 to 10.5 in the Appendix, we present different stages of the halo evolution for all our halo-star combinations.

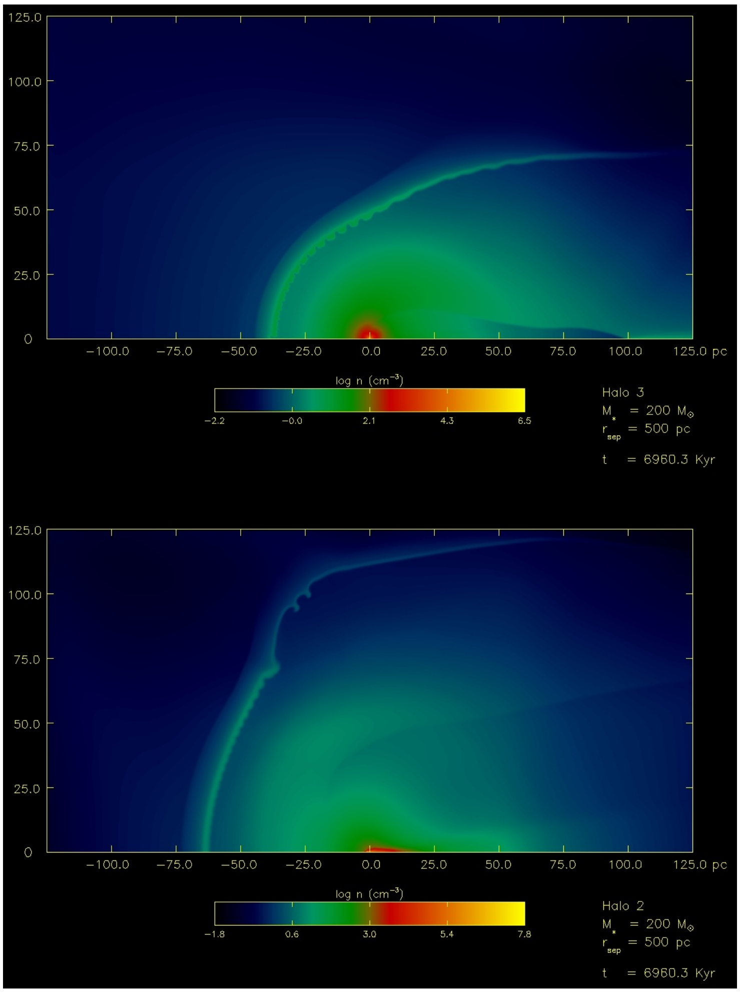

Figure 4.4: Final density structures of the intermediate mass halo 3 and most massive halo 2 after being photoevaporated by a $200\,M_\odot$ star at 500 pc distance.

the hard UV spectrum of the star broadens the I-front, creating temperatures of a few thousand K and ionization fractions of ~ 0.1 in its outer layers that catalyze rapid formation of H_2 via the H^- channel (Ricotti et al., 2001). The arc gets more prominent with continued photoevaporation of the halo (see the next picture to the right). This H_2 arc in the outer layers of the I-front partially shields the halo core from LW photons: the H_2 color scheme right of the front/arc stays reddish or even yellow instead of turning blue. A continuous balance between LW H_2 dissociation and re-formation through the H^- channel can be held here. The H_2 content in the halo is further preserved due to its own H_2 self-shielding action. The denser the gas, the more H_2 can be preserved. In the two middle panels in the middle row of Fig. 4.3, we see nicely the transition between highly affected low-density gas in the outer halo region (green colored) to the less affected, denser gas in the inner regions of the halo (red to orange colored) and the almost unaffected halo core (yellow).

At later times in the halo evolution - see the two panels on the right in the middle row of Fig. 4.3 - we observe serrated structures midway up the arc of the front. These are remnants of dynamical instabilities that are driven by H_2 cooling in the outer layers of the front (see also Whalen & Norman, 2008a; Whalen et al., 2008, 2010). They are more distinctive further out along the arc because of the larger angles of incidence between the photons and the front there (Williams, 2002). These structures are of interest because they are likely to enhance mixing between outflows from the halo and the SN ejecta. We also find these instabilities in case of halo 2 and halo 3 and the $200\,\mathrm{M}_\odot$ star at 500 pc distance, see Fig 4.4. While here in case of the most massive halo 2, the I-front does not come closer than $\sim 60\,\mathrm{pc}$ to the center of the halo, and thus the arc with instabilities stays in the outer halo region, the medium mass halo 3 is again shaped into cometary appearance and the arc with its instabilities is closer ($\lesssim 50\,\mathrm{pc}$) to the halo center. We generally find that more massive stars with higher UV fluxes only create thin H_2 arcs in their outer layers and thus less H_2 cooling and growth of instabilities occurs there. However, in a distance of 500 pc, the strong radiation of the $200\,\mathrm{M}_\odot$ star could already partially be diluted such that the flux of LW photons ahead of the front was smaller when it encountered the halo and therefore a broader H_2 arc with more cooling and consequent I-front instabilities could evolve; see Fig. 4.5 [3].

As the outer layers of the halo are blown off by the radiation front, supersonic flows are also driven back towards the star, e.g. see the greenish veil-like structure above the halo shadow in the second panel from the right in the middle row of Fig 4.3. These flows will collide with and mix with ejecta from the SN that will enter the box from the left border.

In all cases considered, we find that the molecular core is protected by both the shielding from the arc and that of the core itself. By the end of the simulation, a pristine halo core has survived in all our simulations. The most strongly strongly affected halo is halo 1 in case of the $200\,\mathrm{M}_\odot$ star at 250 pc distance. The most massive halo, halo 2, is the least affected one. Only when being photoevaporated by the $200\,\mathrm{M}_\odot$ star at 250 pc distance a distinctive comet-like shape is developed by this halo. In the other two cases, the I-front begins to evaporate the outer halo layers but cannot reach the halo closer than $\sim 60\,\mathrm{pc}$. We find ionization front instabilities in three cases. Such structures are regions where efficient mixing with the SN ejecta is likely happen. They are prone to be strongly dynamically effected by the SN shock leading to extended turbulent layers that mix violent with the incoming SN ejecta and are likely to collapse fast due to cooling by the increase H_2 fraction there and cooling from the SN metals.

We find that the strength of the shadow cast by the halo, while it is shaped into a parabolic appearance during the photoevaporation, depends on the halo mass, the stellar luminosity and the proximity of the star. For a less massive halo, a more luminous star or closer distance between halo and star, the shadow is narrow with almost cometary appearance. On the other hand the shadow becomes broader for a more massive halo, a less luminous star or larger distance. See Fig. 10.2 to 10.4 in the Appendix for an overview of the various halo structures at the end of lifetimes of the stars.

4.3.2 Halo evolution after the death of the star

The main-sequence lifetime of the $25\,\mathrm{M}_\odot$ star is 6.46 Myr and for the $200\,\mathrm{M}_\odot$ 2.2 Myr (Schaerer, 2002). The $25\,\mathrm{M}_\odot$ star explodes in a core-collapse supernova (CCSN) with an explosion energy of $E_{\mathrm{ej}} = 10^{51}$ erg and metal yield of $M_{\mathrm{ej}} = 20\,\mathrm{M}_\odot$ (leading to the formation of a $5\,\mathrm{M}_\odot$ black hole), and the $200\,\mathrm{M}_\odot$ star in a pair-instability supernova

---

[3] For an overview between all halo-star combinations, see Fig. 10.2 to 10.4 in the Appendix.

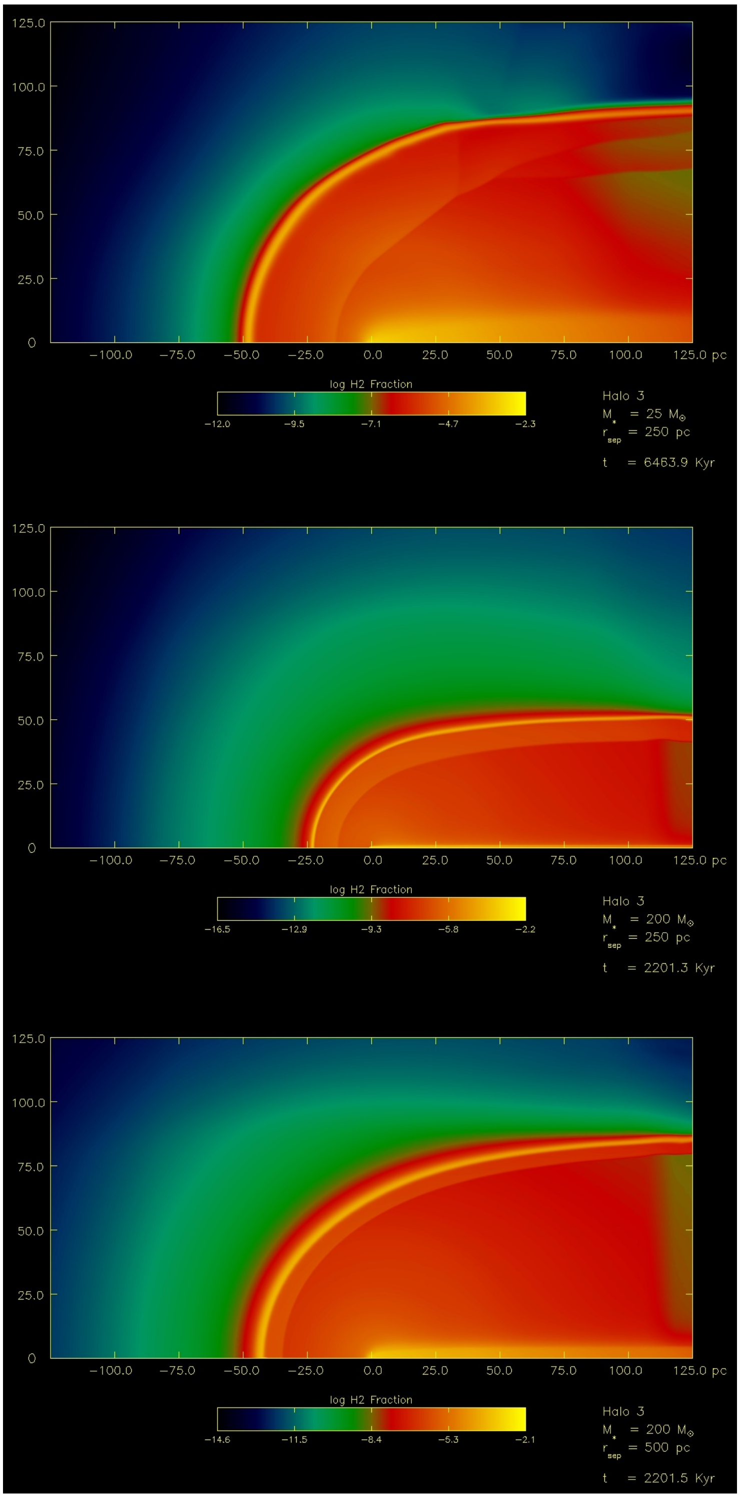

Figure 4.5: Halo 3: comparison of H_2 mass fraction plots for different stars and distances between star and halo center. From top to bottom: $25\,M_\odot$ star at 250 pc distance and $200\,M_\odot$ star at 250 pc and 200 pc. We can clearly see the thinner H_2 arc for $200\,M_\odot$ star at 250 pc distance in the middle panel compared to broader arcs in the other two panels. The plots show roughly the time when the star dies.

(PISN) with $E_{\rm ej} = 42 \times 10^{51}\,$erg and $M_{\rm ej} = 200\,{\rm M}_\odot$[4]. We continue to run the 2D ZEUS-MP simulations for another 2.16 Myr, 0.872 Myr and 4.757 Myr in the $25\,{\rm M}_\odot$ and $200\,{\rm M}_\odot$ star at 250 pc and 500 pc respectively. This is the time required for metals from the SN to reach the left boundary of the grid. The times are taken from the 1D ZEUS-MP SN models. During this additional time radiation is switched off and the photoevaporated, ionized halo environment, i.e. the H II region is allowed to cool and recombine. The additional time ensures that the SN metals encounter a more realistic circumhalo structure at time of collision.

After the death of the star, the halo evolves in the following way. The pressure of the ionized gas continues to crush the shadow cast by the halo downward toward its axis after the explosion and the supersonic backflows keep expanding towards the direction from which the ejecta will come. In the absence of photoevaporating and ionizing UV flux, the ionized gas in the box begins to recombine out of equilibrium, cooling more quickly than it becomes neutral. Moreover, rapid H_2 formation via the H^- channel is triggered in the ionized halo envelope reducing the ionized fractions to ~ 0.1. In denser regions, even those where no ionization happened, additional molecular hydrogen forms as H_2 formation is a two-body process. Temperatures fall to a few thousand Kelvin and may partially reach $\sim 150\,$K, especially in the H_2 arc and the halo core [5]. See Fig. 10.5 to 10.7 in the Appendix for an overview of the state of the halos at the end of the 2D ZEUS-MP simulations.

H_2 cooling plays an important role in our entire study. Being the most important coolant in the primordial environment, it drives cooling and gas condensation in our relic HII regions. In this way local mixing of the pristine gas with the colliding SN ejecta can be enhanced through local gas collapse motions.

4.3.3 Mixing within photoevaporated halos

In Fig. 4.6 & 4.7, we give an overview of the final density structures at the point when the SN ejecta would reach the left border of the box. In combination with that, we show an overview of the enrichment of these halos in Fig. 4.8. We see that in all cases save one the SN ejecta affects mainly the outer layers of the halo. The ejecta mixes with the backflows from the halo and the photoevaporated halo layers. The mixing driven by turbulent gas motions induced from the SN shock wave is strongest and most efficient for the $200\,{\rm M}_\odot$ star. Only in case of *h1sn200*, where the least massive halo, halo 1, gets contaminated by the massive $200\,{\rm M}_\odot$ at a distance of 250 pc, the SN ejecta is able to penetrate into the halo core. When we look at the bottom left panel in Fig. 4.6, we see that compared to the other panels the halo in model *h1sn200* is the most affected one. The ionization front has compressed the halo strongly to $< 20\,$pc in the direction where the SN ejecta comes in. Thus, the ejecta does not need to penetrate many halo layers. In contrast to the other models where both metal-free Population III star formation in the pristine halo core and metal-enriched Population II star formation in the narrow arc, where there is mixing, may happen, in model *h1sn200* only Pop II may occur within the whole halo environment later on. From our analysis in Chen et al. (2017), we find that mixing is weaker for less massive SNe and for more massive halos. PISN have higher energies and larger metal yields compared to CCSN. For equal distance of both SN types, PISN metals therefore can penetrate deeper into halos and enrich them to higher metallicities.

---

[4] See Section 2.5.8 for more details.

[5] If we had included HD in our primordial chemistry network, temperatures down to the cosmic microwave background with $T_{\rm CMB} \sim 57\,$K would have been possible. See Section 2.5.5 for more information.

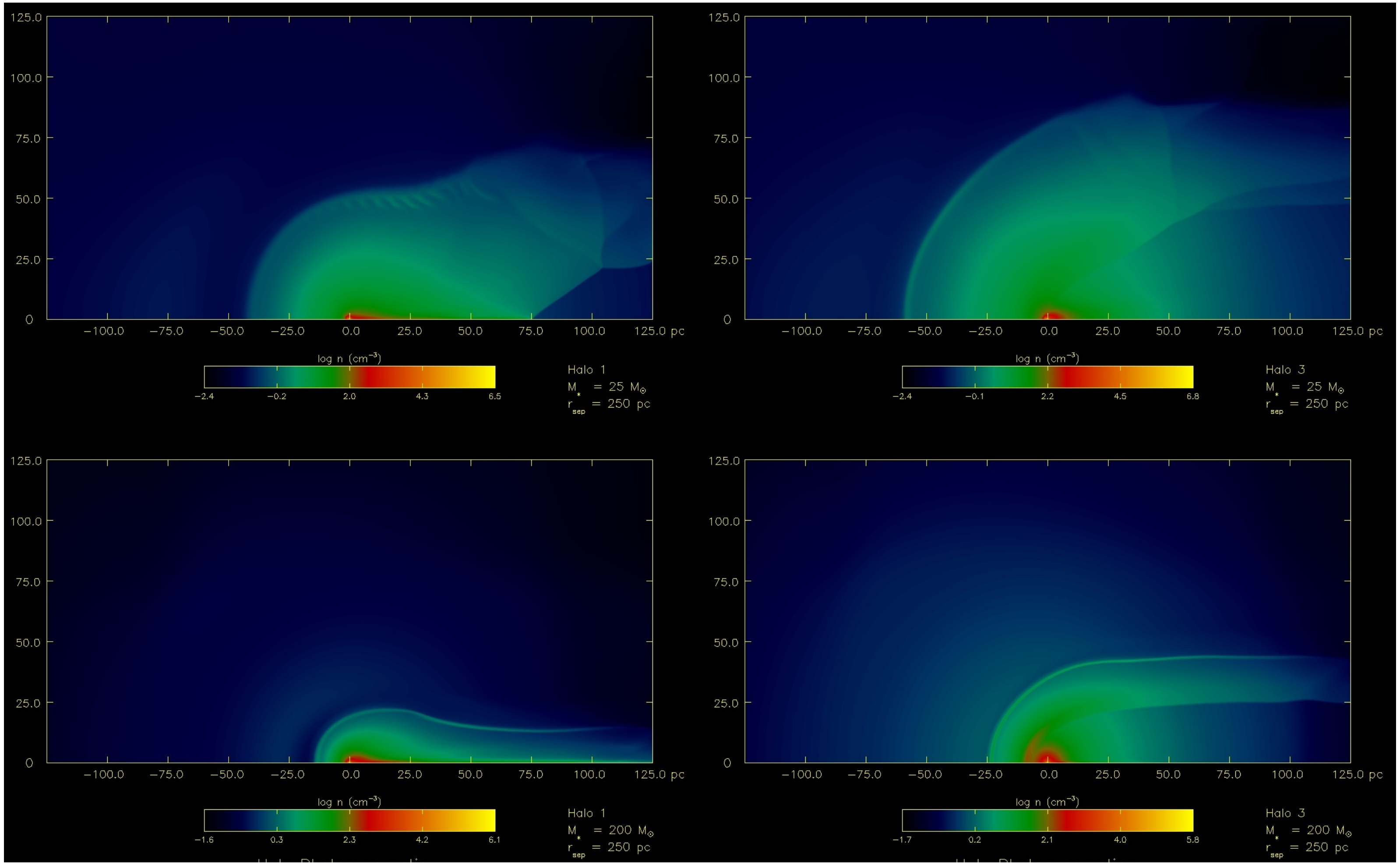

Figure 4.6: Final halo density structure of the runs just before they are further postprocessed with the chemical enrichment and mixing in the CASTRO simulations. Left: halo 1; right: halo 3. Top (bottom) panels show the halo states after photoevaporation by the $25\,M_\odot$ ($200\,M_\odot$) star at 250 pc.

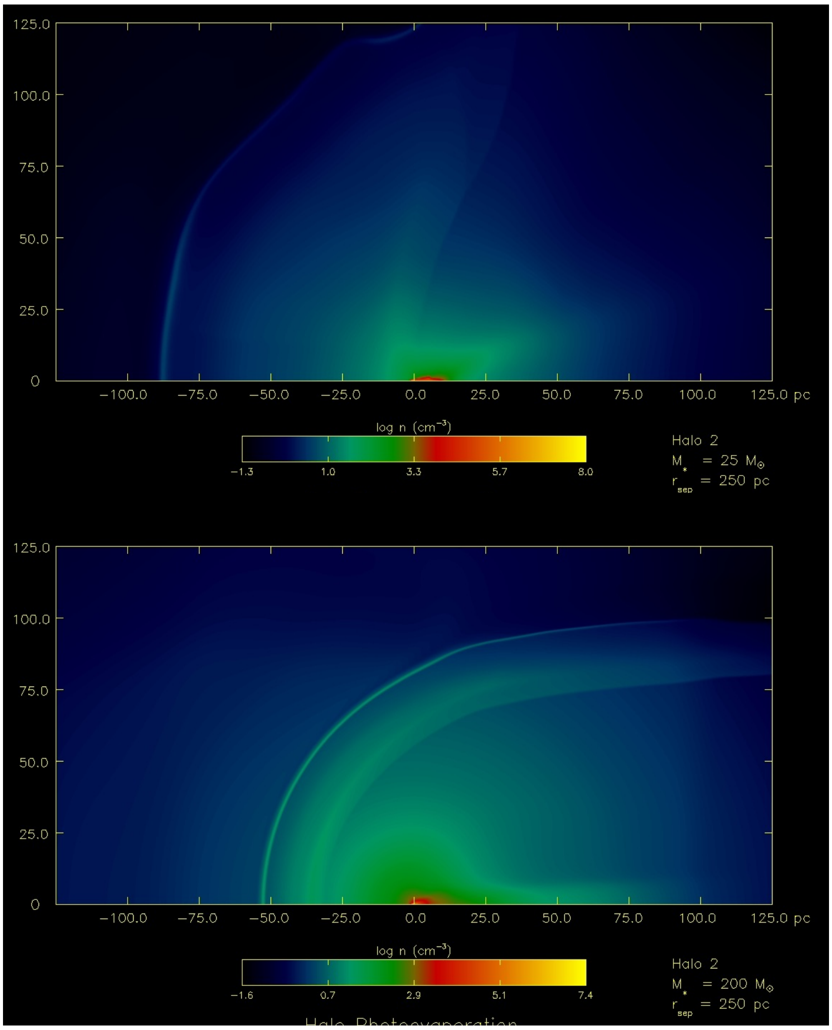

Figure 4.7: Same as Fig 4.6 but for halo 2. Top (bottom) panel shows the halo state after photoevaporation by the $25\,M_\odot$ ($200\,M_\odot$) star at 250 pc.

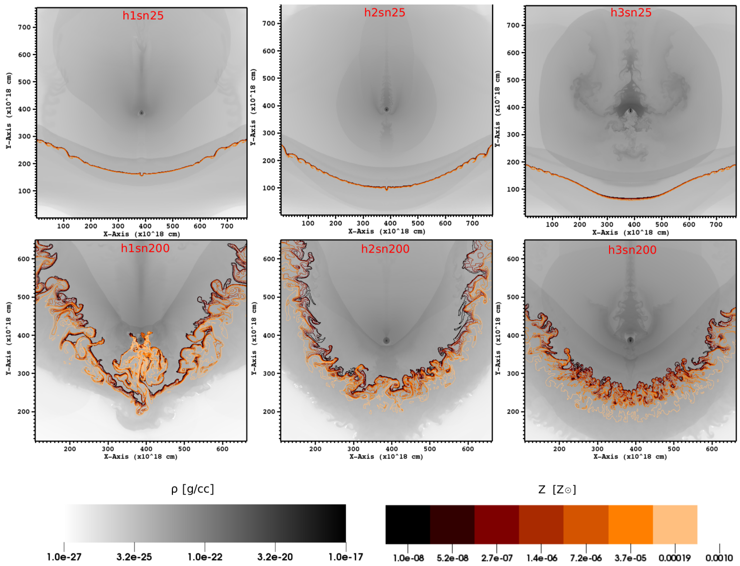

Figure 4.8: Distribution of metals within our halos at a time of 10 Myr after the start of the CASTRO simulations. The lower UV flux and lower SN explosion energy from the $25\,M_\odot$ does not affect the three halos strongly. The SN ejecta wave stalls at a distance of 60 - 100 pc from the halo centers and mixing with the SN levels only occurs mildly in the outer halo layers. In contrast to that, the photoevaporation by the $200\,M_\odot$ star influenced the halos very strongly so that together with the higher SN explosion energies, the SN metals mix more violently with the halo layers and even intrude into the halo core in model *h1sn200*. Image credit: Ke-Jung Chen.

As we can see in the top left panel of Fig. 4.8, in case of model *h1sn25*, in which we have found instabilities in the H_2 arc above, the SN ejecta waves stalls before it reaches this region. Thus we cannot draw any conclusion on whether dynamical instabilities in the outer halo layers enhance mixing of the halo gas with SN metals.

4.4 Caveats

The halos considered in my simulations are idealized as they are isolated. In a realistic environment, halos are part of complex 3D structures within the cosmic web. They are threaded by cosmological filaments. Subsonic turbulent flows arise through accretion from the filaments and through merger of substructures of the cosmic web in the environment of the halos. These turbulent motions may facilitate the propagation of the ionization front and supernova ejecta into deeper layers of the halo enriching the otherwise pristine halo interior (Greif et al., 2008; Smith et al., 2015).

The penetration of ionizing radiation or SN ejecta into our halo may be affected by another shortcoming in our simulations. We only consider a small density range of $10^5 - 10^6\,\mathrm{cm}^{-3}$ within our halos. At this point the gas is in an initial collapse phase with $t_{\rm ff} < 0.2\,\mathrm{Myr}$. This means that during the course our runs, the gas in the central parts of the halo continues to collapse to higher densities, which enable the gas to shield even more against incoming ionizing and photodissociating radiation. The gas might even collapse to form a Population III star. We assume that the impact of radiation and SN ejecta from the external star will be reduced within the central parts of the halo in later stages of the halo collapse. On the other hand, the intermediate and outer layers of the halo are largely unaffected by the collapse and thus still undergo ionization, photodissociation and later mixing with the SN ejecta.

4.5 Discussion and conclusion

I have performed 2D simulations of halo photoevaporation by nearby Population III stars. I have found that photoevaporation affects a halo more strongly, the less massive the halo, the smaller the distance between the halo center and the star that illuminates it, and the more luminous the star is. In all my simulations, the halo core stays unaffected by the ionizing radiation. The halo interior and in particular the halo core is shielded on the one hand through an emerging H_2-rich arc at the outer layers of the ionization front, and on the other hand through efficient H_2 self-shielding within the denser layers of the halo. In three of my simulations, I find that I-front instabilities appear along the H_2 arc until the end of the runs. Such instabilities mark areas in which efficient turbulent mixing can happen when the SN ejecta, after the nearby star has died, collides with the gas of the photoevaporated halo and are as such promising sites for the occurrence of metal-enriched star formation.

Together with the work of my collaborators, we find in Chen et al. (2017), that pre-supernova (pre-SN) photoevaporation of a halo is a crucial step for simulations of chemical enrichment. The pre-SN ionizing UV radiation ablates outer halo layers and drives a backflow of halo material toward the direction of the star. This makes it possible for SN ejecta to mix with the backflow material as well as the thinned out outer halo layers and to reach greater depths in the halo which would otherwise not have been possible. In one case, the ejecta can even penetrate into the halo core. We suggest that Population III star formation may occur in the pristine halo core together with metal-enriched Population II star formation in the efficiently mixed regions within the halo. In order to achieve definite answers in this, we, however, need to include a more advanced chemistry network in our CASTRO simulations, in particular with metal and dust cooling as they play an important role in the formation process of Pop II stars (e.g. Schneider et al., 2006; Klessen et al., 2012). The details of the subsequent star formation history also depend on which stellar population emerges first and how it influences its surrounding by radiation and SN feedback. In this way it could happen that initially pristine halo cores might be enriched by SNe going off in the outer layers of the halo. On the other hand, early star formation in the halo core could destroy otherwise promising star-forming sites in the outer halo regions.

Unfortunately, we cannot draw any conclusion on whether the dynamical instabilities observed in the H_2-rich arc in the outer halo layers of model *h1sn25* enhance mixing of the halo gas with SN metals because the SN ejecta wave stalls before it reaches this location. As I have observed such instabilities also in case of model *h2sn200-2* and *h3sn200-2* in my photoevaporation runs, it would be useful to run CASTRO mixing simulations of these models in the future as well.

In the previous study by Cen & Riquelme (2008), SN ejecta did not penetrate into the halo at all but only mixed with the outermost halo layers. They did not consider halo photoevaporation before the enrichment through the supernova. Thus their outer halo layers were not ablated and thinned out as we find it in our studies which made it difficult for the SN ejecta to intrude into the halo interior. This comparison shows directly the importance of our halo photoevaporation simulations for the enrichment scenario of a halo by a nearby Pop III star. Smith et al. (2015) performed a study similar to ours. In their model, they considered a $3 \times 10^5\,\mathrm{M}_\odot$ halo being partially photoevaporated by a $40\,\mathrm{M}_\odot$ star at 200 pc and then contaminated by its SN ejecta. They found that the SN metals penetrate into the halo core. This is consistent with our models. Compared to our models, their halo was less massive, the star in between the mass range of our stars, and the distance smaller than ours. Thus it is reasonable that the SN ejecta from their less massive star (compared to our core-enrichement model *h1sn200*) was able to intrude into the halo core.

The choice of our two stellar masses was motivated from results of previous numerical simulations (e.g. Bromm et al., 2002; Abel et al., 2002; Greif et al., 2011; Susa et al., 2014; Stacy et al., 2016). The two masses cover the two supernova scenarios, CCSN and PISN, possible for Population III stars (Heger & Woosley, 2002). Within the last decade, several numerical simulations of Population III star formation suggest that Pop III stars form mainly in protostellar clusters in which the mass growth of individual protostars is limited by competing accretion between all stars (e.g. Greif et al., 2011; Smith et al., 2012) and finally by ionizing radiation from the stars that first reach a few ten solar within a couple of thousand years (Hosokawa et al., 2011; Susa et al., 2014; Stacy et al., 2016). The highest protostellar masses found in these simulations is a few ten solar rather than several hundred solar as found in the first simulations where Pop III stars formed in isolation (e.g. Bromm et al., 2002; Abel et al., 2002). Stellar archaeological surveys support this numerical result as they have not conclusively detected chemical signatures from PISN so far (Aoki et al., 2014). Comparisons of numerical simulations of Pop III SN with chemical abundances observed in extremely metal-poor stars suggest that they may have formed from gas that was metal-enriched by CCSN supernovae of $15-40\,\mathrm{M}_\odot$ Pop III stars (e.g. Beers & Christlieb, 2005; Frebel et al., 2005, 2008; Karlsson et al., 2008; Joggerst et al., 2010). Therefore, currently it seems that very massive Pop III stars and consequently PISN were very rare. Our setups including the $25\,\mathrm{M}_\odot$ are likely to be the more representative models to study the real progress of first chemical enrichment. By further extending the parameter space of our initial conditions together with an more advanced chemical network for the mixing simulations, we will continue to examine the transition between Population III and Population II star formation in more detail. Other implementations in futures studies may also include modeling turbulence within the halo, e.g. through accretion from the halo-permeating filaments, to test whether such turbulent motion facilitate the penetration of radiation and SN ejecta in our halos and to see whether they enhance the level of mixing. This will be in particular interesting and relevant for our models with the $25\,\mathrm{M}_\odot$ star as there mixing was only able to occur in the outer layers of the halo. In addition, halo evolution and mixing within a global LW background may be studied to examine how the H_2 mass fraction content and consequently the cooling condition within the halo are influenced by this radiative background.

CHAPTER 5

The fragmentation behavior of Population III protostellar disks

The content of this chapter, except Section 5.3.1 and 5.3.2, will published in Wollenberg, K. M. J., Glover, S. C. O., Clark, P. C., Klessen, R. S., *"The Fragmentation Behavior of Population III Protostellar Disks - Part I"*, MNRAS 2019 (*in prep.*) and Wollenberg, K. M. J., Glover, S. C. O., Clark, P. C., Klessen, R. S., *"The Fragmentation Behavior of Population III Protostellar Disks - Part II: Protostellar Ejections"*, MNRAS 2019 (*in prep.*). The simulations presented in this chapter were performed and analyzed by me. I created all the figures and wrote the text. Simon C. O. Glover provided useful comments on the structure of the whole chapter. Ralf S. Klessen and Paul C. Clark contributed ideas and useful comments to the sections that will be part of the publications.

5.1 Introduction

The different steps in the formation of Population III (Pop III) stars have been studied for almost two decades. At redshifts $z \sim 20 - 50$, primordial gas, consisting mainly of hydrogen and helium, falls into the potential wells of so-called minihalos of mass $\sim 10^6\,\mathrm{M}_\odot$ and with virial temperatures $T_{\mathrm{vir}} \sim 1000\,\mathrm{K}$ (Tegmark et al., 1997; Bromm & Larson, 2004; Glover, 2005; Bromm, 2013). During this process, the gas is heated to temperatures close to T_{vir}, but is able to cool down afterwards via H_2 ro-vibrational line cooling. As the gas continues to cool and condense within the minihalos, it can reach a minimum temperature of $T \sim 200\,\mathrm{K}$ at a number density of $n \sim 10^4\,\mathrm{cm}^{-3}$. This is comparable to the critical density of molecular hydrogen at which its rotational level populations reach local thermodynamical equilibrium (LTE). At this point of minimum temperature, the gas within a minihalo tends to break up into separate clumps of mass of the order of the local Jeans mass, $M_{\mathrm{J}} \sim 1000\,\mathrm{M}_\odot$. These clumps become the birthplaces of Population III stars.

A higher level of ionization in the gas may lead to a further elevated molecular hydrogen fraction due to which the gas is able to cool to temperatures $T < 200\,\mathrm{K}$. In this regime, formation of deuterated hydrogen molecules, HD, is facilitated. When enough HD is created, the gas is able to cool down to even the temperature of the cosmic microwave background ($\sim 57\,\mathrm{K}$ at $z = 20$). An increased ionization fraction can for example arise when the gas in the minihalo is exposed to ionizing radiation of a nearby or progenitor Pop III star (e.g. Oh & Haiman, 2002; Nagakura & Omukai, 2005; Yoshida et al., 2008), to X-rays from Pop III supernova remnants, X-ray binaries or quasars (e.g. Glover & Brand, 2003; Hummel et al., 2015), or to cosmic rays (Hummel et al., 2016). The critical density in this case is $n \sim 10^6\,\mathrm{cm^{-3}}$. The Jeans-unstable, star-forming clumps are less massive, $M_\mathrm{J} < 100\,\mathrm{M_\odot}$, due to the smaller minimum temperature. Star formation dominated by HD chemistry is termed Population III.2 in contrast to that dominated by H_2 described above which is defined as Population III.1 star formation (McKee & Tan, 2008). In this study we concentrate on Population III.1 stars to which we will generally refer to as Population III stars.

The evolution of the star-forming cloud continues as follows. The clumps continue to gravitationally collapse. At densities of $n \sim 10^8$–$10^9\,\mathrm{cm^{-3}}$, three-body H_2 formation dramatically increases the amount of molecular hydrogen available in the gas and consequently increases the cooling rate. However, this rapid formation of H_2 also converts significant amounts of chemical energy into heat, causing the temperature of the gas to increase to around $1000 - 2000\,\mathrm{K}$. At $n \sim 10^{10}\,\mathrm{cm^{-3}}$, the gas becomes optically thick to molecular hydrogen line cooling (Ripamonti & Abel, 2004; Yoshida et al., 2006), but further cooling due to collision-induced emission (CIE) sets in for $n \gtrsim 10^{14}\,\mathrm{cm^{-3}}$ (Ripamonti & Abel, 2004). When the gas reaches densities of $n \gtrsim 10^{16}\,\mathrm{cm^{-3}}$, the gas also becomes optically thick to CIE cooling. At this stage, the only way in which it can dissipate the energy released during the collapse is by collisionally dissociating H_2. This remains effective until all of the H_2 at the center of the collapsing core has been depleted. From there, the collapse proceeds fully adiabatically until a protostar with mass $M \lesssim 0.01\,\mathrm{M_\odot}$ is born (Yoshida et al., 2008).

The newly-born Pop III protostar is embedded within a dense, massive gas envelope, and continues to grow in mass via accretion from its surrounding gas. Since the accretion rate scales with the gas temperature as $\dot{M}_\mathrm{acc} \propto T^{3/2}$, typically values of $\dot{M}_\mathrm{acc} \gtrsim 10^{-3}\,\mathrm{M_\odot\,yr^{-1}}$ are encountered. Through stellar-evolution codes, it has been found that, due to these high accretion rates, pre-main sequence Population III stars are puffed-up objects with large stellar radii, with values of up to a few hundred solar radii being common (Stahler et al., 1986; Omukai & Palla, 2003; Hosokawa & Omukai, 2009; Hosokawa et al., 2010; Smith et al., 2012; Woods et al., 2017; Haemmerlé et al., 2018).

The earliest numerical studies suggested that Pop III stars form in isolation and can become very massive ($\gtrsim 100\,\mathrm{M_\odot}$) (see e.g. Abel et al., 2002; Bromm et al., 2002; Bromm & Larson, 2004). Within the last decade, however, simulations have extended the study of Pop III star formation beyond the formation of the first protostar and have shown that the non-zero angular momentum within the collapsing gas cloud leads to the formation of a self-gravitating protostellar disk that is prone to fragmentation (Clark et al., 2008; Turk et al., 2009; Stacy et al., 2010; Clark et al., 2011b). Instead of a single object, a protostellar cluster arises (Greif et al., 2011; Clark et al., 2011a; Smith et al., 2011; Stacy & Bromm, 2013).

The evolution of an individual protostar depends on its interactions with the surrounding gas and the other objects in the cluster. The protostars compete for further mass growth from their common mass reservoir, yielding highly variable accretion rates (Greif et al., 2011; Greif et al., 2012; Girichidis et al., 2012; Smith et al., 2012; Hosokawa et al., 2016). Some protostars might even stop accreting completely if their gas supply is removed by fragmentation or accretion onto neighboring protostellar companions, a process termed fragmentation-induced starvation in the context of present-day star formation (Peters et al., 2010). Furthermore, during close encounters protostars may be disrupted or may merge (Greif et al., 2011; Greif et al., 2012; Stacy et al., 2016). In addition, the complicated multiple-body dynamics during close interactions can lead to ejection of individual protostars from the protostellar disk or even from the halo. Indeed, previous simulations have found an ejection rate of $\sim 30\%$

(Greif et al., 2011; Stacy & Bromm, 2013; Stacy et al., 2016).

Within the last couple of years simulations have tried to estimate the initial mass function (IMF) of stars in Pop III protostellar clusters and found a top-heavy distribution in which the masses range from subsolar values to over a hundred solar masses (Greif et al., 2011; Clark et al., 2011a; Stacy & Bromm, 2013; Susa, 2013; Hirano et al., 2014; Stacy et al., 2016). From the observational side, stellar archaeology can provide indirect constraints on the Pop III IMF through the search for metal-free stars and for nucleosynthetic signatures of Population III stars in extremely metal-poor stars (EMP) (Beers & Christlieb, 2005; Frebel & Norris, 2015) or ultra metal-poor stars (UMP) (Karlsson et al., 2013). Regarding the search for Pop III survivors, the above-mentioned ejected protostars with $M \lesssim 0.8\,\mathrm{M}_{\odot}$ are of particular interest. They could have survived until present-day under the premise that they did not continue to accrete significantly more mass (Greif et al., 2011). Unfortunately, no observational evidence for such stars has been found in the Milky Way to-date. The search for them is made difficult by their rarity, low brightness and possible pollution through accreted metal-enriched interstellar material that could mask their genuine Population III nature (Frebel et al., 2009; Komiya et al., 2015; Shen et al., 2017). Semi-analytical models suggest that current surveys need to consider a larger number of objects to increase the chance of finding a Pop III survivor (Hartwig et al., 2015a; Ishiyama et al., 2016). Furthermore, low mass satellites of the Milky Way might be a promising region to look for survivors as they are estimated to host a higher fraction of them compared to the Milky Way itself (Magg et al., 2018).

To gain reliable estimates of the Pop III IMF from numerical simulations, the evolution of the protostellar system needs to be followed through the whole accretion period. Accretion is ultimately terminated when some of the protostars have grown massive enough to produce radiative feedback that photoevaporates the accretion disk. This happens after a few 10^3 to 10^5 years (e.g. Stacy et al., 2012; Susa, 2013; Stacy et al., 2016). But before we consider how a protostellar system evolves over such a long time, how massive individual stars become, and how many might be left in the end, we may ask how many protostellar objects form in the first place and how their number depends on the properties of their star-forming cloud. From earlier cosmological studies we know that the degree of fragmentation of the protostellar disk varies strongly from halo to halo (e.g. Greif et al., 2011; Hartwig et al., 2015b; Stacy & Bromm, 2013). This is to be expected if turbulence within the cloud plays a role in determining when and where fragmentation actually occurs (Greif et al., 2008; Greif et al., 2011). It is also reasonable to expect that the amount of angular momentum present at small-scales will have a large impact on protostellar disk formation and evolution (e.g. de Souza et al., 2013; Stacy et al., 2016). However, previous studies have only examined a very limited set of initial conditions, often drawn directly from cosmological simulation. Compared to cosmological simulation, the use of controlled initial conditions which examine the collapse of a gas cloud with pre-defined levels of turbulence or rotation within a small computational box, is first numerically less expensive so that a larger sample can be considered. Second, it allows one to draw conclusions on the specific role, strength and importance of the particular physical parameters applied here. Previous systematic studies of the effects of varying initial level of turbulence (Clark et al., 2011a), rotation (Machida et al., 2008b) or of varying mixtures of those (Riaz et al., 2018) are limited because they only consider one realization per setup. From present-day star formation (Goodwin et al., 2004a,b), however, we know that results from simulations including turbulence may vary strongly. This is due to the randomness of the seed with which the initial turbulent velocity field of the cloud is generated. Thus, in order to be able to derive some general trends regarding the influence of rotation and turbulence, one should consider a sample of several realization per setup.

This is what we attempt to do. In our study, we are interested to see how different levels of initial subsonic turbulence and rotation within the star-forming cloud affect the outcome of Pop III star formation in terms of the total number of objects formed, the overall mass spectrum and the individual accretion history. We pursue this examination under controlled initial conditions starting from a critical Bonnor-Ebert (BE) sphere and apply 10 setups of different combinations of rotation and turbulence with 5 realizations each, that means a total of 50 simulations.

This chapter is structured as follows. In Section 5.2, our numerical approach with the moving mesh code AREPO (Springel, 2010) is explained. Section 5.2.2 outlines the initial conditions of our different setups. In Section 5.3, we present the outcome of our study on the fragmentation behavior of Population III protostellar disks under the influence of different levels of rotation and turbulence. We describe the results in terms of the evolution of sink particle properties and sink dynamical behavior, including number of sinks and mass functions, accretion behavior, mergers and ejections. We discuss some shortcomings of our present study in Section 5.4 before we state our conclusions in Section 5.5.

5.2 Method

5.2.1 Numerical approach

The studies of primordial gas cloud collapse presented in this paper are performed with an updated version of the Voronoi moving-mesh code AREPO (Springel, 2010) including recent improvements to the time integration scheme, spatial gradient reconstruction and grid regularization (Pakmor et al., 2016; Mocz et al., 2015). We model gas hydrodynamics using the HLLD Riemann solver (Miyoshi & Kusano, 2005; Pakmor et al., 2011). We apply the Jeans refinement criterion to make sure that the local Jeans length is always resolved by a minimum number of cells, i.e. in our case 16 cells, in order to avoid artificial fragmentation (Truelove et al., 1997; Bate & Burkert, 1997; Federrath et al., 2011b). The Voronoi mesh-generating points follow a quasi-Lagrangian behavior by being advected with the underlying gas flow. This allows the mesh to follow the growth of density fluctuations under their own self-gravity while continuously adjusting the resolution of the grid. In this way, AREPO is an ideal code to study gas collapse (Springel, 2010; Greif et al., 2011; Greif et al., 2012). Further details of our use of AREPO, including the sink particle module and the treatment of primordial chemistry, can be found in Section 3.2.

5.2.2 Initial conditions

Our simulations are performed in a box with sidelength 13 pc. We start with 128^3 cells and let the code evolve with Jeans (de-)refinement making sure that the Jeans length is always resolved by at least 16 cells.

We use the density profile of a Bonnor-Ebert (BE) sphere (Ebert, 1955; Bonnor, 1956) as the initial condition for our cloud. This density profile is similar to the density profile of the cold, dense cores formed at the center of the gravitationally collapsing gas in cosmological simulations of Pop. III star formation (Abel et al., 2002; Bromm et al., 2002; Yoshida et al., 2008). The density profile follows

$$\rho(r) = \begin{cases} f \times \rho_{\mathrm{BE}}(r) & \text{for } r < R_{\mathrm{BE}} \\ f \times \rho_{\mathrm{BE}}(R_{\mathrm{BE}}) & \text{for } r \geq R_{\mathrm{BE}} \end{cases} \tag{5.1}$$

where $\rho_{\mathrm{BE}}(r)$ is the density distribution of a critical BE sphere (i.e. one on the boundary between stability and instability). The parameter f denotes a density enhancement factor which we use here in order to promote the collapse of our sphere. We use $f = 1.83$ which gives a central particle number density of $n_c = 1.83 \times 10^4\,\mathrm{cm^{-3}}$, and a central mass density of $\rho_c = f \times \rho_{\mathrm{BE}}(0) = 3.7 \times 10^{-20}\,\mathrm{g\,cm^{-3}}$. We set the radius of the sphere to be $R_{\mathrm{BE}} = 1.87\,\mathrm{pc}$ which corresponds to a BE sphere with nondimensional radius of $\xi_{\mathrm{BE}} = 6.5$. The mass within this radius is then $M_{\mathrm{BE}} = 2671\,\mathrm{M_\odot}$. The temperature inside the sphere is initially $T = 200\,\mathrm{K}$ which gives an adiabatic sound speed of $c_{\mathrm{s}} = 1.93\,\mathrm{km\,s^{-1}}$ with an initial adiabatic index of $\gamma = 5/3$ (isothermal sound speed: $c_{\mathrm{s,iso}} = 1.16\,\mathrm{km\,s^{-1}}$). The sphere is located within an environment of uniformly dense gas with $n_{\mathrm{ext}} = n_{\mathrm{BE}}(R_{\mathrm{BE}}) = 1.31 \times 10^3\,\mathrm{cm^{-3}}$ ($\rho_{\mathrm{ext}} = 2.7 \times 10^{-21}\,\mathrm{g\,cm^{-3}}$) and $T_{\mathrm{ext}} = T_{\mathrm{BE}} = 200\,\mathrm{K}$.

We run simulations with four different setups for the BE sphere, differing in the amount of rotational and turbulent kinetic energy present initially in the gas. Our first set of runs have zero rotation and no turbulence – we term these *pure infall* models. We also carry out runs with rotation but no turbulence, turbulence with no rotation, and a set of mixed models with four different combinations of rotation and turbulence. We also ran one of our models with both rotation and turbulence with a more stringent Jeans refinement criterion, namely 32 cells per Jeans length, in order to see how much this affects the outcome. The results of this higher resolution run are discussed in Section 6.4.3. An overview of the models is given in Table 5.1.

We include rotation by letting our initial cloud rotate around the z-axis at a uniform angular velocity Ω_0. By changing Ω_0, we can adjust the ratio of rotational kinetic energy to gravitational potential energy for the cloud, $\beta_{\mathrm{rot}} = E_{\mathrm{rot}}/|E_{\mathrm{grav}}|$. We choose $\beta = 0.01$ and $\beta = 0.1$ as guide values to span a reasonable range from small to high levels of rotation. Due to the lack of direct observations of primordial star-forming clouds, our choice of values is on the one side motivated from observations of nearby molecular cloud cores, where one finds typical values of $\beta \sim 0.02$ (Goodman et al., 1993; Caselli et al., 2002), and on the other side by results from cosmological simulations of Pop. III star formation, which find $\beta \lesssim 0.1$ (Bromm et al., 2002; Yoshida et al., 2006). Our choice also agrees with the values found in the more recent numerical study by Hirano et al. (2014).

In runs with turbulence, we add a homogeneous, isotropic Gaussian random velocity component onto our BE sphere. We do not drive the turbulence but let it freely decay over the course of the simulation. The Gaussian random field is constructed by a combination of randomly distributed phases together with an amplitude following a Rayleigh distribution (Bardeen et al., 1986). The power spectrum of the velocity field is chosen to be $P(k) \propto k^{-4}$, so that most of the power is contained in large-scale modes. We construct the field in Fourier space, transform it into real space and only use its real parts. We use a mixed mode spectrum, i.e. a spectrum consisting of both solenoidal and compressive modes. After deriving the root-mean square value of this field, we invert this value and use it to rescale the velocity of our turbulent field as desired. We carry out runs with two different values of the turbulent α parameter, $\alpha_{\mathrm{turb}} = E_{\mathrm{turb}}/|E_{\mathrm{grav}}|$: a low turbulence case with $\alpha_{\mathrm{turb}} = 0.05$ and a high turbulence

Table 5.1: Overview of simulation setups.

Setup	α_{turb}	β_{rot}	v_{rms} [$\mathrm{km\,s^{-1}}$]	Ω_0 [$\mathrm{s^{-1}}$]
pure infall	-	-	-	-
$\beta01$	-	0.1	-	3.1×10^{-14}
$\beta001$	-	0.01	-	9.8×10^{-15}
$\alpha025$	0.25	-	1.1	-
$\alpha005$	0.05	-	0.5	-
$\alpha025\beta01$	0.25	0.1	1.1	3.1×10^{-14}
$\alpha025\beta001$	0.25	0.01	1.1	9.8×10^{-15}
$\alpha005\beta01$	0.05	0.1	0.5	3.1×10^{-14}
$\alpha005\beta001$	0.05	0.01	0.5	9.8×10^{-15}

case with $\alpha_{\mathrm{turb}} = 0.25$. Our choice of the values here is motivated by the studies from Goodwin et al. (2004a,b). Further numerical details of how we set up the turbulent velocity field are given in Section 3.2.5.

For our chosen initial temperature of 200 K, the ratio between thermal and gravitational energy of our sphere, $\alpha_{\mathrm{therm}} = E_{\mathrm{therm}}/|E_{\mathrm{grav}}| \simeq 0.451$.[1] One can estimate the number of Jeans masses within the sphere by $(E_{\mathrm{therm}}/|E_{\mathrm{grav}}|)^{-3/2}$ which gives us here roughly 3 Jeans masses.

We carry out 5 realizations per setup. Ideally we would like to conduct as many realizations as possible. But since this would become computationally unfeasible, we comprise on 5 realizations per setup. For setups including turbulence each realization has its own random seed. We model the 5 different realizations for setups without turbulence by first choosing 5 uniformly dense boxes which only differ in their random mesh cell positions and then initializing our BE density distribution on them.

We assume a redshift of $z = 20$ for our simulations. However, as the gas in our simulations is always much warmer than the cosmic microwave background and the effects of Compton cooling are negligible, the results we obtain should be largely independent of redshift. For our initial elemental abundances we use $x_{\mathrm{He}} = 0.079$ and $x_{\mathrm{D}} = 2.6 \times 10^{-5}$ (Glover & Abel, 2008). The values of the fractional abundances of $\mathrm{H_2}$, $\mathrm{H^+}$, HD and $\mathrm{D^+}$ are motivated by cosmological simulations of Population III.1 star formation, i.e. Pop. III star formation occurring in minihalos that have not been affected by stellar feedback[2] (e.g. Greif et al., 2008): $x_{\mathrm{H_2}} = 1.0\times10^{-3}$, $x_{\mathrm{H^+}} = 1.0\times10^{-7}$, $x_{\mathrm{HD}} = 3.0 \times 10^{-7}$ and $x_{\mathrm{D^+}} = 2.6 \times 10^{-12}$. All hydrogen and deuterium not included in one of these forms is assumed to be present in the form of neutral atomic hydrogen or deuterium, as appropriate, while all of the helium is assumed to be in neutral atomic form. We also assume that the gas is in charge balance, with a free electron abundance given by $x_{\mathrm{e^-}} = x_{\mathrm{H^+}} + x_{\mathrm{D^+}}$. We summarize our initial conditions in Table 5.2.

---

[1] One of the reasons to increase the density by some factor f was to make sure that our sphere would still collapse when we introduced strong rotation ($\beta_{\mathrm{rot}} = 0.1$) and turbulence ($\alpha_{\mathrm{turb}} = 0.25$), i.e. to ensure that the total energy of the system is still negative, $E_{\mathrm{tot}} = E_{\mathrm{grav}} + E_{\mathrm{therm}} + E_{\mathrm{rot}} + E_{\mathrm{turb}} < 0$.

[2] In contrast to Population III.2 star formation, which takes place in metal-free minihalos that were previously ionized by a nearby population of Pop. III.1 stars (McKee & Tan, 2008).

Table 5.2: Summary of the initial conditions for our simulations.

Parameter	Value
ρ_c	$3.7 \times 10^{-20}\,\mathrm{g\,cm^{-3}}$
$\mathrm{M_{BE}}$	$2671\,\mathrm{M_{\odot}}$
$\mathrm{R_{BE}}$	$1.87\,\mathrm{pc}$
$\mathrm{T_{in}}$	200 K
$x_{\mathrm{H_2}}$	1.0×10^{-3}
$x_{\mathrm{H^+}}$	1.0×10^{-7}
x_{HD}	3.0×10^{-7}
$x_{\mathrm{D^+}}$	2.6×10^{-12}

5.3 Results

5.3.1 Cloud state prior to the formation of the first sink

We have described in detail the different stages of primordial cloud collapse and the role of primordial chemistry in regulating this process in Section 2.5.1. Now we present and discuss specific results on the cloud structure just prior to the formation of the first sink for our 50 runs with different degrees of initial cloud rotation and turbulence.

In Fig. 5.1 to 5.4, we plot radial profiles of number density, n, temperature, T, mass enclosed within a radius R, $M_{\mathrm{enc}}(R)$, and $\mathrm{H_2}$ fraction, $n_{\mathrm{H_2}}/n_{\mathrm{H}}$. The profiles are derived with mass-weighted averages within spherical shells centered on the densest gas cell just before first sink formation [3]. We use logarithmic binning with 40 bins. Each subplot depicts a different setup with the five differently colored lines describing the five realizations per setup. Our profiles are similar to those found in previous studies (e.g. Abel et al., 2002; Yoshida et al., 2006; Stacy et al., 2010; Clark et al., 2011b,a; Greif et al., 2011; Greif et al., 2012). Except for some irregularities and sudden peaks in a few of the lines, we see that the lines of the different realizations per setup show a very similar trend in each property. The best agreement is found for the *pure infall* models in Fig. 5.4 and for the purely rotational runs. Setups including turbulence show a small scatter in their five different realizations.

We now go through some details found for the individual properties. In all our realizations, we reproduce the standard $\rho \propto R^{-2.2}$ density profile (the relation is indicated by the black dashed line) as found in previous studies (e.g. Abel et al., 2002; Yoshida et al., 2006; Stacy et al., 2010; Clark et al., 2011b,a; Greif et al., 2011). This having been tested by both self-consistent cosmological simulations (e.g. Abel et al., 2002; Yoshida et al., 2006; Clark et al., 2011b) and more artificial parameter studies (e.g, Clark et al., 2011a), it seems that the radial density profile is insensitive to the initial cloud profile.

In some of the runs including turbulence, we observe local peaks at same equal radii in the density and $\mathrm{H_2}$ fraction profiles. The peaks appear at distances of $\sim 10-1000\,\mathrm{AU}$ from the densest gas cell. They indicate some region other than the immediate surrounding of the densest gas cell where local gas collapse happens almost simultaneously. The locally increased density, usually between $n = 10^{10}\,\mathrm{cm^{-3}}$ to a few

---

[3] In Table 10.1 in the Appendix we list the exact times at which we have taken the data from each of the realization. Due to our data output scheme, the times differ slightly. However, this does not affect our description of the overall trends.

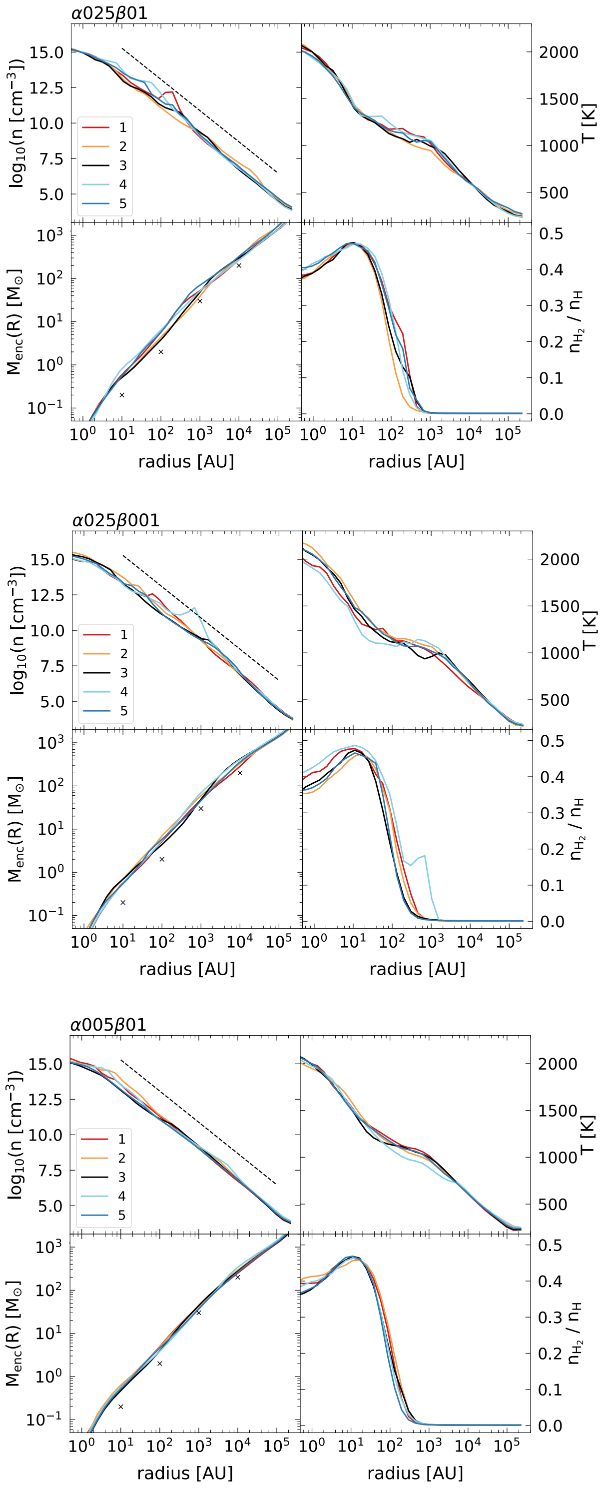

Figure 5.1: Radial profiles of the gas cloud properties number density, n, temperature, T, mass enclosed within radius R, $M_{\mathrm{enc}}(R)$, and H_2 fraction, $n_{\mathrm{H}_2}/n_{\mathrm{H}}$. The profiles are derived from mass-weighted averages taken within spherical shells centered on the densest gas cells just before first sink formation. The title above each plot indicates the name of the setup, while the differently colored lines correspond to the different realizations. The black, dashed line describes the typical $R \propto n^{-2.2}$ density profile as observed in previous studies (e.g. Abel et al., 2002; Yoshida et al., 2006; Clark et al., 2011b; Greif et al., 2011).

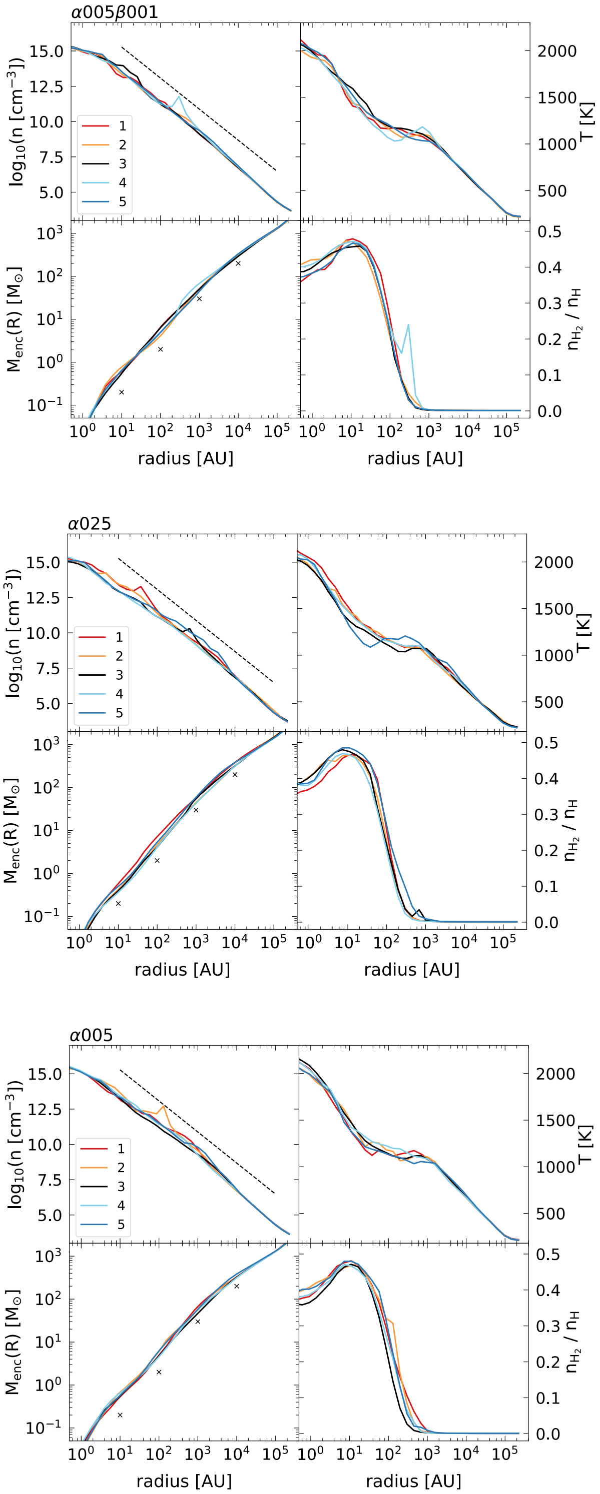

Figure 5.2: As Fig. 5.1, showing the results for more setups.

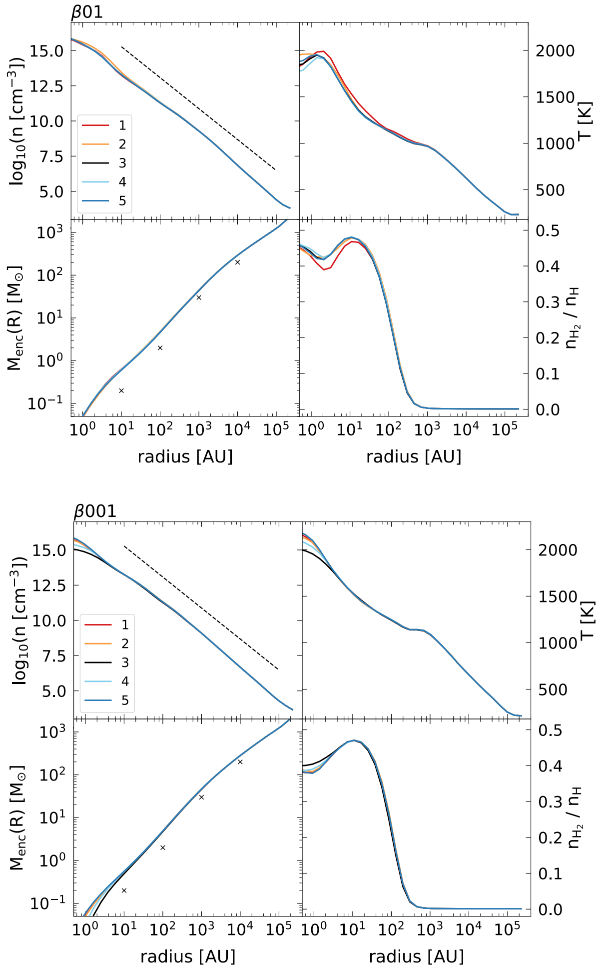

Figure 5.3: As Fig. 5.1, but for the purely rotational setups.

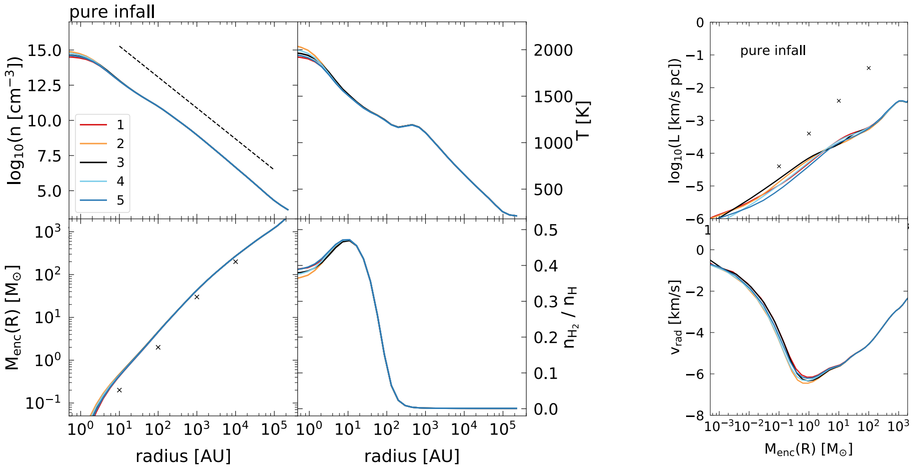

Figure 5.4: Gas property profiles of the *pure infall* models. Left subplot: same mass-weighted profiles of gas properties as in Fig. 5.1. Right subplot: profiles of the specific total angular momentum, L, and the radial velocity, $v_{\rm rad}$, versus the enclosed mass $M_{\rm enc}(R)$. Although no initial angular momentum is added to the Bonnor-Ebert sphere in the *pure infall* runs, some non-zero angular momentum is induced by turbulent gas motions that arise during gravitational collapse. The properties in both subplots are derived from mass-weighted averages taken within spherical shells centered on the densest gas cells just before first sink formation.

$n = 10^{12}\,\mathrm{cm}^{-3}$, boosts three-body H_2 formation. In the temperature profiles, however, we do not see a local drop due to a higher fraction of H_2, but rather small local peaks. This is because the formation of each H_2 molecule releases energy into the gas and there is a battle between this H_2 formation heating and H_2 line cooling that ends in favor of the heating, leading to a small local temperature increase. This whole interplay can be seen best in the subplots for $\alpha025\beta001$ and $\alpha005\beta001$. Such behavior has also been observed in some previous studies (e.g. Turk et al., 2009; Greif et al., 2012; Greif et al., 2011; Stacy et al., 2016). Since we do not observe this in the runs without turbulence, it is likely that these local density peaks can be attributed to effects of turbulence within the initial cloud.

At radii $\lesssim 10\,\mathrm{AU}$, there is a drop in the H_2 fraction. This feature is due to the high temperatures of $T \gtrsim 1500\,\mathrm{K}$ reached at this point in the collapse. This feature has been observed in previous studies as well (e.g, Clark et al., 2011b; Greif et al., 2012).

The profiles of enclosed mass, $M_{\rm enc}(R)$, are very similar in all our setups. The black crosses are a comparison to the results shown in Abel et al. (2002) (see also Fig. 8 in Clark et al. 2011b). We find slightly higher values than in Clark et al. (2011b), which themselves were already higher than the approximate data points taken from Abel et al. (2002). The deviation from Abel et al. (2002) can be attributed to small differences in the density distributions (higher values) near the densest gas cell.

In Fig. 5.5, 5.6 - and in Fig. 5.4 for the *pure infall* models - we display profiles of the total specific angular momentum, L, and the radial velocity, $v_{\rm rad}$ versus the enclosed mass, $M_{\rm enc}(R)$. The data is again derived from mass-weighted averages within spherical shells centered on the densest gas cells just before first sink formation. As for the $M_{\rm enc}(R)$ profile above, we have included data points for L from Abel et al. (2002). The general trend we find is similar to previous studies (e.g. Abel et al., 2002; Stacy et al.,

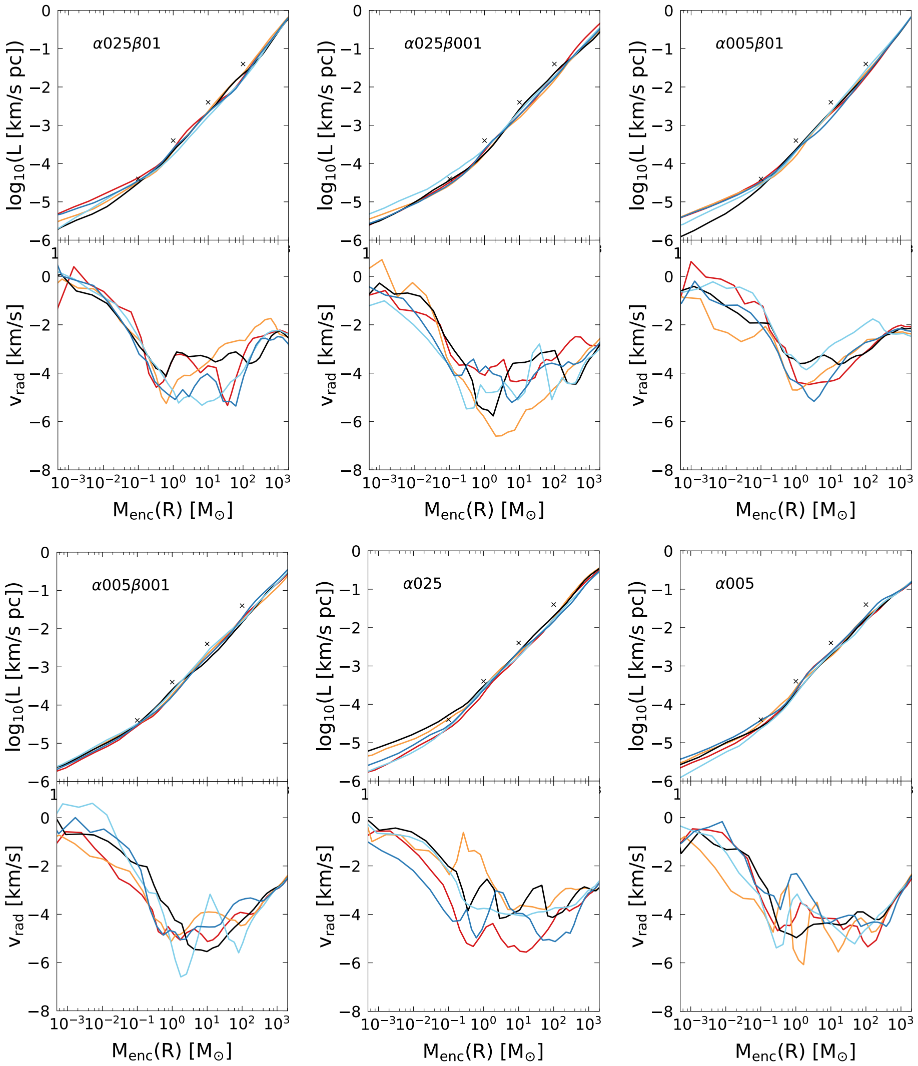

Figure 5.5: Profiles of the specific total angular momentum, L, and the radial velocity, $v_{\rm rad}$, versus the enclosed mass $M_{\rm enc}(R)$. The properties in both subplots are derived from mass-weighted averages taken within spherical shells centered on the densest gas cells just before first sink formation. Overview of most of our setups and their individual realizations. The color scheme is the same as in Fig. 5.1.

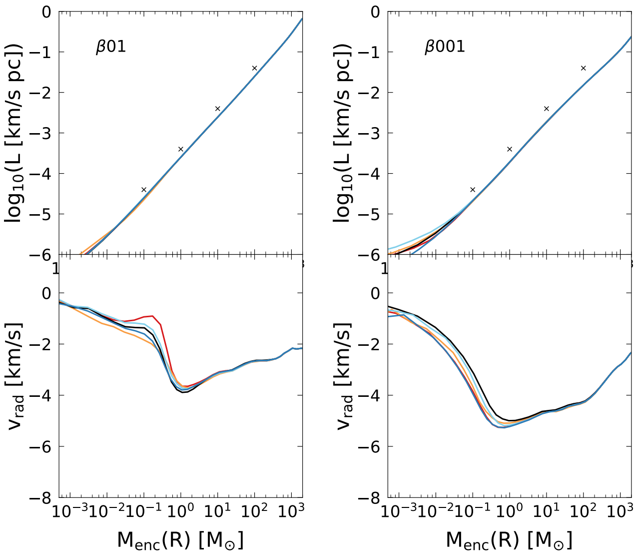

Figure 5.6: Same profiles as in Fig. 5.5, but for the purely rotational runs.

2010; Clark et al., 2011b; Greif et al., 2012; Stacy & Bromm, 2014). The very low L values in the *pure infall* setup are due to the lack of initial angular momentum within the collapsing cloud. The total angular momentum, however, is not zero as turbulent gas motions that arise during gravitational collapse (see e.g. Clark et al., 2011a; Turk et al., 2012) induce some angular momentum in the cloud. We will see the increase in turbulence more clearly later when we compare different velocity profiles and Mach numbers in Section 5.3.2.

Regarding the data from Abel et al. (2002), we find the best overall agreement in setup $\beta = 0.1$, the worst in the *pure infall* models. The general difference in our setups indicates that the angular momentum found in the cosmological simulations by Abel et al. (2002) likely translates into a $\beta > 0.1$. We note that due to our limited resolution of 16 cells per Jeans length, we are not able to resolve turbulent motions arising during gravitational collapse. For this at least 32 cells per Jeans length are needed (see e.g. Greif et al., 2011; Greif et al., 2012). As turbulent gas motions also induce some angular momentum, it might be that we therefore underestimate the true values of L.

The radial velocity profile describes the gas infall velocity. The peak of the profile is usually at around an enclosed mass of $\sim 1\,\mathrm{M}_\odot$. It tends to shift to slightly higher masses for the runs including turbulence. Compared the the other profiles, we immediately see a large scatter and chaotic behavior of the runs including turbulence. Although the overall trend per setup is still visible, the lines of individual realizations show strong fluctuations. This significant variability demonstrates the continuing influence of the initial turbulence within the collapsing cloud in yielding not only a main collapse region but promoting gas instabilities and possible simultaneous collapse at other locations. We have seen such patterns already above in the profiles of density, molecular hydrogen and temperature that can be related to particular striking features in the v_{rad} profile. For example, we see a spike in the bright blue line of setup $\alpha 005 \beta 001$. This happens at $M_{\mathrm{enc}} \sim 10\,\mathrm{M}_\odot$. Looking into Fig. 5.1, we find a corresponding peak in n and $n_{\mathrm{H}_2}/n_{\mathrm{H}}$ at $R \sim 1000\,\mathrm{AU}$. On the other hand, the least scatter is found in the *pure infall* models and the purely rotational runs indicating that there is (so far) only a single collapsing

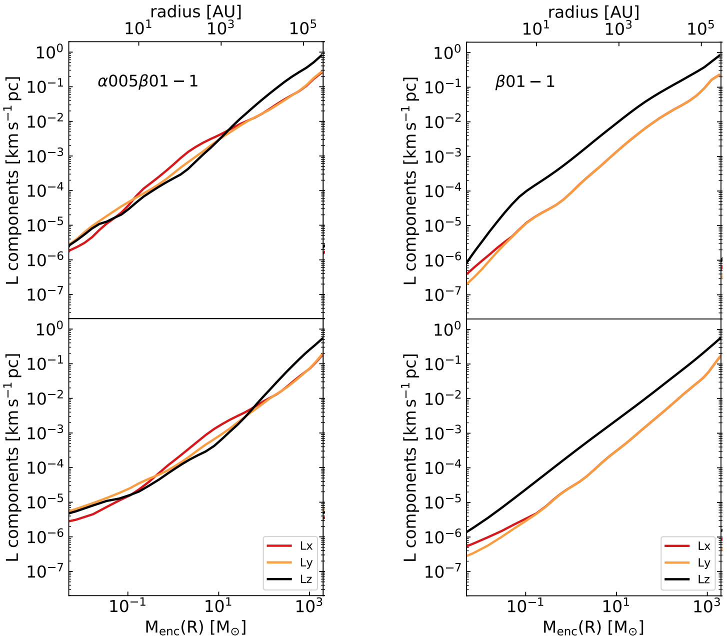

Figure 5.7: Behavior of the L_x, L_y and L_z component of the specific angular momentum vector computed with respect to the densest gas cell versus radius (top panels) and enclosed mass (bottom panels). The values are mass-weighted averages in spherical shells centered on the densest cell just before first sink formation using logarithmic binning with 40 bins.

region.

The largest infall velocities are generally between ~ -3 to $-6\,\mathrm{km\,s^{-1}}$, but in a few of the mixed runs, e.g. $\alpha005\beta001$ and $\alpha025\beta001$, values of $\lesssim -7\,\mathrm{km\,s^{-1}}$ are observed. Previous studies found comparable profiles, albeit with fewer fluctuations than our turbulent runs. Clark et al. (2011a) find magnitudes similar to us while Abel et al. (2002) and Clark et al. (2011b) report magnitudes of $-2.5\,\mathrm{km\,s^{-1}}$. The exact values depend crucially on the evolutionary time within the collapsing cloud at which they are measured and so the large scatter in v_{rad} does not necessarily indicate important differences in the overall trend of the gas collapse.

In Fig. 5.7, we show profiles of the vector components L_x, L_y and L_z of the specific angular momentum versus radius and enclosed mass at a time just before first sink formation. We show here results for the runs $\alpha005\beta01$-1 and $\beta01$-1 as they give a representative guide to the behavior of $\mathbf{L}$ in all of our runs. Similar plots for the rest of our runs can be found in Appendix 10.2.1.

The initial rotation axis of our cloud was the geometric z-axis of our box. When comparing all runs including rotation, it is only the purely rotational runs, here represented by realization $\beta01$-1, for which we observe that L_z is still the dominant component for the plotted radius and mass range. As the relative magnitude between the individual components stays roughly constant, the mass shells of the collapsing cloud rotate around a common axis which is still the initial z-axis. For $R \lesssim 10\,\mathrm{AU}$ or $M_{\mathrm{enc}} \lesssim 10^{-1}\,\mathrm{M}_\odot$ however, we observe that the L_x and L_y approach L_z demonstrating that in the immediate surrounding of the densest gas cell, where the first sink will form,

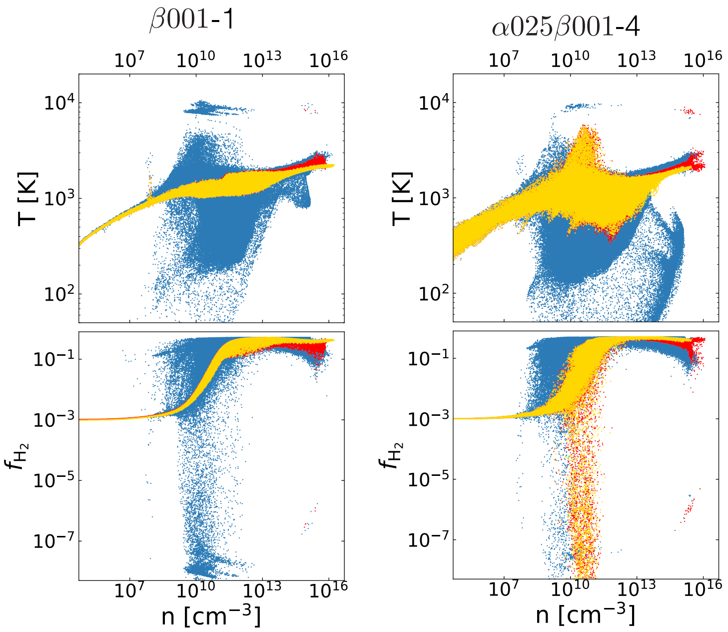

Figure 5.8: Phase plots of temperature and H_2 fraction versus number density of all gas cells. Three different stages of the gas cloud evolution are shown: just prior to sink formation (yellow), just after first sink formation (red), and 1000 yr later (blue).

the gas motions tend to be slightly irregular.

Compared to the purely rotational runs, in the mixed runs, here illustrated by $\alpha005\beta01$-1, L_z is dominant only for $R \gtrsim 10^3$ AU or $M_{\rm enc} \gtrsim 10\,{\rm M}_\odot$. The gap between L_z and L_x, L_y here is found to be more pronounced for higher level of rotation. Below these values, L_x, L_y and L_z get closer to each other when approaching the densest cell and become intertwined indicating that the direction of the specific angular momentum vector is thus in 45° to all three spatial axes which is the direction of the new common rotation axis.

In the purely turbulent runs, the lines of the three different components lie even more closely on top of each other. Thus, again 45° to all three spatial axes is the direction of the new common rotation axis. The variation in the relative magnitudes of the components are very small for $\alpha005$ but for $\alpha025$ may become large for some radius/enclosed mass range. This indicates that at some radii (or enclosed masses) the dominant direction of the specific angular momentum changes in favor of one or two combined components.

In Fig. 5.8, we plot the temperature and the H_2 fraction as a function of the number density for all cells in two representative simulations, $\beta001$-1 and $\alpha025\beta001$-4. Similar plots for the other runs can be found in Appendix 10.2.1. The different colors indicate different times: yellow and red stand for the time just before and just after first sink formation respectively, while blue is ~ 1000 yr later.

The yellow and red cell distributions are similar to one another. They are smoothest for the low level of rotation $\beta001$ (see also Riaz et al., 2018). The show the strongest difference for number densities $n \gtrsim 10^{15}\,{\rm cm}^{-3}$. Here, the red points, which describe a temperature increase and a decrease in H_2 fraction, indicate the direct gas infall/ accretion region onto the first sink that has formed. A small group of cells is even heated up to a few thousand Kelvin through accretion luminosity heating in the immediate surrounding of the sink.

In addition, we find an interesting feature of the yellow and red cell distribution in the panels of $\alpha 025\beta 001$-4. Here, we observe a peak in temperature and a clear drop in the H_2 fraction. This is related to the discussions about Fig. 5.1 to 5.3 as well as 5.5 and 5.6 above: this special behavior indicates locations of gas collapse different from the location of the densest cell.

For the blue cell distribution describing the gas at $t \sim 1000\,\mathrm{yr}$, we directly see that it strongly diverges for $n \gtrsim 10^9\,\mathrm{cm}^{-3}$. One group of cells heats up to $T \sim 10\,000\,\mathrm{K}$. This arises through gas that falls in later on to the protostellar system. As the enclosed mass at that time is larger, its free-fall velocity is higher as well. The infalling gas therefore shocks more vigorously and can become hot enough to destroy molecular hydrogen through collisional dissociation. The decrease in the H_2 fraction at this point is clear in the bottom panels of each subplot. On the other hand at this later stage, the previously rather thin curve of the H_2 fraction is now wider (see the broad distribution of blue points with $f_{H_2} \gtrsim 10^{-1}$ at $n \sim 10^9 - 10^{12}\,\mathrm{cm}^{-3}$). This elevated H_2 fraction still allows the gas in the post-shock region to cool which is indicated in the non-continuous cell distribution for $T > 1000\,\mathrm{K}$ in the corresponding top panels. The higher H_2 fraction originates from gas collapsing slowly in rotating structures within the protostellar disk environment that has formed through the influence of rotation and turbulence in the initial collapsing cloud core. In those substructures the gas does not experience enough compression to collisionally dissociate H_2. At even higher densities, the H_2 fraction is increased by three-body H_2 formation leading to almost fully molecular gas at $n \gtrsim 10^{10} - 10^{15}\,\mathrm{cm}^{-3}$. Here, another significant group of particles diverges toward temperatures $T < 1000\,\mathrm{K}$ and some may even cool to below $100\,\mathrm{K}$. The high molecular hydrogen fraction here makes it possible for the gas to cool while collapsing until our sink criterion may be fulfilled and new sinks form. This overall behavior has also been described in previous studies (see e.g. Stacy et al., 2010; Clark et al., 2011a).

5.3.2 Disk evolution

In Fig. 5.9, we show column density projections of all realizations of setup $\alpha 025\beta 01$ just after first sink formation. They are representative examples for runs including turbulence. The column density projections in 5.10 representatively demonstrate the common behavior for either purely rotational runs (top, described by $\beta 01$-1) or *pure infall* models without any initial rotation or turbulence (bottom, describe by *pure infall-2*). Instead of an axisymmetric disk as we observe in purely rotational models, mixed models or purely turbulent models form irregularly-shaped disks that can have filament-like features, see e.g. realization $\alpha 025\beta 01$-4 in Fig. 5.9. *Pure infall* models, on the other hand, just indicate purely radial infall, from all directions and without a preferred direction, onto the sink particle. These models started from a gas cloud without initial angular momentum. In Fig. 5.4, we saw that during gas collapse some angular momentum builds up. It is, however, too small to promote the formation of a protostellar disk.

In Fig. 5.11, 5.12 and 5.13 we display radial profile of number density, n, sound speed, c_s, radial velocity, v_{rad}, and rotational velocity, v_{rot}, together with the ratios $v_{\mathrm{rad}}/v_{\mathrm{rot}}$ and $v_{\mathrm{rot}}/v_{\mathrm{Kep}}$, where $v_{\mathrm{Kep}} = \sqrt{GM_{\mathrm{enc}}(R)/R}$ is the Kepler velocity, and the radial and turbulent Mach number, $\mathcal{M}_{\mathrm{rad}}$ and $\mathcal{M}_{\mathrm{turb}}$. In Section 5.3.1 above, we have

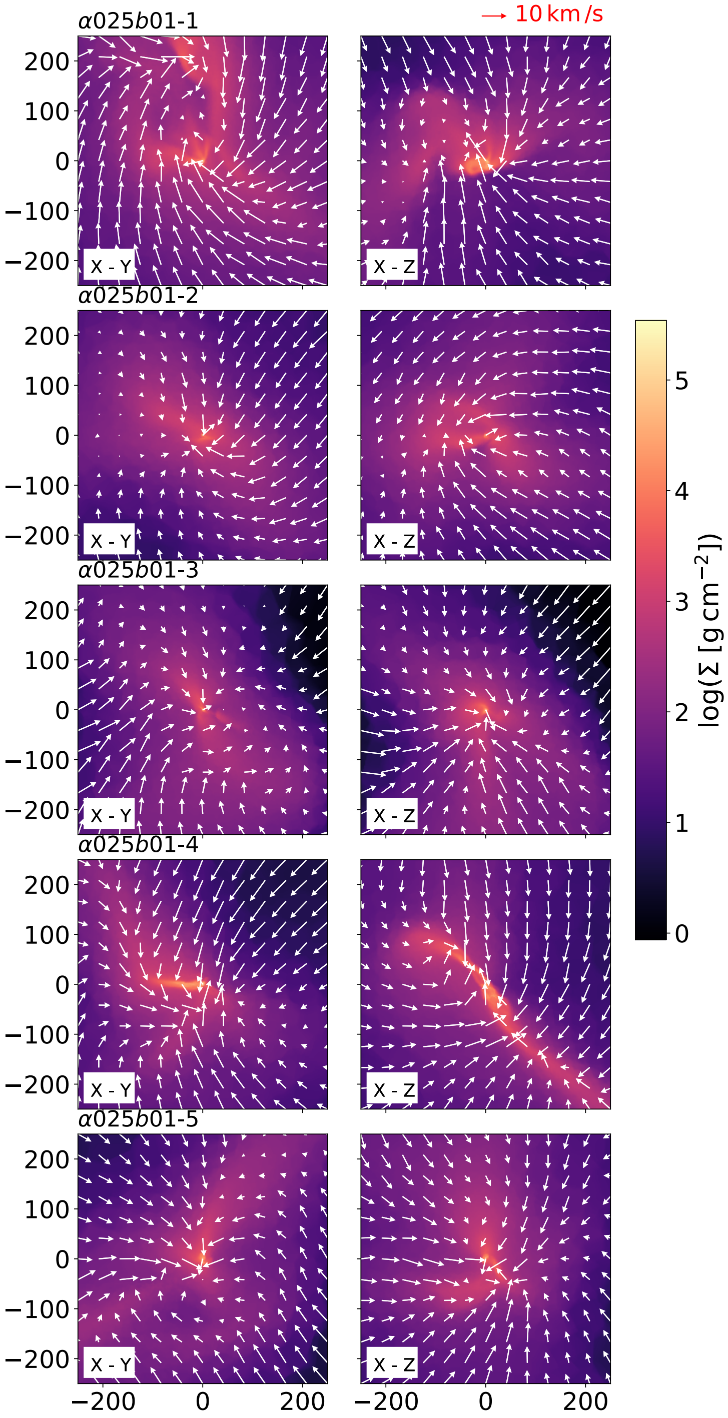

Figure 5.9: Column density projections of the realizations of setup $\alpha 025\beta 01$ just after the formation of the first sink. The arrows indicate the velocity field in the immediate environment of a X-Y (left column) or X-Z slice (right column) through the position of the first sink. The velocities are projected into the respective plane. The projection is 100 AU thick and centered on the position of the first sink.

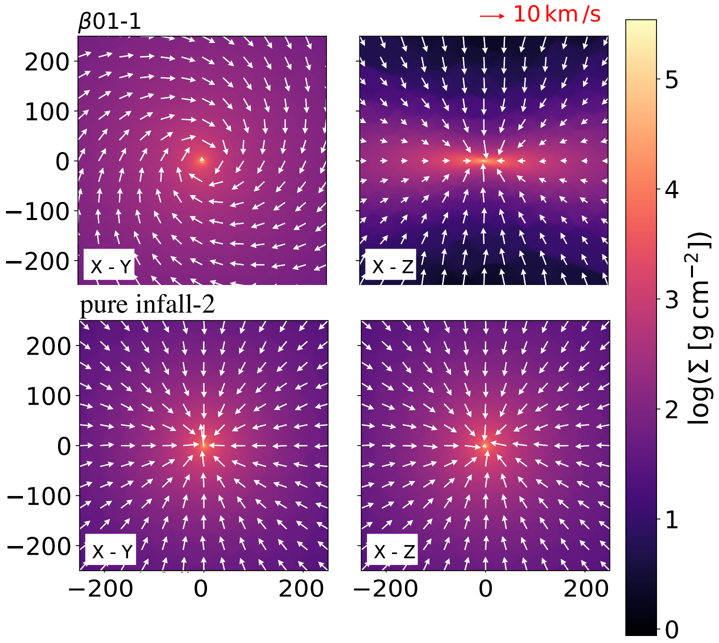

Figure 5.10: Same as in Fig. 5.9, but for the purely rotational run β01-1 and run *pure infall-2*. While in β01-1 a disk forms due to the initial rotation and hence the initial non-negligible amount of angular momentum, the *pure infall* model with no initial rotation or turbulence shows simple radial infall onto the sink from all directions.

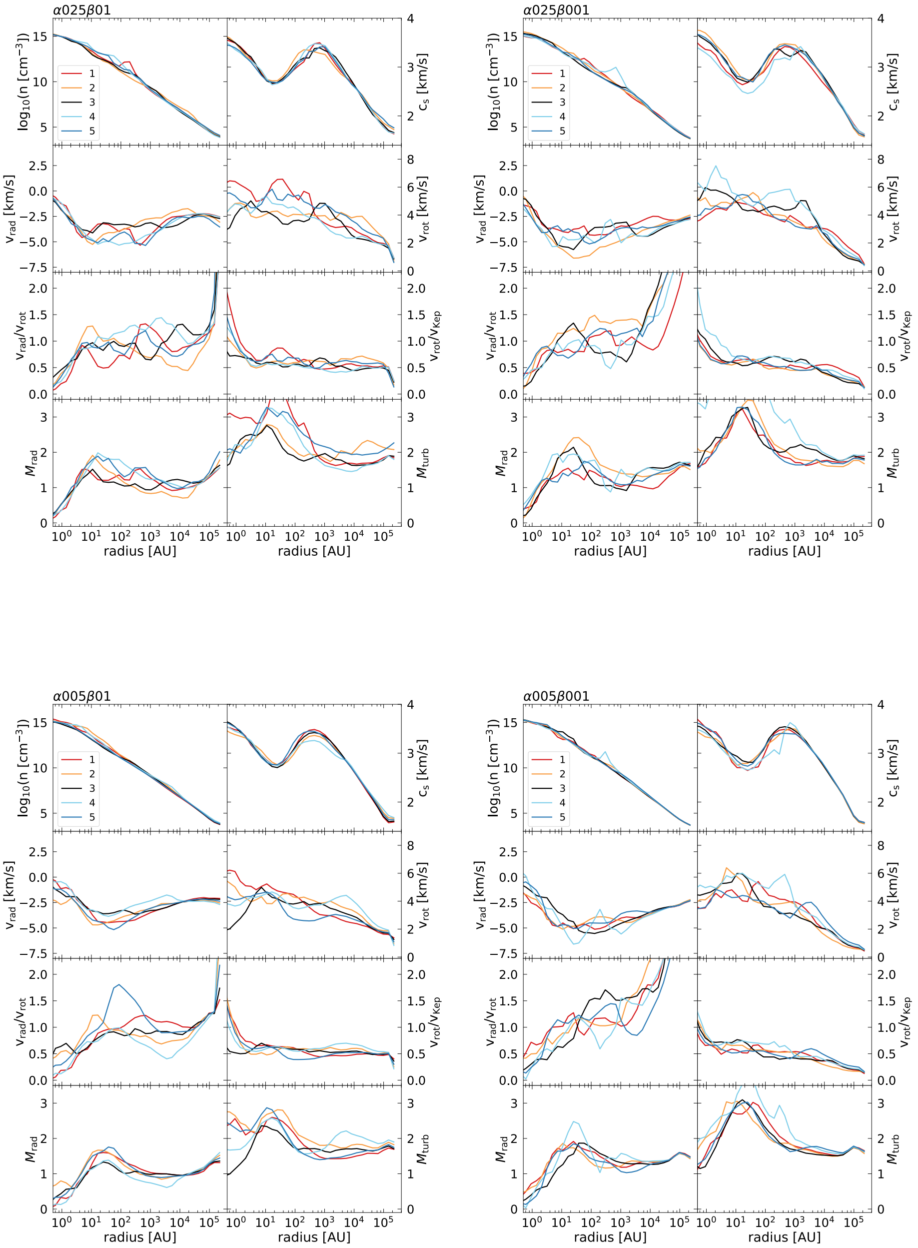

Figure 5.11: Overview of density and velocity structure in the collapsing cloud just before first sink formation. Here, we present the profiles of the mixed setups. From top left to bottom right (in each subplot): number density, n, sound speed, c_s, radial velocity, $v_{\rm rad}$, rotational velocity, $v_{\rm rot}$, the ratios $v_{\rm rad}/v_{\rm rot}$ and $v_{\rm rot}/v_{\rm Kep}$, where $v_{\rm Kep} = \sqrt{GM_{\rm enc}(R)/R}$ is the Kepler velocity, and the radial and turbulent Mach number, $M_{\rm rad}$ and $M_{\rm turb}$. The profiles are centered on the densest cell.

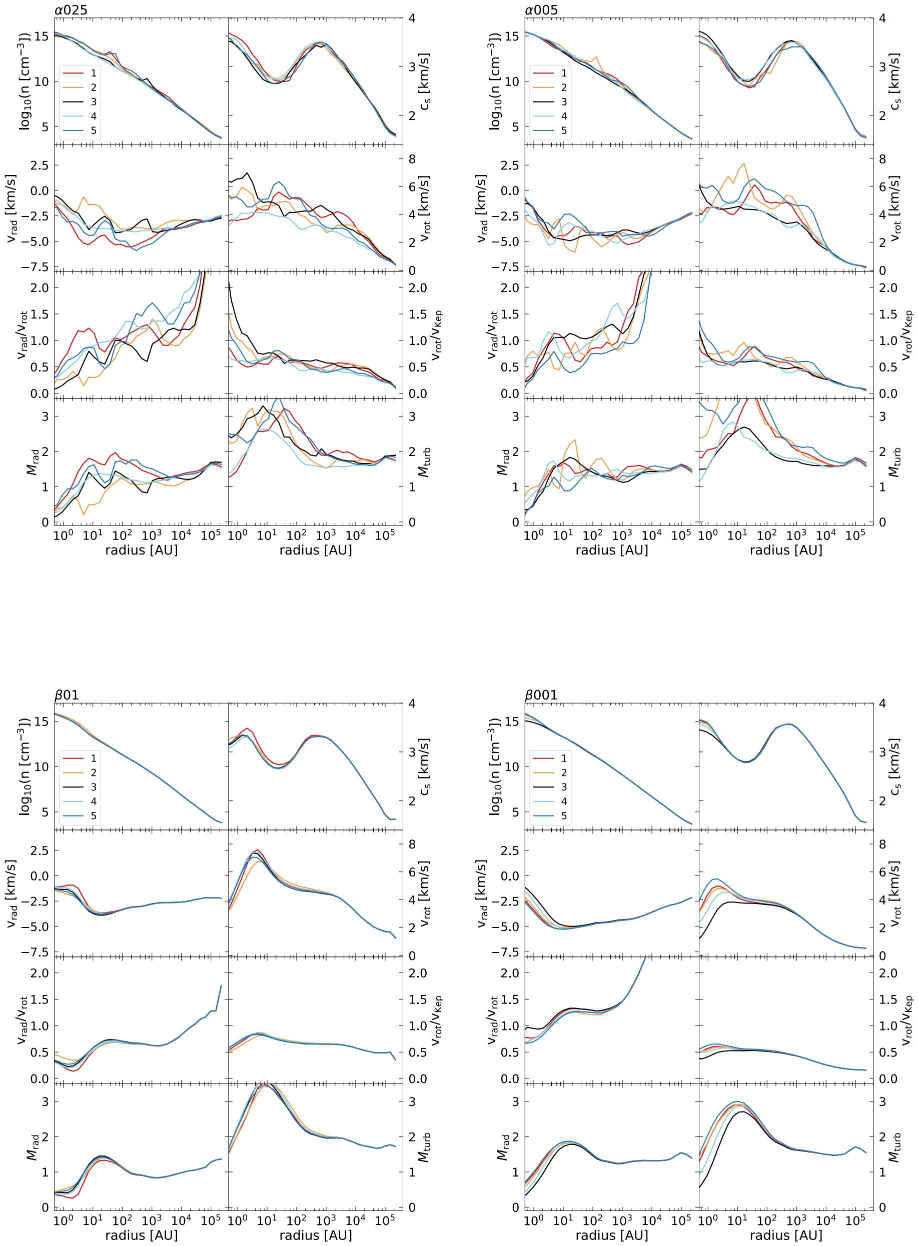

Figure 5.12: Overview of density and velocity structure in the collapsing cloud just before first sink formation. The properties are the same as in Fig. 5.11. Here, we present the profiles of the purely turbulent (top subplots) and the purely rotational setups (bottom subplots).

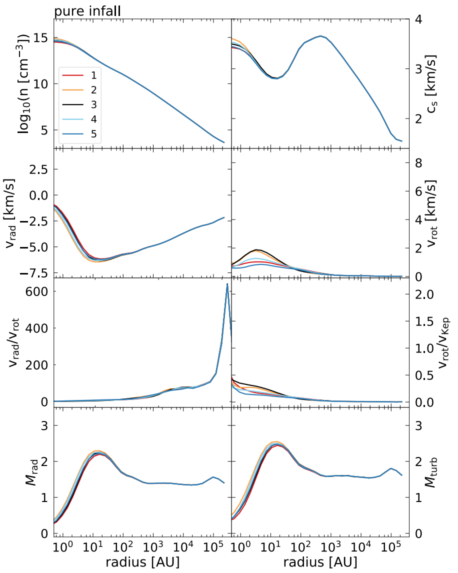

Figure 5.13: Overview of density and velocity structure in the collapsing cloud just before first sink formation. The properties are the same as in Fig. 5.11. Here, we present the profiles of the *pure infall* models.

already describe how we derive n, c_s, and $v_{\rm rad}$. The radial Mach number is defined as $M_{\rm rad} = v_{\rm rad}/c_s$. For $v_{\rm rot}$ and $M_{\rm turb}$, we follow the procedures described in Greif et al. (2012). The rotational velocity per radial bin is computed by summing up the angular momentum of all cells within this bin and by dividing this by the total mass within the bin and the radius of the bin. The turbulent Mach number is derived from

$$M_{\rm turb}^2 \, c_s^2 = \frac{1}{M} \sum_i m_{\rm i} (\mathbf{v}_{\rm i} - \mathbf{v}_{\rm rad} - \mathbf{v}_{\rm rot})^2 \ . \tag{5.2}$$

Here, M is the total mass within the bin and $m_{\rm i}$ and $v_{\rm i}$ are the mass and the velocity of a cell i within the bin.

We immediately see that there is a large scatter between the different realizations in the setups including turbulence in Fig. 5.11 and 5.12. The scatter is smallest for the number density and the sound speed where the lines usually lie well on top of each other save some some local irregularities and peaks or dips [4].

The lines of the other properties fluctuate more strongly. We have already encountered such behavior in Fig. 5.5 where the radial velocity was plotted versus the enclosed mass. The fluctuations originate from the choice of the different random seeds that were employed to set up the subsonic turbulent velocity field for our cloud. The latter introduces local variations in the behavior of the velocity field. In spite of such local variations, we are still able to identify common trends per setup.

The rotational and radial velocity have similar sizes for $R < 1000\,$AU with $0 \lesssim v_{\rm rad}/v_{\rm rot} \lesssim 1.5$. The rotational velocity is slightly larger. Toward larger radii, $v_{\rm rot}$ decreases while $v_{\rm rad}$ increases. In some setups, e.g. $\alpha 025$ and $\alpha 005$, we observe that $v_{\rm rad}$ rises suddenly at $R \gtrsim 1000\,$AU. This location marks the transition between the

---

[4] We have discussed such features already above explaining that they originate from gravitational collapse of gas at locations different from that of the densest cell.

rotationally supported protostellar disk region and the infalling gas envelope. We see that the sudden rise of v_{rad} shifts toward larger radii for higher α and β. Thereby, the influence of β is stronger, in particular for $\beta = 0.1$. This can be seen best in Fig. 5.12 where we show results from the purely turbulent and purely rotational runs. Both rotation and turbulence induce some angular momentum in the gas. This angular momentum leads to the formation of a rotationally support disk. The higher the angular momentum is, the larger the disk grows.

The ratio between the rotational velocity and the Kepler velocity remains at $v_{\mathrm{rot}}/v_{\mathrm{Kep}} \sim 0.5$ for all setups at most of the radii. It increases below a few AU toward the densest cell. Such values indicate a high degree of rotational support in all our runs. $v_{\mathrm{rot}}/v_{\mathrm{Kep}}$ decreases toward larger radii and drops below 0.5 at those radii where we observe the sudden rise of $v_{\mathrm{rad}}/v_{\mathrm{rot}}$ marking the edge of the protostellar disk.

In most of our setups, the turbulent Mach number is comparable to or higher than the radial Mach number. This means that turbulence is the main mechanism that transports angular momentum during the initial collapse and that leads to the formation of a rotationally support of structure. The radial Mach numbers are usually of order unity and only become mildly supersonic at small radii $\sim 10\,\mathrm{AU}$. The turbulent Mach numbers are overall slightly supersonic and also have an increase at small radii $\sim 10\,\mathrm{AU}$.

However, the behavior of the *pure infall* models is different. In these models, we see from Fig. 5.13, that no rotationally supported disk forms ($v_{\mathrm{rad}}/v_{\mathrm{rot}} < 0.5$) and $M_{\mathrm{rad}} \sim M_{\mathrm{turb}}$ suggesting that turbulence is solely induced by radial infall compared to the other cases were some contribution from the rotational velocity adds to the turbulent motions.

In Fig. 5.14, we show the same properties in a few selected runs at a time $\sim 50-68\,\mathrm{yr}$ after first sink formation [5]. The profiles are derived as described above but this time they are centered on the first sink that forms and the masses and velocities of the sink are taken into consideration in the derivation of the properties. The peaks we see in the density profiles indicate where additional sinks might form or have already formed (see also Greif et al., 2012). We see that they appear up to a distance of $\sim 1000\,\mathrm{AU}$ from the first sink.

Within 1000 AU the gas is mostly rotationally supported in all three setups. With an increasing initial degree of turbulence included, setups tend to become dominated by radial infall already at smaller distances from the first sink. Overall, $M_{\mathrm{turb}} > M_{\mathrm{rad}}$ within 1000 AU. The strong fluctuations of the Mach numbers near the first sink are due to the dynamical evolution of the gas under its self-gravity and accretion onto the created sink.

Our values of $v_{\mathrm{rot}}/v_{\mathrm{Kep}}$ are comparable to Greif et al. (2012) although they considered later times where densest region has collapse to $n \simeq 10^{19}\,\mathrm{cm}^{-3}$. They find $0.2 \lesssim v_{\mathrm{rot}}/v_{\mathrm{Kep}} \lesssim 0.7$ while we find $0.1 \lesssim v_{\mathrm{rot}}/v_{\mathrm{Kep}} \lesssim 1.5$ with higher values in runs with higher influence of turbulence and decreasing influence of rotation. Most of our setups lead higher values for this ratio than Abel et al. (2002) who found $v_{\mathrm{rot}}/v_{\mathrm{Kep}} \sim 0.3$. Since this is more similar to our *pure infall* models, which overall had a smaller sub- to transonic turbulent Mach number, this likely stems from smaller turbulence and/or a higher β parameter. We have already discussed this likely possibility above.

---

[5] Most of the plotted data is taken at around $50\,\mathrm{yr}$. However, for some of the realizations of $\beta 01$ the output data closest to this time was printed out at $\sim 60-68\,\mathrm{yr}$. See Table 10.2 in the Appendix for the exact times.

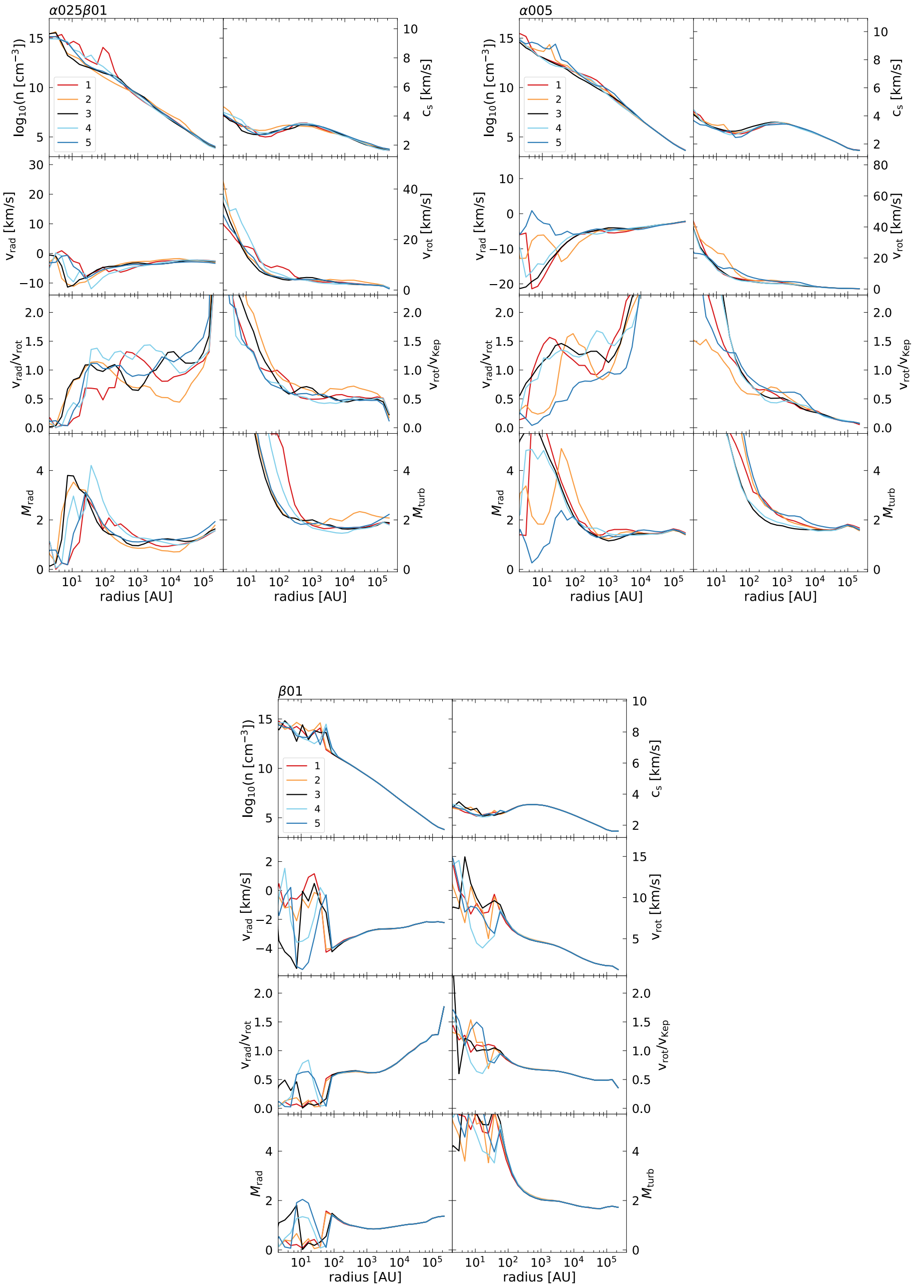

Figure 5.14: Density and velocity profiles of setups $\alpha025\beta01$, $\alpha005$ and $\beta01$ at a time of $\sim 50-70\,\mathrm{yr}$ after first sink formation. The structure of the panels and the derivation of the properties are the same as for Fig. 5.11, 5.12 and 5.13, except that now the profiles are centered on the first sink and sink masses and velocities are included in the derivation of the properties. See Table 10.2 in the Appendix for the exact times at which the date for each realization was extracted.

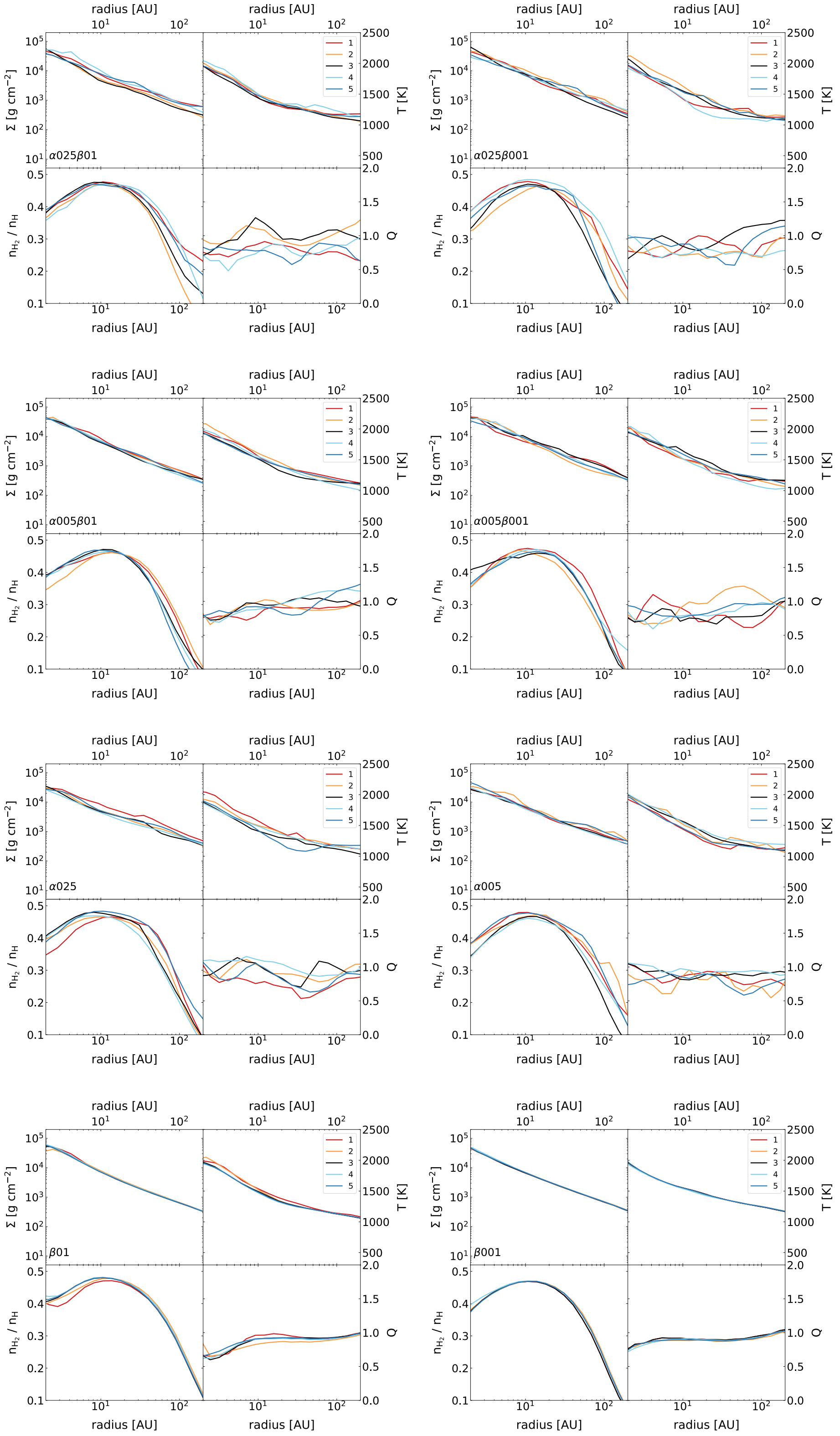

Figure 5.15: Radially, mass-weighted averages of disk properties centered on the first sink. From top left to bottom right: disk surface density Σ, temperature, T, H_2 fraction, n_{H_2}/n_H, and Toomre parameter, Q.

The stability of the rotationally supported disk that forms around the first sink can be estimated by the Toomre parameter

$$Q = \frac{\kappa\, c_\mathrm{s}}{\pi G \Sigma} \ . \tag{5.3}$$

This parameter compares disk self-gravity, described by the surface density Σ, to thermal pressure and rotation within the disk. The latter two are indicated by the sound speed c_s and the epicyclic frequency κ respectively, and act to stabilize the disk against gravitational instability. In case of a Keplerian disk, the epicyclic frequency equals the angular velocity, $\kappa = \Omega = \sqrt{GM(r)/r^3}$. For simplicity, we assume that our disks are Keplerian. The Toomre-Q varies with the radius of the disk as its defining parameters do. Perturbations within in the disk can grow when $Q \lesssim 1$, making this a necessary condition for disk fragmentation.

In Fig. 5.15, we plot the surface density, Σ, temperature, T, H_2 fraction, $n_{\mathrm{H}_2}/n_\mathrm{H}$, and the Toomre parameter, Q, within the disk. The properties are derived using mass-weighted averages within spherical bins around the position of the first sink particle. To study the gas within the disk specifically, we only consider cells with a number density of $n > 10^9\,\mathrm{cm}^{-3}$ (see also e.g. Stacy et al., 2010; Stacy & Bromm, 2014).

As we have already seen in the other profiles above, runs including turbulence show a scatter between the results of their individual realizations, while purely rotational or *pure infall* models have almost none. The largest fluctuations are visible in the Toomre Q parameter.

Our Σ, T, and $n_{\mathrm{H}_2}/n_\mathrm{H}$ profiles and values are comparable to those found in previous studies by Clark et al. (2011b), Greif et al. (2012), and Stacy & Bromm (2014). In particular, we find the characteristic temperature range between $\sim 1000 - 2000\,\mathrm{K}$ within $100\,\mathrm{AU}$ as was described in Clark et al. (2011b). The efficiency of H_2 line cooling together with the cycle of H_2 formation and destruction depending on the thermodynamical behavior of the disk gas, makes it possible that a thermal balance within the disk is kept, similar to the functionality of a thermostat.

Regarding the stability of the protostellar disks, we observe that all our runs have at some point within the $200\,\mathrm{AU}$ around the first sink a Toomre parameter with $Q < 1$ indicating disk instabilities. Runs including turbulence show a highly fluctuating Q. The purely rotational runs are most of the time quasi-stable with $Q \sim 1$ but tend to become unstable towards the immediate surrounding of the sink.

In Fig. 5.16, we show for the example of realization $\alpha005\beta001$-4 how the protostellar disk system evolves in time. The top panels describe the velocity field in the immediate surrounding of a X-Y plane through the position of the first sink that forms. The bottom panels indicate the position of the various sink particles. Both the velocity and the sink positions are projected into the plane. Furthermore, we give profiles of disk properties in $\alpha005\beta001$-4 at the same times as in Fig. 5.16. The profiles are centered on the first sink. We see that as time goes on, all profiles fluctuate strongly. The disk dynamic is ruled by the interplay of sinks, their accretion and heating and the continuous arising of further gravitational instabilities. As we can see from the Toomre parameter, the disk is highly self-gravitating. At times later than $\sim 66\,\mathrm{yr}$, Q fluctuates strongly between values indicating highly unstable regions and those describing stable ones. The red line which describes a time of $\sim 4\mathrm{yr}$ after first sink formation can be a reference line as its Toomre parameter is roughly $Q \sim 1$ at all radii, indicating a quasi-stable state. Comparing the ups and downs in Q of the other lines, we directly see how an increase in the surface density above the red reference line, leads to a drop of that line to $Q < 1$ indicating an unstable disk. Similarly one may easily track the

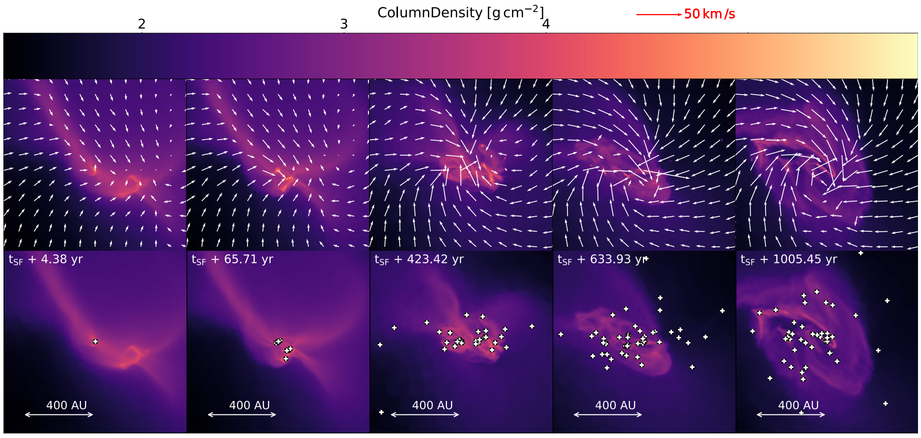

Figure 5.16: Density projection plots (X-Y) of the evolution of realization $\alpha005\beta001$-4. The projections are made for the same times as those of the disk profiles presented in Fig. 5.17. The projection thickness is about half a boxsize ($\sim 6.5\,\mathrm{pc}$), the distance between the position of the first sink and the edge of the simulation box. Top row: density projection plots with arrows indicating the velocity field in the immediate environment of a X-Y plane/slice through the position of the first sink. The velocities are projected into that plane. Bottom row: density profile with sink particles. Some the sinks that have been ejected of the protostellar disk system are already outside of the region presented in the plot.

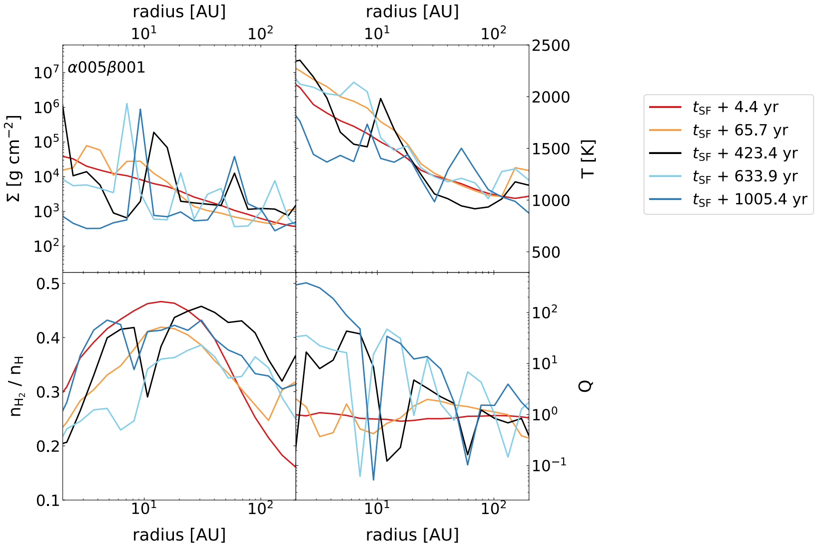

Figure 5.17: Evolution of radially averaged disk properties in realization $\alpha005\beta001$-4. The properties are derived as in Fig. 5.15 above. For the five different times displayed, each profile is centered on the first sink particle.

evolution of the molecular hydrogen fraction by its dependence on changes in the disk temperature: with a pronounced temperature peak, there is a clearly visible dip in the H_2 fraction.

5.3.3 Formation time of the first sink

We start our survey of the results of our large set of simulations by looking at the simple question of how long it takes to form the first sink particle in each of our simulations. The results are listed in Table 5.3 and summarized in Figure 5.18. We see immediately that both a higher initial level of rotation and a higher initial level of turbulence within the collapsing gas cloud delays the onset of star formation. Similar trends were observed in previous studies (see e.g Clark et al., 2011a; Riaz et al., 2018).

In the runs without any turbulence ($\alpha = 0$), the formation time of the first sink is almost identical in each realizations of a given setup, with the largest difference being $\sim 200\,$yr between the formation times of the first sinks in runs β01-1 and β01-2. This suggests that the small amount of numerical noise introduced by the variations in the initial cell distribution in the zero turbulence runs does not have a significant effect on the collapse timescale. On the other hand, the runs with turbulence show a significant spread in the sink formation times, amounting to ~ 0.1 Myr in most cases. This is also clear in Table 5.3, where we list the time at which the first sink forms ($t_{\rm SF}$) for each run. The dashed blue line in Fig. 5.18 shows the free-fall time of the cloud, $t_{\rm ff} = \sqrt{3\,\pi/(32\,G\,\rho_{\rm c})} \simeq 0.34\,$Myr, i.e. the time that it would take for a spherical cloud with a density equal to the initial central density of our Bonnor-Ebert sphere to collapse to a point in the absence of thermal pressure. We see that even in the *pure infall* runs, the time that elapses before the first sink forms is $\sim 2t_{\rm ff}$, demonstrating that pressure forces play a significant role in slowing the collapse of the gas. Including additional support in the form of non-zero turbulence or rotation further slows the collapse, but overall is less important than the support provided by the thermal pressure.

5.3.4 Number and mass of sinks formed

We compare most of our runs at a time of $\sim 1000\,$yr after first sink formation.[6] At this time, many of the runs contain sinks that are massive enough to start producing ionizing photons once the stars that they represent reach the main sequence. Since our simulations do not currently account for this form of feedback, we therefore stop at this point before the lack of this feedback becomes crucial in changing our results. However, we stop our *pure infall* models earlier than $1000\,$yr, as these runs proceed much more slowly than our standard runs. Nevertheless, even at that earlier stage they allow us to draw conclusions regarding their general outcome or trend or regarding the comparison of trends between different resolutions.

In the *pure infall* realizations only one sink forms and grows rapidly via accretion, reaching a mass of over $30\,{\rm M}_\odot$ in only ~ 100 yr. In contrast, all of the other runs show considerable fragmentation within the first 1000 yr, forming anywhere between 15 and ~ 120 sinks. The total number of sinks ($N_{\rm tot}$) and the total mass in sinks ($M_{\rm tot}$) in each realization at the final output time is listed in Table 5.3. This difference in behavior occurs because the *pure infall* runs are the only ones in which no disk forms

---

[6] For technical reasons, the different AREPO simulations do not produce their final output dumps after precisely 1000 yr, but rather in the interval $t = 1000 \pm 10\,$yr. In some runs, additional sinks were created shortly after $t = 1000\,$yr but before the final output dump. For these runs, we perform our comparisons using data from the previous output dump, produced shortly before $t = 1000$ yr.

Table 5.3: Overview of the detailed results of all our simulations regarding the time at which the first sink forms, $t_{\rm SF}$, the final year considered for our analysis, $t_{\rm final}$, the total number of sink particles formed by that time, $N_{\rm tot}$, and the corresponding total mass in sinks, $M_{\rm tot}$.

Realization	$\alpha_{\rm turb}$	$\beta_{\rm rot}$	$t_{\rm SF}$/Myr	$t_{\rm final}$/yr	$N_{\rm tot}$	$M_{\rm tot}/M_\odot$
pure infall-1	-	-	0.631	973	1	69.1
pure infall-2	-	-	0.631	932	1	67.0
pure infall-3	-	-	0.631	683	1	52.2
pure infall-4	-	-	0.631	426	1	35.1
pure infall-5	-	-	0.631	719	1	54.5
$\beta01-1$	-	0.1	0.742	1002	49	36.8
$\beta01-2$	-	0.1	0.743	1001	31	37.9
$\beta01-3$	-	0.1	0.743	1003	42	32.6
$\beta01-4$	-	0.1	0.743	1003	27	36.0
$\beta01-5$	-	0.1	0.743	1005	45	36.8
$\beta001-1$	-	0.01	0.641	1002	28	57.9
$\beta001-2$	-	0.01	0.642	1003	26	50.9
$\beta001-3$	-	0.01	0.641	1003	37	58.8
$\beta001-4$	-	0.01	0.642	1003	43	54.6
$\beta001-5$	-	0.01	0.641	1004	35	56.6
$\alpha025-1$	0.25	-	0.698	995	72	67.0
$\alpha025-2$	0.25	-	0.757	992	40	53.9
$\alpha025-3$	0.25	-	0.766	1008	45	63.7
$\alpha025-4$	0.25	-	0.697	1011	19	51.4
$\alpha025-5$	0.25	-	0.745	1008	118	74.3
$\alpha005-1$	0.05	-	0.670	1003	61	86.3
$\alpha005-2$	0.05	-	0.617	1002	57	66.7
$\alpha005-3$	0.05	-	0.633	1005	63	59.8
$\alpha005-4$	0.05	-	0.657	1002	51	73.7
$\alpha005-5$	0.05	-	0.628	1007	39	60.6
$\alpha025\beta01-1$	0.25	0.1	0.796	1007	41	53.1
$\alpha025\beta01-2$	0.25	0.1	0.857	1012	32	25.0
$\alpha025\beta01-3$	0.25	0.1	0.822	1008	21	33.8
$\alpha025\beta01-4$	0.25	0.1	0.793	1000	53	53.9
$\alpha025\beta01-5$	0.25	0.1	0.900	1002	41	49.7
$\alpha025\beta001-1$	0.25	0.01	0.769	1000	34	50.0
$\alpha025\beta001-2$	0.25	0.01	0.695	1000	55	76.1
$\alpha025\beta001-3$	0.25	0.01	0.742	1031	52	65.8
$\alpha025\beta001-4$	0.25	0.01	0.770	1008	61	83.5
$\alpha025\beta001-5$	0.25	0.01	0.740	1010	44	63.5
$\alpha005\beta01-1$	0.05	0.1	0.714	1007	34	41.7
$\alpha005\beta01-2$	0.05	0.1	0.797	1013	30	35.3
$\alpha005\beta01-3$	0.05	0.1	0.731	1004	39	38.6
$\alpha005\beta01-4$	0.05	0.1	0.816	1009	15	22.6
$\alpha005\beta01-5$	0.05	0.1	0.767	1007	32	33.3
$\alpha005\beta001-1$	0.05	0.01	0.688	1010	40	47.5
$\alpha005\beta001-2$	0.05	0.01	0.655	1006	53	64.0
$\alpha005\beta001-3$	0.05	0.01	0.675	1013	45	63.3
$\alpha005\beta001-4$	0.05	0.01	0.675	1005	81	80.8
$\alpha005\beta001-5$	0.05	0.01	0.686	1007	32	48.1

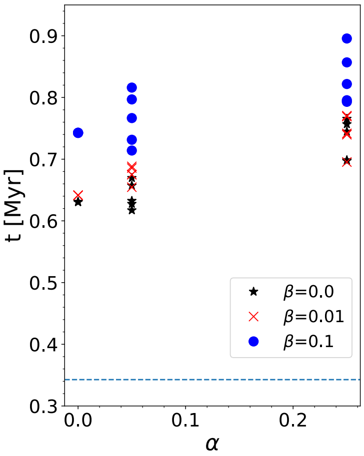

Figure 5.18: Formation time of the first sink particle in each simulation, plotted as a function of α_{turb}. The left-hand panel shows the results for several different values of the rotational β parameter. The right-hand panel shows a comparison of the results of setup $\alpha005\beta001$ for simulations using our standard Jeans refinement criterion, for which the Jeans length is always resolved by at least 16 cells (*red crosses*) and simulations using a more stringent refinement criterion of 32 cells per Jeans length (*orange squares*). The blue dashed line in the left-hand panel indicates the free-fall time of the cloud at its initial central density.

over the course of the simulations. Some non-zero angular momentum arises during the gravitational collapse but is too small to trigger the formation of a disk. See also Fig. 10.18 in the Appendix as an illustration of the velocity field in the surrounding of the sink at a times several hundred years after the formation of the sink. In all of the other runs[7] a dense, gravitationally unstable accretion disk forms which soon fragments.

In Fig. 5.19 and 5.20 we plot the evolution of the total mass in sinks, and the total number of sinks respectively. Each panel illustrates one setup, with the five realizations being described by different colors. We immediately see in almost all panels of both figures that there is a considerable scatter in the results of each setup.

In terms of the total mass accreted, we find that the scatter is smallest for the purely rotational and the *pure infall* runs, consistent with the small spread in initial sink formation times in these runs, and largest for the runs with the highest level of turbulence, particularly in the cases where we also have $\beta > 0$.

In terms of the total number of sinks formed, we find that there is a significant scatter for every setup (except for the *pure infall* case), but that this scatter is clearly larger for the runs with a high level of turbulence. Interestingly, the runs with rotation but no initial turbulence show clear differences in the number of sinks formed from realization to realization. In this case, the only difference between is the initial positioning of the mesh cells. By changing the initial positioning, we change the details of the numerical noise, and this small difference is sufficient to very different fragmentation outcomes, even though the mass going into the fragments varies little from run to run. This high sensitivity to small changes in the initial conditions suggests that the fragmentation

---

[7] The initial angular momentum of the gas in the runs with $\alpha > 0$ and $\beta = 0$ is small and varies from realization to realization. In principle, the angular momentum for a particular realization could be zero, but this is vanishingly unlikely.

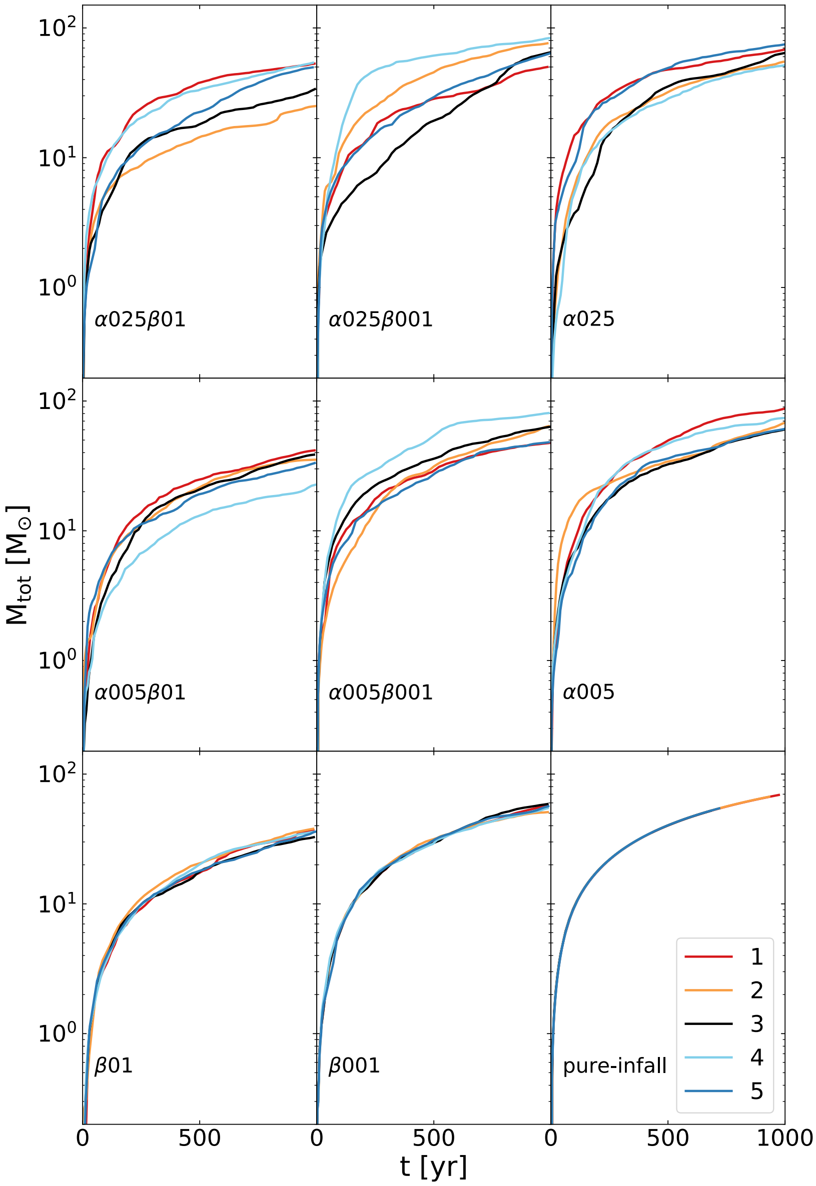

Figure 5.19: Total mass in sinks as a function of time after the first sink is created. Each panel shows the results for the five different realizations of each setup.

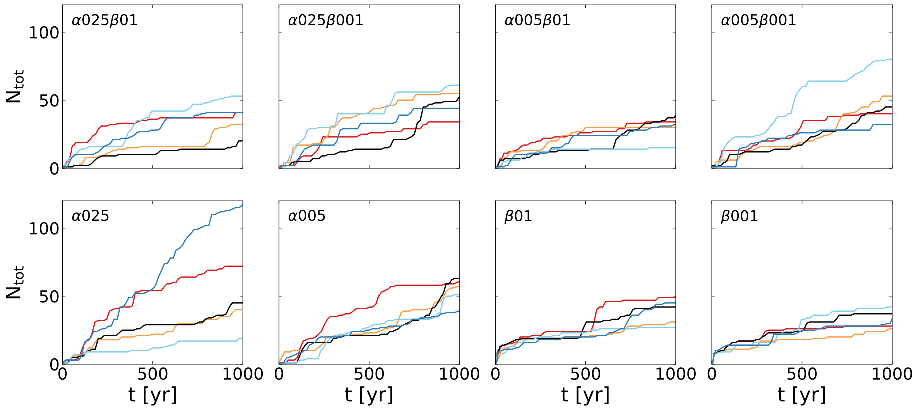

Figure 5.20: Total number of sinks as a function of the time elapsed after the formation of the first sink. The color scheme is the same as in Fig. 5.19.

Table 5.4: Average total number of sinks per setup, $\langle N_{\rm tot}\rangle$, and average total mass in sinks, $\langle M_{\rm tot}\rangle$, at $t \sim 1000$ yr, along with the corresponding standard deviations.

Setup	$\langle N_{\rm tot}\rangle$	$\sigma_{\rm N_{tot}}$	$\langle M_{\rm tot}\rangle[{\rm M}_\odot]$	$\sigma_{\rm M_{tot}}$
pure infall	1	0	35.7	2.1
β01	38.8	8.4	36.0	1.8
β001	33.8	6.2	55.8	2.8
α025	58.8	34.1	62.1	8.5
α005	54.2	8.6	69.4	9.8
α025β01	34.8	11.2	43.1	11.6
α025β001	49.2	9.4	67.8	11.5
α005β01	30.0	8.1	34.3	6.5
α005β001	50.2	16.8	60.7	12.3

of the disk is a chaotic process, a conclusion which is also consistent with the large amounts of scatter we see in the turbulent runs. If so, then this means that in order to study and derive general trends about the effects of turbulence or rotation on Population III star formation, one needs to consider the statistics of a sample of runs with varying initial conditions (initial mesh cell positioning, random seed used for the turbulence, etc.), rather than just comparing single realizations (see also Goodwin et al., 2004a,b, who find a similar result in the context of present-day star formation).

In Fig. 5.21, we plot the average total mass in sinks, $\langle M_{\rm tot}\rangle$, and the average total number of sinks, $\langle N_{\rm tot}\rangle$, per setup versus β (left subplot) or α (right subplot). The different color-coding of the markers denotes different levels of either constant α or β depending on which other one is varied on the x-axis. The error bars show the standard deviation in each quantity. We also list the means and standard deviations in Table 5.4. We see directly from this that the scatter in $N_{\rm tot}$ and $M_{\rm tot}$ is smaller in the purely rotational runs than in the runs containing initial turbulence. In addition, the mean values of these quantities are also smaller in these runs than in most of the turbulent runs.

In panel c) and f), the purely rotational data is illustrated while in i) and l) the purely turbulent runs are displayed. We see directly that the purely rotational runs (together with the *pure infall* models) have the smallest error bars of all data points indicating

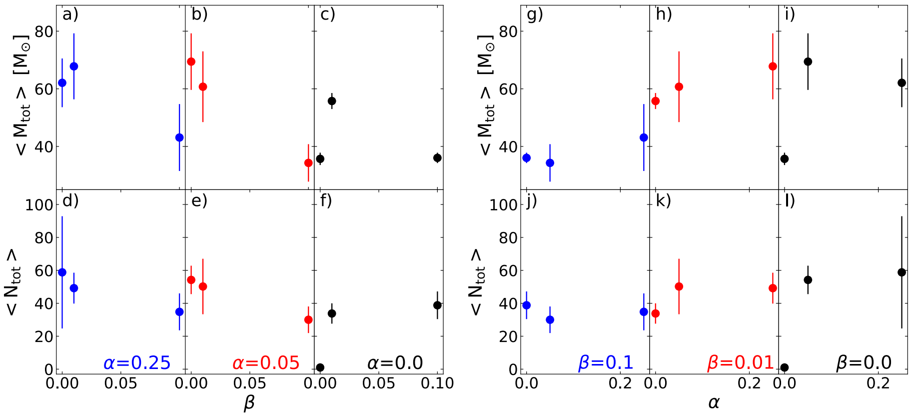

Figure 5.21: Overview of average final total mass in sinks $\langle M_{\rm tot}\rangle$ (top panels) and average final total number of sinks $\langle N_{\rm tot}\rangle$ (bottom panels) per setup versus the rotational β (left panels) or the turbulent α (right panels) parameter. Each column corresponds to runs with a fixed value of either α or β: this is stated in the bottom panel in each column and also indicated by the different colors.

the smallest scatter in results as we have already discussed above. Furthermore, we find that both $\langle N_{\rm tot}\rangle$ and $\langle M_{\rm tot}\rangle$, are smaller for the purely rotational runs than for the purely turbulent runs. Regarding $\langle M_{\rm tot}\rangle$ we find a larger value for a lower level of either rotation or turbulence, while for $\langle N_{\rm tot}\rangle$ the values are similar for both levels.

In the mixed runs, a couple of other trends are obvious. For fixed but non-zero α, adding a small amount of initial rotational energy has little effect – there is no significant difference between $\langle N_{\rm tot}\rangle$ and $\langle M_{\rm tot}\rangle$ in the turbulent runs with $\beta = 0$ and in those with $\beta = 0.01$. On the other hand, adding a much larger amount of rotational energy does lead to a clear difference in outcome: both $\langle N_{\rm tot}\rangle$ and $\langle M_{\rm tot}\rangle$ are significantly smaller in the runs with $\beta = 0.1$ than in the lower β runs, suggesting that in this case the disk is more stable due to a larger differential rotation, i.e. stronger shear motions that allow accumulated gas to be redistributed efficiently thereby keeping the surface density of the disk roughly constant.

Compared to the effect of rotation, a change in the degree of turbulence does not yield very different results in terms of $\langle N_{\rm tot}\rangle$. There is, however, a small difference between low and high α parameter for $\langle M_{\rm tot}\rangle$ which can be seen best in panels g) and h).

Comparison to previous studies

Studies by Clark et al. (2011a) and Riaz et al. (2018) have also examined the effect of varying the initial turbulent energy in simulations of the collapse of metal-free gas clouds. Since these studies were carried out with different hydrodynamical codes from our own study[8], it is interesting to compare their results with ours.

Clark et al. (2011a) consider two different scenarios: the collapse of Bonnor-Ebert sphere with mass 1000 $\mathrm{M}_\odot$ and initial temperature 300 K, taken to be representative of Pop. III.1 star formation, and a Bonnor-Ebert sphere with mass 150 $\mathrm{M}_\odot$ and initial

---

[8] Clark et al. (2011a) used the GADGET code of Springel (2005), while Riaz et al. (2018) used the GRADSPH code of Vanaverbeke et al. (2009).

temperature 75 K, taken to represent Pop. III.2 star formation. The first of these setups is clearly much closer to our own and is the one with which we will compare our results. Riaz et al. (2018) consider a single setup, a uniform sphere with mass $1.3041 \times 10^4\,\mathrm{M}_\odot$ and initial temperature 300 K. Both studies quantified the initial turbulent energy of the gas in terms of the ratio between the rms turbulent velocity $v_{\rm rms}$ and the sound speed $c_{\rm s}$. Clark et al. (2011a) studied cases with $v_{\rm rms}/c_{\rm s} = 0.1, 0.2, 0.4$ and 0.8, while Riaz et al. (2018) studied cases with $v_{\rm rms}/c_{\rm s} = 0.5, 1.0$ and 2.0. In terms of the $\alpha_{\rm turb}$ parameter used in our study, these equate to $\alpha_{\rm turb} \sim 2\times10^{-3}$, 6×10^{-3}, 0.03, and 0.1 for the Clark et al. (2011a) study and $\alpha_{\rm turb} \sim 0.02$, 0.07, and 0.28 for the Riaz et al. (2018) study.

Direct comparison of the numbers and masses of the sinks formed in these studies with the values from our own studies is not informative, owing to the large differences in mass resolution and sink accretion radius ($M_{\rm res} = 0.05\,\mathrm{M}_\odot$, $r_{\rm acc} = 20$ AU for the Clark et al. 2011a study and $M_{\rm res} = 1.133\,\mathrm{M}_\odot$, $r_{\rm acc} = 26$ AU for the Riaz et al. (2018) study, versus an effective mass resolution $M_{\rm res} < 0.01\,\mathrm{M}_\odot$ and $r_{\rm acc} = 2$ AU in the simulations presented here). However, it is still useful to compare overall trends.

Clark et al. (2011a) find that in their lowest $\alpha_{\rm turb}$ run, the gas does not fragment and the final outcome is very similar to our *pure infall* runs. On the other hand, in their other runs, even the relatively small amount of turbulence is enough to lead to significant fragmentation of the gas. Specifically, in these runs the non-zero angular momentum associated with the initial turbulence leads to the formation of a dense, disk-like structure which readily fragments. The relation of the number of fragments formed to the initial turbulent energy is unclear, consistent with our finding that there is considerable scatter from run to run, which can easily overwhelm any weak underlying trend.

On the other hand, Riaz et al. (2018) find that the gas in their runs with $\alpha_{\rm turb} \sim 0.02$ and 0.07 does not fragment, with fragmentation only occurring for their highest $\alpha_{\rm turb}$ run. This stands in stark contrast to our results and those of Clark et al. (2011a). Interestingly, Riaz et al. (2018) report that disk formation does not occur in their low $\alpha_{\rm turb}$ runs, suggesting that the primary reason for the lack of fragmentation in these runs is that their purely turbulent initial conditions start with a much lower level of angular momentum than those in our study or in Clark et al. (2011a). This may be related to the different way in which the turbulent velocity fields are initialized: in Clark et al. (2011a) and in our simulations, the turbulent velocity field contains a mix of compressive and solenoidal modes and has most of the power concentrated on large scales, while in Riaz et al. (2018) the initial turbulent velocity field is purely solenoidal and has power distributed over a wider range of scales. Further investigation of this point would prove worthwhile but is out of the scope of our present study.

Riaz et al. (2018) also consider runs with both turbulence and rotation, similar to our mixed runs. In this case, they find that disk formation and fragmentation occurs even when $\alpha_{\rm turb}$ is small. Their results suggest that increasing β leads to a more stable disk and hence less fragmentation, in agreement with our findings, although as they only consider one realisation of each of their setups, it is impossible to assess the statistical significance of their results.

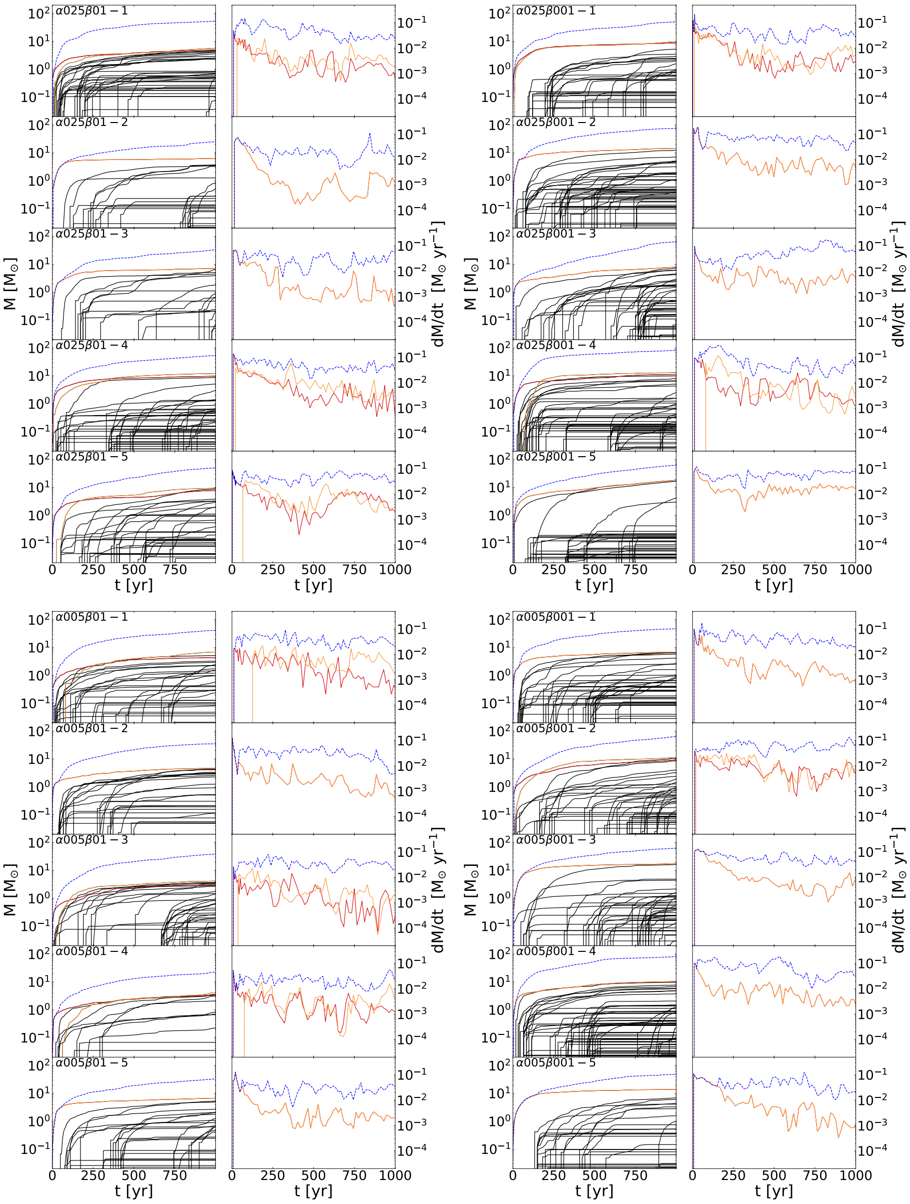

Figure 5.22: Overview of the mass accretion histories of the mixed runs. The left column in each subplot displays the increase of the total mass in sink (blue dashed line), the mass growth of the first (red) and the most massive sink (orange) together with all other sinks (black). The right column in each subplot shows the cumulative accretion rate (blue dashed line) and the accretion rate of the first (red) and most massive sink (orange). The most massive sink is defined to be the sink with the highest mass at $t \sim 1000\,\mathrm{yr}$. As can be seen clearly, the accretion rates are highly time-variable.

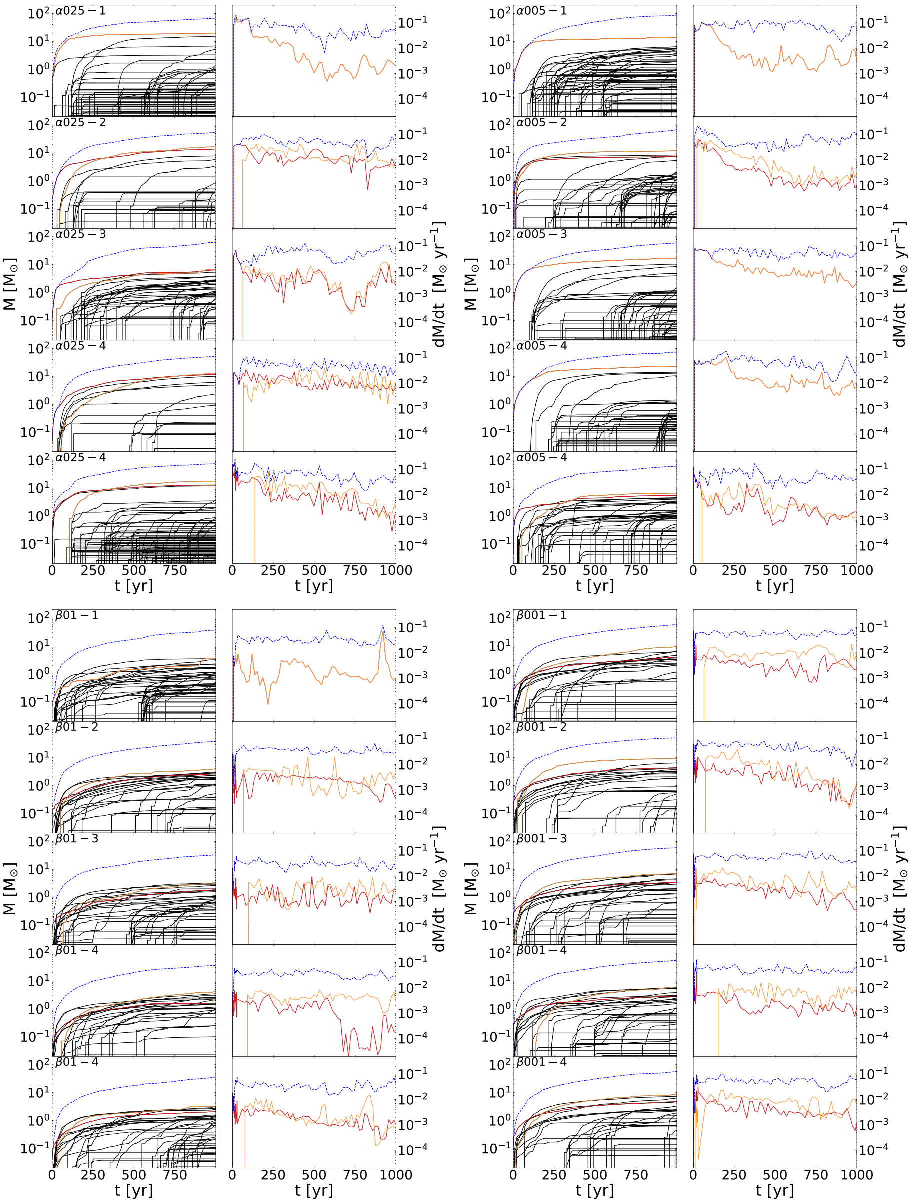

Figure 5.23: Overview of the mass accretion histories of the purely turbulent (top subplots) and the purely rotational (bottom subplots) runs. The color and line scheme is the same as in Fig. 5.22 above.

5.3.5 Mass evolution and accretion behavior

In all of our protostellar systems, we find high cumulative[9] accretion rates $10^{-2} < \dot{M}_{\rm acc} < 1\,{\rm M}_{\odot}\,{\rm yr}^{-1}$. Usually, in the first few years after the first sink has formed $\dot{M}_{\rm acc} \sim 10^{-1}\,{\rm M}_{\odot}{\rm yr}^{-1}$, dropping off slowly with time thereafter, although there are a few realizations in which it increases slowly with time. It rarely falls below values of a few times $10^{-2}\,{\rm M}_{\odot}{\rm yr}^{-1}$ over the period of time studied in our simulations. Only in one realization, $\alpha 005\beta 01$-2, does it drop below $10^{-2}\,{\rm M}_{\odot}{\rm yr}^{-1}$ before $t \sim 1000\,{\rm yr}$.

In Figures 5.22 and 5.23, we show the evolution of the individual and total sink masses (left columns) and individual and cumulative accretion rates (right columns) for all realizations and setups. The evolution of the total mass in sinks and the cumulative accretion rate is given by the blue dashed line. Red lines indicate the behavior of the sink which formed first in each simulation, while orange lines indicate the behavior of the most massive sink (defined as the sink with the highest mass at $t = 1000\,{\rm yr}$). If no red line is visible, this implies that the sink which formed first is also the most massive one.

For all of our runs, the cumulative accretion rate generally remains between 10^{-2} – $10^{-1}{\rm M}_{\odot}\,{\rm yr}^{-1}$ throughout the period we study. There is some scatter between the rate in different realizations of a given setup, with stronger and more irregular variations being visible in the runs including turbulence compared to the purely rotational runs. However, overall the difference between different realizations is relatively small, as is also clear from the fact that the total amount of mass accreted by the sinks after 1000 years, $M_{\rm tot}$, varies by at most a factor of two between the different realizations of a given setup. We find a weak trend indicating that runs with higher levels of rotation have lower cumulative accretion rates. This trend can be seen best when comparing the two purely rotational setups with each other. We have already seen the consequences of this behavior in Section 5.3.4 where we find an obvious gap in the range of values of $\langle M_{\rm tot} \rangle$ between setups including high level of rotation and the rest of the setups. However, the overall difference between the various setups is still small, consistent with the idea that it is the temperature and density structure of the infalling gas, rather than its level of turbulence or rotation, that is primarily responsible for determining the overall accretion rate.

In the left columns of the subplots of Figures 5.22 and 5.23, we show how the mass of each individual sink evolves in each simulation. We find that many sinks stop accreting shortly after their formation, while some continue to accrete over a longer period. However, we do not see a clear relationship between when a sink forms and how long it continues to accrete.

In the following we concentrate on describing the evolution of the most massive sink particle and the first sink particle to form. We find that in all realizations and setups, the most massive sink forms before $t = 200\,{\rm yr}$. The most massive sink after 1000 yr is always one of the first sinks to form, but often not the very first to form (although there are many cases where it is). Initially, the accretion rate onto the first protostar is very large, but as more protostars form it decreases significantly, ending up with a value anywhere between $\sim 10^{-4}\,{\rm M}_{\odot}{\rm yr}^{-1}$ and $\sim 10^{-2}\,{\rm M}_{\odot}{\rm yr}^{-1}$ after $t = 1000\,{\rm yr}$. Something similar is true for accretion onto the most massive sink, although in this case the fall-off in the accretion rate is generally less pronounced. Both rates show much stronger time variability than the cumulative accretion rate, and in some cases short bursts of very rapid accretion are seen (see e.g. run $\beta 01$-1). Both rates also show con-

---

[9] We define cumulative accretion rates as the sum of the accretion rates of all sink particles within a simulation.

siderable variability between the different realizations of a given setup, suggesting that while the turbulence and rotation have only a weak influence on the overall accretion rate, they have a strong influence on *which* sinks accrete the gas.

The values and variability that we find in the accretion rates are in agreement with results from previous numerical studies (e.g. Clark et al., 2011b,a; Greif et al., 2011; Smith et al., 2012; Stacy & Bromm, 2014; Susa et al., 2014; Stacy et al., 2016; Riaz et al., 2018). Directly after its formation, the first sink particle can be expected to have an accretion rate as high as $\gtrsim 10^{-1}\,\mathrm{M_{\odot}yr^{-1}}$ (Yoshida et al., 2006). Within the high density environment around the first sinks, new fragments soon form. From Fig. 5.20, we see that in most realizations, secondary protostars form rapidly after the first. The variability of the accretion rates and their eventual continuous decline stems from the gas dynamics within the protostellar accretion disk where strong gravitational torques redistribute angular momentum and allow more mass to flow to some protostars. Furthermore, it originates from the interactions between the sinks as they compete for accreting material which reduces the accretion onto some of the sinks (e.g. Peters et al., 2010; Smith et al., 2011; Greif et al., 2011). Susa (2013) find that the majority of the high mass stars ($> 30\,\mathrm{M_{\odot}}$) forming in their simulations are the first protostars to form in their halos. We do not see such a trend, although there is usually at least one realization per setup in which the first sink becomes the most massive sink at $t \sim 1000\,\mathrm{yr}$. However, we caution that we cannot yet draw final conclusions about this as we only cover a short period within the accretion history of a primordial protostellar cluster.

5.3.6 Mass function

In Fig. 5.24, we show the mass function of the sinks present at $t \sim 1000$ yr in each realization of each setup. In the diagrams here, we omit the pure infall models, in which only one sink forms over the course of the simulations. Each row represents a different setup with its individual realizations 1 – 5 displayed from left to right in panels one to five. The sixth panel on the right shows the combined mass function for that setup (i.e. the sum of the other five mass functions). The color scheme is the same as in Figures 5.19 and 5.20.

We see immediately that there are considerable differences between the mass functions in the different realizations corresponding to a given setup. Nevertheless, some features of the mass functions remain the same from realization to realization. In most cases, the mass functions are fairly flat, with a large deficit of low mass stars compared to what one would expect from a Salpeter (1955) or Kroupa (2001) mass function. The maximum sink mass is typically $\sim 10\,\mathrm{M_{\odot}}$, although as we have already seen, this sink is generally still accreting at a rate of $10^{-3}\,\mathrm{M_{\odot}\,yr^{-1}}$ or more (see Figures 5.22 and 5.23) and so we would expect to recover larger maximum masses if we were to continue the simulation for longer. The minimum sink mass in each case generally ranges from a few times $10^{-3}\,\mathrm{M_{\odot}}$ to $10^{-2}\,\mathrm{M_{\odot}}$. This minimum mass is set by the local Jeans mass in the fragmenting disk, which ranges from $0.004 \lesssim M_{\mathrm{J}} \lesssim 0.01\,\mathrm{M_{\odot}}$ at time of first sink formation. For comparison, the minimum cell mass at the same time is $\lesssim 10^{-6}\,\mathrm{M_{\odot}}$ in every simulation, making us confident that the low mass cutoff we see in the mass functions is real and not a numerical artefact.

Comparing the combined mass functions, we see that although the distributions are fairly flat overall, they are not completely flat. In particular, the runs with a high level of turbulence appear to peak at a mass of around $0.1\,\mathrm{M_{\odot}}$, while those with pure rotation peak instead at a mass of a few solar masses. We have checked the similarity of all the combined mass functions with the Kolmogorov-Smirnov (KS) test. This confirms the

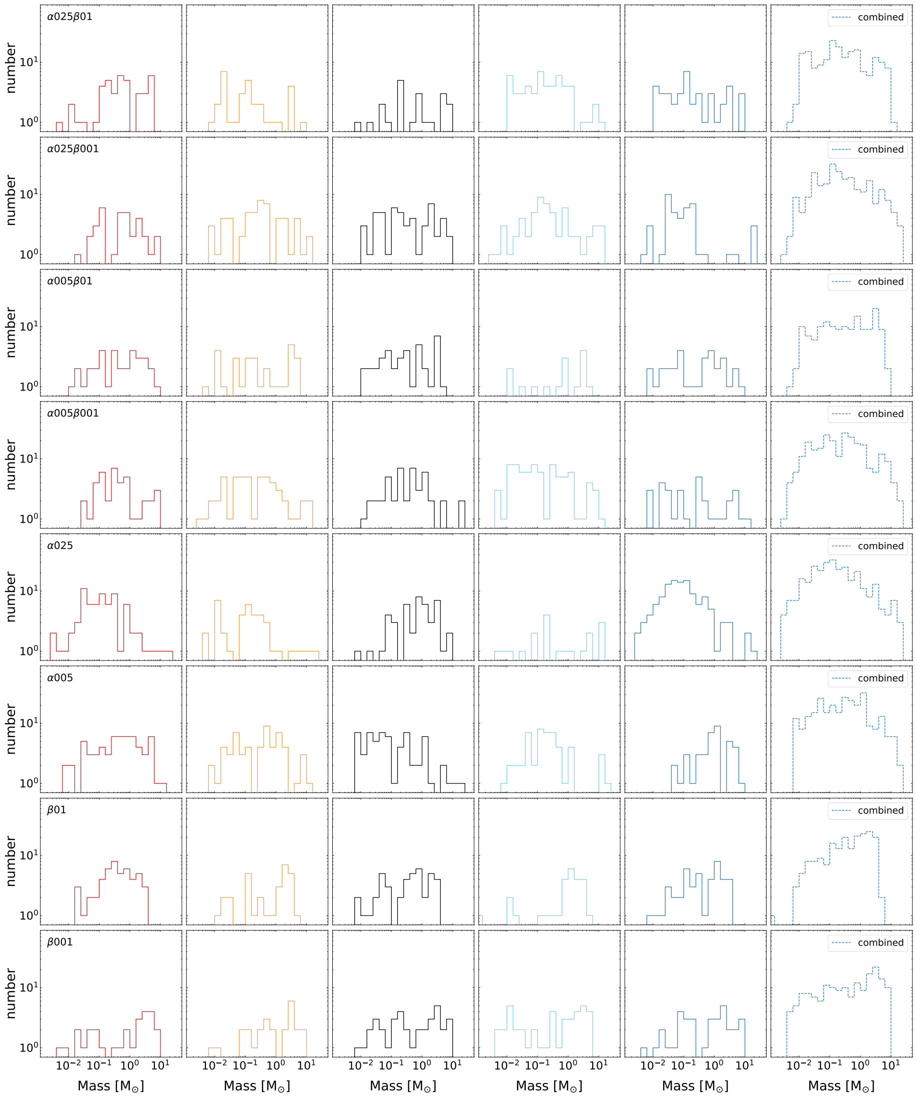

Figure 5.24: The protostellar mass functions produced in the simulations. Each row represents a different setup. The first five columns show the mass function for each of the individual realizations. The last column shows the combined mass function for each setup, which is derived by summing up the contributions of all individual realizations per setup. The choice of color for the realizations is the same as in Figures 5.19 and 5.20.

visual impression that the combined mass functions from the purely rotational runs are in general not consistent with those in the purely turbulent runs. For reference, we list the KS statistic and corresponding p-value for each comparison between setups in Table 10.4 in the Appendix.

Our finding of a flat protostellar mass function is in good agreement with previous studies of fragmentation in Pop. III accretion disks that adopted a sink particle-based approach (e.g. Clark et al., 2011a; Greif et al., 2011; Smith et al., 2011; Stacy et al., 2016). However, the significant differences we see between the mass functions produced by different realizations of the same setup demonstrates the danger involved when drawing conclusions based on only a small number of simulations of fragmentation, particularly in runs where the gas is highly turbulent.

It is also important to emphasize that the mass functions shown here are not predictions of the final protostellar IMF. Our simulations only probe a short period in the history of the accretion disk, they do not account for mergers between sinks (see Section 5.3.7 below), and also they do not account for the effects of radiative feedback, which we expect to play an important role in regulating the high mass portion of the IMF (see e.g. Susa et al., 2014; Stacy et al., 2016).

5.3.7 Stellar encounter and merging

In view of the large number of fragments that form in the gas, and the small size of the region in which they form, close interactions between protostellar fragments are likely. Previous studies have shown that encounters between protostars are indeed a common feature within Pop III protostellar systems and affect the trajectories of the protostars in question, which might lead to dynamical ejections (e.g. Greif et al., 2011; Smith et al., 2011; Susa, 2013; Stacy et al., 2016), formation of binaries or multiple systems (e.g. Stacy et al., 2010, 2013; Riaz et al., 2018), and mergers (e.g. Stacy et al., 2010; Greif et al., 2012; Hosokawa et al., 2016; Stacy et al., 2016). We analyze ejections in the next section. We refrain from exploring the properties of binaries or multiple systems since it is likely that they continue to change over the course of the simulation and since we cover only a short time in our runs is small compared to other studies that have tackled this question (e.g. Smith et al., 2012; Stacy et al., 2013). Our current implementation of sink particles within AREPO does not allow for the possibility of sink merging, so we cannot simulate this self-consistently. Nevertheless, by examining the trajectories of the sink particles, we can study how likely mergers are in our different setups and whether there is any systematic trend with increasing turbulent or rotational energy.

We consider two kinds of close encounters: ones where the protostellar radii actually touch or overlap (referred to later as the touching-radii scenario) and ones where the lower mass (secondary) protostar approaches to within the tidal radius of the more massive (primary) one (referred to later as the tidal-radius scenario). Numerically, therefore, we compare the distance between the protostars to either the sum of the protostellar radii, $R_1 + R_2$, or the tidal radius

$$r_{\mathrm{t}} \approx 2.44 R_1 \left(\frac{\rho_1}{\rho_2} \right)^{1/3}, \tag{5.4}$$

where R_1 is the radius of the primary protostar, and ρ_1 and ρ_2 are the densities of the primary and secondary protostars, respectively. In practice, during the period simulated the protostars will be ‘fluffy’ objects with extended, puffed-up radii (Hosokawa & Omukai, 2009; Hosokawa et al., 2010; Smith et al., 2012; Hirano et al., 2014;

Table 5.5: Overview of the number of encounters in comparison to total number of sinks at the end of the simulation for each realization. N_{tot} is the number of sinks after $t \sim 1000\,\mathrm{yr}$.

Setup	N_{tot}	Touching Radii		Within r_{t}	
		N_{merge}	$N_{\mathrm{merge}}/(N_{\mathrm{tot}}-1)$	N_{merge}	$N_{\mathrm{merge}}/(N_{\mathrm{tot}}-1)$
$\beta 01-1$	49	15	0.3125	29	0.6042
$\beta 01-2$	31	5	0.1667	13	0.4333
$\beta 01-3$	42	5	0.1220	16	0.3902
$\beta 01-4$	27	4	0.1538	12	0.4615
$\beta 01-5$	45	4	0.0909	10	0.2273
$\beta 001-1$	28	10	0.3704	17	0.6296
$\beta 001-2$	26	6	0.2400	12	0.4800
$\beta 001-3$	37	8	0.2222	16	0.4444
$\beta 001-4$	43	10	0.2381	21	0.5000
$\beta 001-5$	35	9	0.2647	18	0.5294
$\alpha 005-1$	61	10	0.1667	24	0.4000
$\alpha 005-2$	57	9	0.1607	23	0.4107
$\alpha 005-3$	63	5	0.0806	19	0.3065
$\alpha 005-4$	51	6	0.1200	17	0.3400
$\alpha 005-5$	39	8	0.2105	17	0.4474
$\alpha 025-1$	72	8	0.1127	24	0.3380
$\alpha 025-2$	40	5	0.1282	16	0.4103
$\alpha 025-3$	45	14	0.3182	26	0.5909
$\alpha 025-4$	19	5	0.2778	11	0.6111
$\alpha 025-5$	118	10	0.0855	31	0.2650
$\alpha 025\beta 01-1$	41	13	0.3250	23	0.5750
$\alpha 025\beta 01-2$	32	2	0.0645	5	0.1613
$\alpha 025\beta 01-3$	21	1	0.0500	6	0.3000
$\alpha 025\beta 01-4$	53	8	0.1538	16	0.3077
$\alpha 025\beta 01-5$	41	4	0.1000	20	0.5000
$\alpha 025\beta 001-1$	34	7	0.2121	17	0.5151
$\alpha 025\beta 001-2$	55	12	0.2222	31	0.5741
$\alpha 025\beta 001-3$	52	4	0.0784	20	0.3922
$\alpha 025\beta 001-4$	61	9	0.1500	21	0.3500
$\alpha 025\beta 001-5$	44	6	0.1395	21	0.4884
$\alpha 005\beta 01-1$	34	7	0.2121	14	0.4242
$\alpha 005\beta 01-2$	30	4	0.1379	10	0.3448
$\alpha 005\beta 01-3$	39	8	0.2105	11	0.2895
$\alpha 005\beta 01-4$	15	2	0.1429	5	0.3571
$\alpha 005\beta 01-5$	32	5	0.1613	11	0.3548
$\alpha 005\beta 001-1$	40	4	0.1026	12	0.3077
$\alpha 005\beta 001-2$	53	6	0.1154	15	0.2885
$\alpha 005\beta 001-3$	45	11	0.2500	21	0.4773
$\alpha 005\beta 001-4$	81	11	0.1375	23	0.2875
$\alpha 005\beta 001-5$	32	5	0.1613	13	0.4194

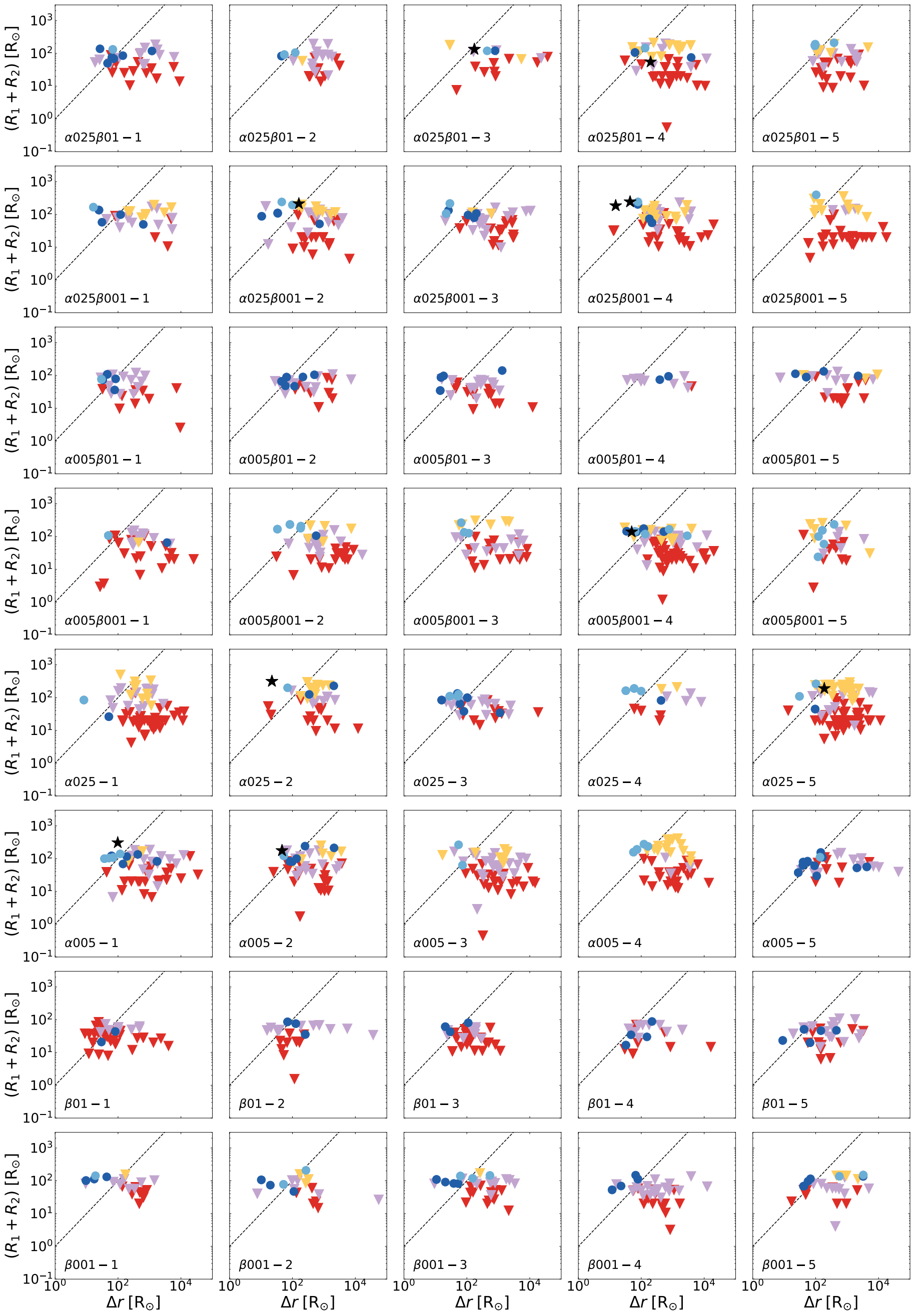

Figure 5.25: Comparison of the sum of the protostellar radii, $R_1 + R_2$, versus the minimum protostellar separation, Δr, for all close encounters in each simulation. The black dashed line indicates where $R_1 + R_2 = \Delta r$. Points above and to the left of this line indicate encounters likely to lead to mergers. Downward triangles describe encounters of low-mass protostars ($\leq 0.8\,\mathrm{M}_\odot$) with other low-mass protostars (red), with medium-mass protostars ($0.8 < M \leq 5\,\mathrm{M}_\odot$; bright violet) and with high-mass protostars ($> 5\,\mathrm{M}_\odot$; yellow colored). Filled circles are encounters of two medium-mass protostars (dark blue) or of a medium-mass and a high-mass protostar (bright blue). Black stars indicate encounters of two high-mass protostars.

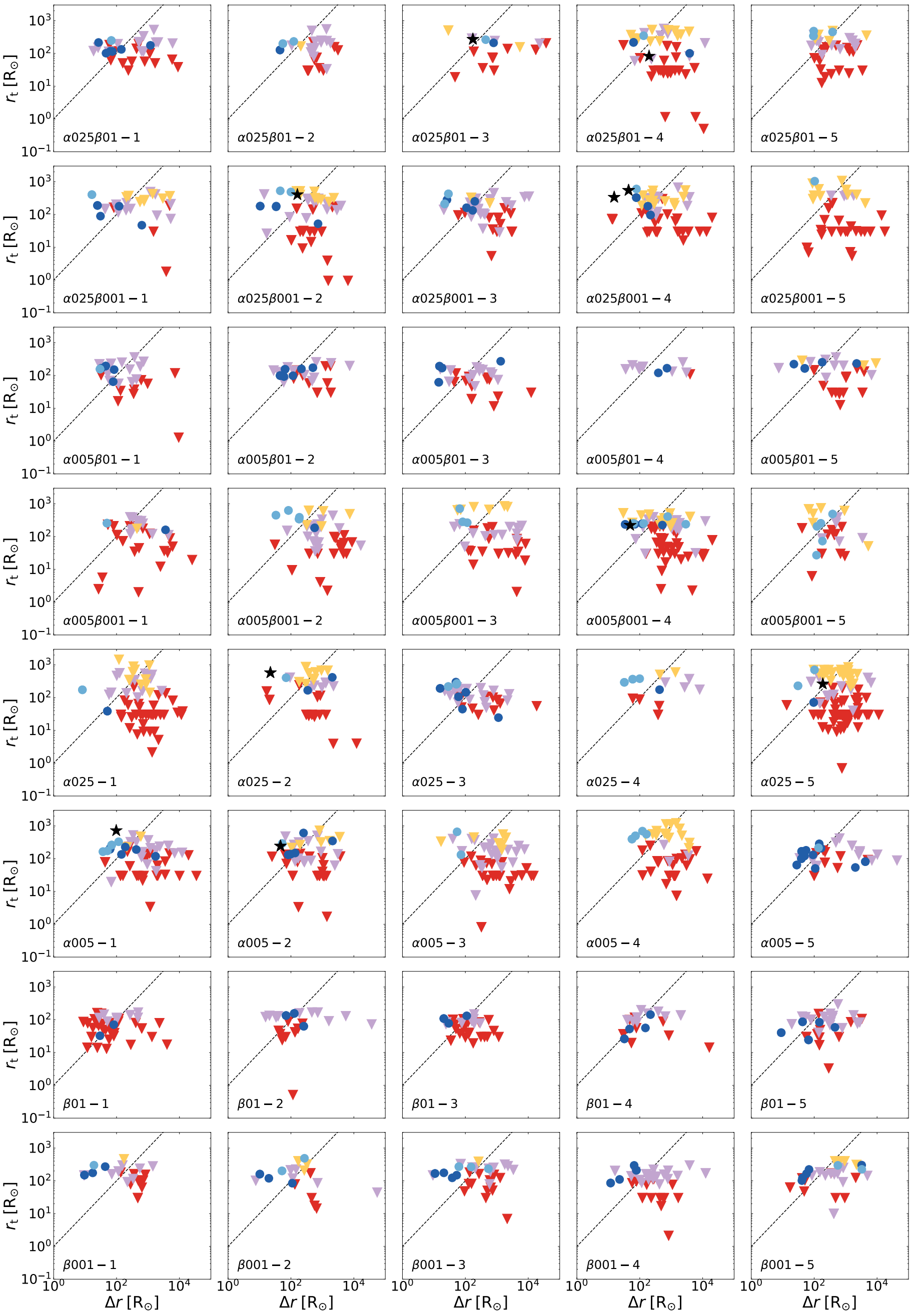

Figure 5.26: Comparison of the tidal radius r_t with the minimum protostellar separation, Δr, for all close encounters in each simulation. The black dashed line indicates where $r_t = \Delta r$. The symbols and the color scheme are the same as in Fig. 5.25.

Hosokawa et al., 2016), whose densities likely do not vary enormously from protostar to protostar. We therefore follow Smith et al. (2012) and approximate the tidal radius as $r_t \sim 3R_1$. Finally, we estimate the evolution of the protostellar radii, R_1 and R_2, by using Eq. (3.3) to (3.6) in Section 3.2.2 of our discussion of the accretion luminosity (see also Smith et al., 2011). Motivated by results from Greif et al. (2012) in which Population III protostar formation was studied without sink particles, we set the initial radius of a newly formed sink to $10\,\mathrm{R}_{\odot}$. We use an accretion rate that is derived by averaging the mass growth over 10 to 20 years. In this way, we smooth out the effects of any rapid increases or decreases in the accretion rate, since more sophisticated protostellar evolution models show that the protostellar radius is more sensitive to the long-term trend of the accretion rate than to its short-term variability (Smith et al., 2012).

We follow the trajectories of the sinks using the information included in the snapshot files from the simulations. Although these are produced with a high cadence, we nevertheless may miss some close encounters that occur in between snapshots. Our results should therefore be considered as lower limits on the number of close encounters.

In Fig. 5.25 and 5.26, we present an overview of the two encounter scenarios for all our setups and realizations. The different symbols and colors indicate which mass range the encountering protostars populate. Downward triangles describe encounters including low-mass protostars ($\leq 0.8\,\mathrm{M}_{\odot}$). Red triangles are encounters of two low-mass protostars, bright violet triangles stand for an encounter between a low-mass and a medium-mass ($0.8 < M \leq 5\,\mathrm{M}_{\odot}$) protostar, and yellow triangles are encounters between a low-mass and a high-mass ($> 5\,\mathrm{M}_{\odot}$) protostar. Filled circles are encounters of two medium-mass protostars (dark blue) or of a medium-mass and a high-mass protostar (bright blue). Black stars indicate encounters of two large-mass protostars. The black dashed line describes where the distance between the protostars equals either the sum of their protostellar radii (Fig. 5.25) or the tidal radius of the primary protostar (Fig. 5.26). Encounters above and to the left of this line are likely to lead to mergers. We can see immediately that close encounters happen in all realizations for both scenarios, with more encounters occurring in the case of the tidal-radius scenario. This becomes even clearer when we compare columns 3 and 5 in Table 5.5, where we list the number of merging candidates, N_{merge} for the two scenarios. The number of merger candidates is always larger in the tidal radius scenario, by anywhere from a factor of two to a factor of several.

Figures 5.25 & 5.26 also show that although close encounters take place between stars with a wide range of masses, the minimum separation Δr tends to decrease with increasing protostellar mass. Therefore, mergers are far more likely to occur between pairs of protostars that include at least one medium-mass star than between pairs of low-mass protostars. However, mergers between high-mass stars are rare in our simulations, simply because few of these stars form within the period studied here.

In Figure 5.27 we show how the number of mergers and fraction of sinks involved in mergers vary as a function of α and β in both the touching radii and the tidal radius scenarios. The exact number values are listed in Table 5.6 & 5.7. We see that although the number of mergers varies as we vary α and β, this is largely driven by the variation in the number of sinks that form: obviously, if one has more sinks, then more mergers are possible. The fraction of sinks that are involved in mergers does not vary strongly with α or β in most cases, remaining constant at around 15% in the touching radii scenario and around 40% in the tidal radius scenario. The main exception is the $\beta 001$ setup: the sinks produced in this setup undergo encounters close enough to lead to mergers at a higher rate than in any of the other setups. However, given the signif-

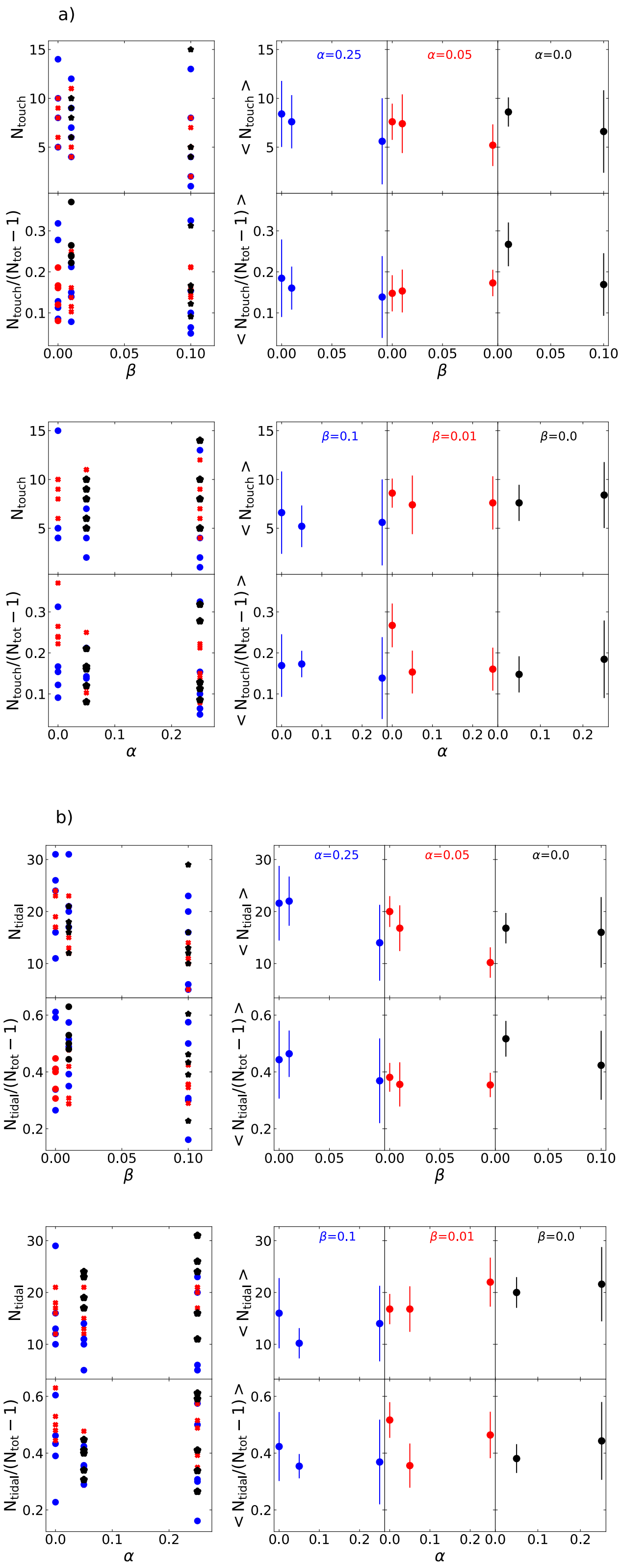

Figure 5.27: Subplot a): number of mergers per realization in the touching-radii scenario, N_{touch}, and ratio between number of such mergers per realization and maximum number of merger per realization, $N_{\mathrm{touch}}/(N_{\mathrm{tot}}-1)$ together with their averages. Subplot b) number of mergers in the tidal-radius scenario, N_{tidal}, and ratio between number of such mergers per realization and maximum number of merger per realization, $N_{\mathrm{tidal}}/(N_{\mathrm{tot}}-1)$ together with their averages. Color-coding in the top diagrams for both a) and b) indicates different values of constant turbulent α parameter, while in the bottom diagrams for both a) and b) the color-coding relates to different levels of constant rotational β parameter.

Table 5.6: Overview of the setup averages for the touching radii scenario. From left to right: name of the setup, average number of close encounters per setup, $\langle N_{\mathrm{touch}} \rangle$, and setup average of the ratio between total number of close encounters per realization and maximum number of merger per realization, $\langle N_{\mathrm{touch}}/(N_{\mathrm{tot}} - 1) \rangle$. The standard deviations in both quantities are also listed.

Setup	Touching Radii	
	$\langle N_{\mathrm{touch}} \rangle$	$\langle N_{\mathrm{touch}}/(N_{\mathrm{tot}} - 1) \rangle$
$\beta 01$	6.6 ± 4.2	0.1692 ± 0.0763
$\beta 001$	8.6 ± 1.5	0.2671 ± 0.0534
$\alpha 025$	8.4 ± 3.4	0.1845 ± 0.0946
$\alpha 005$	7.6 ± 1.9	0.1477 ± 0.0441
$\alpha 025 \beta 01$	5.6 ± 4.4	0.1387 ± 0.0998
$\alpha 025 \beta 001$	7.6 ± 2.7	0.1604 ± 0.0525
$\alpha 005 \beta 01$	5.2 ± 2.1	0.1729 ± 0.0323
$\alpha 005 \beta 001$	7.4 ± 3.0	0.1534 ± 0.0523

Table 5.7: Overview of the setup averages for the tidal-radius scenario. From left to right: name of the setup, average number of close encounters per setup, $\langle N_{\mathrm{tidal}} \rangle$, and setup average of the ratio between total number of close encounters per realization and maximum number of merger per realization, $\langle N_{\mathrm{tidal}}/(N_{\mathrm{tot}} - 1) \rangle$. The standard deviations in both quantities are also listed.

Setup	Within r_{t}	
	$\langle N_{\mathrm{tidal}} \rangle$	$\langle N_{\mathrm{tidal}}/(N_{\mathrm{tot}} - 1) \rangle$
$\beta 01$	16.0 ± 6.8	0.4233 ± 0.1215
$\beta 001$	16.8 ± 3.0	0.5167 ± 0.0629
$\alpha 025$	21.6 ± 7.2	0.4431 ± 0.1370
$\alpha 005$	20.0 ± 3.0	0.3809 ± 0.0508
$\alpha 025 \beta 01$	14.0 ± 7.3	0.3688 ± 0.1492
$\alpha 025 \beta 001$	22.0 ± 4.7	0.4640 ± 0.0818
$\alpha 005 \beta 01$	10.2 ± 3.0	0.3541 ± 0.0429
$\alpha 005 \beta 001$	16.8 ± 4.4	0.3561 ± 0.0779

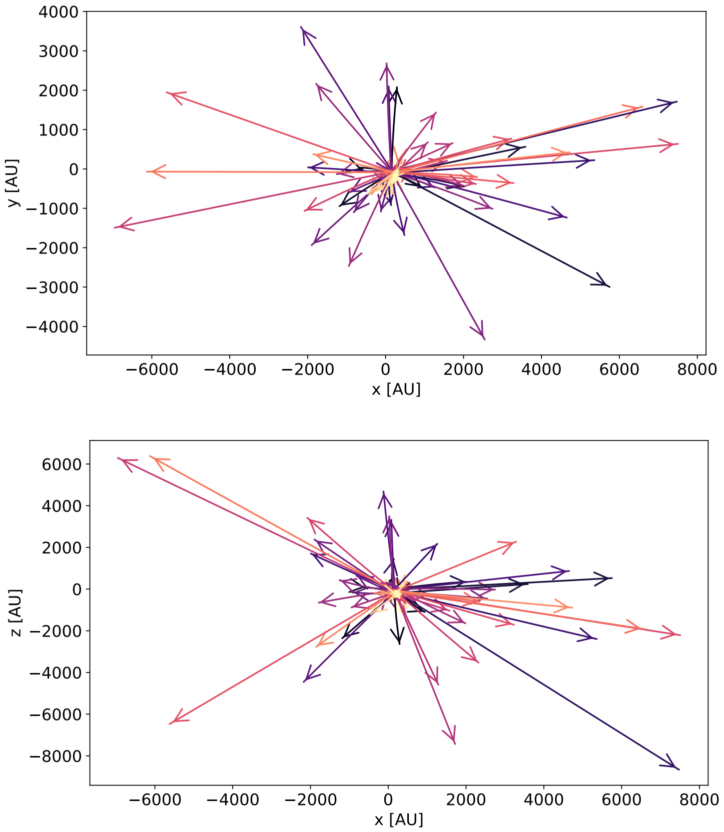

Figure 5.28: Trajectories of the 72 sinks of realization $\alpha025$-1. The figure is centered on the creation point of the first sink. The color scheme from dark to bright shades starting from black to violet to yellow indicates the formation order of the sinks with the darkest as the first sinks that formed. The arrows indicate the direction, in which the sink particle move.

icant variance in the values for each setup, it is unclear whether this represents a real difference or is merely a coincidence.

In summary, we find that close encounters that might lead to mergers occur in all realizations. Depending on what criterion we use for deciding whether two protostars will merge, we find that anywhere between $\sim 10\%$ and $\sim 50\%$ of protostars may merge, emphasising that mergers are common in the dense environment in which the protostars form. This result is consistent with other studies that find a high level of mergers between Pop. III protostars (e.g. Greif et al., 2012; Stacy et al., 2016).

5.3.8 Stellar ejections

Population III protostars that are ejected from their system of origin have been found in several previous simulations (e.g, Greif et al., 2011; Smith et al., 2011; Stacy & Bromm, 2013; Susa, 2013; Stacy et al., 2016). Of particular interest are those with masses of $M \lesssim 0.8\,\mathrm{M}_{\odot}$, as these stars will have lifetimes longer than the Hubble time and hence will survive until the present day, provided that they do not continue to accrete significantly more mass following their ejection (Greif et al., 2011).

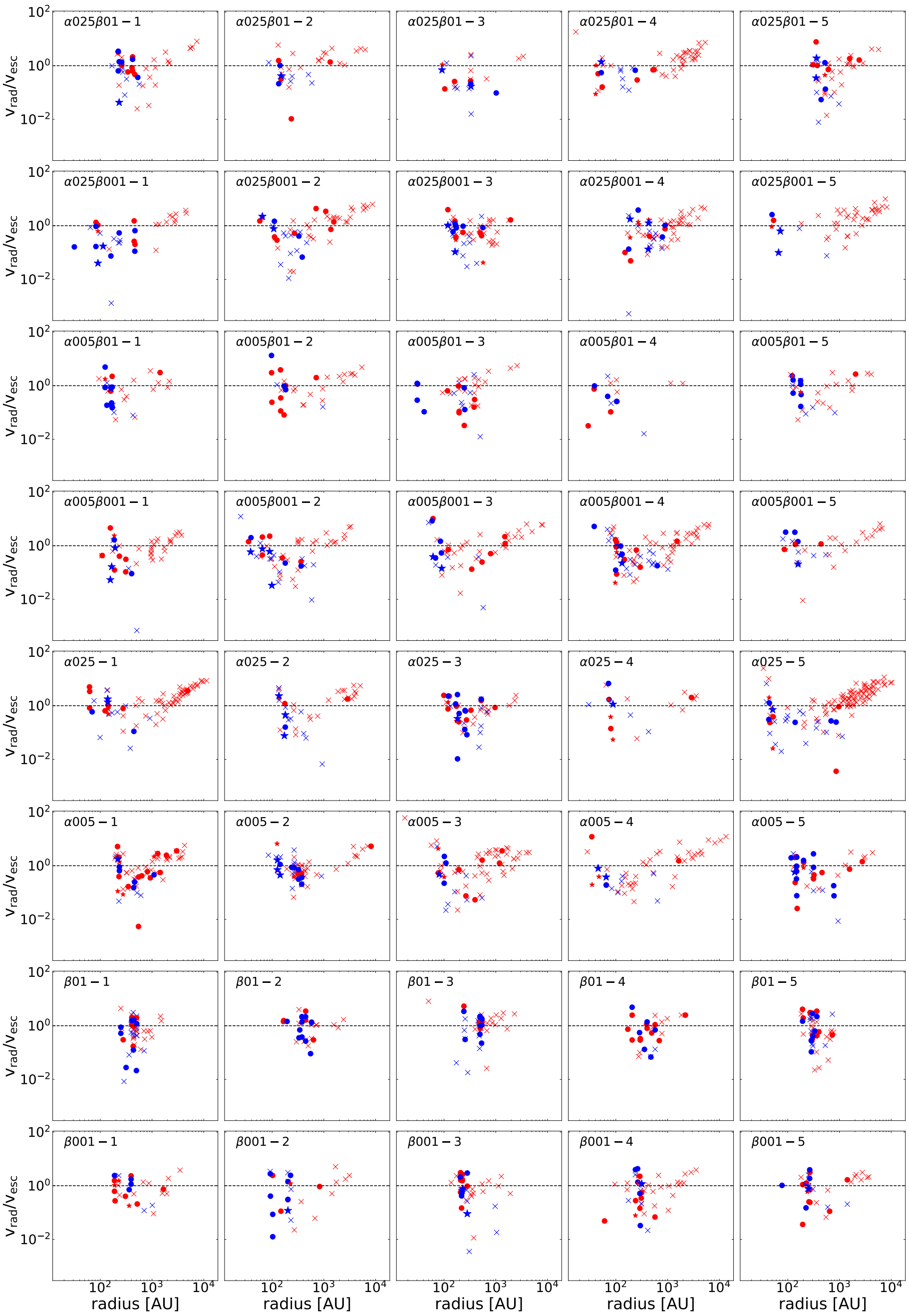

Figure 5.29: Ratio of the radial velocity to the escape velocity of all protostars as a function of distance to the center of mass at $t \sim 1000\,\mathrm{yr}$. Protostars with positive radial velocity are denoted by red symbols, whereas the blue symbols indicate protostars with negative radial velocity which move toward the center of mass. The black dashed line corresponds to $v_{\rm rad} = v_{\rm esc}$; protostars above this line are likely to escape from the system. Crosses, filled circles and stars denote protostars with masses less than $0.8\,\mathrm{M}_\odot$, between $0.8\,\mathrm{M}_\odot$ and $5\,\mathrm{M}_\odot$ and larger than $5\,\mathrm{M}_\odot$, respectively.

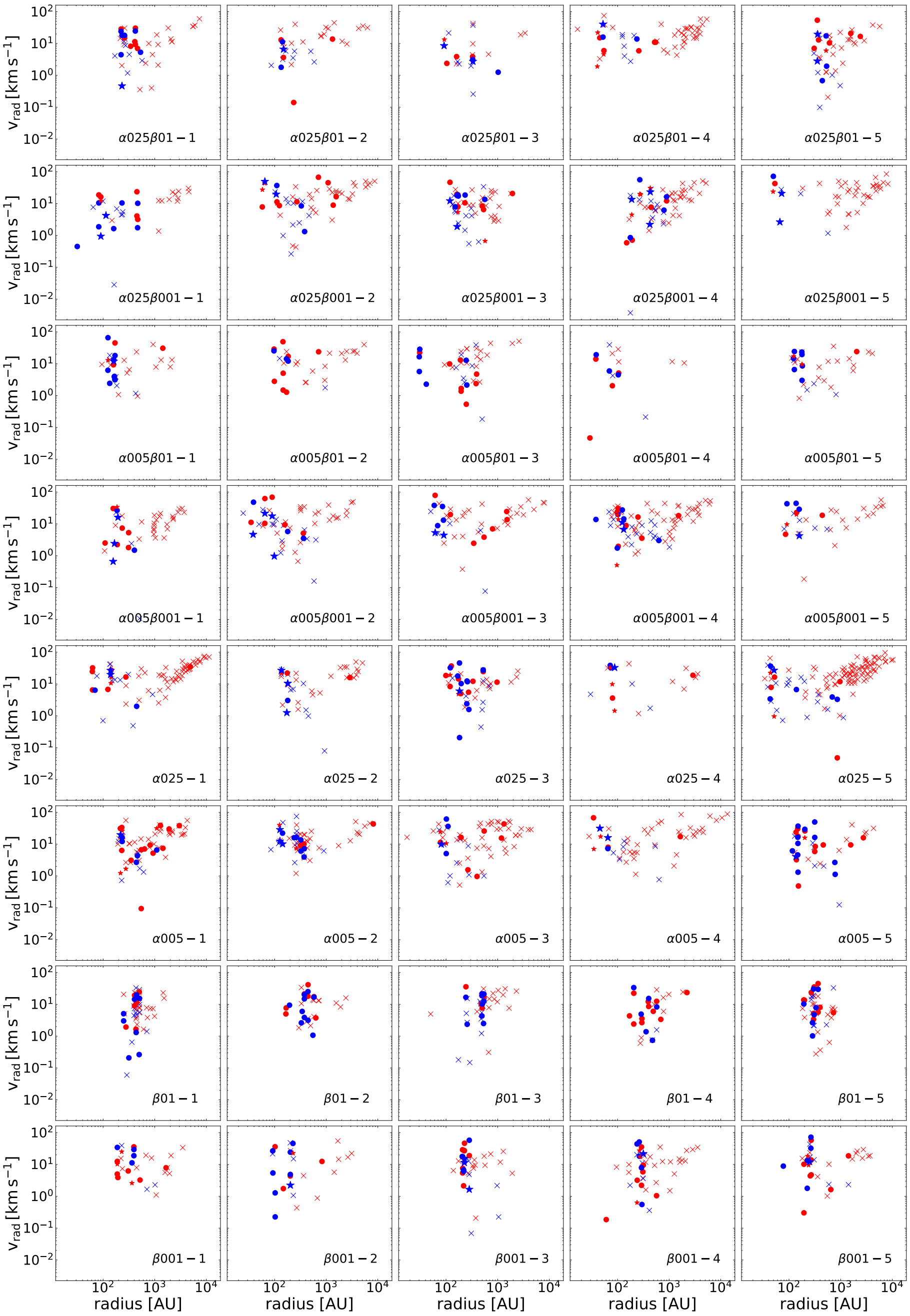

Figure 5.30: Radial velocities of all protostars as a function of distance to the center of mass at $t \sim 1000\,\mathrm{yr}$. Color scheme and symbols are the same as in Fig. 5.29.

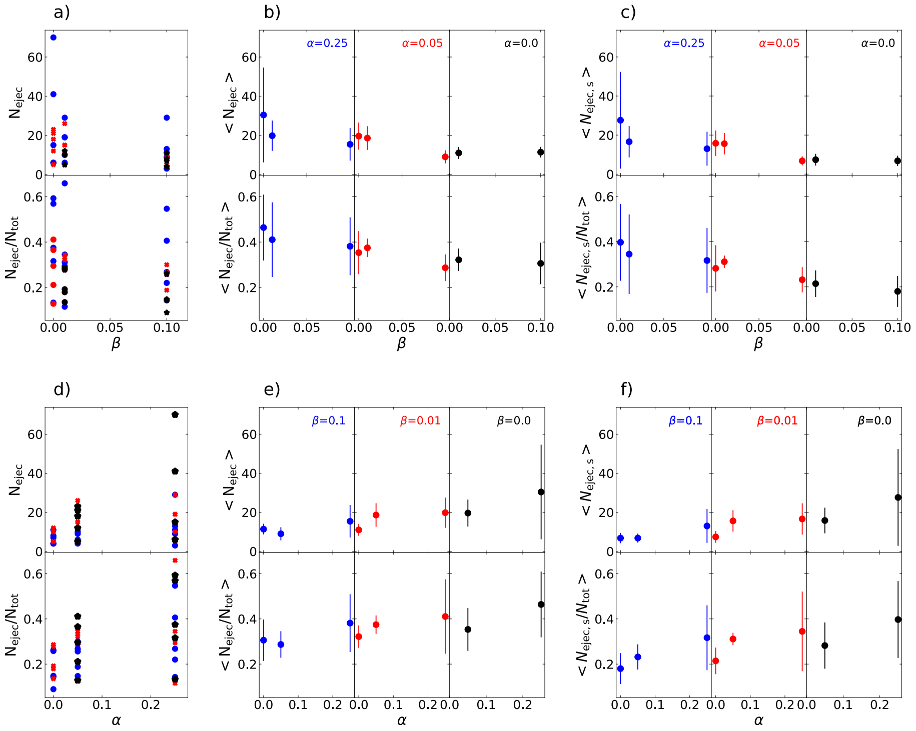

Figure 5.31: Panel a), d) and b), e): number of ejections, $N_{\rm ejec}$, and number of ejections per number of sinks formed, $N_{\rm ejec}/N_{\rm tot}$, together with their averages. Panel c) and f): as b) and e), but only for low-mass ejections ($M \leq 0.8\,{\rm M}_{\odot}$). The color-coding in panels a), b) and c) indicates the value of α, while in panels d), e), and f) it indicates the value of β.

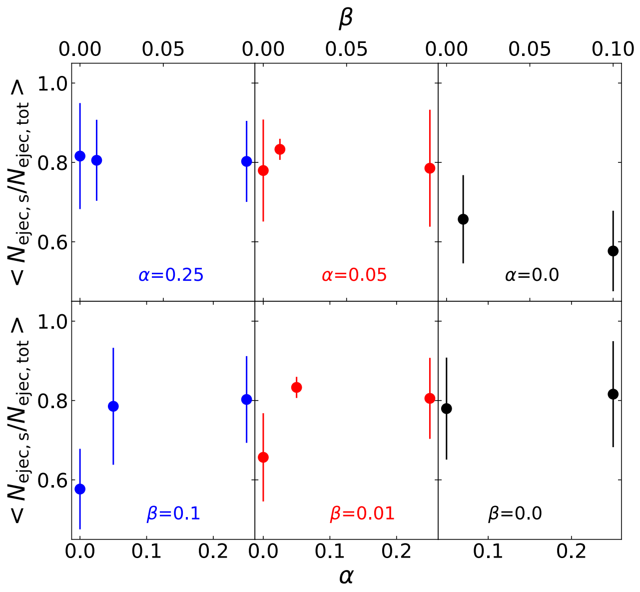

Figure 5.32: Average of the ratio between the number of low-mass sinks ejected and the total number of ejections, $\langle N_{\mathrm{ejec,s}}/N_{\mathrm{ejec,tot}}\rangle$, versus the rotational β parameter (top panels) and the turbulent α parameter (bottom panels).

In all realizations of our setups[10], even in those where only a few protostars form within the time considered, several protostars attain high enough velocities to escape from the system. In most cases, these protostars are primarily of low mass ($M \leq 0.8\,\mathrm{M}_{\odot}$).

In Fig. 5.28, we display the trajectories of all the 72 protostars of realization α025-1 relative to the position where the first sink was formed. As we see, during the ~ 1000 years covered by the simulation, some of the sinks move several thousand AU away from this location, i.e. are ejected.

Figure 5.29 gives an overview of all our realizations showing the ratio of the radial velocity of each sink to the escape velocity as a function of the distance from the center of mass (COM) of the halo. We compute the escape velocity using the expression

$$v_{\mathrm{esc}} = \sqrt{\frac{2GM_{\mathrm{enc}}}{r}}\ , \tag{5.5}$$

where r is the distance between the COM and the location of the sink particle in question, and $M_{\mathrm{enc}}(r)$ is the total mass in gas and sinks enclosed within this distance. Similar to Stacy & Bromm (2013) and Stacy et al. (2016), we derive the center of mass for all gas particles with $n > 10^{12}\,\mathrm{cm}^{-3}$ together with all sinks. We choose this density threshold as we want to consider the escape velocity from the gas within the protostellar disk environment only. We performed the computation for output snapshots at $t \sim 1000\,\mathrm{yr}$. The black dashed line indicates where $v_{\mathrm{rad}} = v_{\mathrm{esc}}$. Protostars above this line have velocities high enough to allow them to escape from the system.

The red symbols indicate protostars with positive radial velocities. Protostars with

---

[10] Since in the *pure infall* models only one object forms, no ejection through multiple-body interaction occurs.

Table 5.8: Overview of setup averages regarding the number of ejections. From left to right: name of the setup, total number of ejections, $\langle N_{\rm ejec} \rangle$, number of low-mass ejections, $\langle N_{\rm ejec,s} \rangle$, the ratio between the total number of ejections and the total number of sinks, $\langle N_{\rm ejec}/N_{\rm tot} \rangle$, the ratio between the total number of low-mass sinks and the total number of sinks, $\langle N_{\rm ejec,s}/N_{\rm tot} \rangle$, and the ratio between the total number of low-mass sinks and the total number of ejected sinks, $\langle N_{\rm ejec,s}/N_{\rm ejec,tot} \rangle$.

Setup	$\langle N_{\rm ejec} \rangle$	$\langle N_{\rm ejec,s} \rangle$	$\langle N_{\rm ejec}/N_{\rm tot} \rangle$	$\langle N_{\rm ejec,s}/N_{\rm tot} \rangle$	$\langle N_{\rm ejec,s}/N_{\rm ejec,tot} \rangle$
β01	11.4 ± 2.7	6.8 ± 2.6	0.306 ± 0.092	0.180 ± 0.069	0.577 ± 0.101
β001	11.0 ± 3.0	7.4 ± 3.0	0.322 ± 0.050	0.214 ± 0.059	0.657 ± 0.111
α025	30.4 ± 24.2	27.6 ± 24.8	0.464 ± 0.145	0.397 ± 0.170	0.816 ± 0.134
α005	19.6 ± 6.9	15.8 ± 6.6	0.353 ± 0.095	0.282 ± 0.102	0.780 ± 0.129
α025β01	15.4 ± 8.3	13.0 ± 8.7	0.381 ± 0.128	0.317 ± 0.143	0.803 ± 0.109
α025β001	19.8 ± 7.7	16.6 ± 8.0	0.411 ± 0.165	0.345 ± 0.176	0.805 ± 0.102
α005β01	9.0 ± 3.3	6.8 ± 2.3	0.287 ± 0.059	0.232 ± 0.056	0.785 ± 0.147
α005β001	18.6 ± 6.1	15.6 ± 5.5	0.375 ± 0.041	0.311 ± 0.027	0.833 ± 0.027

positive radial velocities and $v_{\rm rad} > v_{\rm esc}$ will generally not undergo any close encounters with other protostars as they move away from the dense central region and we can therefore be confident that they will indeed escape from the system. On the other hand, protostars with negative radial velocities (indicated by the blue symbols in Figure 5.29) have a much higher probability of undergoing further close encounters and so it is unclear whether inward moving protostars with $v_{\rm rad} > v_{\rm esc}$ will successfully escape from the system. In addition, we show in Fig. 5.30 an overview of the radial velocities of the sinks versus the distance of the sink from the center of mass at $t \sim 1000\,{\rm yr}$. Some sinks have radial velocities of up to $\sim 100\,{\rm km\,s^{-1}}$.

We first discuss individual realizations and consider both outward and inward moving protostars. In all simulations, there are low-mass protostars ($\leq 0.8\,{\rm M_\odot}$) with $|v_{\rm rad}/v_{\rm esc}| > 1$. For several of the runs this also holds for medium-mass protostars ($0.8\,{\rm M_\odot} < M \leq 5\,{\rm M_\odot}$). In 21 realizations, this condition is also fulfilled for high-mass objects ($> 5\,{\rm M_\odot}$). While the total number of individual objects that are likely to get ejected decreases when we only consider those with positive radial velocity, it remains the case that all of our runs have some low-mass ejections.

For our further analysis, we now solely concentrate on those protostars that have positive radial velocity and move outward from the center of mass as these are the ones most likely to escape the protostellar system. The average number of ejections per setup, $\langle N_{\rm ejec} \rangle$, follows a trend similar to that of the average total number of sinks formed. $\langle N_{\rm ejec} \rangle$ is higher for increasing turbulence and decreasing rotation. The difference between the effects of low and high rotation is slightly stronger than that for low and high turbulence. The average number of low-mass ejections per setup, $\langle N_{\rm ejec,s} \rangle$, resembles the behavior of $\langle N_{\rm ejec} \rangle$.

In Fig. 5.31, we plot $N_{\rm ejec}$ and $N_{\rm ejec}/N_{\rm tot}$ together with their average versus the α and β parameter (for the runs with positive radial velocity). The error bars again indicate the standard deviation from the average value. From the top and bottom panels of b) and e), we see that $\langle N_{\rm ejec} \rangle$ and $\langle N_{\rm ejec}/N_{\rm tot} \rangle$ describe the same trend. First, in b), the values are larger for non-zero turbulence. Second in e), the value are larger for low or zero rotation.

Looking right to left in the top/bottom panels of b) shows that, for constant turbulence, the values mostly decline from zero rotation to high rotation. For both properties the values for the purely rotational runs are about the same. When we look from left to right in the top/bottom panels of e), we see, for constant rotation, that there is an increase from zero turbulence to high turbulence. This trend is even clearer in the purely turbulent runs. This indicates that turbulence defines the outcome in mixed runs: the higher the level of turbulence and the lower the level of rotation, the more ejections occur. However, we also see that the scatter from run to run is much higher in the runs with high levels of turbulence than in the runs with low levels of turbulence.

In general, we find that between $\sim 30-45\%$ of the protostars formed per setup realization can leave their systems of origin, their protostellar disk. The detailed values are given in Table 5.8. Ejection rates of $\sim 30\%$ have also been found in previous studies of primordial star formation (e.g. Greif et al., 2011; Stacy & Bromm, 2013; Stacy et al., 2016) or in studies of present-day, low-mass star formation (e.g. Bate et al., 2003)

Fig. 5.31 also shows the average number of ejections and the average number of ejections per total number of sinks for only the low-mass ejected sinks, i.e. those with $M \leq 0.8\,\mathrm{M}_{\odot}$. As we have already discussed above, these low-mass sinks make up the largest fraction of all ejected sinks. It is therefore not surprising that we find essentially the same trends here as for the full sample: ejections become more common with increasing α and decreasing β, and the scatter between realizations also increases with increasing α.

In Fig. 5.33, we show the mass functions of the ejected protostars. We focus here on those with positive radial velocity. Once again, we see a large variety of mass function shapes when looking at the individual realizations. The combined mass functions per setup again have a top-heavy distribution. Interestingly, they still resemble their corresponding total mass functions in Fig. 5.24. As before, we note that these IMFs are only preliminary as we do not include merging sinks in our simulations. Still it is an interesting result that the IMF of the ejected protostars seems to resemble the total IMF. Such behavior could imply that not only low-mass Pop III survivors might be found in the outskirts of a halo or outside of it but that these regions might also harbor more massive Pop. III stars, potentially even ones massive enough to explode as supernovae.

We have also investigated whether the ejected protostars with $M \lesssim 0.8\,\mathrm{M}_{\odot}$ remain in this mass regime if they continue to accrete via Bondi-Hoyle accretion (Bondi & Hoyle, 1944; Bondi, 1952) on their way out of the protostellar system. The Bondi-Hoyle accretion rate can be written as

$$\dot{M}_{\mathrm{BH}} = 4\pi \frac{(GM)^2 \rho}{(c_{\mathrm{s}}^2 + v^2)^{3/2}}, \tag{5.6}$$

where G is the gravitational constant, M is the mass of the protostar, ρ is the local gas density, c_{s} is the corresponding local sound speed and v is the speed of the accreting protostar with respect to the surrounding gas.

To estimate $\dot{M}_{\mathrm{BH}}$ for each ejected protostar, we need to quantify how ρ and c_{s} vary as a function of position within the minihalo during the time it takes for the protostar to completely escape from the system. Since the time required for the protostar to escape is longer than the ~ 1000 yr modelled in our simulation, we assume that the state of the gas at the end of the simulation provides a reasonable guide to its state at $t \gg 1000$ yr. This is a poor assumption for the very dense gas in the disk, which has a short dynamical timescale, but is a much better approximation for the gas at distances $\gg 1000$ AU from the center of the halo, at least prior to the onset of strong stellar feedback.[11]

---

[11] Feedback in the form of ionizing radiation or supernova explosions will generally increase c_{s} and decrease ρ, thereby significantly reducing $\dot{M}_{\mathrm{BH}}$. Our estimates should therefore properly be regarded as upper limits.

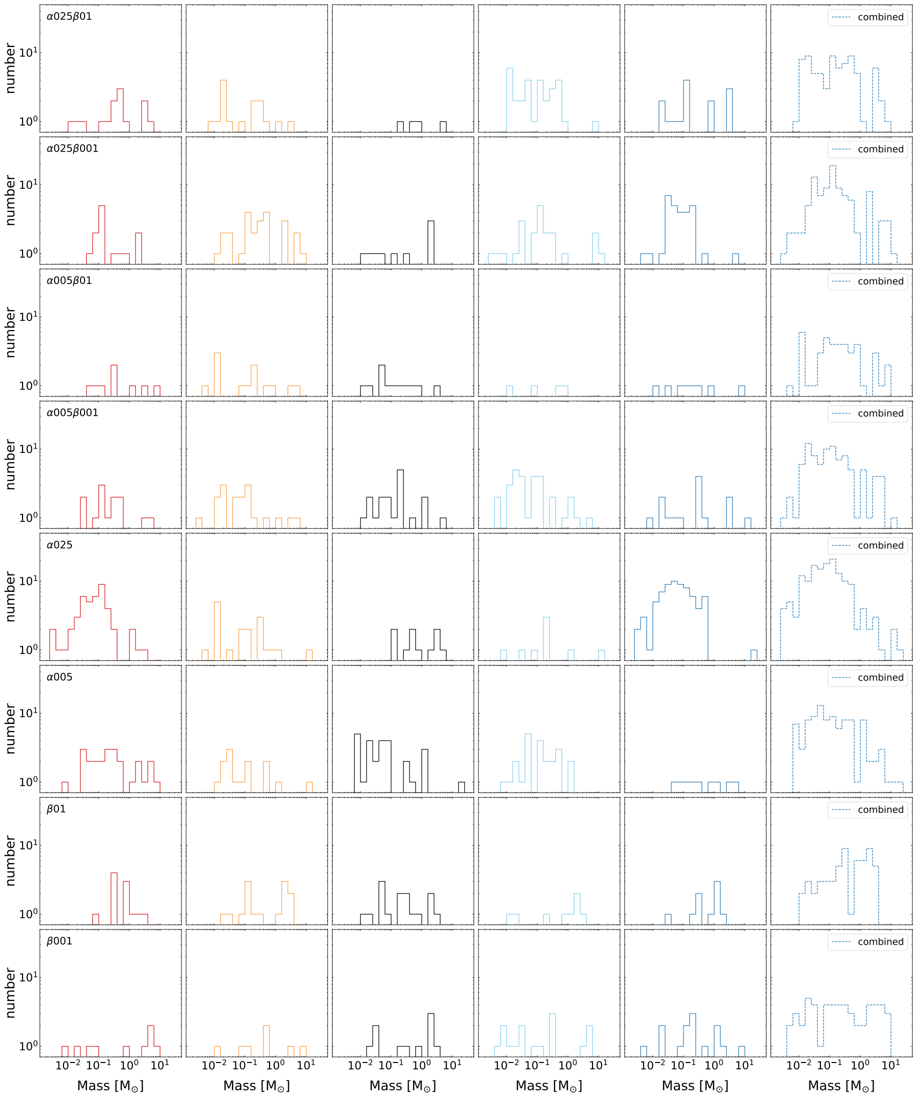

Figure 5.33: Mass functions for ejected sinks with positive radial velocities, shown for each realization of each setup. The final column shows the combined mass function for each setup.

Table 5.9: Number of ejected protostars that still have a mass $\leq 0.8\,\mathrm{M}_\odot$ after our Bondi-Hoyle accretion study: surviving sinks N_{surv}. Further given are total number of sinks found per realization, N_{tot}, number of ejected sinks that fulfill both $|v_{\mathrm{rad}}/v_{\mathrm{esc}} > 1|$ and $v_{\mathrm{rad}} > 0$, N_{ejec}, and the ratio of these two quantities with N_{surv}.

Realization	N_{tot}	N_{ejec}	N_{surv}	$N_{\mathrm{surv}}/N_{\mathrm{tot}}$	$N_{\mathrm{surv}}/N_{\mathrm{ejec}}$
$\beta01-1$	49	11	5	0.1020	0.4545
$\beta01-2$	31	14	7	0.2258	0.5000
$\beta01-3$	42	15	11	0.2619	0.7333
$\beta01-4$	27	8	4	0.1481	0.5000
$\beta01-5$	45	9	3	0.0667	0.3333
$\beta001-1$	28	9	4	0.1429	0.4444
$\beta001-2$	26	7	4	0.1538	0.5714
$\beta001-3$	37	10	5	0.1351	0.5000
$\beta001-4$	43	15	11	0.2558	0.7333
$\beta001-5$	35	14	9	0.2571	0.6429
$\alpha025-1$	72	45	41	0.5694	0.9111
$\alpha025-2$	40	18	15	0.3750	0.8333
$\alpha025-3$	45	10	5	0.1111	0.5000
$\alpha025-4$	19	8	6	0.3158	0.7500
$\alpha025-5$	118	71	70	0.5932	0.9859
$\alpha005-1$	61	25	18	0.2951	0.7200
$\alpha005-2$	57	14	12	0.2105	0.8571
$\alpha005-3$	63	27	23	0.3651	0.8519
$\alpha005-4$	51	23	21	0.4118	0.9130
$\alpha005-5$	39	9	5	0.1282	0.5556
$\alpha025\beta01-1$	41	14	11	0.2683	0.7857
$\alpha025\beta01-2$	32	15	13	0.4063	0.8667
$\alpha025\beta01-3$	21	4	3	0.1429	0.7500
$\alpha025\beta01-4$	53	30	29	0.5472	0.9667
$\alpha025\beta01-5$	41	14	9	0.2195	0.6429
$\alpha025\beta001-1$	34	13	10	0.2941	0.7692
$\alpha025\beta001-2$	55	25	19	0.3455	0.7600
$\alpha025\beta001-3$	52	9	6	0.1154	0.6667
$\alpha025\beta001-4$	61	22	19	0.3115	0.8636
$\alpha025\beta001-5$	44	30	29	0.6591	0.9667
$\alpha005\beta01-1$	34	8	5	0.1471	0.6250
$\alpha005\beta01-2$	30	14	9	0.3000	0.6429
$\alpha005\beta01-3$	39	11	10	0.2564	0.9091
$\alpha005\beta01-4$	15	4	3	0.2000	0.7500
$\alpha005\beta01-5$	32	8	6	0.1875	0.7500
$\alpha005\beta001-1$	40	13	11	0.2750	0.8462
$\alpha005\beta001-2$	53	18	15	0.2830	0.8333
$\alpha005\beta001-3$	45	18	15	0.3333	0.8333
$\alpha005\beta001-4$	81	30	26	0.3210	0.8667
$\alpha005\beta001-5$	32	14	11	0.3438	0.7857

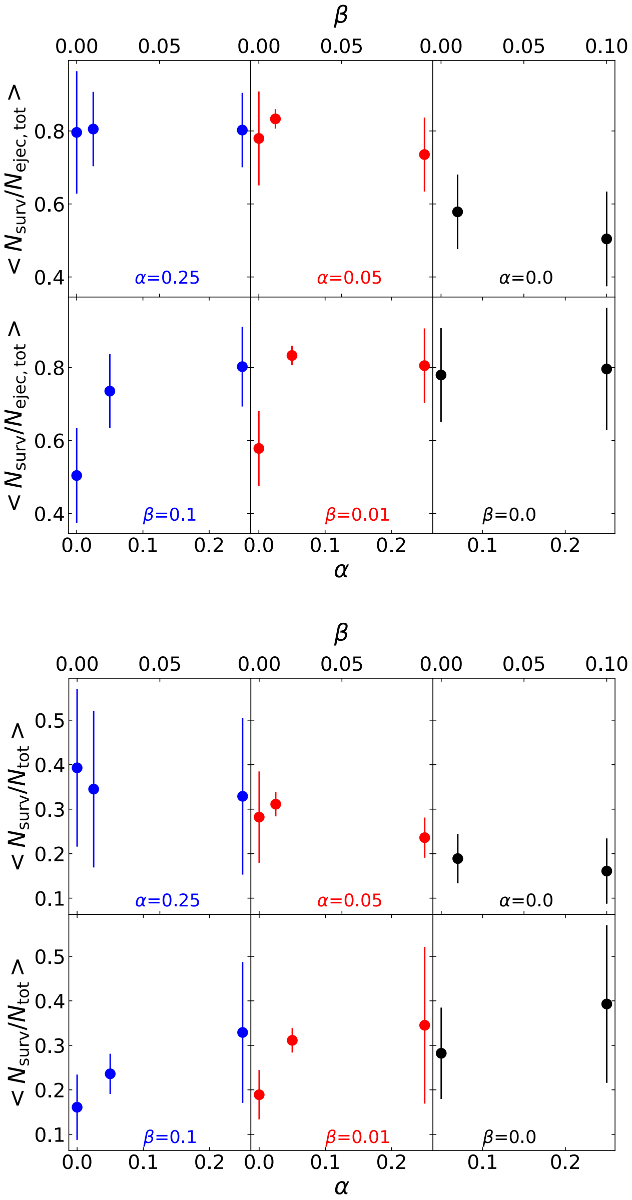

Figure 5.34: Average number of survivors both per total number of ejections, $\langle N_{\mathrm{surv}}/N_{\mathrm{ejec,tot}}\rangle$ (top plots) and average number of survivors per total number of created sinks (bottom plot) versus rotational β and turbulent α parameter. The colors and corresponding text at the bottom of each panel indicate different values of the parameter other than the one varied on the x-axis.

Table 5.10: Overview of setup averages of the survivor study. From left to right: name of the setup, number of survivors $\langle N_{\rm surv}\rangle$, the ratio between survivors and total number of sinks $\langle N_{\rm surv}/N_{\rm tot}\rangle$, and the ratio between survivors and total number of ejected sinks $\langle N_{\rm surv}/N_{\rm ejec,tot}\rangle$.

Setup	$\langle N_{\rm surv}\rangle$	$\langle N_{\rm surv}/N_{\rm tot}\rangle$	$\langle N_{\rm surv}/N_{\rm ejec,tot}\rangle$
β01	6.0 ± 2.8	0.1609 ± 0.0734	0.5042 ± 0.1298
β001	6.6 ± 2.9	0.1889 ± 0.0554	0.5784 ± 0.1023
α025	27.4 ± 25.0	0.3929 ± 0.1772	0.7961 ± 0.1676
α005	15.8 ± 6.6	0.2821 ± 0.1027	0.7795 ± 0.1287
α025β01	13.0 ± 8.7	0.3290 ± 0.1583	0.8024 ± 0.1092
α025β001	16.6 ± 8.0	0.3451 ± 0.1761	0.8052 ± 0.1020
α005β01	6.6 ± 2.6	0.2360 ± 0.0452	0.7354 ± 0.1013
α005β001	15.6 ± 5.5	0.3112 ± 0.0274	0.8330 ± 0.0266

We therefore take data from the final snapshot in each simulation, define a spherical coordinate system centered on the center of mass of the system and consisting of 39 logarithmically-spaced bins, and determine the mass-weighted average values of ρ and $c_{\rm s}$ in each bin. We typically find average sound speeds ranging between 1 to $4\,{\rm km\,s^{-1}}$ and average densities covering a wide range between $10^{-21}\,{\rm g\,cm^{-3}}$ and $10^{-9}\,{\rm g\,cm^{-3}}$. Furthermore, we take into account that the velocity of the protostar changes as it moves further outward. We derive an expression of the velocity as a function of bin i by assuming that the total energy of the protostar remains constant and that the protostellar mass does not change significantly as the protostar moves out of the halo:

$$v_{\rm i} = \sqrt{\frac{2\left(E_{\rm init} + \frac{G M_{\rm enc}(r_{\rm i}) M}{r_{\rm i}}\right)}{M}} \ . \tag{5.7}$$

Here, M is again the protostellar mass, $M_{\rm enc}(r_{\rm i})$ is the mass enclosed within distance $r_{\rm i}$ of the outer edge of bin i from the center of mass. $E_{\rm init}$ is the total energy of the protostar at $t \sim 1000\,{\rm yr}$:

$$E_{\rm init} = \frac{1}{2} M v_{\rm init}^2 - \frac{G M_{\rm enc}(r_{\rm init}) M}{r_{\rm init}} \ . \tag{5.8}$$

Here, $v_{\rm init}$ is the total velocity of the protostar at $t \sim 1000\,{\rm yr}$, $r_{\rm init}$ is the distance between the position of the protostar at that time and the center of mass, and $M_{\rm enc}(r_{\rm init})$ is the mass enclosed within this distance. Knowing the protostellar velocity in bin i together with the range $\Delta r_{\rm i}$ within the bin that the protostar has to cross, we can compute the time $\Delta t_{\rm i}$ the protostar stays within a particular bin and thus the time over which the protostar accretes mass with the Bondi-Hoyle accretion $M_{\rm BH,i}\,(\rho_{\rm i}, c_{\rm s,i}, v_{\rm i})$. We compute the mass growth until the protostar has reached a distance of $r_{\rm final} = 1\,{\rm pc}$ from the center of mass.

Our results are given in Fig. 5.34 and Table 5.9 & 5.10. In this Figure and Table, we examine how many of the ejected stars with initial masses $M < 0.8\,{\rm M_\odot}$ remain in this mass regime after accounting for Bondi-Hoyle accretion during their escape from the dense star-forming region. We term these stars “survivors”, as stars in this mass regime have lifetimes longer than the current age of the Universe and hence may have survived until the present day.

The results summarized in Fig. 5.34 and Table 5.10 demonstrate that a substantial number of the low mass ejected stars continue to have low masses even after accounting for ongoing accretion. We find that between 50 and 80% of the ejected sinks have masses below $0.8\,\mathrm{M}_{\odot}$ after accounting for accretion, corresponding to between 15 and 30% of the total number of sinks formed. The number of survivors shows a clear correlation with the turbulent α parameter, but this seems largely to reflect the fact that more low-mass sinks are injected in runs with high α than in the runs with $\alpha = 0$ (c.f. Figure 5.32) rather than indicating any difference in the effectiveness of accretion as a function of α.

We note also that the scatter from realization to realization is large in most cases. Nevertheless, in every case some low-mass survivors result (and more might be produced if we were to follow the evolution of the system for a longer period). Nevertheless, we stress that the results from this analysis should be treated with some degree of caution. Uncertainties arise due to our choice to represent the density and sound speed using radially averaged values and to neglect any further evolution of the gas distribution. A much more significant caveat is our lack of a sink merging method, as we discuss further in Section 5.4 below.

Finally, when computing the velocity of the ejected protostars at later times, we have assumed that the masses of the protostars do not change. Obviously, this assumption is violated to some extent, since all of the protostars continue to accrete at least a little gas. However, if the mass accreted is small, the change in v_i due to the change in mass of the protostar will also be small and hence our estimate of the mass growth should remain approximately valid. As a test of the assumption, we have therefore compared the mass growth during the Bondi-Hoyle accretion period to the original protostellar mass at $t \sim 1000\,\mathrm{yr}$. If the additional mass is more than half of the original mass, we say that the protostar has undergone significant mass growth, in which case our estimate of its final (post-accretion) mass will be a lower limit. We find that in two realizations of setups $\beta 01$ and $\alpha 005 \beta 01$, as well as in one realization of setups $\alpha 025$ and $\alpha 005$, one of the surviving protostars shows significant mass growth. In the rest of the realizations of these and all other setups, significant mass growth is only found for those protostars whose final mass is in any case $> 0.8\,\mathrm{M}_{\odot}$. We therefore can conclude that the numbers of surviving protostars we find, i.e. those protostars that have $M \lesssim 0.8\,\mathrm{M}_{\odot}$ even after continued Bondi-Hoyle accretion, give overall reasonably accurate estimates for our halos within the limits of our calculation.

So far, no single Pop III survivor has been observed in the Milky Way. The closest candidates are the most metal-poor stars found to-date by Keller et al. (2014) and Caffau et al. (2012). The observational search for low-mass Pop III survivors is difficult because of their low brightness. Interesting regions for this search are the Milky Way halo (e.g. Caffau et al., 2013; Keller et al., 2014) and nearby dwarf galaxies (e.g. Kirby et al., 2011; Frebel et al., 2014). A recent study by Magg et al. (2018) suggests that in particular the low-mass satellites of the Milky Way could be promising regions for the search for Pop III survivors as they are estimated to have a higher fraction compared to the Milky Way. Furthermore, semi-analytical models suggest that current surveys should be further extended to increase the probability of finding Pop III survivors (Hartwig et al., 2015a; Ishiyama et al., 2016).

5.4 Caveats

In the sections above, we have already mentioned a few of the caveats with our study. Here, we discuss some general limitations of our approach that should be addressed in future work.

A major uncertainty in our simulations arises due to lack of a sink merging method. Several previous studies have demonstrated that up to $\sim 60\%$ of the sinks undergo encounters that are close enough to plausibly lead to mergers (Greif et al., 2011; Greif et al., 2012; Stacy & Bromm, 2013; Stacy et al., 2016). In our study in Section 5.3.7, we also have found that close encounters between two sink particles happen sufficiently often that at least some of these encounters will likely lead to mergers. However, the number of sinks involved in mergers is highly sensitive to the criterion we use to determine whether two sink particles should merge. The two criteria we examine in Section 5.3.7 – direct physical collision and tidal capture – are both over-simplifications compared to the complicated and messy physics of real protostellar mergers. Therefore, although our results help to emphasize the importance of treating protostellar mergers in future studies of Pop. III star formation, doing so in a physically realistic fashion will not be easy.

With frequent mergers, the total number of sinks will be reduced, which will subsequently affect the overall dynamical interaction between the remaining sinks in a way which cannot be reliably accounted for by post-processing. Sinks may grow faster in mass, either directly due to mergers, or indirectly due to unimpeded accretion with high accretion rates as fewer sinks compete for the common mass reservoir. This may lead to a change in the shape of the mass function. Since the number of ejected protostars follows the behavior of the total number of sinks, it is likely that the number of ejections will decline as well.

Another shortcoming of our studies is our standard resolution of 16 cells per Jeans length. It has been shown in previous studies that the turbulent gas motions that arise during gravitational collapse of the gas cloud are only resolved with resolutions of 32 cells per Jeans length or higher (e.g. Greif et al., 2011; Greif et al., 2012). The actual amount of turbulence is therefore underestimated in our runs. We have performed a resolution study in which we re-ran the whole setup $\alpha005\beta001$ again with a resolution of 32 cells per Jeans length. As these simulations proceeded significantly more slowly than their low resolution counterparts, we stopped them earlier at $\sim 460\,\mathrm{yr}$ and compared the two samples at that time. The total mass in sinks is larger in all runs with the higher resolution. In four out of five realizations, we furthermore find a larger number of fragments. As disk fragmentation is a chaotic process and is additionally complicated when turbulent velocity fields are included, it is thus unpredictable when fragmentation happens and how many sinks exactly form. It can very well be that by the end of the simulation, all run of the higher resolution sample will have a higher total number of sinks compared to their low resolution counterparts. This again demonstrates the importance of considering a sample of realizations instead of just a single run in order to be able to derive general trends in simulations that include turbulence. It also emphasizes that the number of sinks formed in these simulations should be treated with a great degree of caution: it is far more sensitive to small changes in the physical or numerical setup of the simulations than quantities such as the total mass of gas accreted or the fraction of sinks that are ejected.

Finally, all of the simulations carried out in this study assume purely hydrodynamical flow and neglect the effects of magnetic fields. This is a common approximation in the study of Pop. III star formation, but the accuracy of this approximation is uncertain. Primordial magnetic seed fields can be generated early in the history of the Universe, e.g. by early Universe phase transitions (Sigl et al., 1997) or the Biermann battery mechanism (Biermann, 1950; Xu et al., 2008). These seed fields are extremely weak ($B = 10^{-30}$–$10^{-18}\,\mathrm{G}$), but can be efficiently amplified to $B \sim 10^{-5}\,\mathrm{G}$ or more through the action of the small-scale turbulent dynamo (Kazantsev, 1968; Schleicher et al., 2010; Sur et al., 2010; Schober et al., 2012) that is driven through turbulent motions arising during the initial collapse of the gas. The impact of this field on the physics of the Pop. III accretion disk remains largely unexplored. Ordered magnetic fields could provide efficient magnetic braking, enabling faster inflow of gas from the accretion disk onto the central protostar, and reducing or completely suppressing fragmentation (Hennebelle & Ciardi, 2009; Seifried et al., 2011; Machida & Doi, 2013; Peters et al., 2014). However, the field produced by the turbulent dynamo is initially highly disordered, and hence may have much less impact initially. Although our simulations are unable to address this, they do provide a context for assessing whether the fragmentation behaviour found in future simulations that do include the magnetic field differs from the hydrodynamical case in a statistically significant fashion, or whether it falls within the range of outcomes found in purely hydrodynamical runs.

5.5 Conclusion

We have presented a statistical analysis of an ensemble of 3D simulations of Population III.1. star formation under the influence of different levels of rotation ($\beta = 0.01$, $\beta = 0.1$) and subsonic turbulence ($\alpha = 0.05$, $\alpha = 0.25$). The simulations have been performed with the Voronoi moving-mesh code AREPO whose quasi-Lagrangian nature makes it an ideal code to study gas collapse. Our version of AREPO includes an updated and self-consistent primordial chemistry network together with a treatment for a variable adiabatic index and accretion luminosity heating. We follow the collapse of a primordial Bonnor-Ebert sphere until the formation of the first protostar and the creation of highly gravitationally unstable protostellar disk system that subsequently fragments and evolves into a Population III protostellar cluster. Individual protostars that collapse beyond our resolution limit are represented using sink particles. In order to examine the evolution of this cluster, we continue to follow the interactions between the protostars for $1000\,\mathrm{yr}$ after the formation of the first protostar. For each combination of initial conditions, we have run five realizations which vary either in the random number seed used to initialize the turbulent velocity field or the cell configuration of the Voronoi mesh in runs without turbulence.

We find very significant scatter in the results of the individual realizations of setups including turbulence. Our results demonstrate that in order to find general trends in simulations including turbulence, one should always consider a sample of realizations instead of only a single run. The scatter is generally much smaller for the simulations without turbulence but the numerical noise which is introduced by the variations in the initial cell configuration onto which the Bonnor-Ebert profile is initialized, is still enough to produce different fragmentation outcomes.

The main results of the various quantities of our analysis can be summarized as follows.

1. Fragmentation of the protostellar disk occurs in all our setups except the *pure infall* runs, i.e. those with no initial rotation or turbulence. There, only one protostar forms over the whole course of the simulation. On average, the amount of fragmentation is larger in runs including turbulence. In mixed runs that include both bulk rotation and turbulence, the higher the level of rotation is, the more stable the protostellar disk system becomes against fragmentation.

2. Within the $1000\,\mathrm{yr}$, the cumulative accretion rate generally remains high of the order of $\dot{M} \sim 10^{-2} - 10^{-1}\,\mathrm{M}_{\odot}\,\mathrm{yr}^{-1}$. There is only a small scatter in the accretion

histories of the different setups. Runs including turbulence show a more strongly variable cumulative accretion rate. The overall small difference between the setups is in agreement with the idea that the density and temperature of the infalling material are primarily responsible for the size of the accretion rate rather than the level of turbulence and rotation.

3. The mass function covers a large range of masses from a few $10^{-3}\,\mathrm{M}_{\odot}$ to several tens of solar masses for all runs. Its shape is fairly flat for simulations including turbulence, i.e. overall indicating top-heavy distributions as already observed in previous studies of Population III star formation (e.g. Greif et al., 2011; Clark et al., 2011a; Susa et al., 2014; Stacy et al., 2016). In contrast, the purely rotational runs lead to a completely different distribution with fewer fragments in the low-mass regime and much more towards the high-mass end.

4. Between $\sim 30-45\%$ of all protostars that form in each run get ejected from their system of origin over the course of the simulation. This number is similar to what has been found in previous simulations of Population III star formation (Greif et al., 2011; Stacy & Bromm, 2013; Stacy et al., 2016). The mass functions of the ejected protostars still resemble the total mass functions. The average number of ejections follows the trend of the average total number of protostars: it is higher for increasing level of turbulence and decreasing level of rotation.

5. Most of the ejected protostars, namely on average between $\sim 20-40\%$ of the total number per setup, have a mass of $M < 0.8\,\mathrm{M}_{\odot}$. We find that even under assumption of continued accretion via the Bondi-Hoyle modus, between $\sim 50-80\%$ of all ejected protostars, that is $\sim 15-40\%$ of the total number per setup, still remain in this small-mass regime. This means that they are promising candidates of Population III stars that could have survived until today (Yoshida et al., 2006; Greif et al., 2011).

We note that the exact shape of the mass function and the corresponding quantities, such as absolute number of ejections, would possibly change if we were to account for protostellar mergers, which are likely to be common in these dense clusters. We intend to address this issue in future work. It would also be interesting to explore how the system continues to evolve at times much greater than 1000 yr, but to do this it will be necessary to include a treatment of ionizing and photodissociating radiation from massive Pop. III stars, which will star to become important at these times (see e.g. Susa et al., 2014; Stacy et al., 2016).

CHAPTER 6

The fragmentation behavior of Population III protostellar disks: resolution study

The content in Section 6.4.3 will be partially included in the publication Wollenberg, K. M. J., Glover, S. C. O., Clark, P. C., Klessen, R. S., *"The Fragmentation Behavior of Population III Protostellar Disks - Part I"*, MNRAS 2019 (*in prep.*). I performed and analyzed the simulations described in this chapter and wrote the text. All figures below were also created by me. Simon C. O. Glover contributed useful ideas and comments on the structure of this chapter.

6.1 Motivation

The simulations in this chapter have been conducted to test the robustness of the results presented in Chapter 5 against variations in the two main conditions that introduce restrictions in the numerical resolution: the Jeans resolution criterion and the sink particle method, more precisely the sink particle accretion radius. For the runs in Chapter 5 we employed a resolution of 16 cells per Jeans length and a sink particle accretion radius of $r_{\rm acc} = 2\,\mathrm{AU}$. We used this combination as it allowed a numerically feasible, time-efficient yet physically and numerically accurately enough study of our large ensemble of simulations.

The Jeans resolution criterion by Truelove et al. (1997) ensures that the local Jeans length is always resolved by a certain number of cells to avoid 'artificial fragmentation'. As a consequence of the discretization of the equations of self-gravitational hydrodynamics in multi-grid codes, small perturbations in the gas can occur during gas collapse that may become larger than the local Jeans length within a few cells. Those cells may separate each other from the behavior of the rest of the gas structure resulting in unphysical fragmentation of it. In order to prevent this scenario from happening, the Jeans length should be resolved by a minimum number of cells which is four cells in the original case of isothermal gas (Truelove et al., 1997) and at least eight cells for a variable equation of state (e.g. Turk et al., 2012). Moreover, it has been found that turbulent gas motions arising during gravitational collapse are only resolved for ≥ 32 cells per Jeans length (e.g. Federrath et al., 2011b; Greif et al., 2012). Since we use only 16 cells per Jeans length for our simulations, we need to check how our findings may be affected by a higher number of cells.

The second restriction in our numerical resolution that we are going to examine in this chapter is the size of the sink particle accretion radius. Sink particles have been introduced to avoid the problem that numerical computations become infeasible when the hydrodynamical time steps become extremely small (of the order of seconds and below) as the code follows the evolution of gas collapse to protostellar densities. This problem can be circumvented by replacing gravitationally bound, collapsing gas fragments with collisionless, non-gaseous particles of the same mass (Bate et al., 1995). These sink particles or sinks can continue to grow in mass via accretion and interact with their environment gravitationally. In this way, a collapsing gas cloud can be followed beyond the formation of protostellar fragments without too much numerical cost, and both its large-scale evolution as well as the small-scale interaction of individual sinks can be studied. A sink has an accretion radius that regulates the region of influence around it from which it takes up material for its mass growth. The behavior of the gas itself, e.g. possible fragmentation within this region is not resolved. In simulations of Population III star formation without the use of sink particles, it has been found by Greif et al. (2012) that fragmentation of the protostellar disk occurs down to the surface of the protostar. With a newly formed Pop III protostar having a radius of $\sim 10\,\mathrm{R}_\odot \sim 0.05\,\mathrm{AU}$ and with us employing a sink accretion radius of $r_\mathrm{acc} = 2\,\mathrm{AU}$, we are very likely to underestimate fragmentation within our runs. Because of this, we need to test the influence a smaller sink accretion radius may have on the outcomes of the study in Chapter 5.

In the following sections, we therefore analyze and discuss whether, where and how strongly these two conditions affect the results presented in Chapter 5. The tests we consider are

1. Varying the accretion radius of the sink particle, i.e. 0.5, 1, and 2 AU (at constant 8 cells per Jeans length), and

2. Varying the Jeans resolution, i.e. 8, 16, and 32 cells per Jeans length (at constant sink accretion radius of 2 AU).

We perform three test series. In the first and second one, we examine 1. and 2. with simulations of the collapse a rigidly rotating Bonnor-Ebert sphere. In addition, we conduct a third test series by increasing the Jeans resolution of one of our mixed setups of Chapter 5 to 32 cells per Jeans length. We include this third test because we try to understand whether the additional turbulent motions, which arise during gravitational collapse and which are only resolved for a resolution of ≥ 32 cells per Jeans length, influence the initial, pre-defined turbulence and how this might affect the outcome and conclusion we have found in Chapter 5.

In our tests, we examine effects on the gas cloud structure just before sink formation, the disk properties directly after sink formation, the time of first sink formation, the evolution of total number of sinks and total mass in sinks, the mass function and the accretion histories. As we have already described and discussed details of the physics of these aforementioned stages in the Population III star formation procedure in Chapter 5 and Section 2.5.1, we refrain from repeating this here and only mention and discuss physical details in special cases and where appropriate for the understanding of our analysis.

This chapter is structured as follows: the numerical method and the initial conditions are explained in Section 6.2.2. In Section 6.3, we present our results on the study with varying accretion radius. After this, in Section 6.4, we go through the results for varying the Jeans resolutions in purely rotational and mixed runs.

Table 6.1: Overview of the test setups.

Setup	$N_{\rm real}$	cells / $\lambda_{\rm J}$	r$_{\rm acc}$ [AU]	$n_{\rm thresh}$ $[\rm cm^{-3}]$	α	β	$v_{\rm rms}$ $[\rm km\,s^{-1}]$	Ω_0 $[\rm s^{-1}]$
05AUracc	1	8	0.5	2×10^{16}	-	0.04	-	1.4×10^{-14}
1AUracc	1	8	1	4×10^{15}	-	0.04	-	1.4×10^{-14}
2AUracc	1	8	2	1×10^{15}	-	0.04	-	1.4×10^{-14}
8Jeans	1	8	2	1×10^{15}	-	0.04	-	1.4×10^{-14}
16Jeans	1	16	2	1×10^{15}	-	0.04	-	1.4×10^{-14}
32Jeans	1	32	2	1×10^{15}	-	0.04	-	1.4×10^{-14}
$\alpha005\beta001$	5	16	2	1×10^{15}	0.05	0.01	0.5	9.8×10^{-15}
$\alpha005\beta001$	5	32	2	1×10^{15}	0.05	0.01	0.5	9.8×10^{-15}

6.2 Method

6.2.1 Numerical approach

For our simulations here, we employ the same AREPO setup as in Chapter 5. We use a variety of threshold densities for sink creation and accretion radii. The specific details for each setup are listed in Table 6.1.

The studies are simulated in a box with sidelength of 13 pc and reflective boundary conditions. In the beginning, the mesh within the box consists of 128^3 cells and is evolved under the Jeans (de-)refinement criterion that ensures that the Jeans length is resolved by a specific number of cells. For our test runs we employ several different numbers of cells for the Jeans criterion. The individual choice per setup is listed in the third column of Table 6.1.

6.2.2 Initial conditions

We assume a redshift of $z = 20$ for our studies. The exact value should not be particularly important as the gas in our simulations is always warmer than the cosmic microwave background and is not strongly affected by Compton cooling. The initial conditions here are the same as in Chapter 5. Deviations from that are described in the following two subsections.

Bonnor-Ebert sphere setup for purely rotational runs

For the runs discussed in Section 6.3 and 6.4.1, we use a BE sphere of mass $\rm M_{BE} = 1418\,M_{\odot}$ and radius $\rm R_{BE} = 1.87\,pc$ which corresponds to a nondimensional radius of $\xi_{\rm BE} = 6.5$. The density is not enhanced, so $f = 1$ and the initial central density of the sphere is $\rho_c = \rho_{\rm BE}(0) \simeq 2.0\times10^{-20}\,\rm g\,cm^{-3}$ ($n \sim 10^4\,\rm cm^{-3}$). The surrounding of the sphere is filled with a uniformly dense gas with $\rho_{\rm ext} = \rho_{\rm BE}(R_{\rm BE}) \simeq 1.4\times10^{-21}\,\rm g\,cm^{-3}$ ($n_{\rm ext} \sim 7\times10^2\,\rm cm^{-3}$). The initial temperature is inside and outside the BE sphere the same: $T_{\rm BE} = T_{\rm ext} = 200\,\rm K$. This yields an adiabatic sound speed of $c_{\rm s} = 1.93\,\rm km\,s^{-1}$ with an initial adiabatic index of $\gamma = 5/3$ (isothermal sound speed: $c_{\rm s,iso} = 1.16\,\rm km\,s^{-1}$). In these two test setups, the sphere is given a rigid rotation around the z-axis. The rotation is defined by $\beta = 0.04$ which corresponds to an angular

Table 6.2: Impact of varying the sink accretion radius.

Setup	$t_{\rm SF}$/Myr	$t_{\rm final}$/yr	$N_{\rm tot}$	$M_{\rm tot}/M_\odot$
05AUracc	1.441435	1009	102	43.1
1AUracc	1.441435	1010	32	48.6
2AUracc	1.441435	1003	41	44.3

frequency of $\Omega_0 = 1.4 \times 10^{-14}\,{\rm s}^{-1}$. For our chosen parameter set, the ratio between thermal and gravitational energy of our sphere is $\alpha_{\rm therm} = E_{\rm therm}/|E_{\rm grav}| \simeq 0.85$.

In the first test series with these physical parameters presented in Section 6.3, we conduct three simulations with a constant Jeans resolution of 8 cell per Jeans length and a sink accretion radius of $r_{\rm acc} = 0.5, 1,$ and 2 AU respectively.

In the three runs of the second test series described in Section 6.4.1, the sink accretion radius is held constant $r_{\rm acc} = 2\,{\rm AU}$, while the Jeans resolution is either 8, 16 or 32 cells per Jeans length respectively.

Table 6.1 contains a summary of the properties specific for each test run together with the choice of accretion radius and Jeans resolution.

Bonnor-Ebert sphere setup for mixed runs

The properties for the third test series with the runs including both rotation and turbulence (mixed runs) in Section 6.4.3 are the same as already described in Section 5.2.2 above. For completeness, we recap the most relevant points here. We consider a BE sphere of mass $\rm M_{BE} = 2671\,M_\odot$ and radius $\rm R_{BE} = 1.87\,pc$. The density of the BE sphere is enhanced by a factor $f = 1.83$ here. This yields a central mass density of $\rho_c = f \times \rho_{\rm BE}(0) \simeq 3.7 \times 10^{-20}\,{\rm g\,cm^{-3}}$ ($n_c \simeq 1.83 \times 10^4\,{\rm cm^{-3}}$). In the mixed runs, the sphere is located within in a uniformly dense environment, of which the density is $\rho_{\rm ext} = \rho_{\rm BE}(R_{\rm BE}) \simeq 2.7 \times 10^{-21}\,{\rm g\,cm^{-3}}$ ($n_{\rm ext} \simeq 1.31 \times 10^3\,{\rm cm^{-3}}$). The internal and external temperatures are again the same and set to $T_{\rm BE} = T_{\rm ext} = 200\,{\rm K}$. The rigid rotation in the mixed runs is described by $\beta = 0.01$ and $\Omega_0 = 9.8 \times 10^{-15}\,{\rm s}^{-1}$. In addition, we add a non-driven, subsonic turbulent velocity component with a power spectrum of $P(k) \propto k^{-4}$ to the BE sphere. The field is described by the turbulent α parameter where $\alpha = E_{\rm turb}/|E_{\rm grav}|$. For our test, we use $\alpha = 0.05$. Since we have enhanced the central density here, we find that $\alpha_{\rm therm} = E_{\rm therm}/|E_{\rm grav}| \simeq 0.451$ is smaller than for the other two test runs. This choice was made in the first place to ensure that our BE sphere would still collapse in the presence of both a high degree of rotation and turbulence (see also Section 5.2.2). We consider two different resolutions: 16 and 32 cells per Jeans length. For each, we carry out 5 realizations. The realizations differ in the initial random seed used to model the turbulent velocity field. In all 10 realization, a sink accretion radius of $r_{\rm acc} = 2\,{\rm AU}$ is used. See Table 6.1 for a summary of the parameters.

6.3 Effects of varying sink particle accretion radius

In Section 6.3.1, the results of the comparison of the three test runs with different sink particle accretion radii are presented. A short summary is given in Section 6.3.2.

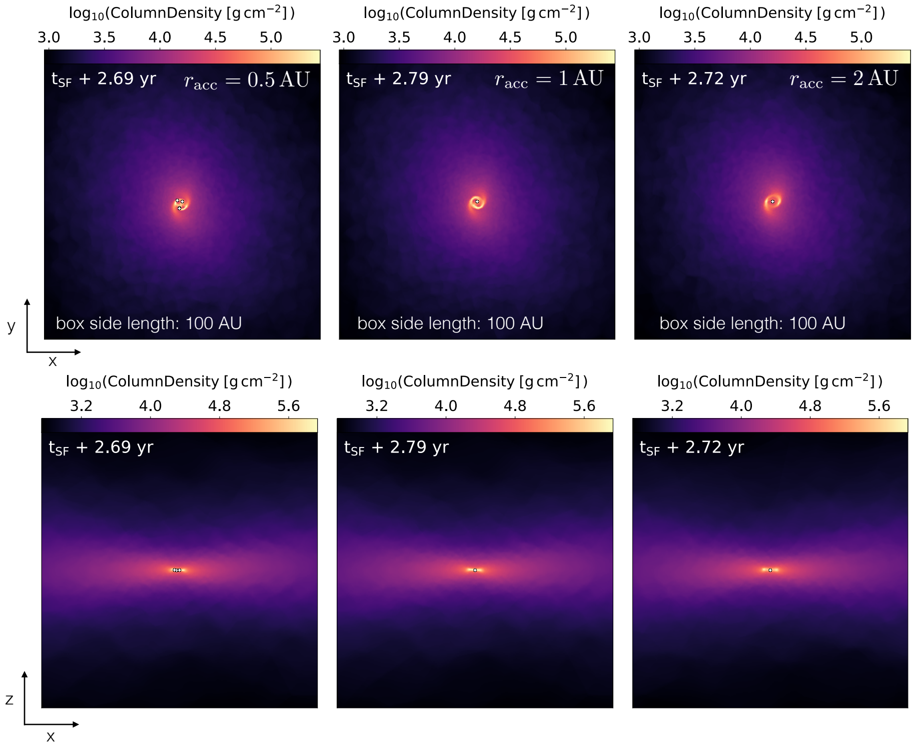

Figure 6.1: Column density projections just after the first sink particles have formed. In the two plots on the left which display the column density for setup *05AUracc*, already 4 sinks have formed. The projections are centered on the first sink.

6.3.1 Results

Effects of different accretion radii only start to become relevant once the first sink particle has formed. We therefore begin the presentation of our analysis at the time of first sink formation. For completeness, we add a plot of radially averaged profiles of gas cloud properties prior to first sink formation in Fig. 10.19 in Appendix 10.3.

Time of first sink formation

In all three test runs the first sink forms at exactly the same time, $t_{\rm SF} = 1.441435\,{\rm Myr}$. The small differences in their sink formation threshold densities do not affect the moment of sink formation much as the free-fall time at $n \gtrsim 10^{15}\,{\rm cm}^{-3}$ is $t_{\rm ff} \lesssim 1.1\,{\rm yr}$.

Compared to the free-fall time of the initial central density of the BE sphere which is $\rho_c = 2.0 \times 10^{-20}\,{\rm g\,cm}^{-3}$ yielding $t_{\rm ff} \approx 0.47\,{\rm Myr}$, the time of first sink formation is delayed substantially. This is due to the non-negligible thermal pressure support in the BE sphere as can be seen from the ratio between thermal and gravitational energy which is $\alpha_{\rm therm} = E_{\rm therm}/|E_{\rm grav}| \approx 0.854$.

Disk structure

The initial rigid rotation of the BE sphere with $\beta = 0.04$ induces a non-zero angular momentum in the collapsing cloud which is roughly conserved during the collapse

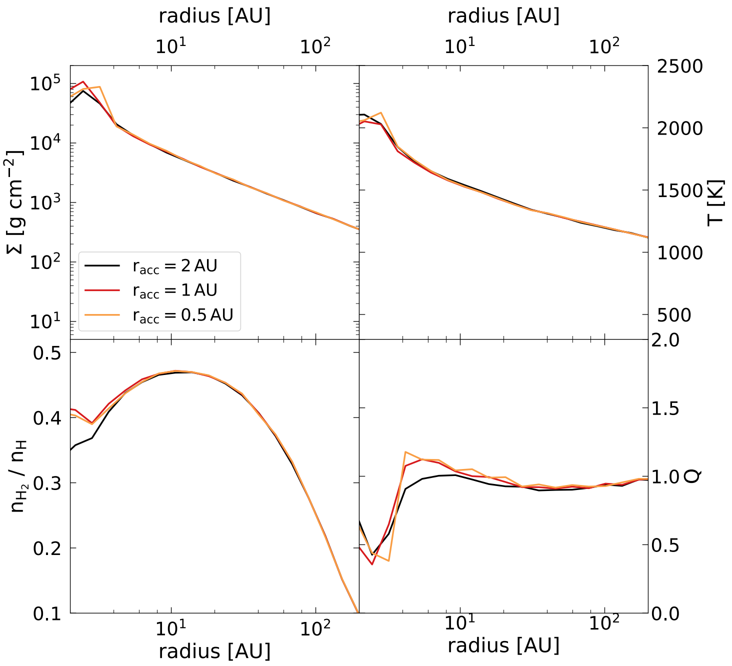

Figure 6.2: The differences between the test runs with different sink accretion radii appear mostly close to the first sink. From top left to bottom right: disk surface density Σ, temperature, T, H_2 fraction, n_{H_2}/n_H, and Toomre parameter, Q. The values are derived from mass-weighted averages within spherical shells centered on the first sink. In order to track the gas at disk densities, only gas cells with $n > 10^9\,\mathrm{cm}^{-3}$ have been considered here.

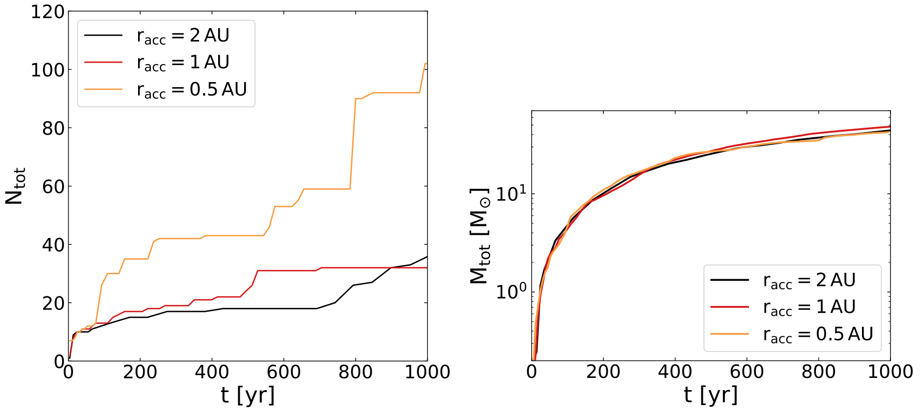

Figure 6.3: Left panel: evolution of total number of sinks. Right panel: evolution of total mass in sinks.

leading to the formation of a protostellar disk within which the gas angular momentum is redistributed.

The radially averaged profiles of disk surface density, Σ, temperature, T, and molecular H_2 fraction, n_{H_2}/n_H in Fig. 6.2 are very similar between the three different realizations. The main differences appear within a few AU close to the first sink. The largest local variations are in the Toomre parameter which still shows a overall similar trend for all three runs: the disk is highly self-gravitating until $\sim 2\,$AU distance from the accretion radius of the first sink. Closer than that the Toomre-Q suddenly drops to $Q < 1$ indicating an unstable disk region in the immediate surrounding of the sink. Indeed in setup *05AUracc*, 4 sink particle have already formed within $\sim 3\,$yr after first sink formation.

We note here the first difference between runs with different accretion radii: the smaller the accretion radius, the more likely it is that a larger number of protostellar fragments, here sinks, is created within the same time. Previously, the study by Greif et al. (2012) which simulated the first years of Population III star formation without the help of sink particles showed fragmentation of the protostellar disk even down to the surface of the protostar. Thus it is reasonable that more sinks form in at least one of our tests with an accretion radius smaller than our standard value of $r_{\rm acc} = 2\,$AU.

Number of sinks and mass in sinks

In the left panel of Fig. 6.3, we see that the total number of sinks, $N_{\rm tot}$, is significantly higher for *05AUracc* than for *1AUracc* and *2AUracc* both of which have roughly the same number of sinks after $t \sim 1000\,$yr. The divergence between the runs already begins within 100 yr after the first sink has formed. For almost 900 yr, *1AUracc* has a higher number sinks than *2AUracc*. However, for $t > 500\,$yr, *1AUracc* stagnates in the formation of new sinks while *2AUracc* increases $N_{\rm tot}$ strongly over the final 100 yr. From the exact values listed in Table 6.2, we see that *05AUracc* has more than twice as much sinks as *2AUracc* and even more than three times as much as *1AUracc*.

In spite of the partially very large differences in $N_{\rm tot}$, we find that the evolution of total mass in sink, $M_{\rm tot}$, is not significantly affected. Indeed, when we look at the right panel of Fig. 6.3, we see that *05AUracc* and *2AUracc* evolve identically for $t \gtrsim 600\,$yr while *1AUracc* rises slightly above these two. This is also apparent when we look

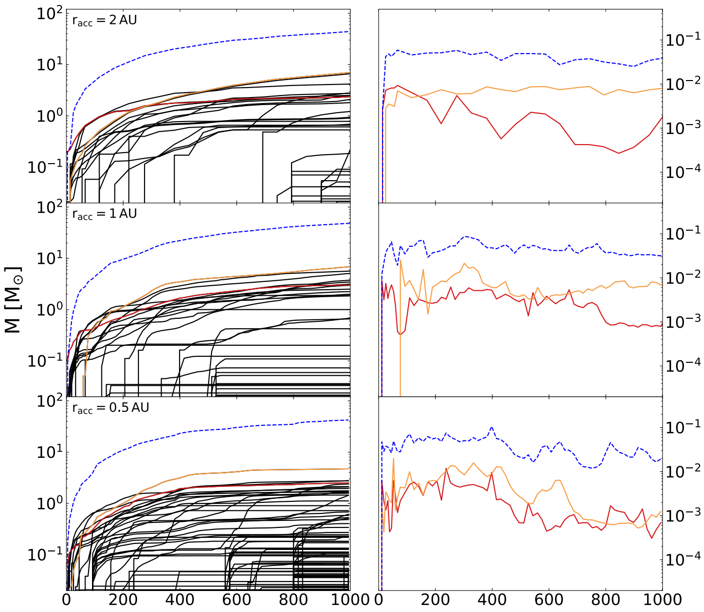

Figure 6.4: Comparison of mass accretion histories for runs with different sink accretion radii. Left column: evolution of the total mass in sinks (blue dashed line), mass growth of the first (red) and the most massive sink (orange) together with all other sinks (black). Right column: cumulative accretion rate (blue dashed line) together with the accretion rate of the first (red) and most massive sink (orange). The most massive sink is defined as the sink with the highest mass at $t \sim 1000\,\mathrm{yr}$.

at the exact values as given in Table 6.2. The largest difference between the runs is $\Delta M_{\mathrm{tot}} < 6\,\mathrm{M}_\odot$.

We further note that, as expected from $\beta = 0.04$, the final values of N_{tot} and M_{tot} lie between the average values we found for $\beta 001$ and $\beta 01$ in the previous Chapter; for comparison see Section 5.3.4.

Accretion history

From comparing the right panels of Fig. 6.4, we observe that both the cumulative accretion rate[1] as well as the accretion rates of the first and most massive sink become more variable for decreasing accretion radius. A reason for this may be the rising number of sink particles which compete for the common accretion reservoir. This is for example visible in Fig. 6.5 of run *05AUracc*. Apart from this trend, there are no significant differences between the runs. For all three, new sink formation continues over the whole time period. Often a whole bunch of sinks (best visible the graphs of for $r_{\mathrm{acc}} = 0.5\,\mathrm{AU}$) is created within a short time period. This may happen when a highly self-gravitating substructure of the disk such as a spiral arm fragments. Some sinks only accrete for a short time while other continue to accrete until the end of the simulation. The cumulative accretion rate remains roughly between $2 \times 10^{-2} - 4 \times 10^{-2}\,\mathrm{M}_\odot\,\mathrm{yr}^{-1}$. It lies between the values for $\beta 001$ and $\beta 01$ in Section 5.3.5. Accretion rates for the first and most massive sinks are mainly below $10^{-2}\,\mathrm{M}_\odot\,\mathrm{yr}^{-1}$. All rates decrease steadily.

---

[1] This is the sum of the accretion rates of all sinks.

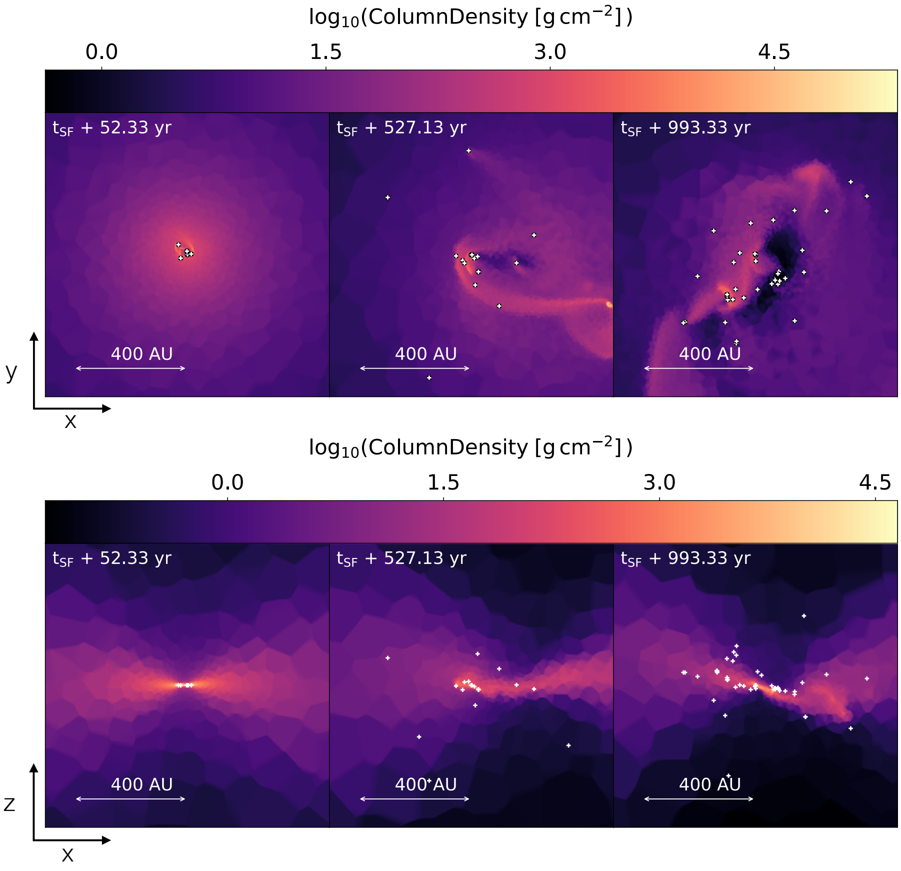

Figure 6.5: Column density projections of the evolution of the run with $r_{\text{acc}} = 0.5\,\text{AU}$. Over the course of the simulation the protostellar disk tilts. Until the end of the simulations 102 sink have formed in this setup. They agglomerate in small sub-clusters and compete heavily for their common mass reservoir leading to highly variable accretion rates. Some sinks get ejected from the disk as can be seen best in the middle and right panel of the x-z-projections. The figures are centered on the first sink and have a thickness of 250 AU.

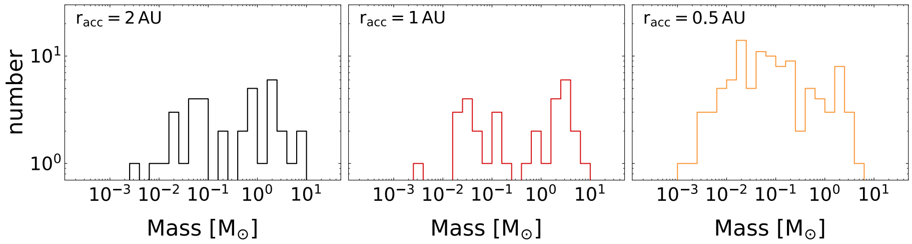

Figure 6.6: Comparison of the sink mass functions.

Mass function

The mass function is top-heavy in all three runs. Interestingly, the mass function of *05AUracc* does not appear as wedge-shaped as the other purely rotational runs in Chapter 5 but resembles more the distributions of the setups including turbulence in Section 5.3.6. A possible reason for that behavior could be its significantly higher number of sink particles compared to each of the individual purely rotational realizations in Chapter 5. The mass functions of *1AUracc* and *2AUracc*, for example, which have less than half of the number of sinks as *05AUracc*, are more similar to those realization.

The range of the sink masses here is $10^{-3} - 10\,\mathrm{M}_{\odot}$. The upper-mass cut-off of the mass function is identical to what we have found in Section 5.3.6 for $\beta001$ and $\beta01$. Setup *1AUracc* and *2AUracc* seem to have the highest peak at a few solar masses while for *05AUracc* the main peak is clearly at lower masses between $10^{-2} - 10^{-1}\,\mathrm{M}_{\odot}$.

6.3.2 Summary I

We find that varying the sink particle accretion radius changes the total number of sinks considerably within the time period of $\sim 1000\,\mathrm{yr}$ considered here. The setup with the smallest accretion radius, $r_{\mathrm{acc}} = 0.5\,\mathrm{AU}$, yields almost three times as much sinks as the other two. This divergence establishes itself already within 100 yr after first sink formation. This will likely have an impact in quantities such as the number of ejections. As we have already seen in Chapter 5, the number of sinks is highly sensitive to small changes in the setup of the simulation. Hence, single number values cannot be trusted but instead the total number of sinks and corresponding quantities must be statistically examined through the analysis of an ensemble of simulations.

The variance in the number of sink particles has none or only minor influence in the total mass in sinks, the mass growth and accretion history, and the general shape of the sink mass function.

This said, we conclude that choosing a smaller sink accretion radius than the in Chapter 5 employed 2 AU changes quantitative results such as the total number of sinks but qualitative findings like the shape of the mass function are less affected.

6.4 Effects of varying number of cells per Jeans length

The following sections contain the results of the two test series on varying Jeans resolution at constant sink accretion radius ($r_{\mathrm{acc}} = 2\,\mathrm{AU}$). In Section 6.4.1, the comparison of the three purely rotational runs ($\beta = 0.04$) with 8, 16, and 32 cells per Jeans length is presented. Section 6.4.2 gives a short summary of the most important results of these

Table 6.3: Overview of detailed results for varying resolution of the Jeans length.

Setup	$t_{\rm SF}$/Myr	$t_{\rm final}$/yr	$N_{\rm tot}$	$M_{\rm tot}/M_\odot$
8Jeans	1.441435	1003	41	44.3
16Jeans	1.441387	1009	32	44.6
32Jeans	1.440376	1005	41	48.5

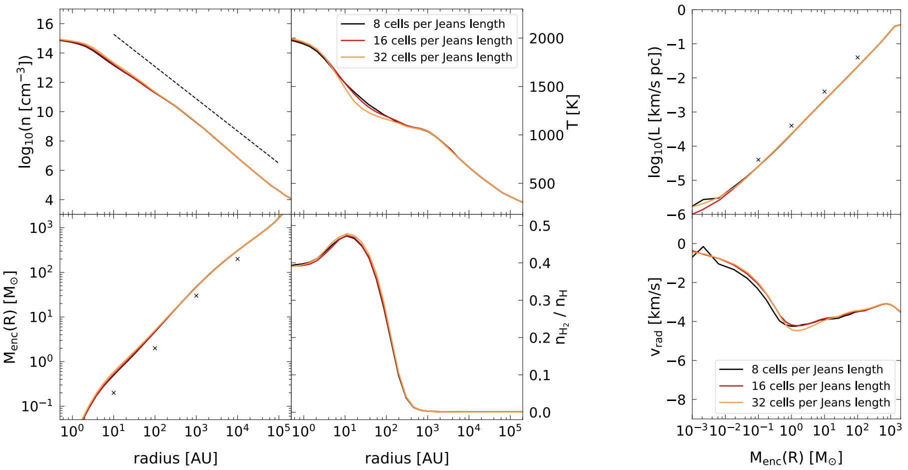

Figure 6.7: The radial profiles of many physical quantities vary only slightly in the runs with different numbers of cells per Jeans length. A slightly higher radial velocity for the 16 and 32 cells per Jeans length runs, leads to an increase in the molecular hydrogen fraction and consequently a smaller temperature below 1000 AU. Left subplot: radial, mass-weighted averages of cloud properties just prior to first sink formation. From top left to bottom right: number density, n, temperature, T, mass enclosed within radius R, $M_{\rm enc}$, molecular hydrogen fraction, $n_{\rm H_2}/n_{\rm H}$. Right subplot: mass-weighted averages of the total specific angular momentum, L, and the radial velocity, $v_{\rm rad}$, within in the cloud. The properties are plotted against the enclosed mass. In both subplots, the averages are derived within spherical shells centered on the densest gas cells just before first sink formation.

simulations. Afterwards in Section 6.4.3, the differences between the runs with 16 and 32 cells per Jeans length of setup $\alpha005\beta001$ from Chapter 5 containing both rotation ($\beta = 0.01$) and turbulence ($\alpha = 0.05$) are examined. As the higher resolution runs proceed more slowly, some of the runs in Section 6.4.3 had not been finished when this chapter was written up. In this case, the detailed analysis of quantities such as the total number of sinks and the total mass in sinks is conducted at the last available time of the slowest run. Section 6.4.4 summarizes the main results of this third test series.

6.4.1 Results: purely rotational runs with $\beta = 0.04$

State of the gas cloud prior to the formation of the first sink

The radial profiles of number density, n, temperature, T, mass enclosed within radius R, $M_{\rm enc}$, molecular hydrogen fraction, $n_{\rm H_2}/n_{\rm H}$ for the three different runs are very similar to each other as can be seen in the left subplot of Fig. 6.7. They show slight differences for radii below 1000 AU, which is in particular visible in the temperature profile. Here, the runs with 32 and 16 cells per Jeans length partially have a smaller temperature than the 8 cells per Jeans length run. This is due to a tiny increase in the molecular hydrogen fraction.

In general, our profiles resemble those found in previous studies (e.g. Abel et al., 2002; Yoshida et al., 2006; Stacy et al., 2010; Clark et al., 2011b,a; Greif et al., 2011; Greif et al., 2012). We recover the standard $\rho \propto R^{-2.2}$ density profile which we indicate here with the black dashed line. Furthermore, we compare our results for the enclosed mass to data points (black crosses) as approximately taken from Abel et al. (2002). Our line diverges from the points more for decreasing radius. This behavior may be attributed to differences in the density distribution. Finally, we remark that the overall drop in the H_2 fraction at radii $\lesssim 10\,\mathrm{AU}$ is a feature is due to the high temperatures of $T \gtrsim 1500\,\mathrm{K}$ and has been also observed in earlier studies (e.g, Clark et al., 2011b; Greif et al., 2012).

In the right diagram of Fig. 6.7, the total specific angular momentum, L, and the radial velocity, v_{rad} as a function of the enclosed mass, M_{enc} is displayed. While all three runs have identical specific angular momentum until the immediate surrounding of the densest cell, e.g. $M_{\mathrm{enc}} \lesssim 10^{-2}\,\mathrm{M}_{\odot}$, the radial velocity profiles begin to diverge already at $M_{\mathrm{enc}} \sim 10^{2}\,\mathrm{M}_{\odot}$. The latter corresponds roughly to a distance of $R \sim 1000\,\mathrm{AU}$. As we have seen in the left subplots, slight changes in the temperature and $H_2 fraction$ profiles occur below this distance between the three runs. It is possible that the slightly higher radial infall velocity of setup *32Jeans* leads to a slightly faster compression of the gas yielding in a slightly faster increase in the $H_2 fraction$ that is enough at this level to push the temperature of the gas to lower values compared to the other runs. Similar behavior can be assumed to happen for setup *16Jeans* albeit not as easily visible.

Time of first sink formation

Setup *8Jeans*, *16Jeans* and *32Jeans* form their first sink at $t_{\mathrm{SF}} = 1.441435\,\mathrm{Myr}$, $t_{\mathrm{SF}} = 1.441387\,\mathrm{Myr}$ and $t_{\mathrm{SF}} = 1.440376\,\mathrm{Myr}$ respectively. We observe that the point of first sink formation shifts to earlier times for higher resolved Jeans length. The difference between *8Jeans* and *16Jeans* is rather small ($\Delta t < 50\,\mathrm{yr}$) and might be an intrinsic numerical effect. The difference to *32Jeans* ($\Delta t \sim 1000\,\mathrm{yr}$) could also still originate from numerical effects. On the other hand, it has been shown in previous studies that from a resolution of 32 cells per Jeans length on, turbulent gas motions arising during gravitational collapse can be resolved (see e.g. Greif et al., 2011; Greif et al., 2012). This additional turbulence might suffice to affect the collapse time. Since we only have one realization per resolution here, however, we cannot draw a definite conclusion on what exactly influences the collapse time here. As in Section 6.3, we find for all three runs that the creation time of the first sink is delayed due to substantial pressure support within the BE sphere as it is again $\alpha_{\mathrm{therm}} = E_{\mathrm{therm}}/|E_{\mathrm{grav}}| \approx 0.854$.

Disk structure

In Fig. 6.8 we show face-on and edge-on views of the protostellar disks shortly after first star formation. In the edge-on view in the bottom panels, the different cell sizes per resolution are apparent. Different from the profile of disk properties in Fig 6.2 in Section 6.3, the profiles in Fig 6.9 here have still small but more obvious variations in the whole radius range. As in Fig 6.2 the divergence is largest in the Toomre parameter.

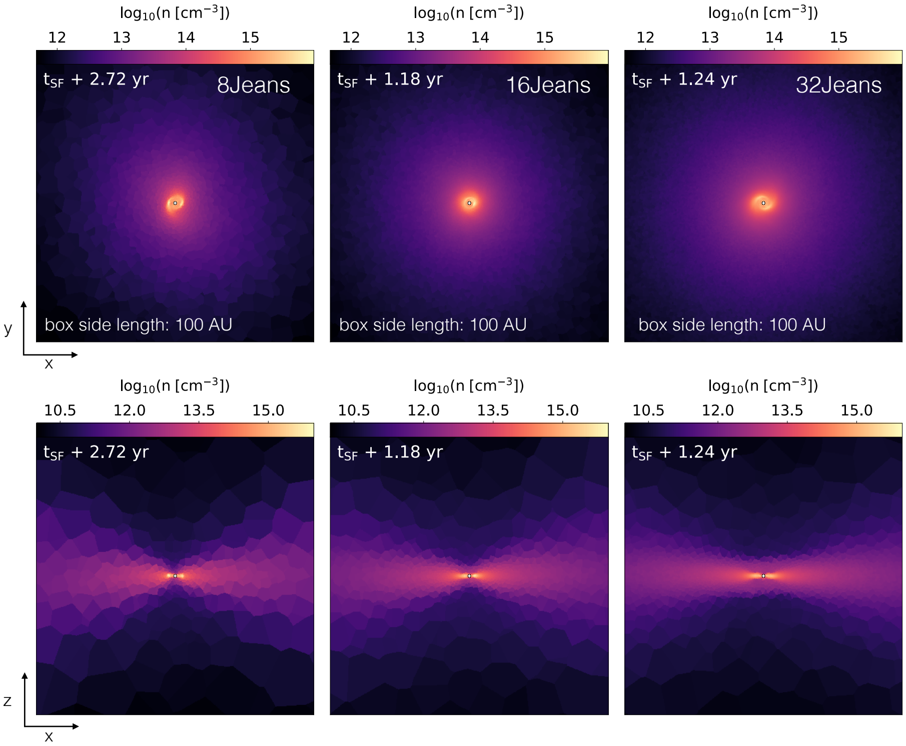

Figure 6.8: Number density slices just after the first sink particles have formed. In edge-on plots (bottom panels), one can nicely see how the mesh becomes finer with increasing resolution per Jeans length. The slices are centered on and cut at the position of the first sink.

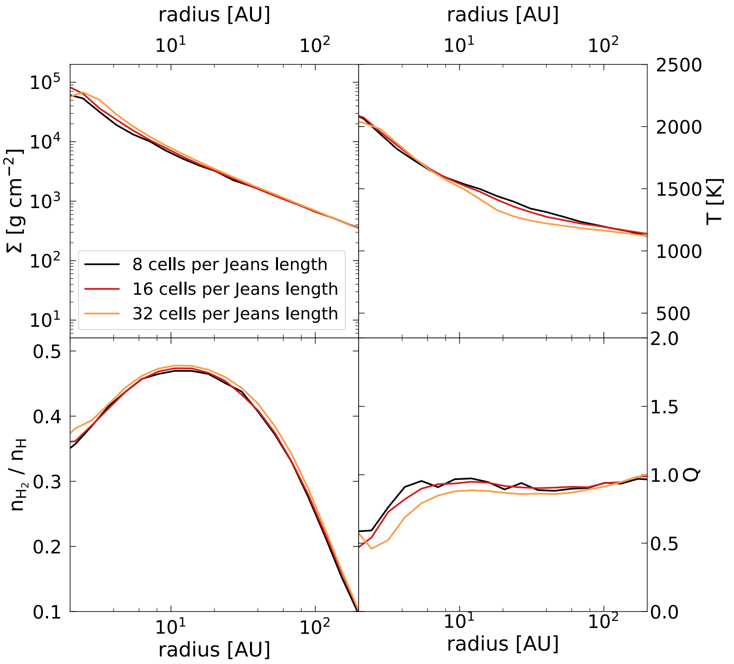

Figure 6.9: The differences between the test runs with different sink accretion radii appear mostly close to the first sink. The profiles were derived at the same time as the projections in Fig. 6.8. Until that time only one sink has formed in each of the runs. From top left to bottom right: disk surface density Σ, temperature, T, H_2 fraction, n_{H_2}/n_H, and Toomre parameter, Q. The values are derived from mass-weighted averages within spherical shells centered on the first sink. In order to track the gas at disk densities, only gas cells with $n > 10^9\,\mathrm{cm}^{-3}$ have been considered here.

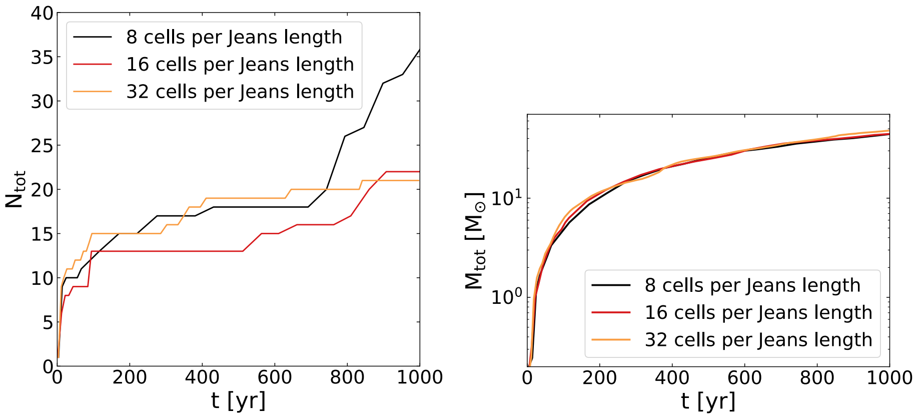

Figure 6.10: Left panel: evolution of total number of sinks. Right panel: evolution of total mass in sinks.

In addition, the other properties already begin to vary at a distance of 200 AU from the first sink and not just in the immediate surrounding of it. Interestingly the differences close to the sink surface are smaller than in Fig 6.2. The well-visible temperature decrease in setup *32Jeans* at $R \lesssim 100\,\mathrm{AU}$ that we have also seen in Fig. 6.7 is still present after the first sink has formed.

The disk environment around the first sink is again strongly self-gravitating as inferred from the Toomre-Q plot which is $Q \lesssim 1$ for most of the radius range. The line of setup *32Jeans* is slightly below the other two lines. As in Fig 6.2, the immediate surrounding of the sink ($R < 10\,\mathrm{AU}$) is Toomre-unstable. It is likely that additional fragments will form there soon.

Different resolution per Jeans length affects the thermodynamical evolution of the gas. The is enough for variation in the density, temperature and H_2 fraction to occur and manifest in the profiles. Although the overall shape of the profile is still similar, local variation may trigger differences in the evolution of the protostellar disk system such as locally enhanced fragmentation.

Number of sinks and mass in sinks

The evolution of the of the total number of sinks, N_{tot}, begins to diverge almost immediately after first sink formation as apparent in the left subplot of Fig. 6.10. The initial steep increase in N_{tot} flattens later on. It may, however, be interrupted by another sudden increase, as happens for setup *8Jeans* at $t \sim 700\,\mathrm{yr}$. This is likely due to the fragmentation of a substructure such as a spiral arm within the protostellar disk. Fig. 6.11 shows projections of three different times in the evolution of setup *8Jeans*. The disk develops spiral arms to more efficiently redistribute accumulated angular momentum. We find the highest total number of sinks in *8Jeans* although its number evolution proceeds below that of *32Jeans* for roughly 700 yr. Also setup *16Jeans* finally yields a slightly higher N_{tot} than *32Jeans*. Therefore, we may conclude that we do not find a definite trend for the total number of sinks in relation to a change of the Jeans resolution here.

We see in the right subplot of Fig. 6.10 that in spite of the differences in the total number of sinks, all three runs have a similar evolution of the total mass in sinks. Some small divergences are visible, for example at $t \lesssim 200\,\mathrm{yr}$ which however is balanced

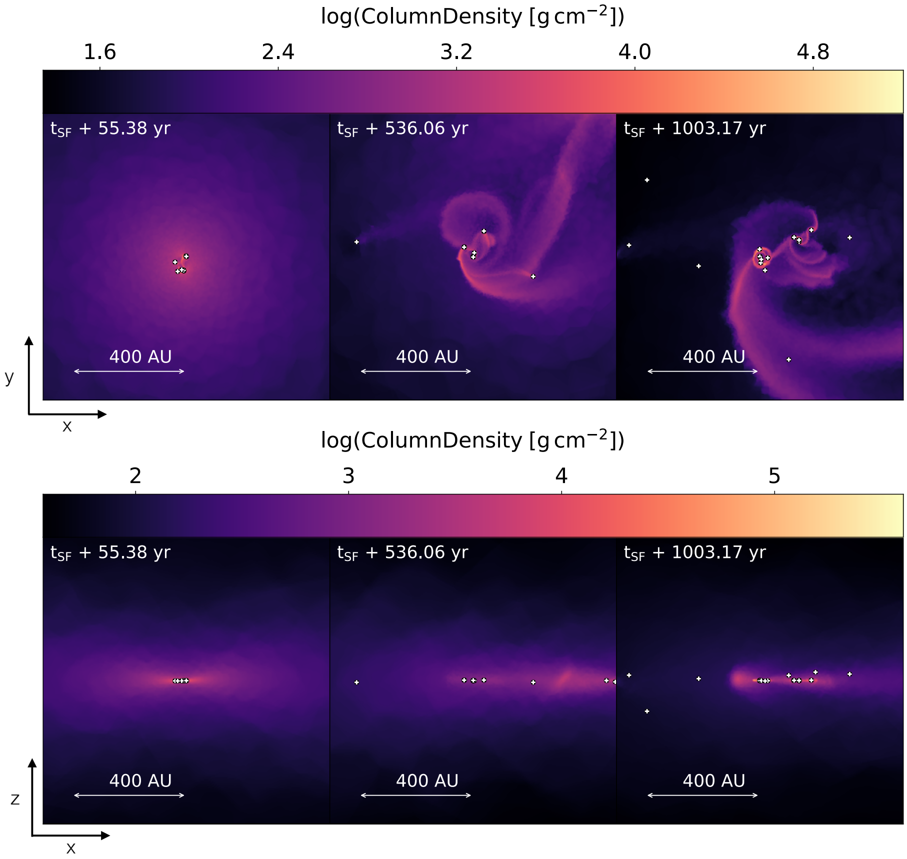

Figure 6.11: Column density projections of the evolution of run *8Jeans*. The disk develops spiral arms over the course of the run to more efficiently redistribute accumulated angular momentum. Some sink particles are ejected from the protostellar system. The plots are centered on the first sink. The thickness is 6.5 pc.

later on. At $t \sim 1000\,\mathrm{yr}$, the curve of setup *32Jeans* lies slightly above the other two lines.

The values of N_{tot} for setup *16Jeans* and *32Jeans* lie below the average values found in setup for $\beta001$ and $\beta01$ in Chapter 5. Nevertheless, the mass evolution is as expected and M_{tot} lies because of $\beta = 0.04$ between the average values we found for setups $\beta001$ and $\beta01$.

Accretion history

The cumulative mass accretion rates, as displayed by the blue dashed lines in the right column of Fig. 6.12, have on average very similar values of a few $10^{-2}\,\mathrm{M_{\odot}yr^{-1}}$ for all three runs. Consequently, the final total mass in sinks is about the same in all three cases, as we have discussed above. The profiles of *32Jeans* are more variable than of the other two setups. In particular the red line of the first sink has wild ups and downs. It is likely that it heavily competes in its accretion with neighboring sinks. The left panels demonstrate the typical picture of sink formation all over the course of

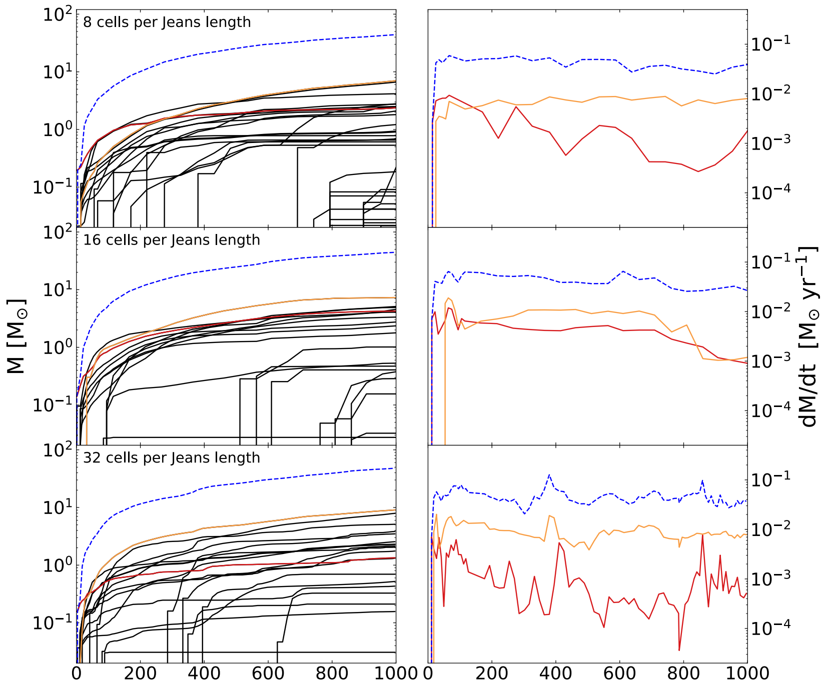

Figure 6.12: Comparison of mass accretion histories for varying resolution of the Jeans length. Left column: evolution of the total mass in sinks (blue dashed line), mass growth of the first (red) and the most massive sink (orange) together with all other sinks (black). Right column: cumulative accretion rate (blue dashed line) together with the accretion rate of the first (red) and most massive sink (orange). The most massive sink is defined as the sink with the highest mass at $t \sim 1000\,\mathrm{yr}$.

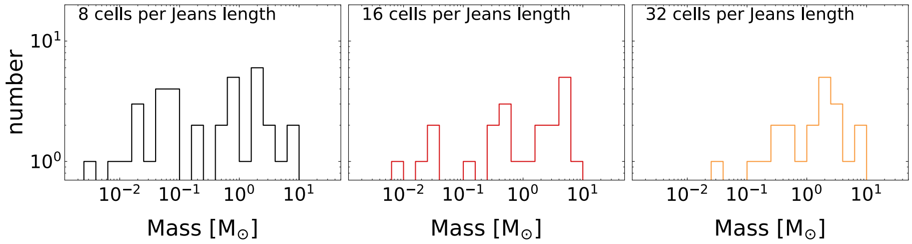

Figure 6.13: Comparison of the sink mass functions for varying resolution of the Jeans length.

the simulation with some sinks accreting only for a short time and then stall in their mass growth, while other increase their mass continuously. Overall, we do not find differences in the mass accretion histories of the three runs that are likely to change the general outcome.

Mass function

The sink mass functions in Fig. 6.19 show again more or less flat spectra indicating top-heavy distributions. Due to limited total number of sinks ($N_{\rm tot} < 40$ for all runs) within the simulated 1000 yr, the spectra are not as distinct as for example the one of setup *05AUracc* in Fig 6.6 above. The mass ranges again between a few $10^{-3}\,M_\odot$ to about $10\,M_\odot$. Here, local peaks are found for a few solar masses.

6.4.2 Summary II

We observe small divergences in the profile of the radial infall velocity, the temperature and the H_2 fraction for run *32Jeans*. But there seem to be no apparent consequences on the quantities we analyzed. We conclude that varying jeans resolution in a purely rotational setup has no major effects on the outcome of the simulation.

6.4.3 Results: mixed runs with $\alpha = 0.05$ and $\beta = 0.01$

State of the gas cloud prior to the formation of the first sink

In Fig. 6.14, we see that the profiles of gas properties just before the formation of the first sink particle are overall very similar for 16 (solid lines) and 32 (dashed lines) cells per Jeans length. They generally resemble those found in previous numerical studies (e.g. Abel et al., 2002; Yoshida et al., 2006; Stacy et al., 2010; Clark et al., 2011b,a; Greif et al., 2011; Greif et al., 2012), e.g. we recover the standard $n \propto R^{-2.2}$ density profile as indicated by the black dashed line in the number density subplot.

The main deviation between the solid and dashed lines, i.e. that we may attribute to the difference in resolution, is visible in the profiles of the temperature and the molecular hydrogen fraction within a radius of 1000 AU from the densest cell. We can observe that the dashed lines cover smaller temperatures than the solid lines within this radius. This corresponds to a tiny increase in the molecular hydrogen fraction: here, the dashed lines proceed slightly above the solid lines. This is sufficient for the gas to cool down more. We have already encountered this behavior in Section 6.4.1 above where it also emerged clearer for higher resolution.

Table 6.4: Overview of the detailed results of the simulations of setup $\alpha005\beta001$ with 16 and 32 cells per Jeans length resolution. From left to right: name of the realizations (the runs with 32 cells per Jeans length are indicated by the prefix "32"), time of first sink formation, t_{SF}, intermediate time, t_{inter}, in years after t_{SF} considered for our analysis, the final year of the simulations, t_{final}, the total number of sinks formed until t_{inter} and the corresponding total mass in sinks, and finally the total number of sinks formed until t_{final}, N_{tot}, and the corresponding total mass in sinks, M_{tot}.

Realization	t_{SF}/Myr	t_{inter}/yr	t_{final}/yr	$N(t_{\mathrm{inter}})$	$M(t_{\mathrm{inter}})/M_\odot$	N_{tot}	$M_{\mathrm{tot}}/M_\odot$
$\alpha005\beta001-1$	0.688	461	1010	25	26.8	40	47.5
$\alpha005\beta001-2$	0.655	469	1006	17	28.6	53	64.0
$\alpha005\beta001-3$	0.675	465	1013	16	34.5	45	63.3
$\alpha005\beta001-4$	0.675	471	1005	55	49.4	81	80.8
$\alpha005\beta001-5$	0.686	457	1007	25	24.6	32	48.1
32-$\alpha005\beta001-1$	0.693	468	1018	34	47.5	53	78.8
32-$\alpha005\beta001-2$	0.659	462	938	47	40.9	67	78.1
32-$\alpha005\beta001-3$	0.680	463	463	19	49.0	19	49.0
32-$\alpha005\beta001-4$	0.680	466	554	38	56.3	39	64.8
32-$\alpha005\beta001-5$	0.689	469	1004	28	32.5	45	62.0

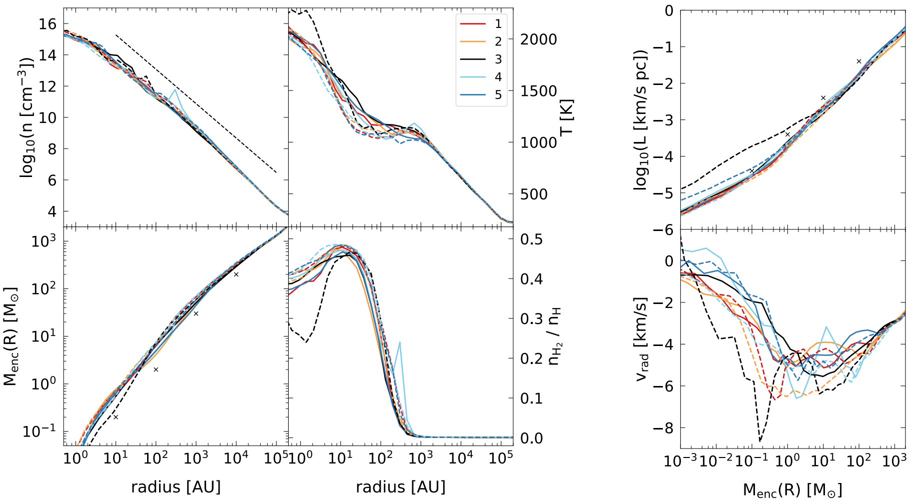

Figure 6.14: State of the gas cloud in the different realizations of setup $\alpha005\beta001$ just before the first sink forms. Solid lines represent the profiles derived from the runs with 16 cells per Jeans length resolution whereas dashed lines describe their higher resolution equivalent. Left subplot: radial, mass-weighted averages of cloud properties just prior to first sink formation. From top left to bottom right: number density, n, temperature, T, mass enclosed within radius R, M_{enc}, molecular hydrogen fraction, $n_{\mathrm{H}_2}/n_{\mathrm{H}}$. Right subplot: mass-weighted averages of the total specific angular momentum, L, and the radial velocity, v_{rad}, within in the cloud. The properties are plotted against the enclosed mass. In both subplots, the averages are derived within spherical shells centered on the densest gas cells just before first sink formation.

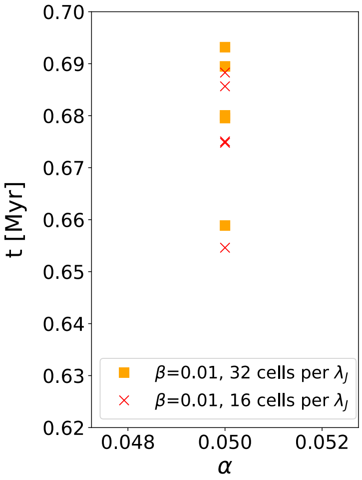

Figure 6.15: Comparison of the collapse times of setup $\alpha005\beta001$ for simulations using our standard Jeans refinement criterion, for which the Jeans length is always resolved by at least 16 cells (*red crosses*) and simulations using a more stringent refinement criterion of 32 cells per Jeans length (*orange squares*) plotted as a function of the turbulent α parameter.

In addition, we notice several features that arise due to the initial turbulent velocity field. As they have been explained in greater detail in Section 5.3.1 above, we omit a thorough discussion here and simply mention them briefly. For example, the bumps in the solid bright blue line as well as in the solid and dashed black line are due to some local density enhancement apart from the main collapse region. Such behavior has also been reported in earlier studies (e.g. Greif et al., 2012). Related to these bumps are peaks and dips at the same radii in the profiles of temperature and molecular hydrogen fraction. Beside of that, the highly fluctuating profiles of the radial velocity further indicate the influence of the turbulence.

The black dashed line of realization 32-$\alpha005\beta001-3$ deviates most strongly from all the other profiles within a radius of about 30 AU, corresponding to a enclosed mass of $2\,\mathrm{M}_\odot$. In this region, 32-$\alpha005\beta001-3$ has an elevated total specific angular momentum and a sharp dip in the radial velocity profile which describes the velocity of the gas infall. The value is higher than in the other realizations and indicates a strongly collapsing region in which shocks appear. This is visible in the temperature profile where the gas is overall hotter than in the other realizations within $\sim 10\,\mathrm{AU}$. This temperature increase is enough to dissociate some of the molecular hydrogen, as we can see in the drop of the molecular hydrogen fraction profile. Within this strong infall region, the first sink is about to form. The overall behavior of the 32-$\alpha005\beta001-3$ profiles is still similar to that of the other realizations. Local variations, in particular in the immediate surrounding of the densest cells are likely to occur because it is a highly dynamical region. We therefore refrain from doing a more detailed analysis here.

Time of first sink formation

The choice of resolution affects the collapse time of setup $\alpha005\beta001$ slightly. In Fig. 6.15, we compare the time required to form the first sink particle in runs with 16 cells per Jeans length (red crosses) and 32 cells per Jeans length (yellow squares). The higher resolution delays the collapse a bit, but the effect is small ($\Delta t < 0.01\,\mathrm{Myr}$). One

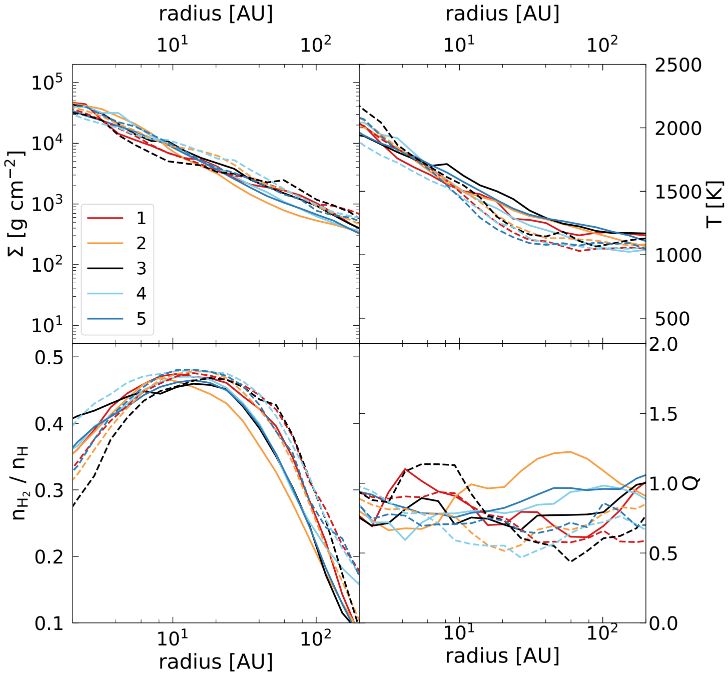

Figure 6.16: Mass-weighted radially averaged disk properties just after the formation of the first sink particle. The profiles vary locally more due to the presence of the turbulent velocity field which is particularly visible for the Toomre parameter. As in Fig. 6.9 the lines of the realizations with 32 cells per Jeans length indicate slightly enhanced molecular hydrogen fractions and smaller temperatures. From top left to bottom right: disk surface density Σ, temperature, T, H_2 fraction, n_{H_2}/n_H, and Toomre parameter, Q. The values are derived from mass-weighted averages within spherical shells centered on the first sink. In order to track the gas at disk densities, only gas cells with $n > 10^9\,\mathrm{cm}^{-3}$ have been considered here.

reason for the delay could be that additional turbulence, arising in gas motions during gravitational collapse, can now be resolved due to the higher resolution (see also Greif et al., 2011; Greif et al., 2012), and adds up with the pre-defined turbulent velocity field to slow down the overall collapse of the cloud. From Table 5.3 and Fig. 5.18 in Chapter 5, we can see that in runs with a higher degree of turbulence the formation of the first sink happens later than in a comparable run with lower turbulence level.

We further remark that the behavior described above is in contrast to the relation found in the previous Section 6.4.1 where the sink formed earlier for each higher level of resolution. The difference between the formation times there is similarly small as here. As we have noted in 6.4.1, because we only have one realization per resolution there, we cannot draw a final conclusion in what influences the exact collapse time and why the relation above is contrary to what we find here.

Disk structure

In Fig. 6.16, a direct comparison of the profiles of disk properties just after first sink formation is given. Overall, the realizations of both resolutions (solid lines: 16 cells per Jeans length; dashed lines: 32 cells per Jeans length) resemble each other. Different from the behavior of the purely turbulent setups in the two previous sections, the

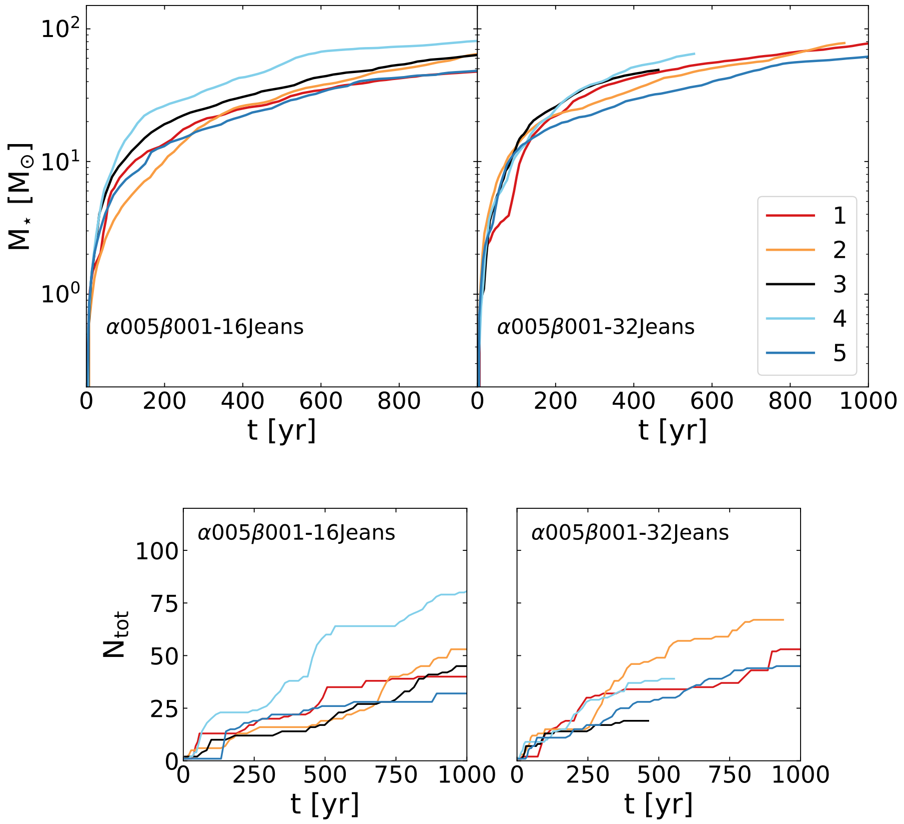

Figure 6.17: Evolution of total mass in sinks (top panels) and total number of sinks (bottom panels). The color scheme indicates the individual realizations. It is explained in the legend of the top right panel and is the same for all panels. Since some of the higher resolution runs did not finish until this section was written, three lines are cut off earlier than the 1000 yr of the total time covered by the simulation.

lines here vary more strongly locally as a consequence of the pre-defined initial turbulent velocity field. This is what we have already observed in Chapter 5. The Toomre parameter, Q, shows the highest variations and indicates strongly self-gravitating protostellar disk environments around the first sink for all realizations. Again, similar to the observation in Fig. 6.14 and Fig. 6.9, the higher resolution profiles show a enhanced molecular hydrogen fraction and a correspondingly reduced temperature within $\sim 10-200\,$AU around the first sink.

Number of sinks, mass in sinks, and accretion history

The higher resolution runs lead generally to larger total number of sinks and larger total mass in sinks. In Fig. 6.17, the evolution of the total mass in sinks, M_{tot}, (top panels) and the total number of sinks, N_{tot}, (bottom panels) is displayed. In Table 6.4, the exact values are given. Since some of the higher resolution runs did not finish until this section was written, we unfortunately do not have data at $t = 1000\,$yr for all our runs. However, we can compare the simulations at the final time of the shortest run which is 32-$\alpha005\beta001-3$ which is 463yr after first sink formation. For technical reasons, the different AREPO simulations do not produce their output dumps at exactly the same times but rather in an interval of $t \pm 10\,\mathrm{yr}$. For our analysis, we therefore compared the results in the output dumps for each realization before and after $463\mathrm{yr}$. We paid special attention that the used output dump did not include a significant increase in number of sinks and total mass in sinks after $463\mathrm{yr}$. Similarly, we made sure that we did not strongly underestimate the values of these quantities when using an output dump before that time. In column 3 of Table 6.4, the exact times of the used output dumps are listed. They are denoted as t_{inter} standing for intermediate times in contrast to the final output times, t_{final}, at the end of the simulation. In column 5 and 6 of Table 6.4, the detailed values for the number of sinks, $N(t_{\mathrm{inter}})$, and the total mass in sinks, $M(t_{\mathrm{inter}})$, at that time are tabulated. We immediately see that the values for both $N(t_{\mathrm{inter}})$ and $M(t_{\mathrm{inter}})$ are generally larger in case of the runs with higher resolution (denoted by the prefix "32"). This overall trend also continues until $t \sim 1000\,\mathrm{yr}$ for 32-$\alpha005\beta001-1$, 32-$\alpha005\beta001-2$, and 32-$\alpha005\beta001-5$. The only exception is realization 32-$\alpha005\beta001-4$ for which $N(t_{\mathrm{inter}})$ smaller compared to its lower resolution counterpart $\alpha005\beta001-4$. Disk fragmentation is a chaotic process and is additionally complicated when turbulent velocity fields are included. Thus, how many sinks exactly form and when this happens is highly unpredictable (see also the left panels in the two plots in Fig. 6.18). This again demonstrates the importance of considering a sample of realization instead of just a single run in order to be able to derive general trends in simulations that include turbulence. But as we have already seen e.g. in Section 5.3.4 or 6.3, even for a varying total number of sinks, the total mass remains about the same. The accretion histories given in Fig. 6.18, do not differ much for both different realizations of one resolution and correlated realization of different resolution. However, it is visible that the cumulative accretion rates of the higher resolution runs are overall slightly larger than those of the lower resolution ones. This explains the trend for M_{tot}.

Mass function

Both the mass functions of the individual realizations and the combined mass functions of each setup are flat, i.e. indicate a top-heavy mass distribution. The mass range for both ranges between a few $10^{-3}\,\mathrm{M}_{\odot}$ to a few 10 solar. When checking the similarity of the two combined mass functions here and between the combined mass function of the higher resolution run with all other turbulent setups with the Kolmogorov-Smirnov test, we find that both are drawn from the same underlying distribution. See Table 10.4 in the Appendix for the detailed values.

6.4.4 Summary III

Compared to the two other test series, we find significant variations in several quantities in the resolution study of $\alpha005\beta001$. The most considerable difference to the other tests is the overall increase in total mass in sinks with higher resolution. This is a consequence of slightly enhanced cumulative accretion rates throughout the realizations. For most of the runs, the number of sinks is also a bit higher than in the lower resolution equivalents. Despite of these changes, we still find a top-heavy mass function. Similar to what was observed in the previous section, we realizations with 32 cells per Jeans length have both larger radial velocities, slightly higher H_2 fractions, and lower temperatures within $\sim 200\,\mathrm{AU}$ of the location where the first sink forms.

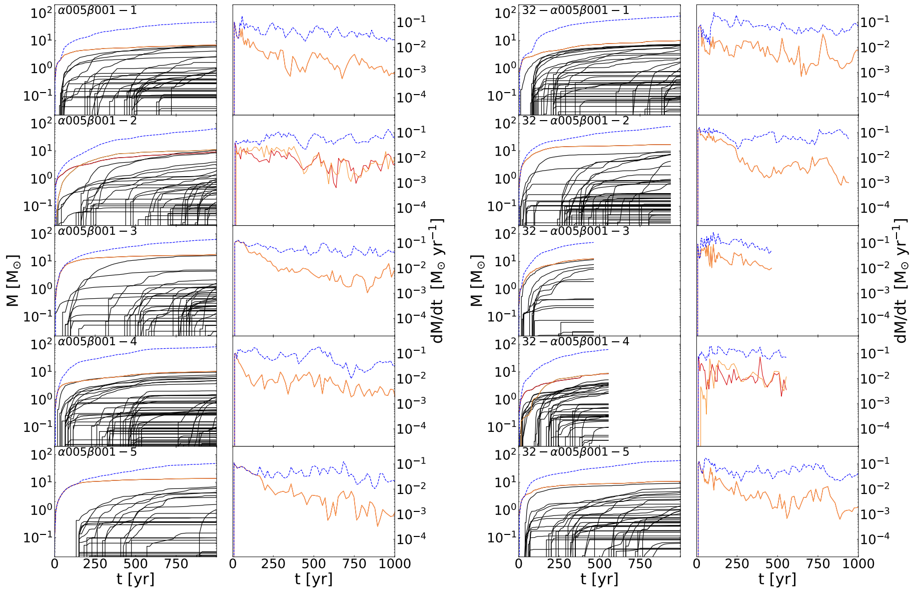

Figure 6.18: Comparison of mass accretion histories for $\alpha005\beta001$ with 16 cells per Jeans length (left) and 32 cells per Jeans length (right). There is no significant difference between the two resolutions. Description of the subplots: in the left column, evolution of the total mass in sinks (blue dashed line), mass growth of the first (red) and the most massive sink (orange) together with all other sinks (black). In the right column, cumulative accretion rate (blue dashed line) together with the accretion rate of the first (red) and most massive sink (orange). The most massive sink is defined as the sink with the highest mass at $t \sim 1000\,\mathrm{yr}$. Three of the runs with 32 cells per Jeans length resolution had not been finished until this chapter was written and therefore some lines are cut off early.

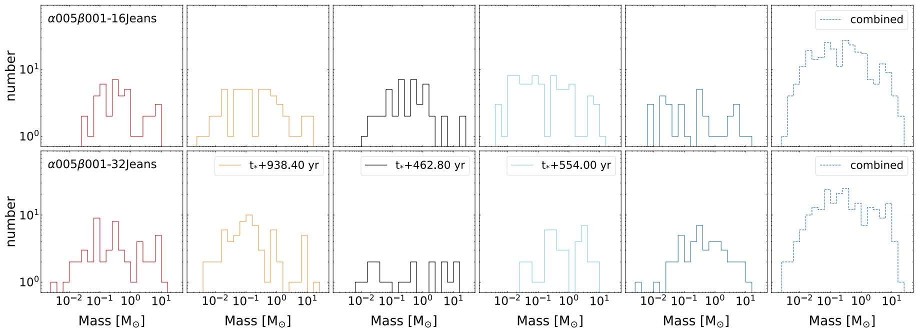

Figure 6.19: Comparison of the sink mass function of setup $\alpha005\beta001$ when derived with in simulations with 16 cells per Jeans length (top panels) and 32 cells per Jeans length resolution (bottom panels). For unfinished runs the time at which the mass function is derived is stated.

6.5 Discussion and conclusion

We have performed three test series in which we examine how sensitive our physical results of the study presented in Chapter 5 are to variations in the two resolution conditions of our numerical approach, namely the number of cells per Jeans length and the size of the sink particle accretion radius. Our simulations consider the collapse of a rigidly rotating Bonnor-Ebert sphere to which we added a subsonically turbulent velocity field component in one of our tests. The three test series are

1. Varying accretion radii, i.e. 0.5, 1, and 2 AU (at constant 8 cells per Jeans length),

2. Varying Jeans resolution, i.e. 8, 16, and 32 cells per Jeans length (at constant sink accretion radius of 2 AU), and

3. Varying Jeans resolution for a setup including turbulence (at constant sink accretion radius of 2 AU), i.e. re-running setup $\alpha 005 \beta 001$ from Chapter 5 with a resolution of 32 cells per Jeans length.

Overall, we find that variations in the resolution criteria do not affect the results of Chapter 5 significantly. The main quantity that is influenced is the fragmentation behavior of the Population III protostellar disk, i.e. the number of sink particles that are created. This, however, has only, if at all, a mild effect on the total mass in sinks; the mass functions retain their flat spectrum, i.e. the top-heavy distribution. It might have a stronger effect on the number of protostellar ejections. But since we have not included a sink merging method, which likely affects the total number of sinks and their dynamically interaction more severely, we therefore refrain from drawing conclusion about that here.
Our main findings can be summarized in more detail as follows:

- A smaller sink particle accretion radius leads to a larger number of sinks. This is consistent with the outcome of previous simulations that found that Pop III protostellar disk fragmentation occurs even down to the direct protostellar surface (Greif et al., 2012) and that with increasing sink accretion radius the actual amount of fragmentation is underestimated (e.g. Clark et al., 2011a; Smith et al., 2011, 2012). Among our runs, the realization with $r_{\mathrm{acc}} = 0.5\,\mathrm{AU}$ yields by far the highest number of sinks. The one with $r_{\mathrm{acc}} = 1\,\mathrm{AU}$ has the second largest number for most of the time and is only surpassed by the one with $r_{\mathrm{acc}} = 2\,\mathrm{AU}$ within the last 100 yr of the total 1000 yr after formation of the first sink particle that are covered in our simulations. It is possible that this behavior is reversed again at some later stage. We note that only a short period within the total accretion time of Population III protostellar systems, which is $\sim 10^4 - 10^5\,\mathrm{yr}$ (see e.g. Stacy et al., 2012; Susa et al., 2014; Stacy et al., 2016), is considered in our studies, and, as disk fragmentation happens chaotically, it is rather unpredictable when fragmentation happens and how many sinks exactly form during the whole lifetime of a protostellar system.

- The number of cells per Jeans length does not have a strong influence on the number of sinks. In the test series with only rotation, we observe a smaller number of sinks for more cells per Jeans length. The run with 8 cells per Jeans length yields roughly twice as many sink particles as the other two within the time span considered. The run with 16 cells per Jeans length surpasses its higher resolution counterpart within the last 100 yr. In contrast to that, four out of five realizations of the re-run of setup $\alpha005\beta001$ yield a larger number of sinks compared to their lower resolution equivalents.

The comparison of these two test series illustrates the relevance of performing a sample of realizations instead of only a single run. In detail this means that in simulations including turbulence a sample should consist of realizations of the same initial conditions but with varied random number seed used for initializing the turbulent velocity field. For purely rotational runs, this corresponds to slight differences in the initial mesh configuration. This is because in Chapter 5 we have seen that even samples without turbulence, where simply the random position of the mesh cells is varied before initializing the Bonnor-Ebert density profile, yield variations in their outcome of total number of sinks and total mass within them. It is therefore possible that the behavior we find in the purely rotational runs here is just one particular outcome. A clearer trend might be found within a statistic of several realizations.

- The total mass in sinks is not considerably affected by the different choices of resolution in the two purely rotational test series. For setup $\alpha005\beta001$, on the other hand, we observe a higher total mass in sinks with increasing resolution which is already apparent at $t \sim 500\,\mathrm{yr}$ and remains true in at least three out of five at $t \sim 1000\,\mathrm{yr}$. The other two runs had not yet been finished by the time this chapter was written up. As turbulent gas motions arising during gravitational collapse are resolved for Jeans resolution above 32 cells per Jeans length, it is possible that this additional turbulence adds to the pre-existing turbulent velocity field in setup $\alpha005\beta001$ and enhances its effects. In Chapter 5, it was seen that runs including turbulence generally lead higher values of M_{tot}, in particular setup $\alpha025\beta001$ yields on average a larger M_{tot} than $\alpha005\beta001$.
- The mass functions remain fairly flat in all runs considered. This means there is a large deficit in low mass stars different from what is expected from a Salpeter (1955) or Kroupa (2001) mass function. This trend is consistent with what has been found in previous numerical studies of Population III star formation (e.g. Clark et al., 2011a; Greif et al., 2011; Smith et al., 2011; Susa et al., 2014; Stacy et al., 2016). The flat structure emerges clearer the more sinks are created in a run. This can be seen best for the combined mass functions of both $\alpha005\beta001$ setups and for purely rotational run with $r_{\mathrm{acc}} = 0.5\,\mathrm{AU}$.
- In runs with a resolution of 32 cells per Jeans length, we observe higher radial velocities within $\sim 200\,\mathrm{AU}$ around the densest cell just before the formation of the first sink particle. This is accompanied by a tiny increase in the molecular hydrogen fraction leading to a locally reduced temperature. This divergence is still visible after sink creation. We note that Turk et al. (2012) also observed for higher resolution a change in the thermodynamical behavior of the gas before the formation of protostars. They considered one run with 16, 32, and 64 cells per Jeans length respectively. The behavior of the gas infall velocity and molecular hydrogen fraction is similar to ours albeit more enhanced and locally varying, but they find an increase in gas temperature which is in contrast to our observation. A direct comparison between their work and ours is difficult because of our different initial setups, e.g. they derive their star-forming clouds self-consistently from cosmological simulations in which they also account for small-scale, turbulently amplified magnetic fields, while we study a non-magnetized BE sphere collapse within an isolated volume and controlled pre-defined initial rotation and

turbulence within our cloud. Besides, such a comparison is beyond the scope of our resolution study presented in this chapter. However, as both our simulations and theirs indicate that the gas thermodynamics is sensitive to the level of resolution, future studies should examine this behavior and its influence on Pop III star formation in more detail.

- We find that both a smaller sink accretion radius as well as a higher number of cells per Jeans length results in more highly variable accretion rates. The value of the rate, however, is not considerably changed.

So far we have neglected magnetic fields in our studies. They are likely to stabilize protostellar disk against fragmentation and reduce the number of fragments. If fewer sinks compete for a common mass reservoir, they may be able to individually keep up higher mass accretion rates and grow to larger masses within shorter time. In the next chapter, we are going to analytically examine the size of small-scale, tangled magnetic field needed to stabilize Pop III protostellar disk.

CHAPTER 7

Stabilizing Population III accretion disks with magnetic fields

This chapter contains a revised version of the publication *"Stabilizing Population III Accretion Disks with Magnetic Fields"*, Wollenberg, Katharina M. J.; Glover, Simon C. O.; Bromm, Volker; Klessen, Ralf S., Proceedings article in Memorie Della Società Astronomica Italiana, Vol. 88 n.4, 2017, p. 864-865. In this original work, we addressed the topic by comparing a critical magnetic field strength, which was needed to stabilize an unstable Population III protostellar disk, to a saturated magnetic field strength, which was received from small-scale dynamo action under the same disk conditions. The critical magnetic field strength was derived with an extended Toomre criterion. In the following study, we have combined the concepts behind these two magnetic field strengths to a general formula. Furthermore, we have extended the datasets that we examine by including results from our simulations presented in Chapter 5. I performed the analytical computations, analyzed them, created the figures, and wrote the text. All authors provided useful comments on the method section and the interpretation of the results.

7.1 Introduction

Numerical simulations of Population III (Pop III) star formation show that the protostellar accretion disks that form around the first Pop III protostars are prone to gravitational fragmentation (see e.g. Clark et al., 2011b; Greif et al., 2012), which we have also witnessed in our own simulations in Chapter 5 and 6. This can reduce the amount of mass reaching the central star, and also provides a mechanism for forming low-mass Pop III stars that may survive until the present day. However, most simulations of Pop III accretion disks have so far neglected the role of magnetic fields. In simulations of present-day star formation, it has been found that sufficiently strong magnetic fields induce a magnetic pressure that adds to the stabilization of accretion disks as well as providing magnetic braking which aids the inward transport of angular momentum (e.g. Hosking & Whitworth, 2004; Machida et al., 2005; Hennebelle & Teyssier, 2008; Price & Bate, 2007; Duffin & Pudritz, 2009; Hennebelle et al., 2011; Peters et al., 2011; Seifried et al., 2011).

So far little is known about the origin and evolution of magnetic fields in the early Universe. It is assumed that the first magnetic fields have occurred in the form of magnetic seed fields of the order of $B = 10^{-30} - 10^{-18}\,\mathrm{G}$ that may have been produced during inflation (Turner & Widrow, 1988), early Universe phase transitions (Sigl et al., 1997) or the Biermann battery mechanism (Biermann, 1950; Xu et al., 2008). An effective mechanism to amplify these weak seed field is the small-scale or turbulent dynamo (SSD) (Kazantsev, 1968; Kulsrud et al., 1997). A procedure of random stretching, twisting and folding of magnetic field lines in a turbulently moving plasma converts kinetic into magnetic energy. The small-scale gas motions during early phases of star formation (Abel et al., 2002; Bromm & Larson, 2004; Wise & Abel, 2007; Greif et al., 2008; Clark et al., 2011a) are efficient enough to drive this dynamo and generate a strong, tangled magnetic field with field strengths of up to $B \sim 10^{-5}\,\mathrm{G}$ (Schleicher et al., 2010; Sur et al., 2012; Peters et al., 2012; Turk et al., 2012; Schober et al., 2012; Schleicher et al., 2013). Most studies in this context, however, only consider the prestellar gas collapse phase and not protostellar accretion disks. In this Chapter we therefore make an attempt to estimate the strength of this tangled field on the scale of the disk and compare it to an estimate of the field strength required to stabilize the disk against gravitational fragmentation. In Section 7.2 we explain our analytical approach. We apply our method to data from Population III protostellar disk from the studies by Clark et al. (2011b) and Greif et al. (2012) as well as to some of our realizations from Chapter 5. The results are described in 7.3 and shortcomings of our study are discussed in 7.4. Finally, we give a conclusion in Section 7.5.

7.2 Method

We make estimations on stabilization of Toomre-unstable Population III protostellar disks found in the studies by Clark et al. (2011b) (black dashed line in figure 2 together with the sound speed values from figure 16) and Greif et al. (2012) (data for all four halos MH1 – MH4 as shown in figure 2 and 3) as well as in five realization of our simulations presented in Chapter 5. In Section 7.2.1, we first describe a version of the Toomre criterion that has been extended to account for magnetic fields within the disk. We present an expression of the saturation field strength of a tangled, small-scale magnetic field gained through amplification via a turbulent dynamo in Section 7.2.2. This expression is then combined with the extended Toomre criterion in Section 7.2.3. The new version of the extended Toomre criterion allows us to examine the size of the change in the Toomre parameter due to the presence magnetic field.

7.2.1 Extended Toomre criterion

The hydrodynamical Toomre parameter (Toomre, 1964) reads

$$Q_{\mathrm{hyd}} = \frac{\kappa\, c_{\mathrm{s}}}{\pi G \Sigma} \tag{7.1}$$

where c_{s} is the speed of sound, κ is the epicyclic frequency, G is the gravitational constant and Σ is the disk surface density. While the disk self-gravity (denominator) induces perturbations and instabilities within the disk, the combined action of thermal pressure and rotation (numerator) acts to stabilize the disk. Consequently, a Toomre parameter of $Q > 1$ indicates a stable disk and $Q < 1$ an unstable one.

For our study here, we use an extended version of the Toomre criterion that takes into account the stabilizing effect of a magnetic field within the disk. We assume that the magnetic field is highly tangled with little large-scale coherence, and hence that we can account for its effects simply by modifying the effective speed of sound used in the Toomre criterion (Kim & Ostriker, 2001). We therefore have

$$Q_{\mathrm{mag}} = \frac{\kappa\,(c_{\mathrm{s}}^2 + v_{\mathrm{A}}^2)^{1/2}}{\pi\, G\, \Sigma}\ , \tag{7.2}$$

Table 7.1: Values of the parameters in Equation 7.4 to compute the efficiency factor ϵ for solenoidal and compressive turbulent driving.

Parameter	solenoidal	compressive
p_0	0.020	0.037
p_1	2.340	1.982
p_2	23.33	-0.027
p_3	2.340	3.601
p_4	1	0.395
p_5	0	0.003
p_6	0	0

where v_A is the Alfvén velocity, $v_\mathrm{A} = B/\sqrt{4\pi\rho}$, which describes the speed in which changes of the magnetic field configurations, with the magnetic field strength B, propagate through a gas of density ρ.

7.2.2 Saturation field strengths of the small-scale dynamo

Weak, small-scale magnetic fields can be rapidly amplified by the turbulent or small-scale dynamo (SSD; e.g. Kazantsev (1968)). In a procedure of random stretching, twisting and folding of magnetic field lines in a turbulently moving plasma, kinetic energy is converted into magnetic energy. The small-scale gas motions during early phases of star formation (Abel et al., 2002; Bromm & Larson, 2004; Wise & Abel, 2007; Greif et al., 2008; Clark et al., 2011b) are efficient enough to drive this dynamo. Thus, initially weak magnetic seed fields can be amplified to dynamically significant values during the gravitational collapse of primordial gas (see e.g. Schober et al., 2012). The final saturation field strength is not known precisely and so we make the following ansatz:

$$\frac{B_\mathrm{sat}^2}{8\pi} = \frac{1}{2}\epsilon\,\rho\,u_\mathrm{turb}^2 \ . \tag{7.3}$$

Here, u_turb is the turbulent velocity and ρ is the disk density. The efficiency factor ϵ accounts for the back-reaction from the field on the turbulence. Its value depends on the nature of the turbulence. We use equation 3 in Federrath et al. (2011a) to compute ϵ for both solenoidal (i.e. divergence-free $\nabla \cdot \mathbf{v} = 0$, where $\mathbf{v}$ is the velocity vector of the fluid) and compressive (i.e. curl-free $\nabla \times \mathbf{v} = 0$) turbulent flows[1]. The original equation is a fitting function for three different quantities. Adapted to the ϵ factor, it reads

$$\epsilon_\mathrm{s,c}(x) = \left(p_0\,\frac{x^{p_1} + p_2}{x^{p_3} + p_4} + p_5\right) x^{p_6} \tag{7.4}$$

where $x = \mathcal{M}_\mathrm{turb} = u_\mathrm{turb}/c_\mathrm{s}$ is the turbulent Mach number and the parameters p_0, p_1, p_2, p_3, p_4, p_5, and p_6 vary for solenoidal and compressive turbulence and are listed in Table 7.1. In Fig. 7.1, the trend of Eq. (7.4) for both types of turbulence is illustrated. We immediately see that ϵ is always larger in the solenoidal compared to the compressive case.

---

[1] We will indicate the type of turbulence by a subscript: "s" for solenoidal and "c" for compressive.

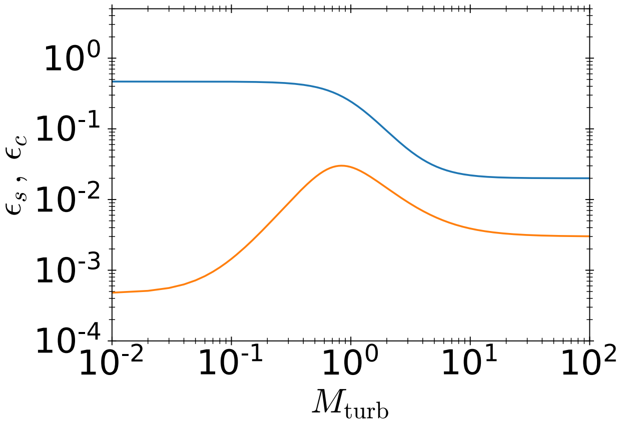

Figure 7.1: Efficiency factor ϵ versus turbulent Mach number M_{turb} for solenoidal (blue) and compressive (orange) turbulence.

7.2.3 Combined formula: Toomre criterion with efficiency factor of the small-scale dynamo

The equation of saturation field strength, Eq. (7.3), can be restructured to

$$\frac{B_{\mathrm{sat}}^2}{4\pi\rho} = \epsilon\, u_{\mathrm{turb}}^2 \tag{7.5}$$

$$v_{\mathrm{A,sat}}^2 = \epsilon\, u_{\mathrm{turb}}^2 \tag{7.6}$$

where we substituted B_{sat} by the corresponding Alfvén velocity, $v_{\mathrm{A,sat}} = B_{\mathrm{sat}}/\sqrt{4\pi\,\rho}$. The extended Toomre criterion, Eq. (7.2), can then be rewritten with Eq. (7.6) so that

$$Q_{\mathrm{mag}} = \frac{\kappa\,\sqrt{c_{\mathrm{s}}^2 + \epsilon\, u_{\mathrm{turb}}^2}}{\pi\, G\, \Sigma}\ . \tag{7.7}$$

If κ, c_{s}, u_{turb}, Σ, and hence Q_{hyd} are known from hydrodynamical simulations, we can compute the size of the ϵ factor and then the magnetic Toomre parameter Q_{mag}. When comparing Q_{mag} with Q_{hyd}, we can see how much a saturated, small-scale tangled magnetic field within the disk increases the value of the Toomre parameter and therefore, in the case of a previously unstable disk with $Q_{\mathrm{hyd}} < 1$, whether this increase is sufficient enough for the disk to now be stabilized in the presence of this magnetic field, i.e. $Q_{\mathrm{mag}} > 1$. As we consider Keplerian disks, instead of the epicyclic frequency, we can employ the Keplerian frequency in the Toomre criterion, i.e. $\kappa = \Omega_{\mathrm{K}}$.

7.3 Results

In our estimations we distinguish two cases: we first examine transonic turbulence with $u_{\mathrm{turb}} = c_{\mathrm{s}}$ in Section 7.3.1, and then mildly supersonic turbulence where $u_{\mathrm{turb}} \gtrsim c_{\mathrm{s}}$ in Section 7.3.2.

Table 7.2: Overview of the results for the models taken from Clark et al. (2011b) (first row) and Greif et al. (2012). From left to right: name of the model, disk radius at which stability is examined, corresponding sound speed, purely hydrodynamical Toomre parameter, and magnetic Toomre parameter derived with ϵ–parameter for solenoidal ($\epsilon_s = 0.24$) and compressive ($\epsilon_c = 0.03$) turbulent forcing. The values in the first line were extracted from fig. 2 (dashed black line) in Clark et al. (2011b). The other rows correspond to fig. 2 and 3 in Greif et al. (2012), in which disk properties of protostellar systems in four different minihalos (MH1 – MH4) are plotted. The values were extracted at disk radii for which the respective (hydrodynamical) Toomre parameter indicated an unstable disk according to $Q_{\rm hyd} < 1$. The values of the magnetic Toomre parameter were computed via Eq. (7.9). The ϵ parameter values used here were calculated with Eq. (7.4) where $x = M_{\rm turb} = 1$ because of transonic turbulence.

Model	R [AU]	c_s [km s^{-1}]	$Q_{\rm hyd}$	$Q_{\rm mag,s}$	$Q_{\rm mag,c}$
Clark	20	2.0	0.70	0.91	0.72
MH1	10	2.5	0.90	1.17	0.93
MH2	1	3.5	0.70	0.91	0.72
MH2	10	2.5	0.75	0.98	0.77
MH3	1	4.0	0.60	0.78	0.62
MH3	10	2.5	0.60	0.78	0.62
MH4	1	4.5	0.65	0.85	0.67
MH4	10	2.5	0.55	0.72	0.57

7.3.1 Transonic turbulence: $u_{\rm turb} = c_{\rm s}$

For transonic turbulence, Eq.(7.7) can be further simplified to

$$Q_{\rm mag} = \frac{\Omega_{\rm K}\, c_{\rm s} \sqrt{1+\epsilon}}{\pi G \Sigma} \tag{7.8}$$

$$= \sqrt{1+\epsilon}\; Q_{\rm hyd}\ . \tag{7.9}$$

The efficiency factor takes the values $\epsilon_{\rm s} \approx 0.24$ and $\epsilon_{\rm c} \approx 0.03$. The results for the data extracted from Clark et al. (2011b) and Greif et al. (2012) are listed in Table 7.2. We find that in almost all cases $Q_{\rm mag} < 1$ regardless of the nature of turbulence, implying that in general the magnetic field is not strong enough to stabilize the disk. The only case in which the field (only from solenoidal turbulence) is strong enough to provide stabilization (run MH1 in Greif et al. 2012) is unusual in that the disk is already very close to stability ($Q_{\rm hyd} \sim 0.9$), and so only a little extra support is needed to provide complete stabilization. Our findings are further illustrated in Fig 7.2 (a). We see clearly that although all *cyan* (compressive) and *dark blue* (solenoidal) triangles and circles lie above the *red* ($Q_{\rm hyd}$) symbols, there is only one *dark blue* triangle that also is above the dashed black line that marks the transition value $Q = 1$ from disk instability $Q < 1$ to stability $Q > 1$. This is the data point for MH1, for which the small-scale dynamo produces a sufficiently amplified magnetic field in case of our assumed model of solenoidally driven, transonic turbulence to provide disk stabilization according to the extended Toomre criterion in equation (7.2).

We see a similar trend for the data from our own simulations. The detailed results are given in column 10 and 12 of Table 7.3 and in the five plots in 7.2 (b). Neither compressive nor solenoidal transonic turbulent motions are strong enough to create a disk-stabilizing small-scale magnetic field. There are only two realizations, α005-2 at $R = 13.9$ AU and $\alpha 025\beta 01$-1 at $R = 8.2$ AU with $Q_{\rm mag,s} \sim 0.96$ and $Q_{\rm mag,s} \sim 0.98$

Table 7.3: Overview of disk property values and results of the magnetic Toomre parameter for some selected realizations taken from the study in Chapter 5. For each model, we consider two different radii. From left to right: name of the realization, disk radius at which stability is examined, corresponding disk surface density, Kepler frequency, sound speed, turbulent velocity, turbulent Mach number, hydrodynamical Toomre parameter, and combinations of ϵ efficiency factor together with corresponding magnetic Toomre parameter. Here, we distinguish between transonic turbulence indicated c_s in brackets behind the parameter, and mildly supersonic turbulence where u_turb is put in the brackets. Parameters corresponding to compressive or solenoidal turbulent driving are denoted with subscript "c" or "s" respectively. The transonic magnetic Toomre parameter were computed with with Eq. (7.9) using $\epsilon_c = 0.03$ and $\epsilon_s = 0.24$. For the supersonic case we applied Eq. (7.7) with turbulent velocities derived via Eq. (7.10). The ϵ factor values were calculated with Eq. (7.4) according to the specific $x = M_\mathrm{turb} = u_\mathrm{turb}/c_\mathrm{s}$ in each model. The data is extracted at times directly after first sink formation.

Realization	R [AU]	Σ [$\mathrm{g\,cm^{-2}}$]	Ω_K [$\mathrm{s^{-1}}$]	$\mathrm{c_s}$ [$\mathrm{km\,s^{-1}}$]	$\mathrm{u_{turb}}$ [$\mathrm{km\,s^{-1}}$]	M_turb	$\mathrm{Q_{hyd}}$	$\epsilon_\mathrm{c}(\mathrm{c_s})$	$\mathrm{Q_{mag,c}(c_s)}$	$\epsilon_\mathrm{s}(\mathrm{c_s})$	$\mathrm{Q_{mag,s}(c_s)}$	$\epsilon_\mathrm{c}(\mathrm{u_{turb}})$	$\mathrm{Q_{mag,c}(u_{turb})}$	$\epsilon_\mathrm{s}(\mathrm{u_{turb}})$	$\mathrm{Q_{mag,s}(u_{turb})}$
β01-1	2.8	4.1e+04	1.6e-08	3.5	10.8	3	0.66	0.03	0.67	0.24	0.74	0.009	0.69	0.049	0.81
	4.8	1.9e+04	9.9e-09	3.2	11.7	3	0.80	0.03	0.81	0.24	0.89	0.008	0.84	0.040	0.99
α025-5	2.8	2.7e+04	1.3e-08	3.4	11.1	3	0.79	0.03	0.80	0.24	0.88	0.008	0.82	0.047	0.96
	23.7	3.0e+03	1.6e-09	2.7	10.1	3	0.71	0.03	0.72	0.24	0.80	0.007	0.75	0.039	0.89
α005-2	4.8	2.2e+04	8.6e-09	3.2	14.1	4	0.61	0.03	0.61	0.24	0.68	0.006	0.64	0.033	0.78
	13.9	4.6e+03	3.0e-09	2.8	15.2	5	0.86	0.03	0.87	0.24	0.96	0.005	0.93	0.028	1.17
α025β01-1	3.7	2.6e+04	1.2e-08	3.2	10.5	3	0.69	0.03	0.70	0.24	0.77	0.008	0.72	0.047	0.84
	8.2	8.2e+03	5.2e-09	2.8	8.8	3	0.87	0.03	0.88	0.24	0.97	0.009	0.90	0.050	1.05
α005β001-4	3.7	3.2e+04	1.2e-08	3.4	9.5	2	0.59	0.03	0.60	0.24	0.66	0.010	0.62	0.056	0.71
	258.8	1.3e+02	7.7e-11	2.5	6.2	2	0.72	0.03	0.73	0.24	0.81	0.011	0.75	0.068	0.86

respectively, where solenoidal turbulence comes close it. As above, in both cases the hydrodynamical Toomre parameter is already quite high with $Q_{\mathrm{hyd}} \sim 0.86$ and $Q_{\mathrm{hyd}} \sim 0.87$.

7.3.2 Supersonic turbulence: $u_{\mathrm{turb}} \gtrsim c_{\mathrm{s}}$

From the example realizations of our simulations from Chapter 5, we can also compute mass-weighted average turbulent velocities. For that we divide a radius of $1000\,\mathrm{AU}$ around the first sink particle into 39 spherical, logarithmically-spaced bins and derive a mass-weighted average of the turbulent velocity of gas with $n > 10^9\,\mathrm{cm}^{-3}$ within each bin[2] via

$$u_{\mathrm{turb}} = \sqrt{\frac{1}{M}\sum m_{\mathrm{i}}(\mathbf{v}_{\mathrm{i}} - \mathbf{v}_{\mathrm{rad}} - \mathbf{v}_{\mathrm{rot}})^2}\ , \tag{7.10}$$

where M is the total mass of a bin i, $\mathbf{v}_{\mathrm{rad}}$ and $\mathbf{v}_{\mathrm{rot}}$ the mass-weighted radial and rotational velocity vectors of this bin, and m_{i} and $\mathbf{v}_{\mathrm{i}}$ are the mass and the velocity vector of a cell i within the bin. The rotational velocity is computed by summing up the angular momentum of all cells within this bin and by dividing this by the total mass within the bin and the radius of the bin. We find mildly supersonic turbulent velocities with turbulent Mach numbers typically of the order of $\mathcal{M}_{\mathrm{turb}} \sim 2-3$. The highest value is $\mathcal{M}_{\mathrm{turb}} \sim 5$ for realization $\alpha 005$-2 at $R = 13.9\,\mathrm{AU}$.

Our results are listed in column 14 and 16 of Table 7.3. In two realizations, $\alpha 005$-2 and $\alpha 025\beta 01$-1 (at $R = 13.9\,\mathrm{AU}$ and $R = 8.2\,\mathrm{AU}$ respectively), solenoidal turbulent driving can create a sufficiently high small-scale magnetic field for disk stabilization. Indeed, we have encountered these two runs already in Section 7.3.1 above where their solenoidal magnetic Toomre parameter values were already close to $Q \sim 1$. Here, we further find that also the values for compressive turbulence of these two realizations are high with $Q_{\mathrm{mag,c}}(u_{\mathrm{turb}}) \geq 0.9$. Comparably high values can also be seen for solenoidal turbulent driving in $\beta 01$-1 (at $R = 4.8\,\mathrm{AU}$) and $\alpha 025$-5 (at $R = 2.8\,\mathrm{AU}$). Our findings are furthermore shown in 7.2 (b) denoted by circles. While the *cyan* circles describing the compressive values overall still lie at levels similar to the *red* triangles, i.e. the Q_{hyd} values, the *dark blue* circles of the solenoidal values take higher positions. In four out of five cases, the *dark blue* circles are close to or already above the dashed line of $Q = 1$.

7.4 Discussion

We acknowledge that we have made several simplified assumptions and that our results are highly speculative. In the following, we discuss some important shortcomings of our study.

The efficiency parameter ϵ of the small-scale dynamo depends upon the turbulent power-spectrum and the driving mechanism of the turbulence. As gas is compressible by nature, a realistic turbulent power spectrum for the turbulent velocity may be somewhat steeper than the 3D Kolmogorov spectrum for incompressible turbulence ($P(k) \propto k^{-11/3}$; Kolmogorov 1941). Often $P(k) \propto k^{-4}$ is used (see e.g. Goodwin et al., 2004a,b; Clark et al., 2011a). The fit formula of Federrath et al. (2011a) with which we compute our ϵ value, is derived from externally-driven solenoidal and compressive

---

[2] We choose this density threshold in order to study the gas within the protostellar disk specifically (see also e.g. Stacy et al., 2010; Stacy & Bromm, 2014)

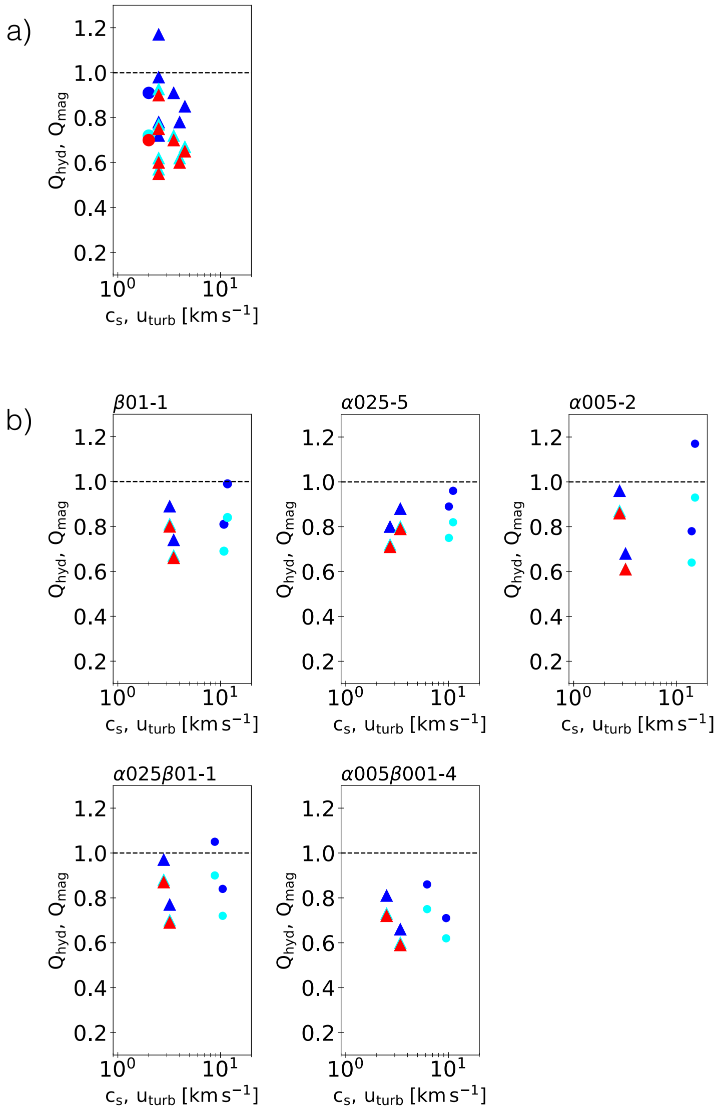

Figure 7.2: Hydrodynamical (red symbols) and magnetic (cyan symbols for compressive and dark blue symbols for solenoidal turbulence) Toomre parameter versus the sound speed or the turbulent velocity. The black dashed line at $Q = 1$ indicates the transition between disk instability $Q < 1$ and stability $Q > 1$. Plot (a): results for the models taken from Clark et al. (2011b) (circles) and Greif et al. (2012) (triangles). For these two datasets just transonic turbulence was considered. Only in one setup of Greif et al. (2012), described by the single dark blue triangle above the black dashed line, solenoidal turbulent driving can yield a saturated, small-scale magnetic field that is strong enough to stabilize the unstable protostellar disk. Plot (b): overview of the results of our five example realizations from Chapter 5. For all five models, both transonic (triangles) and mildly supersonic (circles) turbulence were examined. Supersonic, solenoidal turbulent driving is able to create disk-stabilizing small-scale magnetic fields in two, almost three cases (α005-2, α025β01-1, and possibly β01-1). In all realizations, transonic turbulence is not effective enough to amplify a small-scale magnetic field to values high enough for disk stabilization.

turbulence. In their study with self-consistently evolving turbulence, Sur et al. (2012) find ϵ–values of $0.2-0.4$ at the end of their simulation. However, Sur et al. (2012) only considered the evolution of magnetic field amplification during the prestellar gas collapse phase and during the initial protostellar accretion phase but stop their simulation before they can examine the just forming accretion disk. Natural driving mechanism of turbulence in accretion disks may be for example accretion itself or processes such as the magneto-rotational instability (see e.g. Balbus & Hawley, 1998, for a review). To account for the uncertainties in our approach, it is a reasonable choice to span a wider parameter space by considering several ϵ–values for both types of turbulent driving.

Furthermore, Greif et al. (2012) find that the protostars which develop in their disks are puffed-up objects. In particular, some of their primary protostars evolve to radii as large as $\sim 200\,\mathrm{R}_{\odot} \sim 1\,\mathrm{AU}$. Hence, the star can extend beyond radii which we considered to be part of the protostellar disk in our analysis of the data from Greif et al. (2012). However, we extracted our values at a time during which the radii of the primary protostars were still considerably smaller than 1 AU.

For the study of mildly supersonic turbulence, we extract disk data from our realizations at a time just after the formation of the first sink particle. This ensures that the protostellar disk is roughly Keplerian and that the turbulent velocities we derive are only slightly in the supersonic regime; see also Fig. 5.11 - 5.13. Higher supersonic gas motions likely change the appearance of our Pop III protostellar disks considerably, e.g. through shocks, so that its Keplerian character and its overall shape may not be preserved for a long time. Indeed, we observe that our protostellar systems are highly dynamical and in particular the disk environment of runs including turbulence changes dramatically already over the short period covered by our simulations; see e.g. Fig. 5.14 for example velocity profiles 50 years after the first sink particles has formed, or Fig. 5.16 for an overview of the evolution of realization $\alpha 005\beta 001$-4 illustrated in density projections. While the Toomre criterion can also be defined for supersonic turbulence, its validity may no longer be given when the disk appearance changes dramatically, i.e. the disk becomes very thick or is dissolves into a more filamentary structure (Toomre, 1964).

7.5 Conclusions

We have combined an extended Toomre criterion, which takes into account the stabilizing effect of a magnetic field within the disk, with an expression for the saturation magnetic field strength of a small-scale tangled magnetic field after amplification via the small-scale, turbulent dynamo. Through this combination, we derive an expression for a magnetic Toomre-stability parameter that depends on the hydrodynamical Toomre parameter and the efficiency parameter of the turbulent dynamo. This relation allows us to estimate whether a Toomre-unstable protostellar disk in a purely hydrodynamical environment may be stabilized through the presence of a saturated small-scale magnetic field.

We apply our formula on data taken from some of the highest-resolution simulations until today by Clark et al. (2011b) and Greif et al. (2012) as well as some of the realizations from our study presented in Chapter 5. The data corresponds to disk evolution for $t < 100\,\mathrm{yr}$ after first sink formation. Our simple estimates show that small-scale dynamo action alone does not seem to be able to produce a strong enough magnetic field to stabilize a Population III accretion disk, unless the disk is already very close to stability and/or mildly supersonic. However, we find that in many cases, Q_{mag}

is close to $Q = 1$, demonstrating that the effects of the field cannot be completely neglected. Whether partial disk stabilization is possible and how the disk stability evolves over a longer time period, needs to be addressed by detailed numerical computations.

It is possible that at later times the small-scale field will be further amplified and will evolve into a large-scale, coherent field via the α-Ω–dynamo (e.g. Steenbeck & Krause, 1966; Vainshtein & Ruzmaikin, 1971; Ruzmaikin et al., 1988; Pudritz & Silk, 1989; Arshakian et al., 2009). Then other magnetic field related processes which affect the mass growth and with that the stability of the disk, e.g. jets and outflows (e.g. Blandford & Payne, 1982; Machida et al., 2008a), also need to be accounted for.

CHAPTER 8

The fragmentation behavior of Population III protostellar disks in presence of a uniform magnetic field

We note that the content presented in this chapter is considered preliminary. This is because the numerical methods, particularly the use of the ideal magnetohydrodynamics module of AREPO with its divergence cleaning scheme in combination with the sink particle module is still under development in order to adapt it to our numerical needs. Furthermore, we so far have performed test simulations of only two out of the 45 realizations of Chapter 5 which we want to study. This said, the results presented in this chapter have to be treated with caution but give a first insight into the numerical performance and possible physical effects of the presence of magnetic fields in the context of Population III star formation and protostellar disk evolution. I performed the test simulations, analyzed them, created the figures, and wrote the text. Simon C. O. Glover contributed to the interpretation and discussion of the results. Paul C. Clark and Rüdiger Pakmor provided useful ideas regarding the analysis of the numerical performance.

8.1 Introduction

The first magnetic seed fields possibly appeared already very early in the history of the Universe. It is assumed that they may have been created during inflation (Turner & Widrow, 1988), early Universe phase transitions (Sigl et al., 1997) or the Biermann battery mechanism (Biermann, 1950; Kulsrud et al., 1997; Xu et al., 2008). They were still very weak with field strengths of the order of $B = 10^{-30} - 10^{-18}\,$G. But there are ways that may have amplified them to dynamically important magnitudes early-on in the formation of the first structures. Turbulent gas motion arising for example as gas falls into dark matter halos (Wise & Abel, 2007; Greif et al., 2008), as gas is accreted into the center of the halo (e.g. Klessen & Hennebelle, 2010; Elmegreen & Burkert, 2010; Federrath et al., 2011b), or as it condenses to form the first stars, the so-called Population III (Pop III) stars (e.g. Sur et al., 2010; Clark et al., 2011b; Turk et al., 2012) are sufficient to drive a small-scale dynamo (SSD) (Kazantsev, 1968; Kulsrud et al., 1997). In a procedure of random stretching, twisting and folding of magnetic field lines a strong tangled field of up to $B \sim 10^{-5}\,$G is generated (Arshakian et al., 2009; Schleicher et al., 2010; Sur et al., 2010, 2012; Schober et al., 2012; Turk et al., 2012).

Observations of present-day magnetic fields ranging from cloud core scales (e.g.

Girart et al., 2006, 2009) to galactic dimensions (e.g. Beck, 2015, for a review) find mainly large-scale coherent fields. A mechanism such as the α-Ω dynamo that operates in differentially rotating disks may order small-scale tangled field into a coherent, large-scale structure (e.g. Steenbeck & Krause 1966; Vainshtein & Ruzmaikin 1971; Arshakian et al. 2009; and in particular in primordial context Pudritz & Silk 1989; Tan & Blackman 2004).

From numerical studies of present-day star formation it is known that magnetic fields can affect the star-forming process in many ways. For example they effectively transfer angular momentum by magnetic braking in circumstellar disks (e.g. Mouschovias & Paleologou, 1979; Mellon & Li, 2008, 2009; Hennebelle & Ciardi, 2009; Hennebelle et al., 2011; Commerçon et al., 2011), or through jets and outflows (Blandford & Payne, 1982; Konigl & Pudritz, 2000; Banerjee & Pudritz, 2006). Furthermore, magnetic pressure can support circumstellar disks against fragmentation (e.g. Hosking & Whitworth, 2004; Machida et al., 2005; Hennebelle & Teyssier, 2008; Duffin & Pudritz, 2009; Peters et al., 2011; Seifried et al., 2011).

Cosmological simulations have shown that Population III stars formed in dark matter minihalos of mass $\sim 10^5 - 10^6\,\mathrm{M}_\odot$ at redshift $z \sim 20 - 50$ (Tegmark et al., 1997; Bromm & Larson, 2004; Glover, 2005; Bromm, 2013). Initially it was concluded from numerical studies that Pop III stars form as single, massive objects (see e.g. Abel et al., 2002; Bromm et al., 2002; Bromm & Larson, 2004). Simulations within the last decade, however, have found that a Pop III stellar cluster is created due to the fragmentation of the protostellar disk that arises because of non-zero angular momentum in the collapsing, star-forming gas cloud (Greif et al., 2011; Clark et al., 2011b,a; Smith et al., 2011, 2012; Stacy & Bromm, 2013; Stacy et al., 2016).

Examining the formation of Population III stars under the influence of primordial magnetic fields has received increasing attention only recently (e.g. Tan & Blackman, 2004; Maki & Susa, 2004; Silk & Langer, 2006; Machida et al., 2006; Maki & Susa, 2007; Schleicher et al., 2010; Sur et al., 2010; Federrath et al., 2011b; Sur et al., 2012; Turk et al., 2012; Latif & Schleicher, 2016). The evolution of protostellar disk and possible fragmentation has been studied in just a few numerical studies so far (Machida et al., 2008a; Machida & Doi, 2013; Peters et al., 2014). Machida et al. (2008a) and Machida & Doi (2013) performed parameter studies of the collapse of primordial Bonnor-Ebert spheres with different levels of rotation and magnetic field strengths. They consider large-scale, uniform magnetic fields that are directed parallel to the rotation axis. They found that both magnetic braking and magnetically-driven outflows and jets effectively redistribute angular momentum which leads to disk stabilization or even prevents disk formation in case of strong magnetic fields (the so-called magnetic braking catastrophe). Peters et al. (2014) examined the influence of a small-scale, turbulent magnetic field on the collapse of a rapidly rotating gas cloud that they extracted from one of the halos in the cosmological simulation by Greif et al. (2011). They find that magnetic pressure supports the protostellar disk against fragmentation and only a single Pop III star forms.

In the following study, we want to address what influence a large-scale uniform magnetic field of size $B = 5 \times 10^{-6}\,\mathrm{G}$ has on the collapse of our Bonnor-Ebert sphere setups from Chapter 5. In particular we are interested whether the presence of the magnetic field leads to stabilization of the protostellar disks and results in a reduction in the total number of sinks that form. We are further interested in examining the total mass growth of the sinks and of individual sinks and want to check whether the influence of the magnetic field, e.g. via disk stabilization, promotes the formation of a few rapidly growing, very massive sinks as has been observed in some simulations in present-day star formation (e.g. Wang et al., 2010; Peters et al., 2011). Finally, in order to estimate the quality of our physical results, we will perform two analyses on the performance of our numerical method in particular regarding the divergence cleaning scheme and an additional MHD refinement criterion.

This chapter is structured as follows: in Section 8.2 the numerical method and the initial conditions are explained. Our results are described in Section 8.3. In Section 8.4, we examine the performance of our ideal MHD computations. The discussion and conclusion are presented in Section 8.5.

8.2 Methods

8.2.1 Numerical approach

The simulations in this chapter were performed with the Voronoi moving-mesh magnetohydrodynamics (MHD) code AREPO (Springel, 2010; Pakmor et al., 2011). Our version of the code contains recent updates of the time integration scheme, the spatial gradient reconstruction and the grid regularization (Pakmor et al., 2016; Mocz et al., 2015). The ideal MHD gas dynamics were modeled with the HLLD Riemann solver (Miyoshi & Kusano, 2005). The Powell divergence cleaning scheme was applied (Powell et al., 1999; Pakmor & Springel, 2013). For some of our runs, we in addition use a recently implemented MHD refinement criterion that refines a cell when the value of the spurious magnetic field divergence, $\nabla\cdot\mathbf{B}$, has become large so that $2r_{\rm cell}\,\nabla\cdot\mathbf{B}/B > C$ where $C = 0.1$, $r_{\rm cell}$ is the cell radius, and B is the magnetic field strength[1]. Ideal MHD is applicable to Population III star formation as the ionization degree in primordial gas is sufficiently high for a strong coupling between ions, electrons and neutrals, i.e flux freezing is maintained (Maki & Susa, 2004, 2007).

Our simulation box has a side length of 13 pc and reflective boundary conditions. The mesh consists initially of 128^3 cells. We employ a Jeans (de-)refinement criterion that ensures that the Jeans length is resolved by a specific number of cells, which is 16 cells per Jeans length in our runs. Furthermore, we use sink particles with a formation threshold density of $n = 10^{15}\,{\rm cm}^{-3}$ and an accretion radius of $r_{\rm acc} = 2\,{\rm AU}$. For further details of the numerical method, including our primordial chemistry network and the sink particle module, see Section 3.2.

8.2.2 Initial conditions

Our simulations are carried out at a redshift of $z = 20$. Since the gas in our simulations is always warmer than the cosmic microwave background and is not strongly affected by Compton cooling, the exact redshift should not be important. We perform two MHD simulations for each of the realizations α025-5 (i.e. purely subsonic turbulence with $\alpha = 0.25$) and β01-1 (i.e. purely rotational with $\beta = 0.1$) from Chapter 5. The initial conditions are identical to what we have described in Section 5.2.2 but we briefly recap the most important points in the following. We start with a Bonnor-Ebert sphere of mass $\rm M_{BE} = 2671\,M_\odot$, radius $\rm R_{BE} = 1.87\,pc$, and density $\rho_c = f \times \rho_{\rm BE}(0) \simeq 3.7 \times 10^{-20}\,{\rm g\,cm}^{-3}$ ($n_c \simeq 1.83 \times 10^4\,{\rm cm}^{-3}$), which is enhanced by a factor $f = 1.83$. The sphere resides within a uniformly dense environment with density $\rho_{\rm ext} = \rho_{\rm BE}(R_{\rm BE}) \simeq 2.7 \times 10^{-21}\,{\rm g\,cm}^{-3}$ ($n_{\rm ext} \simeq 1.31 \times 10^3\,{\rm cm}^{-3}$). The temperature inside and outside the

---

[1] We will sometimes denote the divergence of the magnetic field $\nabla\cdot\mathbf{B}$ as "divB" in our discussion and in the figures.

sphere are the same: $T_{\mathrm{BE}} = T_{\mathrm{ext}} = 200\,\mathrm{K}$. In the purely rotational run, a rigid rotation around the geometrical z-axis is added to the sphere. The initial frequency is $\Omega_0 = 3.1 \times 10^{-14}\,\mathrm{s}^{-1}$ and the rotational β parameter is $\beta = E_{\mathrm{rot}}/|E_{\mathrm{grav}}| = 0.1$. In the purely turbulent setup, a non-driven, subsonic turbulent velocity component with a power spectrum of $P(k) \propto k^{-4}$ is superimposed onto the BE sphere. The initial turbulent α parameter is $\alpha = E_{\mathrm{turb}}/|E_{\mathrm{grav}}| = 0.25$. The density enhancement was introduced to reduce the ratio of thermal energy to gravitational energy to $\alpha_{\mathrm{therm}} = E_{\mathrm{therm}}/|E_{\mathrm{grav}}| \simeq 0.451$ in order to guarantee that the BE sphere would still collapse when additional physics such as rotation, turbulence or magnetic fields are added. For the studies in this chapter, we add a large-scale, uniform magnetic field in z-direction with initial field strength $B_0 = 5 \times 10^{-6}\,\mathrm{G}$ to our simulation box. The magnetic field can be further described by its mass-to-flux ratio (Mouschovias & Spitzer, 1976)

$$\mu = \frac{M}{\Phi}\bigg/\left(\frac{M}{\Phi}\right)_{\mathrm{crit}} \tag{8.1}$$

where $\Phi = B_0\,R^2\pi$ is the flux of the magnetic field with initial field strength B_0 through the cross section of our cloud of mass M and radius R, and

$$\left(\frac{M}{\Phi}\right)_{\mathrm{crit}} = \frac{c_1}{3\pi}\sqrt{\frac{5}{G}} \tag{8.2}$$

is the critical mass-to-flux ratio with $\mathrm{c}_1 = 0.53$ (Strittmatter, 1966; Mouschovias & Spitzer, 1976), and G is the gravitational constant. For our Bonnor-Ebert sphere we estimate $\mu \simeq 21$. Our field strength value is motivated on the one hand from previous simulations of the amplification of primordial magnetic seed fields by the small-scale dynamo that find saturation field strengths of the the order $B \sim 10^{-6}\,\mathrm{G}$ (Sur et al., 2010, 2012; Schober et al., 2012). On the other hand, we follow the work by Machida et al. (2008a) who investigate the collapse of rotating primordial Bonnor-Ebert spheres in presence of large-scale, uniform magnetic fields with initial field strengths $B_0 \sim 10^{-9} - 10^{-5}\,\mathrm{G}$. Our combination of $\beta = 0.1$ and $B = 5 \times 10^{-6}\,\mathrm{G}$ with $\mu \sim 20$ is roughly comparable to their model 5 with $\beta = 0.1$ and $B = 10^{-6}\,\mathrm{G}$ with $\mu = 30$ which is observed to be in a transition zone between partial to full stabilization of the protostellar disk as well as launching of a jet. We therefore expect our magnetic field to be dynamically important and to observe interesting features in particular regarding disk stabilization.

8.3 Results

8.3.1 Formation time of the first sink

We find that the presence of an initially uniform magnetic field, delays the onset of sink formation in case of the purely rotational runs ($\Delta t \sim 8700\,\mathrm{yr}$) but shifts it to earlier times in the purely turbulent realizations ($\Delta t \sim 3800\,\mathrm{yr}$). This effect is, however, still small, i.e. $\Delta t < 0.01\,\mathrm{Myr}$. The difference between the MHD runs with and without the additional divB refinement is $\Delta t < 0.2\,\mathrm{kyr}$. As we have already discussed in greater detail in Chapter 5, the free-fall time of the cloud is $t_{\mathrm{ff}} = \sqrt{3\pi/(32G\rho_{\mathrm{c}})} \simeq 0.34\,\mathrm{Myr}$. The formation of the first sink takes more than twice as long due to the significant thermal pressure within the cloud that counteracts the gravitational infall. The presence of a magnetic field does not affect this considerably here.

Table 8.1: Overview of the test setups. From left to right: name of the realization, values of the α and β parameter, time of first sink formation, $\mathrm{t_{SF}}$, total number of sinks, N_{tot}, and total mass in sinks, M_{tot}, at $t \sim 1000\,\mathrm{yr}$, average accretion rate $\langle \dot{M} \rangle$, number of sinks $N_{\mathrm{tot,comp}}$ when mass in sinks $M_{\mathrm{tot,comp}}$ is reached.

Realization	α	β	$\mathrm{t_{SF}}$/Myr	N_{tot}	$M_{\mathrm{tot}}/M_{\odot}$	$\langle \dot{M} \rangle/(\mathrm{M_{\odot}\,yr^{-1}})$	$N_{\mathrm{tot,comp}}$	$M_{\mathrm{tot,comp}}/M_{\odot}$
α025-5	0.25	-	0.744704	118	74.3	7×10^{-2}	16	9.4
α025-5-nodivB	0.25	-	0.740864	11	9.7	1×10^{-2}	11	9.3
α025-5-divB	0.25	-	0.740814	12	14.8	2×10^{-2}	5	9.3
β01-1	-	0.1	0.742465	49	36.8	4×10^{-2}	23	9.2
β01-1-nodivB	-	0.1	0.742935	23	10.4	1×10^{-2}	23	9.2
β01-1-divB	-	0.1	0.751169	20	10.0	1×10^{-2}	18	9.2

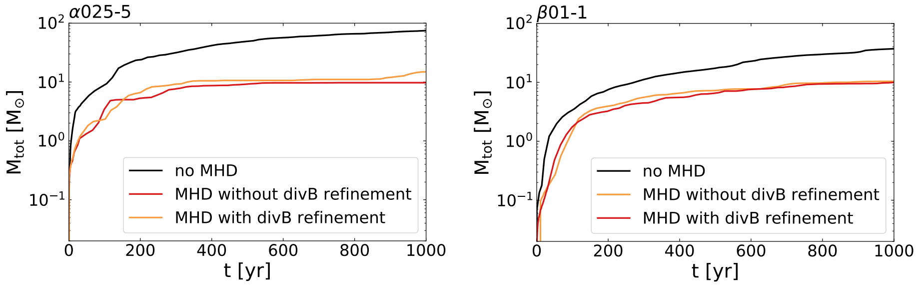

Figure 8.1: Evolution of the total mass in sinks, M_{tot}, in the purely turbulent realizations (left panel) and the purely rotational realizations (right panel). M_{tot} decreases when in addition to turbulence and rotation a magnetic field is included in our simulations. The difference between the runs with and without additional divB refinement is tiny.

8.3.2 Number and mass of sinks formed

Both the total number of sinks, N_{tot}, and the total mass in sinks, M_{tot}, is reduced in the presence of a magnetic field in addition to rotation and turbulence. This is illustrated in Fig. 8.1 & 8.2, and the exact values at $t \sim 1000\,\mathrm{yr}$ are given in Table 8.1. While in the original model α025-5 without magnetic fields 118 sinks were created within $t \sim 1000\,\mathrm{yr}$ (see also Chapter 5 for more details), this quantity becomes a factor of ten smaller when a magnetic field of initially $B = 5 \times 10^{-6}\,\mathrm{G}$ is included. Something similar is true for the purely rotational run in which the total number of sinks in the MHD run is smaller than half of the value in the run without a magnetic field.

The evolution of the total mass in sinks is dramatic. M_{tot} decreases by a factor of five to eight in the purely turbulent run and by a factor of more than three in the purely rotational model. Within $t \sim 1000\,\mathrm{yr}$, the runs including magnetic fields have only just approached or exceeded $M_{\mathrm{tot}} = 10\,\mathrm{M_{\odot}}$, whereas the runs without MHD pass this mass value already early on in their evolution, usually at $t \lesssim 500\,\mathrm{yr}$.

In Fig. 8.3, we see that the MHD mass functions at $t \sim 1000\,\mathrm{yr}$, although they include fewer sinks, follow roughly the shape of the non-MHD distribution. There is no significant difference except that the upper mass limits are at smaller masses compared to the non-MHD cases. We also compared the mass functions when all three realizations of a setup have reached about the same total mass in sinks. The results are displayed in Fig. 8.4 and the exact values are listed in Table 8.1. While for setup α025-5 we find a reduction of the number of sinks in the MHD realization, for setup β01-1 there is no or only a slight decrease. Overall, we conclude that the total mass in

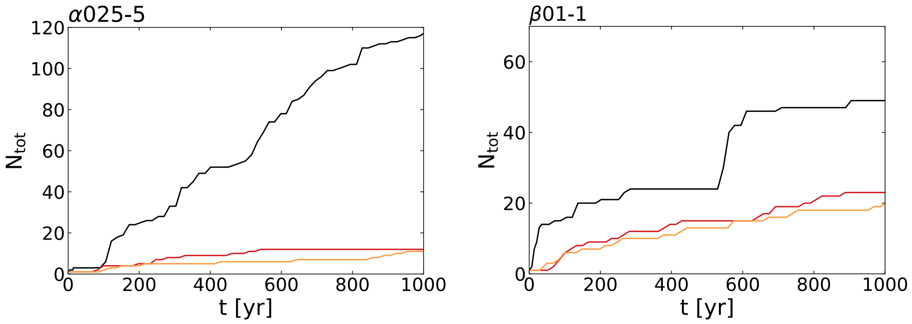

Figure 8.2: Number evolution in the purely turbulent model (left panel) and the purely rotational model (right panel). The total number of sinks decreases considerably in the presence of a magnetic field in addition to turbulence and rotation. The color scheme is the same as in Fig. 8.1.

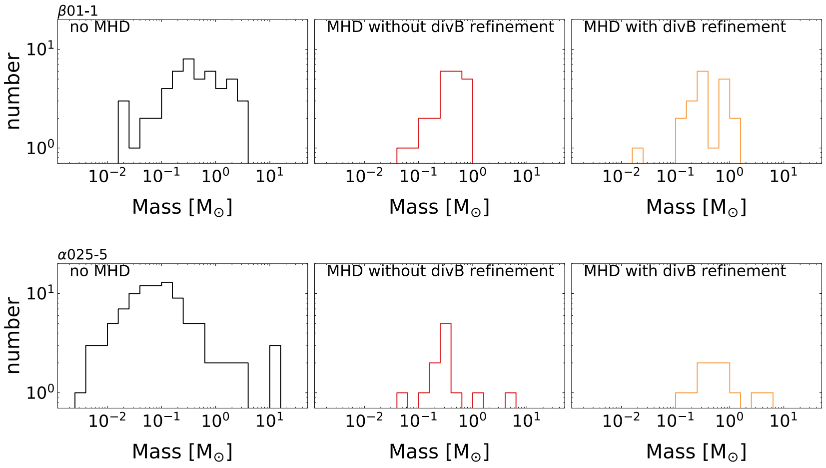

Figure 8.3: Comparison of the sink mass functions at $t \sim 1000\,\mathrm{yr}$.

sinks is more affected by the magnetic field than the number of sinks.

8.3.3 Accretion history

The cumulative accretion rate[2] in MHD runs is on average smaller and more strongly variable than in runs without a magnetic field. This leads to a reduced total mass in sinks in the MHD runs. Such behavior was also reported in present-day star formation (e.g. Peters et al., 2011). The average accretion rate values are listed in Table 8.1. An overview of the time evolution of the sink mass growth and accretion rates is given in Fig. 8.5. We immediately see the sharp drops of the cumulative accretion rates (blue dashed lines) but also in the accretion rates of the first (red line) and most massive sinks (orange line) in MHD runs. These sudden drops are a reaction to the expansion of a magnetically driven bubble that perturbs the disk configuration and pushes material away from the sinks so that accretion process is disturbed. The evolution of the bubble

---

[2] This is the sum of the accretion rates of all sinks.

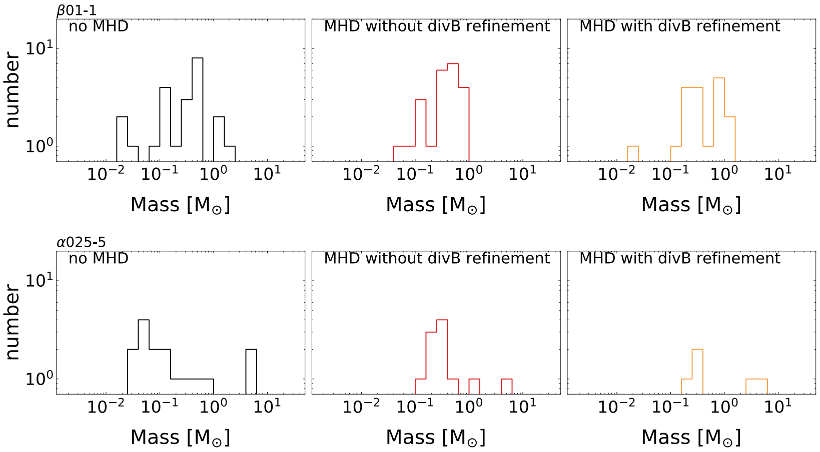

Figure 8.4: Comparison of the sink mass functions at the same total mass in sinks per setup. For β01-1 this is $M_{\rm tot,comp} \sim 9.2$, and for α025-5 it is $M_{\rm tot,comp} \sim 9.3 - 9.4$. While the MHD realizations of purely turbulent setup show a decrease in the number of sinks compared to the non-MHD case, it stays about the same for all realizations of β01-1.

is displayed in Fig. 8.6, 8.7 & 8.8. The bubble originates from the inner disk region and is driven by magnetic pressure. Together with material that is being funneled through the accretion disk to the center of the disk where the accreting sinks are, also large amounts of magnetic flux are transported. The magnetic field accumulates there in the center of the disk as it cannot diffuse outwards due to the ideal MHD condition. The magnetic pressure eventually is strong enough to balance or even counteract on the gravitational infall of material, thereby pushing material away from disk center and reducing the magnetic flux. Such bubbles have been observed in previous ideal MHD studies in present-day star formation (e.g. Zhao et al., 2011; Seifried et al., 2011; Peters et al., 2011; Seifried et al., 2013). Machida et al. (2008a) reported that one of their setups develops a jet that has similar structure to a magnetically-driven bubble.

In Fig. 8.5, we see that the cumulative accretion rate is less affected in the purely rotational run. Here, the magnetic pressure can more easily dilute along the less dense polar direction of the protostellar disk and thus the pressure on the material within the disk is reduced. It is likely that accretion through the disk can therefore continue (see also Peters et al., 2011; Hennebelle et al., 2011, as related examples in present-day star formation). On the other hand, in the purely turbulent run no extended accretion disk forms but rather a thick pseudo-disk without any cavities. It gets completely perturbed by the magnetic pressure driven bubble, see Fig. 8.8

In the purely turbulent MHD runs, the masses of the most massive sinks are $\sim 6\,\mathrm{M}_\odot$ at $t \sim 1000\,$yr and carry the majority of the total mass in sinks. This largest mass value is, however, about three times smaller than in the run without magnetic field. In the purely turbulent MHD realization, the most massive sink has $< 2\,\mathrm{M}_\odot$ which is also smaller than in the non-MHD case. Different from what has been observed in simulations of present-day star formation (e.g. Wang et al., 2010; Peters et al., 2011; Commerçon et al., 2011), we do not find that one of the sink particles, usually the first sink to form, undergoes significantly stronger and faster mass growth (at least for some time) compared to secondary sinks.

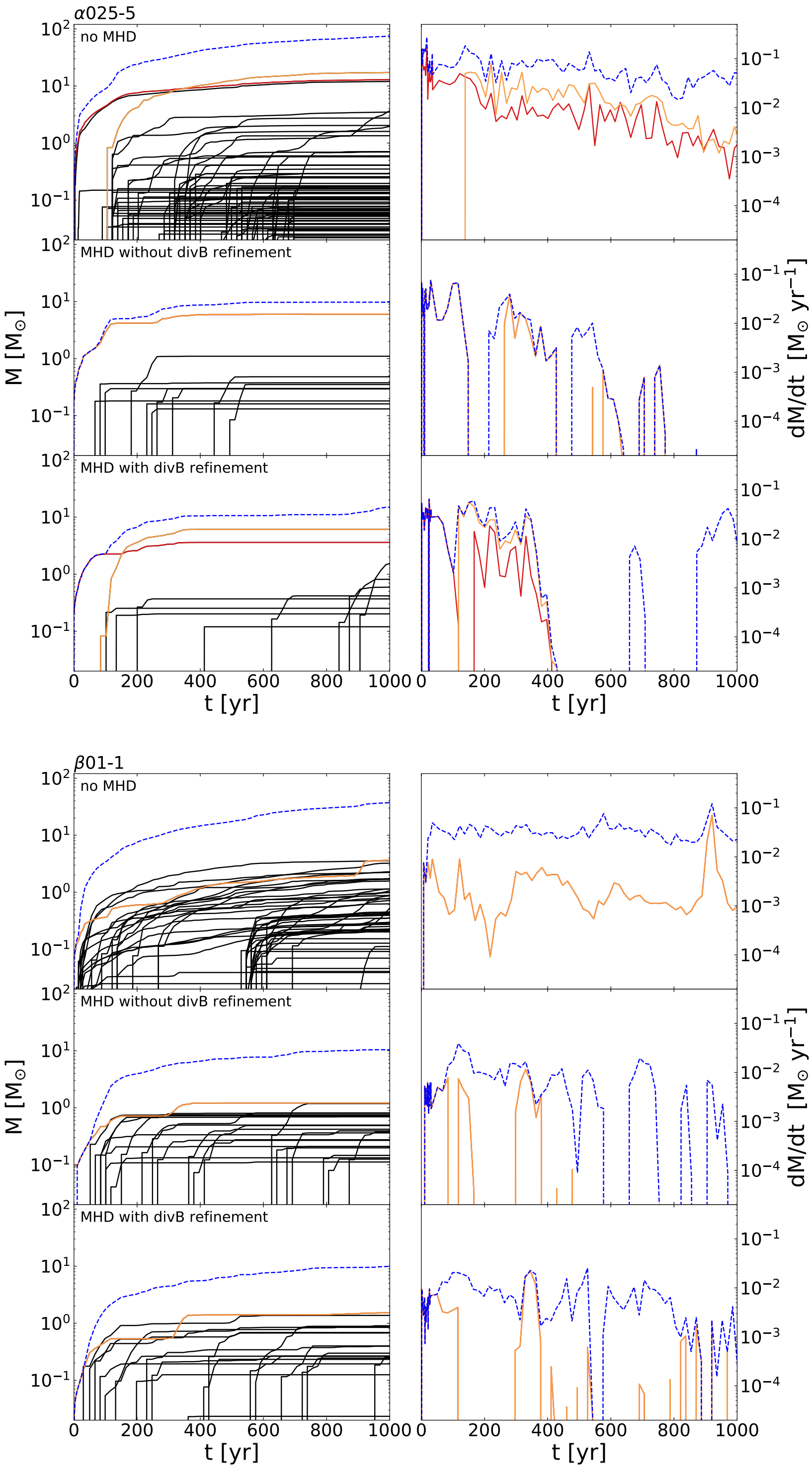

Figure 8.5: Comparison of mass accretion histories between. The top subplots show the evolution for the three runs of realization $\alpha025$-5, the bottom subplots refer to $\beta01$-1. The exact identification of each run is given in the left panel in each row. Left column: evolution of the total mass in sinks (blue dashed line), mass growth of the first (red) and the most massive sink (orange) together with all other sinks (black). Right column: cumulative accretion rate (blue dashed line) together with the accretion rate of the first (red) and most massive sink (orange). The most massive sink is defined as the sink with the highest mass at $t \sim 1000\,\mathrm{yr}$. When only an orange line is visible, then the first sink is also the most massive one.

8.3.4 Disk structure

Similar to what we have observed in Chapter 5, in both the purely rotational run β01-1 and the purely turbulent run α025-5 a protostellar disk forms which has a Keplerian rotational velocity profile at around the time of first sink formation. However, on the long run the disk loses its Keplerian rotation as it is disturbed by fragmentation and formation of secondary sink particles and by the expansion of the magnetically-driven bubble. It continues to evolve in a pseudo disk-like fashion (Galli & Shu, 1993a,b; Peters et al., 2011). As an illustration of the disk evolution see Fig. 8.6, 8.7 & 8.8.

The formation of disks in our simulations is different from the results of Machida & Doi (2013). They find that for an uniform magnetic field with initial field strength B_0 of

$$B_0 \gtrsim 10^{12} \left(\frac{n_0}{1\,\mathrm{cm}^{-3}} \right)^{-2/3} \tag{8.3}$$

where n_0 is the initial density in the sphere, magnetic braking is so efficient in redistributing the angular momentum in the surrounding of the center of the collapsing cloud, i.e. where the first protostar will form, that no protostellar disk forms. In our study the magnetic field is always larger than this critical value and we still observe the formation of disks.

The influence of the magnetically driven bubble can also be seen in the profile plots of the disk properties in Fig. 8.9. Within a radius of a few hundred AU around the first sink particle, the surface density and temperature drop as the magnetically driven bubble perturbs the disk environment and pushes material away from the disk center. The remaining gas has a high molecular hydrogen fraction and is therefore able to cool the gas to $T \lesssim 1000\,\mathrm{K}$. We show the profiles of realization β01-1 with divB refinement and α025-5 without divB refinement as representative examples for all runs.

The high magnetic pressure in the inner disk region can stabilize the disk against fragmentation (Lynden-Bell, 1966). In order to test whether this is also the case in our simulations, we plot the hydrodynamical Toomre parameter (dashed lines) (Toomre, 1964)

$$Q_{\mathrm{hyd}} = \frac{\kappa\, c_{\mathrm{s}}}{\pi G \Sigma} \tag{8.4}$$

together with the magnetic Toomre parameter (solid lines) (Kim & Ostriker, 2001)

$$Q_{\mathrm{mag}} = \frac{\kappa\,(c_{\mathrm{s}}^2 + v_{\mathrm{A}}^2)^{1/2}}{\pi\, G \Sigma} \; . \tag{8.5}$$

The effect of the magnetic pressure is included on the Toomre formula through the Alfvén velocity, $v_{\mathrm{A}} = B/\sqrt{4\pi\,\rho}$ which describes how fast changes in the magnetic field strength B propagate through a plasma of density ρ. We note that as a first approximation we use the total magnetic field strength here. In a prospective, more detailed investigation, we plan to examine the contribution of each magnetic field component separately. In the formulae above, there are furthermore the sound speed c_{s}, the gravitational constant G, and the disk surface density Σ. We use an approximation for the epicyclic frequency in the form of

$$\kappa = \left[R \frac{d\Omega^2}{dR} + 4\Omega^2 \right] \tag{8.6}$$

where $\Omega^2 = L_{\mathrm{z}}^2/R^4$ with the value of angular momentum z-direction L_{z} and R being the radius of a spherical shell centered on the first sink particle. We chose this expression

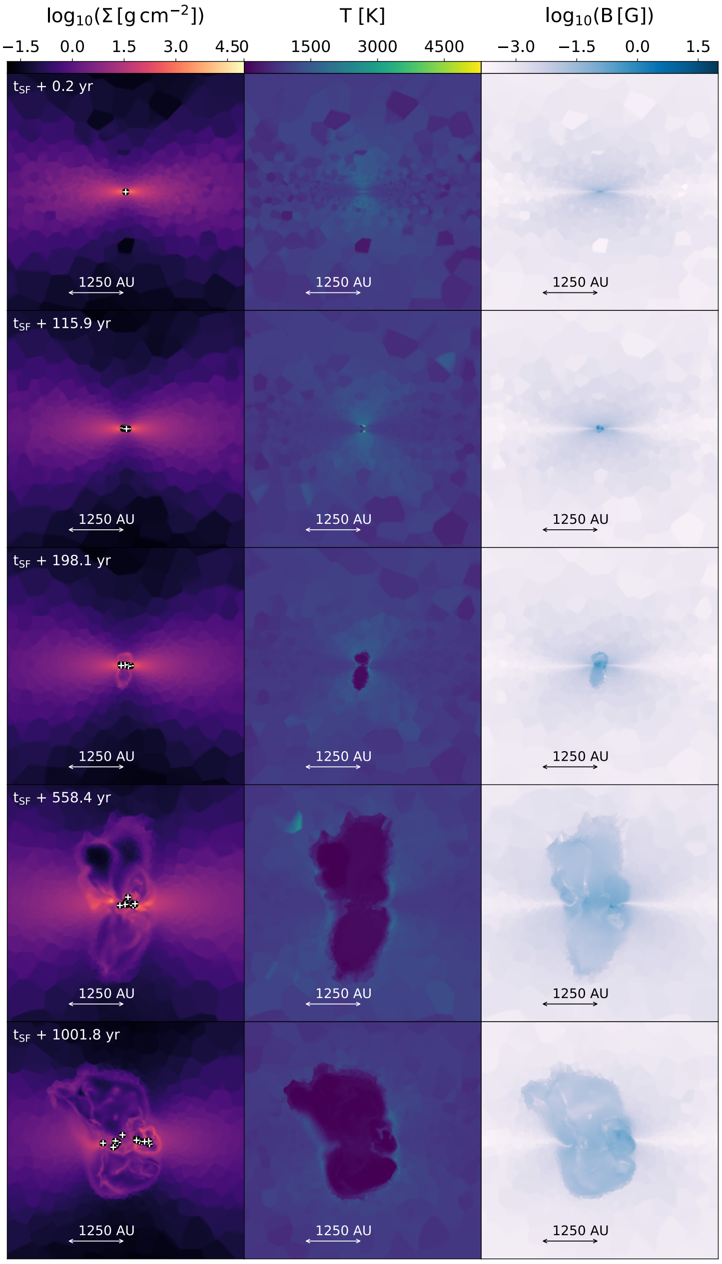

Figure 8.6: Edge-on projections of the column density, temperature, and magnetic field strength evolution of the protostellar disk in realization β01-1 with divB refinement. The magnetic field gets particularly strongly amplified in the center of the disk. As the magnetic field is not diffused outwards, a consequence of ideal MHD, it accumulates at the center of the disk. When the magnetic pressure at the center of the disk becomes comparable to the gravitational infall due to accretion onto and through the disk, a magnetic pressure bubble breaks out at the center. The projections are centered on the location of first sink formation. The thickness of the projection is 50 AU. Sink particles are denoted in the column density plots.

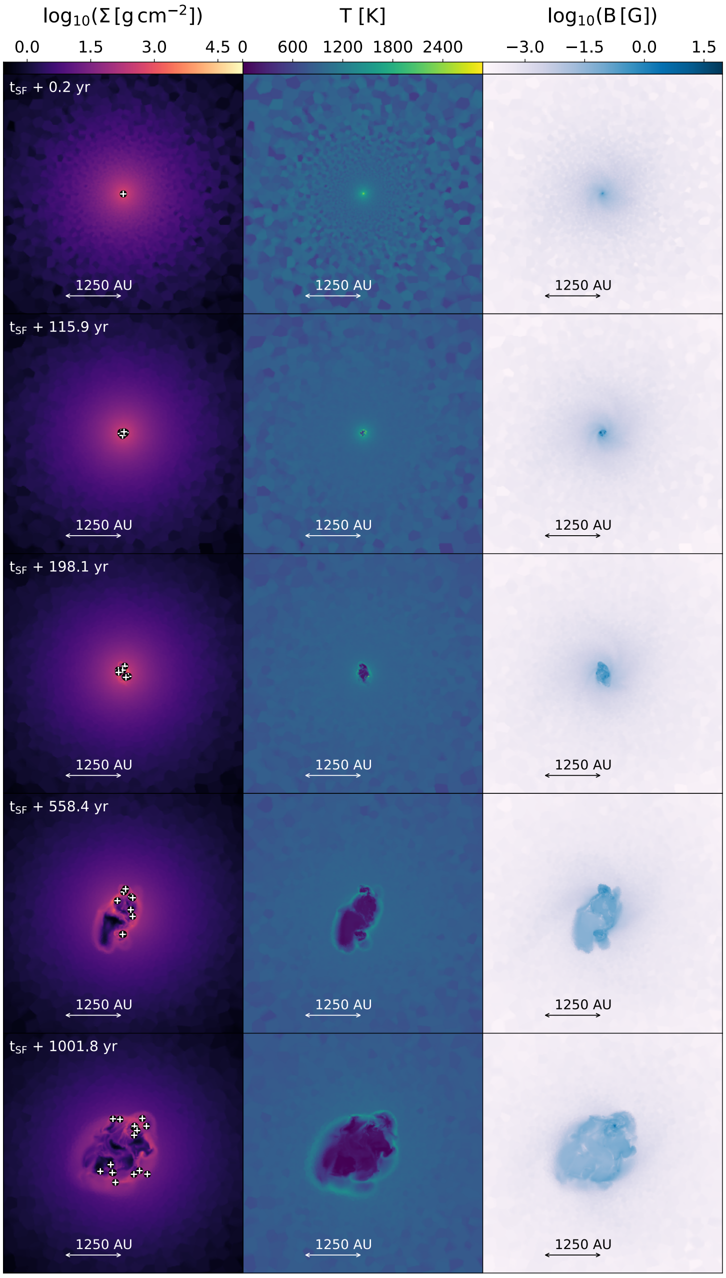

Figure 8.7: Same as Fig. 8.6 but face-on.

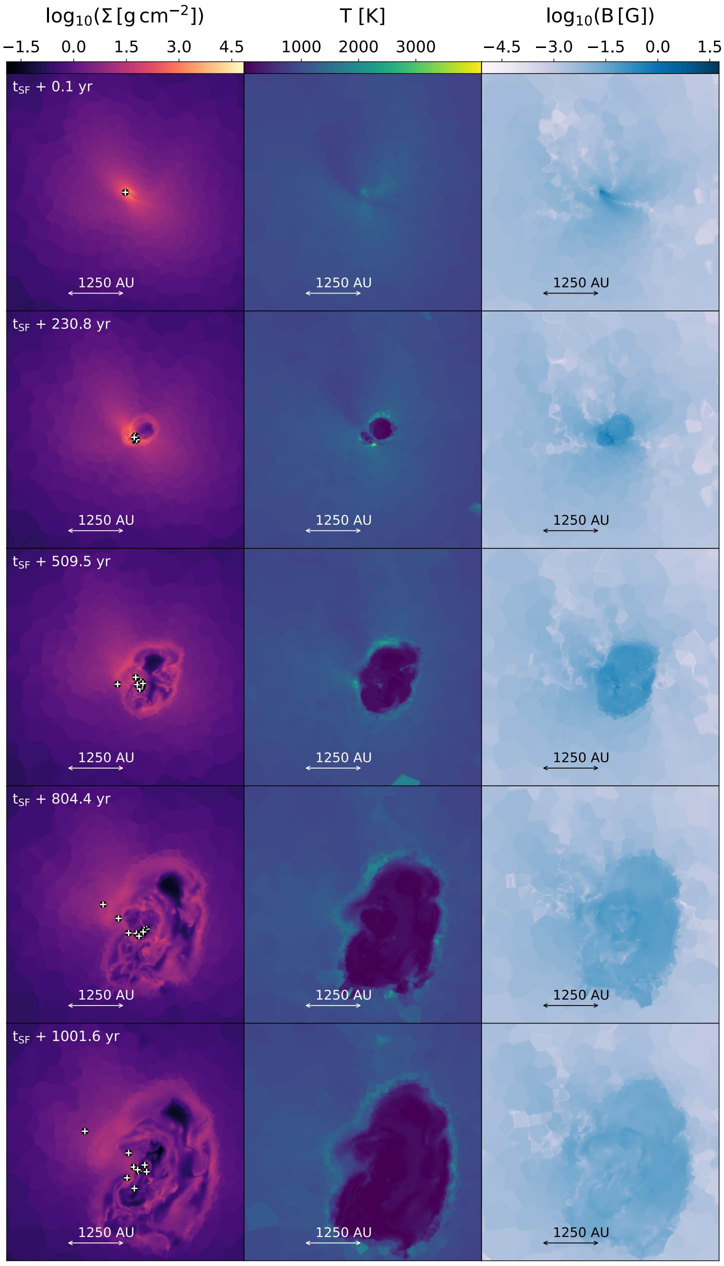

Figure 8.8: Edge-on projections of the column density, temperature, and magnetic field strength evolution of the protostellar disk in realization α025-5 without divB refinement. The pseudo-disk gets violently disrupted by the expansion of the magnetically-driven bubble. The projections are centered on the location of first sink formation. The thickness of the projection is 50 AU. Sink particles are denoted in the column density plots.

β01-1

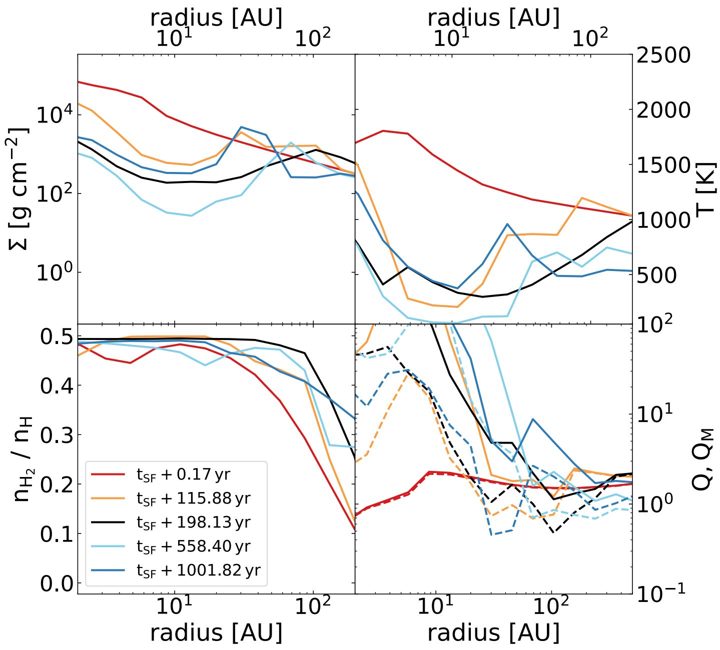

α025-5

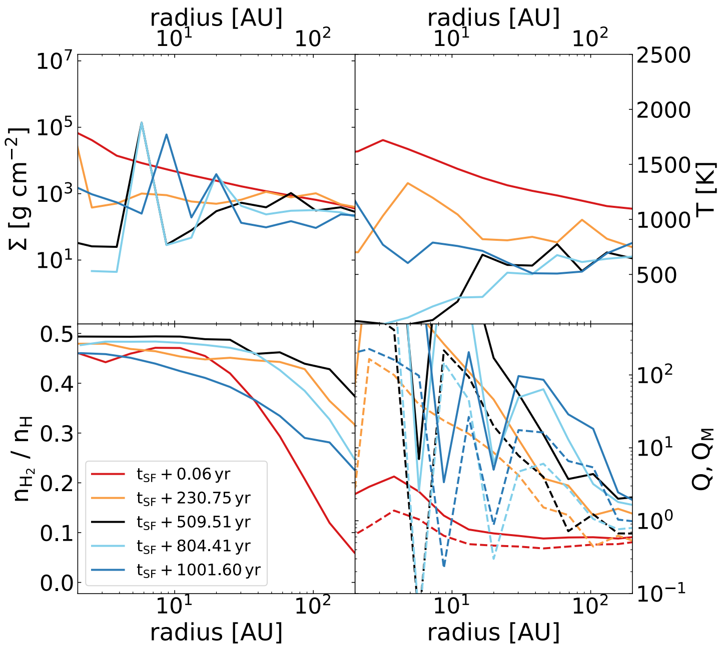

Figure 8.9: Mass-weighted radially averaged disk properties for five different times after first sink formation. Left: realization β01-1 with divB refinement. Right: realization α025-5 without divB refinement. In the bottom right panels both hydrodynamical and magnetic Toomre parameter have been plotted: Q (dashed lines) and Q_{M} (solid lines). It can be seen that the value of the magnetic Toomre-Q is always the larger of the two. This is due to the contribution of the non-zero Alfvén velocity in the extended Toomre criterion Eq. 8.5. From top left to bottom right: disk surface density Σ, temperature, T, H_2 fraction, $n_{\mathrm{H}_2}/n_{\mathrm{H}}$, and both hydrodynamical and magnetic Toomre parameter, Q (dashed lines) and Q_{M} (solid lines). The values are derived from mass-weighted averages within spherical shells centered on the first sink. In order to track the gas at disk densities, only gas cells with $n > 10^9\,\mathrm{cm}^{-3}$ have been considered here.

because with the break-out of the bubble the disk structure changes dramatically and rotation is no longer close to Keplerian.

From Fig. 8.9, we see that the magnetic Toomre parameter is always larger than the hydrodynamical one. The only exception is the red lines in the plot of β01-1 which is the profile directly after first sink formation. At this time the magnetic pressure in the disk is possibly not very strong yet. As the magnetic field enhances the stability of the protostellar disk, fewer protostellar fragments form. Disk stabilization through magnetic pressure has also been observed in several previous numerical studies of present-day star formation (e.g. Hosking & Whitworth, 2004; Machida et al., 2005; Hennebelle & Teyssier, 2008; Duffin & Pudritz, 2009; Peters et al., 2011; Seifried et al., 2011). Peters et al. (2011) who examined massive present-day star formation also with ideal MHD point out that in their simulations it is not magnetic pressure that dominantly stabilizes the protostellar disk but it is shearing motions within the disk that are indirectly induced through magnetic field configuration by how it shapes the protostellar system. Compared to our study, they only find an order of unity difference between the hydrodynamical and magnetic Toomre parameter and therefore conclude that the support of magnetic pressure against disk fragmentation is negligible. In our case, however, we find often more than an order of magnitude difference between the two Toomre parameters. Therefore the magnetic pressure adds some contribution in the stabilization of the disk. Whether in our study also shear motions contribute to disk stability, will be examined in the future.

Finally, we do not find evidence for a jet in any of our MHD simulations. Why this is the case needs to be addressed in a future analysis that concentrates on examining the structure of the magnetic field and velocity field in the disk region. Following Machida et al. (2008a), our purely rotational run might be too rotation-dominated due to its high rotational $\beta = 0.1$ to drive a jet.

8.3.5 Evolution of the magnetic field

In Fig. 8.10, we show the density dependence of the averaged total magnetic field strength $\langle|\mathbf{B}|\rangle$ for the four runs at time of first sink formation (left plot) and at the end of the simulation (right plot). The magnetic field is strongly coupled to the gas. In both setups, α025-5 and β01-1, the magnetic field roughly follows the relation $B \sim \rho^{2/3}$ (thin black dashed line) which is typically for the evolution of an ideal magnetic field during spherical collapse. This profile is followed aside from some local variations until the end of the simulation.

The two MHD runs per setup do not vary much directly after the formation of the first sink particle. But they have evolved differently for $n > 10^8\,\mathrm{cm}^{-3}$ by the end of the simulations. The density corresponds roughly to material within the protostellar disk. It is likely the magnetically-driven bubble that disrupts the disks appreciably affects the way the magnetic field is amplified within the disk. The average field values for the purely rotational setup are slightly smaller than those of the purely turbulent runs. These differences likely stem from the different overall collapse behavior of the two setups. They approach each other more at later time in the simulations.

The initial central density of our Bonnor-Ebert sphere was $n_0 \sim 10^4\,\mathrm{cm}^{-3}$ and the initial magnetic field strength $B_0 = 5 \times 10^{-6}\,\mathrm{G}$. With the $B \sim \rho^{2/3}$ evolution this yields $B \sim 100\,\mathrm{G}$ for $n \sim 10^{15}\,\mathrm{cm}^{-3}$ at time of first sink formation which is about what we see in Fig. 8.10.

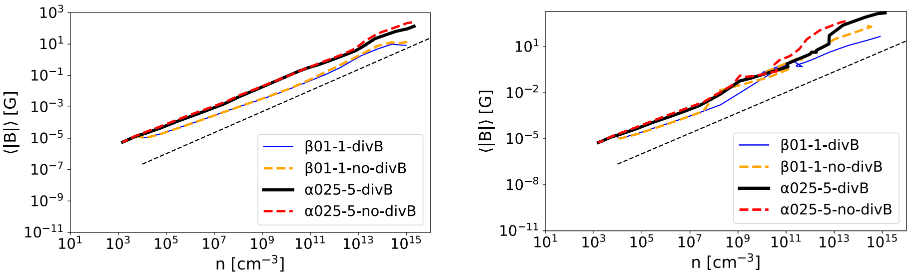

Figure 8.10: Profile of the radially averaged absolute value of the magnetic field strength, $|\mathbf{B}|$, versus number density, n. Left plot: profiles at time of first sink formation. Right plot: profiles at around $t \sim 1000\,\mathrm{yr}$. The average is derived in logarithmically spaced bins and centered on the densest cell. Indicated by the thin black dashed line is the relation $B \sim \rho^{2/3}$.

8.4 Analysis of the performance of the divergence cleaning methods

Due to the discretization of the equations of (ideal) magnetohydrodynamics (MHD), non-vanishing values of $\nabla \cdot \mathbf{B}$ appear in numerical computations. They tend to increase quickly and can be become dynamically important so that they effect the physical behavior of the simulated fluid. It is thus one of the main challenges of computational MHD to try to preserve $\nabla \cdot \mathbf{B} = 0$. There are methods such the *constrained transport scheme* by Evans & Hawley (1988); Gardiner & Stone (2005) which conserves $\nabla \cdot \mathbf{B} = 0$ by construction. This scheme is very accurate. The application of this scheme on an unstructured grid such as in AREPO is currently under investigation (e.g. Mocz et al., 2014, 2016). Another popular method are divergence cleaning schemes such as by Powell et al. (1999) or by Dedner et al. (2002) that act to minimize the divergence errors by adding $\nabla \cdot \mathbf{B}$ source terms to the momentum, energy, and induction equation. This introduces a diffusion of spurious $\nabla \cdot \mathbf{B}$ during the evolution of the simulated fluid and thus hinders further growth. The Powell divergence cleaning scheme is the current default for ideal MHD calculations in AREPO (Pakmor & Springel, 2013) and as such also used for our simulations. Furthermore, we run a second test series of our simulations with a recently implemented additional MHD refinement criterion. When the divergence error within a cell with radius r_{cell} becomes too large, i.e. $2r_{\mathrm{cell}}\,\nabla \cdot \mathbf{B} > 0.1|\mathbf{B}|$, the cell is split and the grid further refined. We will refer to this additional refinement as "divB refinement". The 0.1 or 10% constraint is motivated from test simulations with different cleaning schemes and is a commonly used value.

We can examine the performance of these divergence cleaning methods by analyzing the time evolution of the relative divergence error[3] $(\mathrm{divB})\,\mathrm{r}_{\mathrm{cell}}/|\mathbf{B}|$. In Fig. 8.11, we show $(\mathrm{divB})\,\mathrm{r}_{\mathrm{cell}}/|\mathbf{B}|$ for all cells within a radius of 10^6 AU around the location where the first sink particle formed. The size of divergence errors in individual cells becomes larger over time. Interestingly, the increase is stronger in runs with additional divB refinement. Furthermore, we find in these runs that cells with significant divergence error accumulate at radii $\gtrsim 10^5$ AU which is about a quarter of the radius of the original Bonnor-Ebert sphere profile edge. In contrast to that the runs without the additional MHD refinement show less strong deviations. This difference likely originates from

---

[3] We denote the divergence of the magnetic field $\nabla \cdot \mathbf{B}$ as "divB" in our further discussion and in the figures.

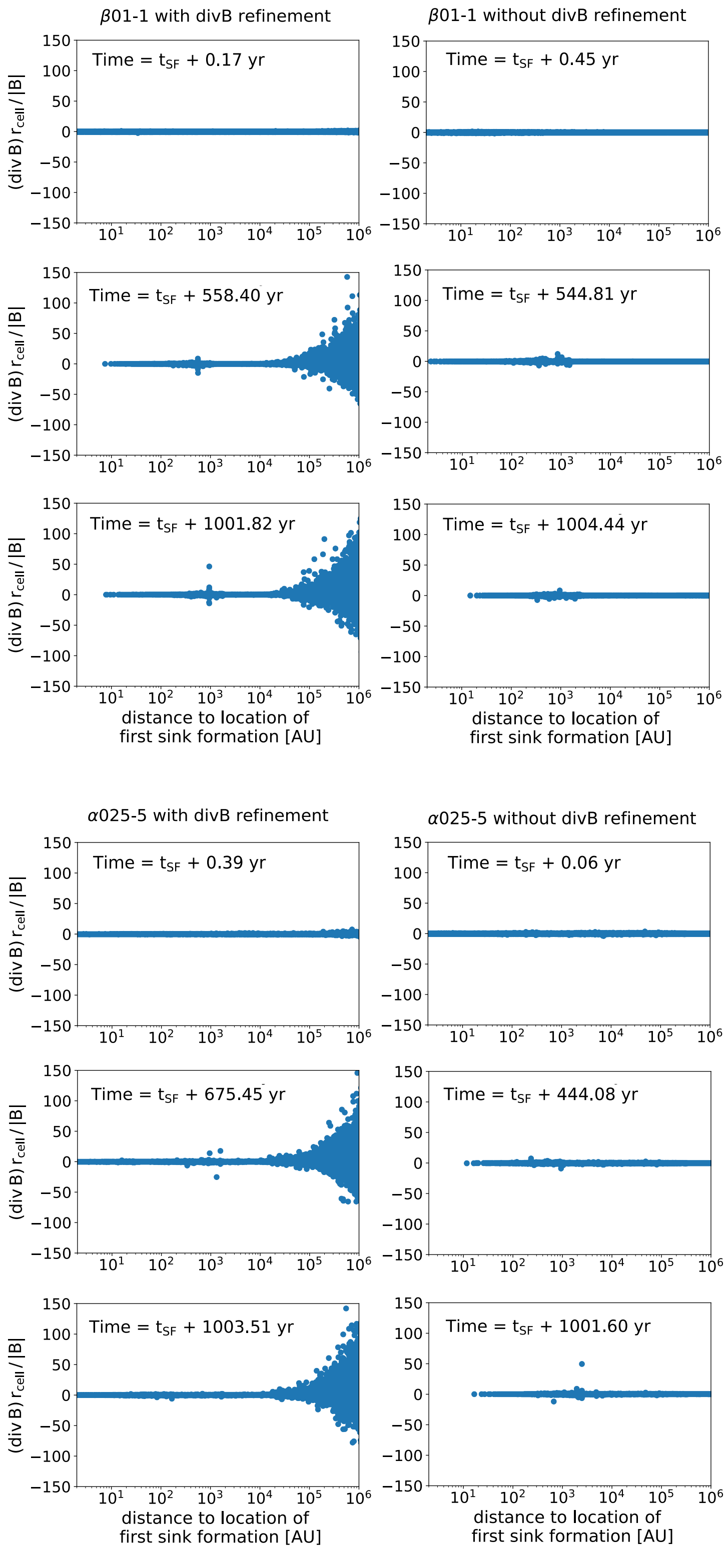

Figure 8.11: Relative divergence error of the magnetic field $(\mathrm{divB})\,r_{\mathrm{cell}}/|\mathbf{B}|$, for a cells in a radius of 10^6 AU around the location of the formation of the first sink particle.

the numerical behavior of the divB refinement. However, it seems as if the additional divB refinement is somehow unable to cope with our type of astrophysical problem and worsens the amount of divergence errors instead of improving the problem. All of the runs show a few odd cells at around 1000 AU. This is at approximately the edge of the protostellar disk. Investigating the detailed origin of these features is beyond our current study but will be addressed in a future project.

In Fig. 8.12, the time evolution of the volume-weighted average of the relative divergence error $(\mathrm{divB})\mathrm{r}_{\mathrm{cell}}/|\mathbf{B}|$ is presented. For each time, i.e. output dump, we compute this quantity within three different radii around the location where the first sink particle has formed. As we have seen above in Fig. 8.11, the specific size of the relative divergence error and and the number of the cells that have it varies with the distance to the location of first sink formation. This is in particular true for the runs with divB refinement. Compared to a non-weighted version of this quantity, individual outlier cells are "smoothed out" within the total volume of a sphere. The three different exemplary radii that we chose are 1000 AU, 20000 AU, and 6.5 pc. The first radius is motivated from the appearance of outlier cells that we observe in Fig. 8.11. The second one is motivated from results at the end of our simulations in Chapter 5 in which several realizations show ejected sink particles that are up to 10000 AU away from the center of mass (gas and sink particles combined) in the last snapshot. We take a larger value to simply account for the fact that the center of mass and the location where the first sink has formed are likely to be different or have begun to differ at some point. Finally, the largest radius is simply the half the size of our simulation box.

For the simulations with additional divB refinement, the volume-averaged relative divergence error increases with the considered volume. Its value steadily increases for the radius of 6.5 pc over time and reaches $\sim 50\%$ at $t \sim 1000\,\mathrm{yr}$. This is what we expected from the behavior observed in Fig. 8.12 where in particular error values of cells at radii larger than 10^5 AU increased considerably. On the other hand, within 1000 AU or 20000 AU, the volume-averaged relative divergence error rises strongly within hundred years after first sink formation but then stays about the same or decreases slightly. The values are $< 6\%$.

The runs without additional divB refinement have a different behavior. Here, the relative divergence error weighted by the volume of radius 6.5 pc overall seems not to vary at all and has values close to zero. The lines for the other two radii fluctuate. But here the absolute values for 20000 AU are smaller than for 1000 AU. Their values are overall $< |0.6\%|$, an order of magnitude smaller than in the runs with divB refinement.

In other comparable simulations (*private communication with Paul Clark*), typically relative divergence errors smaller than a few ten percents are found. While we find this behavior for our volume-averaged relative divergence error, this is strongly violated when we look at individual cells.

8.5 Conclusions

We have performed four 3D test simulations of Population III.1 star formation under the influence of either turbulence (α=0.25) or rotation (β=0.1) in combination with a uniform magnetic field size $B = 5 \times 10^{-6}\,\mathrm{G}$. The simulations have been carried out with the Voronoi moving-mesh ideal magnetohydrodynamics (MHD) code AREPO (Springel, 2010; Pakmor & Springel, 2013). Our version of AREPO contains an updated and self-consistent primordial chemistry network together with a treatment for a variable adiabatic index and accretion luminosity heating. The non-magnetic initial

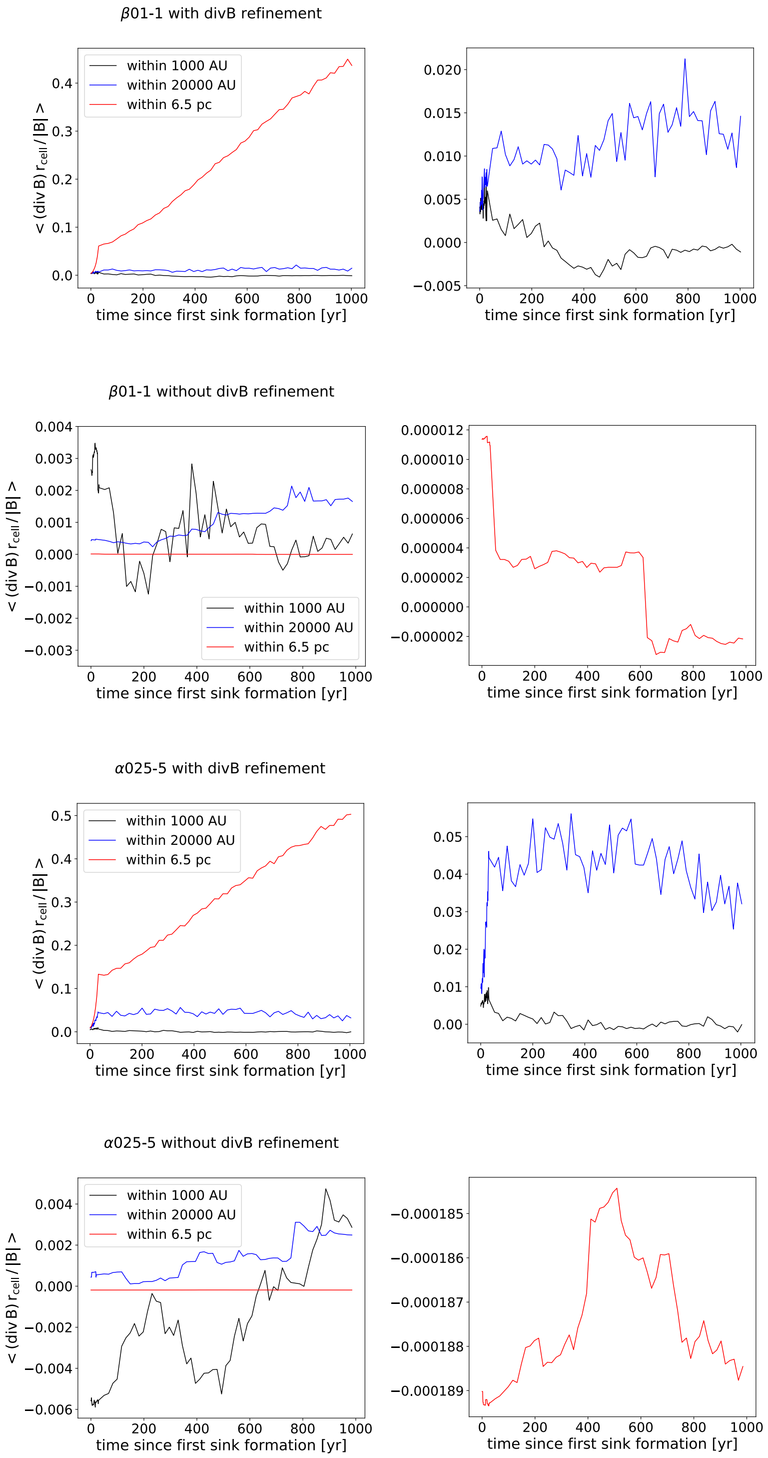

Figure 8.12: Time evolution of the volume-weighted relative divergence error of the magnetic field. Each row belongs to one realization the name of which is denoted oat the top of each panel on the left. For each time value, we computed the relative divergence error within three different radii (denotes by the red, blue and black line) around the first sink particle. In the figures on the right simply show a "zoomed-in" version of the amplitude-wise smallest lines of the left plot; the color-scheme is kept.

conditions of the two realizations considered were picked from the study presented in Chapter 5. In this way, direct comparison between results with and without magnetic field was possible. Our simulations follow the collapse of a magnetized, primordial Bonnor-Ebert sphere until the formation of the first protostar and the creation of protostellar disk system. We use sink particles to replace individual protostars that have collapsed beyond our resolution limit.

The quality of our results depends on the performance of our numerical methods. The largest challenge of MHD simulations is minimizing non-zero values of divergence of the magnetic field that arise due to the discretization of the MHD equations. For this purpose, we employ the Powell divergence cleaning scheme (Powell et al., 1999; Pakmor & Springel, 2013). Furthermore, we have tested a recently implemented MHD refinement criterion in a second rerun of each of setup. We find better performance of the code with smaller divergence errors for the runs without the additional refinement criterion. We may pursue another test series with a different divergence cleaning scheme in the future.

The focus of the analysis in this Chapter was on the examination of the fragmentation behavior of the Population III protostellar disk in the presence of a magnetic field. Compared to the non-MHD versions, we find that the total number of protostars is in reduced more in the MHD runs of the purely turbulent setup than in those of the purely rotational one. For both setups, we find a substantial decrease in the total mass in sinks in MHD compared to non-MHD simulations. Tackling the exact reasons for that is complex but we have some general trends. With the flux of material to the center of the disk were the protostars reside and accrete, also the magnetic field is dragged along due to the ideal MHD condition and accumulates there. When the magnetic pressure in the disk has become strong enough to counteract gravitational infall and accretion, it drives a magnetic bubble that disrupts the disks (see e.g Seifried et al., 2011; Peters et al., 2011, in the context of present-day star formation). The accretion rates of the protostars become extremely variable and steady high-mass growth is not possible anymore. No protostar was able to grow $> 10\,\mathrm{M}_{\odot}$ over the considered 1000 yr. The cumulative accretion rate that was already before the expansion of the bubble smaller than in the non-MHD case further decreases. The growing magnetic pressure in the protostellar disk is likely responsible for stabilizing the disk against fragmentation. In an analysis of the Toomre parameter, we have found that the magnetic Toomre parameter, that includes an additional contribution by magnetic pressure that adds to disk stabilization similar to the thermal sound speed, is usually large than the hydrodynamical one and generally indicates disk stability, i.e. $Q > 1$. Such was found in both Population III (Peters et al., 2014) as well as present-day star formation (e.g. Hennebelle & Teyssier, 2008; Seifried et al., 2011).

In this first attempt to study Population III star formation with turbulence and rotation in combination with a magnetic field, we have found that the magnetic field has significant impact on the star-forming process and the evolution of the protostellar disk. We conclude that it is important to pursue further numerical studies on the influence of magnetic field in the Pop III context. We plan to extend the current study by running a larger sample of our runs from Chapter 5. Furthermore, we want to test the effects of varying initial magnetic field strengths. We will add to our analysis also investigations of the strength and role of the different components of the magnetic field, e.g. in stabilizing the disk. It might also be interesting to start with a small-scale tangled magnetic field instead of a large-scale, uniform one and compare the outcomes.

CHAPTER 9 Conclusion and outlook

9.1 Conclusion

In this thesis, we have examined the fragmentation behavior of Population III.1 protostellar disks under the influence of rotation, turbulence, and magnetic fields. We have investigated how the protostellar mass function may be affected by the different physics and which consequences may be inferred for later times in the evolution of the star-forming halo and its surroundings in terms of protostellar ejections and in terms of the impact of radiative feedback on later chemical enrichment of neighboring halos. For this purpose, we have performed both numerical simulations and analytical estimations. Moreover, tests on the performance of our numerical methods and on the sensitivity of our results to the numerical resolution were conducted. We will now present the main results and conclusions of our studies together with details on the respective methods applied.

How the first stars regulated star formation: enrichment by nearby supernovae

In Chapter 4, we have used the ZEUS-MP radiation-hydrodynamics code (Norman, 2000; Hayes et al., 2006) to assess the role of photoevaporation of a pristine halo by a near-by Population III star prior to the star's supernova explosion. We have evaluated how this may affect the chemical enrichment of this halo when the ejecta wave of the Pop III supernova washes over it. Pop III stars supposedly emitted copious amounts of ultraviolet (UV) radiation (e.g. Bromm et al., 2001b; Omukai & Palla, 2001; Schaerer, 2002; Hosokawa et al., 2011) of which Lyman-Werner (LW) photons of energies in the range 11.18 - 13.6 eV are of particular importance as they are able to dissociate molecular hydrogen, H_2, the main coolant in primordial gas. One photon destroys one H_2 molecule. In this way, Pop III radiative feedback directly affected the cooling and star formation efficiency of the primordial gas in the surrounding of the star. We considered a $25\,M_\odot$ and a $200\,M_\odot$ star at 250 pc and 500 pc from the center of the halo. They explode in a core-collapse supernova and a pair-instability supernova respectively. We found:

- A halo is more strongly affected by the photoevaporation the less massive it is, the smaller the distance between the halo and the star is, and the more luminous the star is.
- Halo cores stay largely unaffected by the LW radiation as they are shielded by molecular hydrogen in two ways. First, in the halo itself sufficiently high H_2 column densities are able to protect the halo core through H_2 self shielding. Second,

due to an increased ionization fraction in the outer layers of the ionization front, a H_2 enriched arc forms through the H^- channel there as the radiation front passes the halo. In the arc, a continuous balance between H_2 photodissociation by LW photons and re-formation through the H^- channel is maintained.

- Outer layers of the halo are ablated or thinned out by the radiation. This makes it easier for the metal ejecta wave from the Pop III supernova to intrude deeper into the halo. Furthermore strong turbulent mixing of the metals with the ablated layers is promoted.

We conclude that pre-supernova halo photoevaporation plays a crucial role in modeling metal enrichment realistically. Similar results have only been observed by Smith et al. (2015) before who examined the influence of a $40\,\mathrm{M}_\odot$ star at 200 pc. Our study therefore extends the parameter space.

The fragmentation behavior of Population III protostellar disks under the influence of rotation, turbulence, and magnetic fields

In Chapters 5, 6, and 8 we have studied the collapse of a primordial Bonnor-Ebert sphere until the formation of the first protostar and the creation of a highly gravitationally unstable protostellar disk system that subsequently fragments and evolves into a Population III protostellar cluster. We have employed the sink particle method to replace individual protostars which collapse beyond our resolution limit. The 3D numerical simulations have been performed with the Voronoi moving-mesh code AREPO (Springel, 2010; Pakmor & Springel, 2013). Our version of AREPO includes an updated and self-consistent primordial chemistry network together with a treatment for a variable adiabatic index and accretion luminosity heating, all of which has been tested separately by us before the production runs (see Section 3.2.3, 3.2.4, and 3.2.2).

In Chapter 5, we have examined the star formation process under the influence of different levels of rotation ($\beta = 0.01$, $\beta = 0.1$) and subsonic turbulence ($\alpha = 0.05$, $\alpha = 0.25$) and have also run a setup with no initial rotation or turbulence. For each combination of initial conditions, five realizations have been conducted which vary either in the random number seed used to initialize the turbulent velocity field or the cell configuration of the Voronoi mesh in runs without turbulence. Per combination of initial conditions, i.e. for each setup, we have averaged over the five realizations. Our main results are:

- In order to be able to derive general trends, it is important to analyze an ensemble of realizations based on the same initial conditions instead of just a single run. This is in particular crucial when turbulence is studied. In our simulations, we observe very significant scatter in the results of the individual realizations of setups including turbulence. Although the scatter is generally much smaller in runs without turbulence, the numerical noise which is introduced by the variations in the initial cell configuration onto which the Bonnor-Ebert profile is initialized, is still enough to produce different fragmentation outcomes. The studies by Goodwin et al. (2004a), Goodwin et al. (2004b) found similar results in simulations of present-day star formation. However, numerical studies of Population III star formation, and in particular those which studied the effects of different levels of turbulence, have so far considered only one realization for each combination of initial conditions (e.g. Clark et al., 2011a; Riaz et al., 2018). Our results demonstrate that in both parameter studies within a controlled test setup and in self-consistently derived cosmological simulations, general trends can only be reliably deduced by analysis of the statistics of an ensemble.

- Fragmentation of the protostellar disk into numerous protostellar fragments and the creation of a protostellar cluster is the normal case. It is only the realizations without initial rotation or turbulence that form just one protostar over the entire course of the simulation. Turbulence promotes fragmentation. In mixed runs, i.e. those which include both rotation and turbulence, increasing levels of rotation provide some stabilization against fragmentation.

- Protostellar mass growth occurs at high cumulative accretion rates ($\dot{M} \sim 10^{-2} - 10^{-1}\,\mathrm{M_{\odot}\,yr^{-1}}$) and is determined by the thermodynamical behavior of the gas and not by rotation or turbulence. The latter two may slightly affect the variability of the accretion rate which however does not change the overall behavior.

- The mass function is top-heavy with a mass range from a few $10^{-3}\,\mathrm{M_{\odot}}$ to several tens of solar masses. This is in agreement with previous studies (e.g. Greif et al., 2011; Clark et al., 2011a; Susa et al., 2014; Stacy et al., 2016). However, we find that the shape of the mass function still differs. While runs including turbulence have a flat spectrum, purely rotational ones show fewer fragments in the low-mass regime and much more towards the high-mass end. As it is found self-consistently from cosmological simulations (Abel et al., 2002; Bromm & Larson, 2004; Wise & Abel, 2007; Greif et al., 2008; Clark et al., 2011a), we expect that there is at least some level of turbulence in the gas in more realistic environments and thus suggest that the realistic Pop III protostellar mass function will tend to have a more flat distribution.

- About $\sim 30-45\%$ of all protostars are ejected over the course of the simulations. Comparable values were observed in earlier numerical studies (Greif et al., 2011; Stacy & Bromm, 2013; Stacy et al., 2016). With the help of our statistical analysis we have discovered that the mass functions of the ejections retain the shape of the total mass functions. We also find that the average number of ejections reflects the trend of the average total number of stars: it increases for a higher level of turbulence and for a lower level of rotation.

- Of particular interest are ejected Pop III protostars with masses of $M < 0.8\,\mathrm{M_{\odot}}$ because their lifetimes are longer than the Hubble time and thus they may have survived until present-day and could still be observable in our Galaxy (Yoshida et al., 2006; Greif et al., 2011; Kippenhahn et al., 2012; Hartwig et al., 2015a). From our simulations, we find that per setup $\sim 60 - 80\%$ of the ejected protostars which is $\sim 20 - 40\%$ of the total number of protostars fall in this regime. Protostars that get ejected from their system of origin, continue to accrete as they move through the envelope of the gas cloud in which the system formed. Therefore, for the subsolar, low-mass ejections we have estimated how much more mass they would gain when assuming Bondi-Hoyle accretion until they reached a distance of 1 pc from the center of mass of the protostellar system in which they were created. We find that still $\sim 50 - 80\%$ of all ejected protostars, that is $\sim 15 - 40\%$ of the total number per setup, have $M < 0.8\,\mathrm{M_{\odot}}$.

- Although our sink particle treatment does not allow for sink merging, we have made a simple estimation that shows that sink merging is relevant and should be considered in future simulations. Previous studies observed that up to 60% of all sink particles merge (Greif et al., 2011; Greif et al., 2012; Stacy & Bromm, 2013; Stacy et al., 2016).

In Chapter 8, we have re-run two of the realizations from Chapter 5, namely one with $\alpha = 0.25$ and one with $\beta = 0.1$, together with an ideal, initially uniform magnetic field directed parallel to the rotation axis and an initial field strength of $B_0 = 5\times10^{-6}$ G. This has influenced the before-mentioned results as follows:

- The number of protostellar fragments decreases. The purely turbulent run seems to be affected more than the purely rotational one. A possible reason for the reduction of fragmentation is that the protostellar disk is now, in addition to thermal pressure, also supported by a substantial contribution from magnetic pressure. In the context of Population III star formation this has been observed before by Peters et al. (2014), however they started with a turbulent, small-scale tangled magnetic field. In present-day star formation it was previously addressed by e.g. Hennebelle & Teyssier (2008) or Seifried et al. (2011).

- The cumulative accretion rate is smaller and extremely variable. Consequently, the total mass growth of the protostars is significantly reduced compared to the non-magnetic case. Overall, accretion is strongly affected by a magnetically-driven bubble which arises from the center of the disk and disturbs the disk environment while expanding. The bubble is a consequence of ideal magnetohydrodynamics in which the magnetic field is frozen into the plasma and follows its flow during accretion into the center of the disk. There, it accumulates until the magnetic pressure is strong enough to counteract gravitational infall and accretion and drives the bubble. Peters et al. (2011) reported similar extreme variations in the cumulative accretion rate. But in contrast to them, we do not find that the mass growth an individual sink is particularly enhanced compared to the other members of the cluster.

- Due to the discretization of the equations of magnetohydrodynamics (MHD) in numerical schemes, spurious values of the divergence of the magnetic field occur. To keep them small, we have employed the Powell divergence cleaning scheme (Powell et al., 1999; Pakmor & Springel, 2013). In a second set of our runs, we have furthermore tested a recently implemented additional MHD refinement criterion with the same purpose. We find better numerical performance, i.e. overall fewer and smaller divergence errors, in runs without the additional refinement criterion.

The studies presented in Chapter 6 have investigated the sensitivity of our results from Chapter 5 on variation in the size of the sink accretion radius and the number of cells per Jeans length. For this purpose, we have performed simulations with three different test series. We have re-run one complete setup, i.e. all five realizations of one combination of turbulence and rotation, of Chapter 5 with 32 cells per Jeans length instead of the originally used 16 cells per Jeans length. The initial condition for the second and third test series is a Bonnor-Ebert sphere with only rotation. We note that with a sink particle accretion radius of 2 AU, our runs are among the simulations with the highest resolution in the immediate surrounding of the sink that study the fragmentation behavior of Population III protostellar disks (Clark et al., 2011b; Greif et al., 2011; Greif et al., 2012; Stacy et al., 2016). In particular, we have a higher resolution than previous runs that addressed the influence of different levels of turbulence in this context (see Clark et al., 2011a; Riaz et al., 2018). We find:

- The number of protostellar fragments formed is very sensitive to the size of the accretion radius: a smaller sink accretion radius yields a larger amount of fragments. This is in agreement with the previous studies that demonstrated that fragmentation occurs down until the protostellar surface (Greif et al., 2012). On the other hand, a higher number of cells per Jeans length increaeses the number of fragments only slightly.

- For a higher number of cells per Jeans length, in particular 32 cells (or higher, see also Greif et al. 2011, Greif et al. 2012, and Turk et al. 2012), additional turbulence, which arises during gravitational collapse of the gas, is resolved. This further enhances effects attributed to a higher level of turbulence, for example an increase in fragmentation, as observed in Chapter 5. Furthermore, we find slight differences in the temperature and molecular hydrogen profiles, which, however, seems not to have considerable influence in the overall evolution of the gas cloud.

- In spite of the in parts substantial difference in the total number of protostellar fragments, the total mass accreted onto them stays about the same for the different resolutions. We observe that accretion rates become more variable, without changing their overall magnitude, for decreasing accretion radius and increasing resolution per Jeans length. The mass functions remain top-heavy.

We conclude that the formation of a Population III protostellar cluster due to the fragmentation of a Population III protostellar disk is a generic outcome of the collapse of our primordial star-forming clouds that have some initial degree of rotation and turbulence. While turbulence promotes fragmentation, rotation and magnetic fields may provide some stabilization and thus reduce the number of fragments. Total stabilization of the protostellar disk is, however, so far not observed in our systems. While rotation and turbulence have no significant influence in the protostellar mass growth, the dynamical evolution of the protostellar system in presence of magnetic fields may lead to significant reduction. Despite the deviations in the fragmentation of the disk and the accretion behavior of the protostars, we find that the top heavy mass function ranging from subsolar to a few ten solar masses remains an overall robust result. It is likely that some ejected Pop III protostars, even if they continue to accrete for some longer period, stay in the mass regime of $M \lesssim 0.8\,\mathrm{M}_\odot$, which makes them promising candidates to still be observable today. For the first time in the field of Population III star formation, we have shown that analyzing the statistics of an ensemble of realizations based on the same initial conditions is, in particular for simulations including turbulence, crucial for the deduction of general trends.

Stabilizing protostellar disk with tangled small-scale magnetic fields

In Chapter 7, we have analytically explored the possibility of stabilizing unstable Population III protostellar disks with magnetic pressure induced by a strong small-scale tangled magnetic field that is amplified by the turbulent, small-scale dynamo. For this purpose, we have derived a novel expression of the Toomre criterion that includes the velocity of the turbulent flow, u_{turb}, that drives the small-scale dynamo and an efficiency factor, ϵ, of the dynamo:

$$Q_{\mathrm{mag}} = \frac{\kappa \sqrt{c_{\mathrm{s}}^2 + \epsilon\, u_{\mathrm{turb}}^2}}{\pi G \Sigma} \quad . \tag{9.1}$$

We have applied this to data of unstable Population III protostellar disks which were extracted from simulations by Clark et al. (2011b), Greif et al. (2012), and our own studies from Chapter 5. We find that disk stabilization according to the Toomre criterion, i.e. $Q_{\rm mag} > 1$, only occurs when the disk is already close to stability in the hydrodynamical case or when the turbulence in the disk gas is mildly supersonic. In a numerical study, Peters et al. (2014), observed full disk stabilization and the creation of only one Population III protostar in the presence of a turbulent, small-scale tangled magnetic field. We suggest that the role of small-scale magnetic fields in Population III star formation needs to be addressed by further detailed numerical computations and best by the statistical analysis of an ensemble of runs before general conclusions can be drawn.

A question remains: how realistic are very massive Population III of mass $> 100\,{\rm M}_\odot$ such as the $200\,{\rm M}_\odot$ star assumed in the simulations of halo photoevaporation? Our studies on the fragmentation behavior of Population III protostellar disks and the evaluation of disk stabilization by magnetic fields have so far not identified a possible pathway for the formation of these massive Population III stars. We note however shortcomings of our studies such as the lack of sink particle merging or the relative shortness of our runs that likely affect the outcome. Susa et al. (2014) considered the evolution of Pop III protostellar system for $\sim 10^5\,{\rm yr}$ after the formation of the first protostar and found in three out of six halos stars with $\gtrsim 100\,{\rm M}_\odot$ and in one case a star with $\gtrsim 200\,{\rm M}_\odot$ that forms in isolation. It seems that the formation of these massive stars is possible but it is likely a rare phenomenon. More simulations of the whole accretion period $\sim 10^4 - 10^5\,{\rm yr}$ are needed as a comparison to Susa et al. (2014). From the observation of extremely metal-poor stars that may contain nucleosynthetic yields of the pair-instability supernova of a $\sim 200\,{\rm M}_\odot$ star, nothing has been conclusively detected so far (Karlsson et al., 2013; Aoki et al., 2014). The chemical abundances in these stars are better described by yields from core-collapse supernovae of Pop III stellar progenitors with mass $15 - 40\,{\rm M}_\odot$ (e.g. Beers & Christlieb, 2005; Frebel et al., 2005, 2008; Karlsson et al., 2008; Joggerst et al., 2010; Keller et al., 2014).

9.2 Outlook

In Chapter 8, we have already presented some preliminary results of our re-runs of the simulations from Chapter 5 with a uniform magnetic field. As a next step, we want to extend these ideal magnetohydrodynamics simulations to the whole ensemble. In the same fashion as the statistical analysis of the effects of different levels of turbulence and rotation before, we plan to perform a parameter study with varying initial magnetic field strengths. It will be interesting to investigate the magnetic field structure with its different components and their individual evolution in more detail. Furthermore, it is important to evaluate the contribution of the individual field components in magnetically-induced mechanisms such as magnetically-driven outflows, jets, and protostellar disk stabilization through magnetic pressure or magnetic braking in more detail. This can be compared to previous studies for example by Machida et al. (2008a) or Machida & Doi (2013), and will greatly expand the so far considered parameter space. Another way to address this topic in the future should also be via starting with a turbulent, small-scale magnetic field instead of large-scale coherent one as it is expected to be a more realistic and natural initial condition in Population III star formation (Schleicher et al., 2010; Schober et al., 2012). Only Peters et al. (2014)

has used this approach before. However, they conducted just three runs with varying initial magnetic field strengths and, as we have found in this thesis, the statistics of an ensemble of realizations with the same initial conditions yields more reliable results when turbulence is included.

In a second project, we intend to examine our runs from Chapter 5 for Population III protostellar multiplicity. Previous numerical studies suggest that Population III binarity is common phenomenon (Turk et al., 2009; Stacy et al., 2010; Stacy & Bromm, 2013; Riaz et al., 2018). We will analyze how the frequency of Pop III binaries and properties such as separation of the companions, their mass ratio, and the orbital period depend on the turbulence and rotation of the initial star-forming gas cloud. Pop III binaries are of interest as from them other binary objects may evolve. For example, close massive binary Pop III stars may end up as binary black holes which could become detectable through their emission of gravitational waves (e.g. Hartwig et al., 2016; Belczynski et al., 2017; Pacucci et al., 2017; Schneider et al., 2017). Furthermore, the creation of an X-ray background (Glover & Brand, 2003) could be supported by luminous X-ray binaries from Pop III progenitors and could delay or even suppress further Pop III star formation as their radiation dissociate hydrogen molecules (Hummel et al., 2015; Ricotti, 2016).

We have stopped our simulations in Chapter 5 at around $1\,000\,\mathrm{yr}$ after the formation of the first protostar. We did this because in some of our realizations, individual Pop III protostars had grown to masses $> 10\,\mathrm{M}_{\odot}$ at which point ionizing radiative feedback will become increasingly important and will likely affect accretion (e.g. Hosokawa et al., 2011; Stacy et al., 2012, 2016). Therefore, in order to continue running our simulations over a longer time period within the accretion history of Pop III protostars ($\sim 10^4 - 10^5\,\mathrm{yr}$) and to evaluate whether accretion might eventually be shut off completely due to radiative effects, we need to implement a method for ionizing and photodissociating radiation of massive Population III stars in our code. Currently, some first tests in this direction are conducted with the AREPO radiative transfer module SPRAI (Jaura et al., 2018).

Finally, we need to include a method of sink particle merging into our version of AREPO. We expect that sink merging will have a substantial effect on total the number of sinks and corresponding quantities such as the number of ejections as well as on mass growth of individual sinks as previous studies found merger rates of up to 60% (Greif et al., 2011; Greif et al., 2012; Stacy & Bromm, 2013; Stacy et al., 2016).

List of publications

The results presented in this thesis have been published or are in preparation for publication in the following papers:

1. *Stabilizing Population III Accretion Disks with Magnetic Fields*, **Wollenberg, K. M. J.**, Glover, S. C. O., Bromm, V., Klessen, R. S., Proceedings article in Memorie Della Società Astronomica Italiana, Vol. 88 n.4, 2017, p. 864-865
2. *How the First Stars Regulated Star Formation. II. Enrichment by Nearby Supernovae*, Chen, K.-J., Whalen, D. J., **Wollenberg, K. M. J.**, Glover, S. C. O. and Klessen, R. S., 2017, ApJ, 88, 864
3. *The Fragmentation Behavior of Population III Protostellar Disks - Paper I*, **Wollenberg, K. M. J.**, Glover, S. C. O., Clark, P. C., Klessen, R. S., MNRAS 2019 (*in prep.*)
4. *The Fragmentation Behavior of Population III Protostellar Disks - Paper II: Protostellar Ejections*, **Wollenberg, K. M. J.**, Glover, S. C. O., Clark, P. C., Klessen, R. S., MNRAS 2019 (*in prep.*)

CHAPTER 10
Appendix

10.1 Additional material: halo photoevaporation

On the next few pages we present the evolution of all three halos at different points in time in the 2D ZEUS-MP simulations of halo photoevaporation. In the first figure Fig. 10.1, the states of the three halos at the beginning of the simulations is given. This can be seen as an addition to Fig. 4.2. In Fig. 10.2 to 10.4, we show the density, H_2 mass fraction and temperature states within all three halos and for all three combinations of stellar mass and distance from the star to the center of the halo at the time the star dies. Finally, Fig. 10.5 to 10.7 illustrate the states of the halos at the end of our 2D ZEUS-MP simulations, i.e. this is the state that is mapped onto the AMR grid in CASTRO.

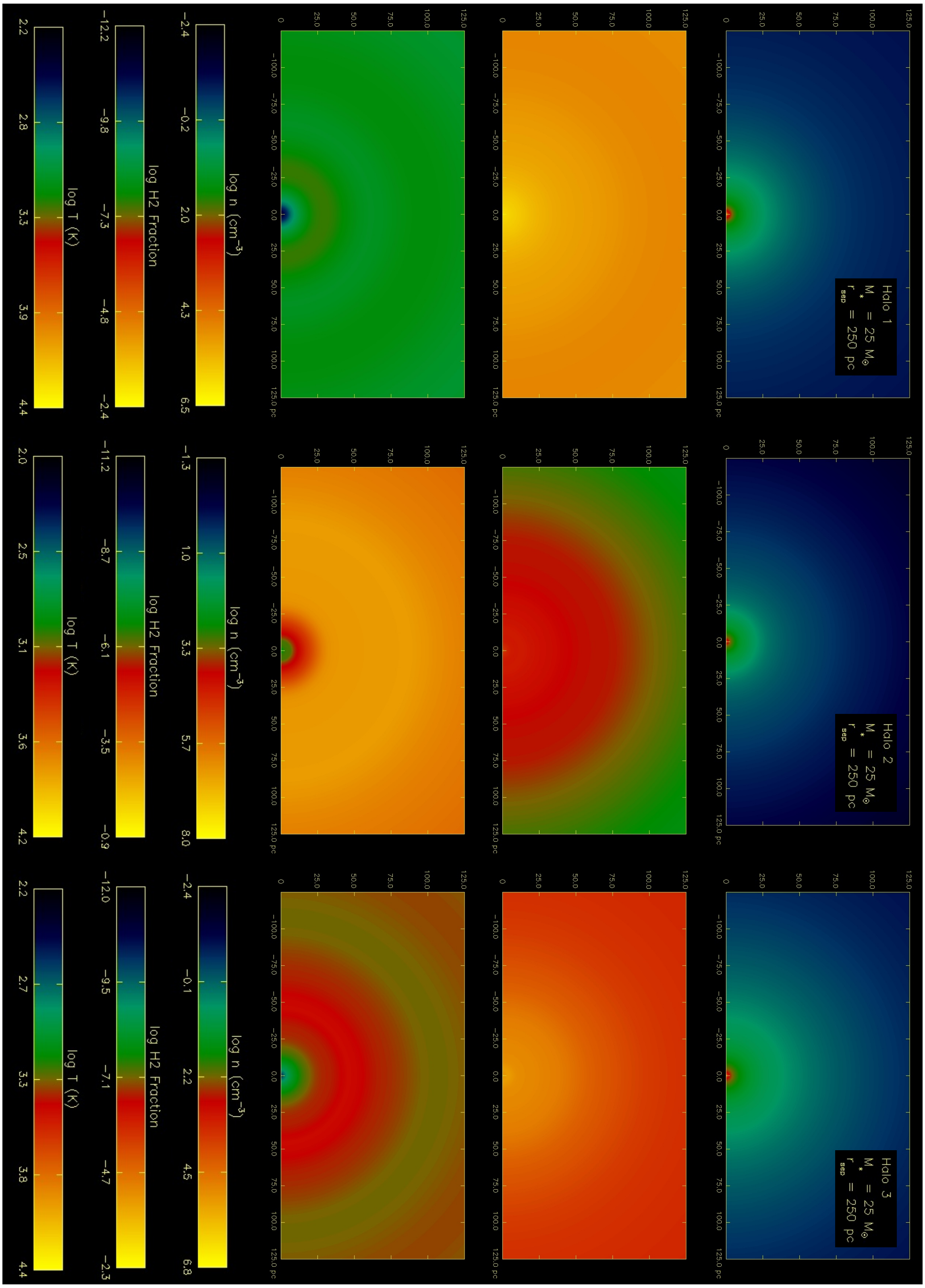

Figure 10.1: From left to right: initial conditions of halo 1, 2 and 3. From top to bottom: density, H_2 fraction and temperature. The corresponding colorbars are listed at the bottom of each column. The figures of H_2 fraction and temperature display differing colors not necessarily because they indicate very different number values but because the colorbars are gauged per individual run and not equalized for all simulations.

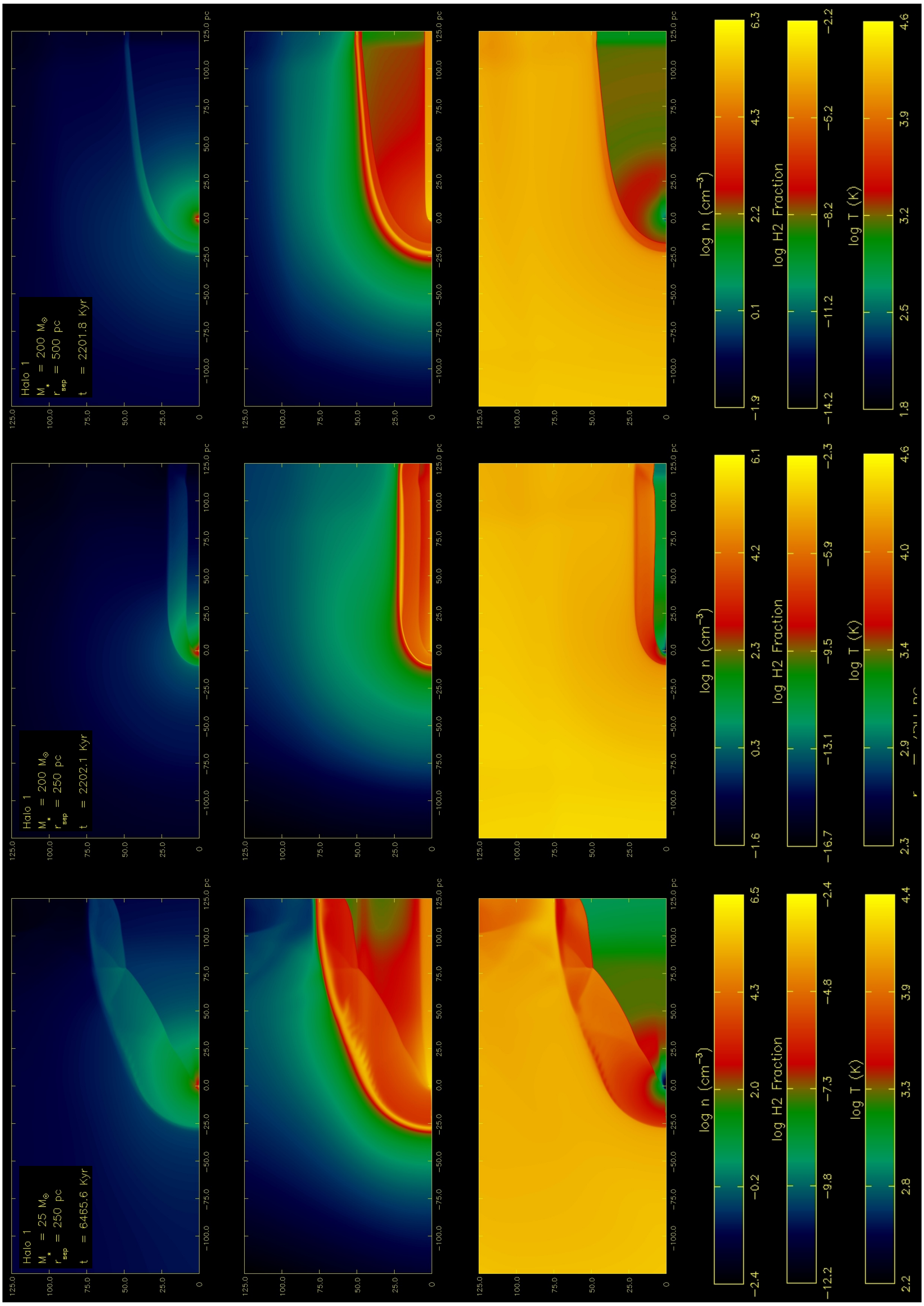

Figure 10.2: From left to right: state of halo 1 at around the time when the star dies for all three combinations of stellar mass and distance from the halo center. The $25\,M_\odot$ dies after 6.46 Myr, the $200\,M_\odot$ star after 2.2 Myr. From top to bottom: density, H_2 mass fractions and temperature with their respective colorbar at the bottom of each column.

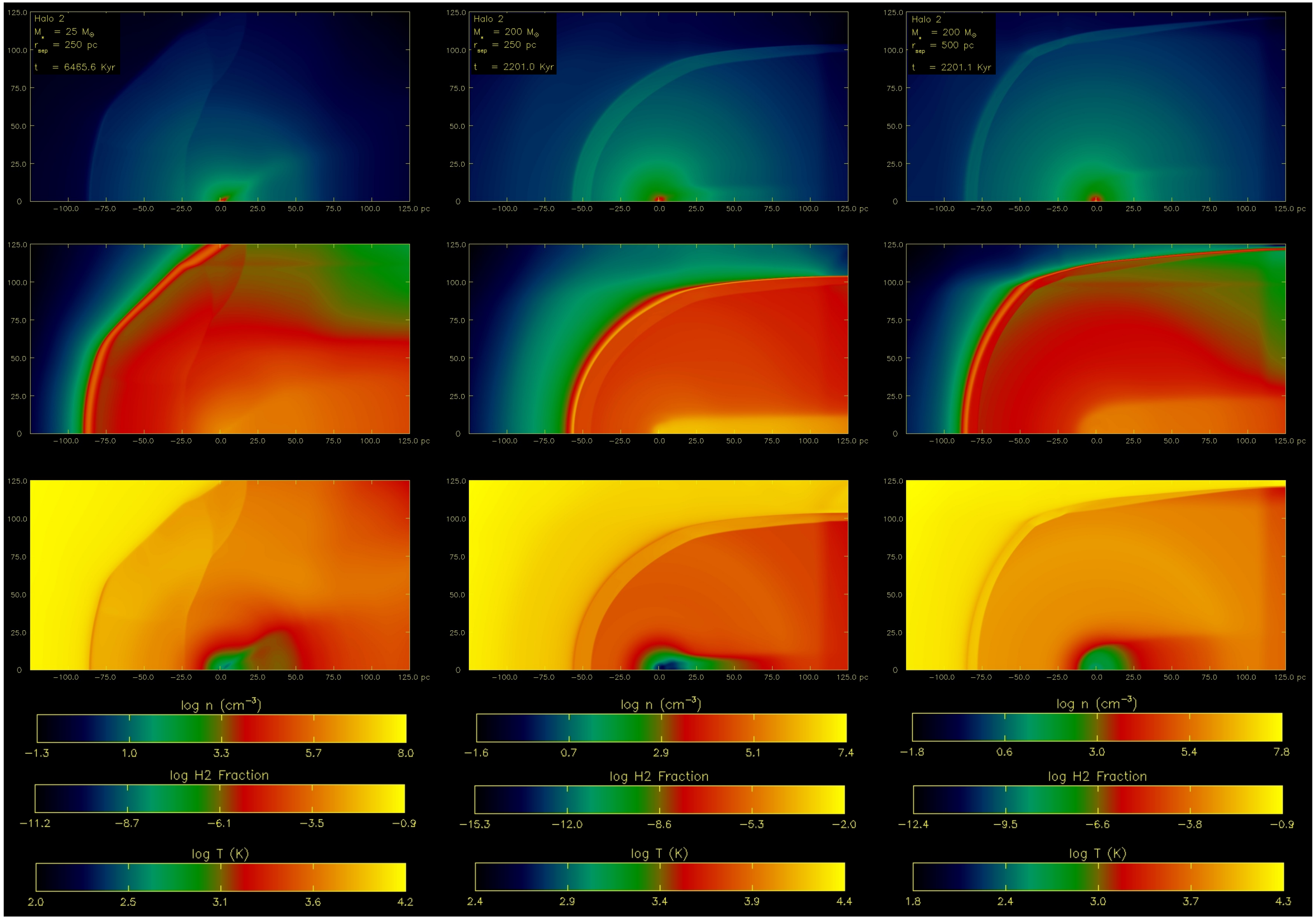

Figure 10.3: From left to right: state of halo 2 at around the time when the star dies for all three combinations of stellar mass and distance from the halo center. The 25 $M_\odot$ dies after 6.46 Myr, the 200 $M_\odot$ star after 2.2 Myr. From top to bottom: density, H_2 mass fractions and temperature with their respective colorbar at the bottom of each column.

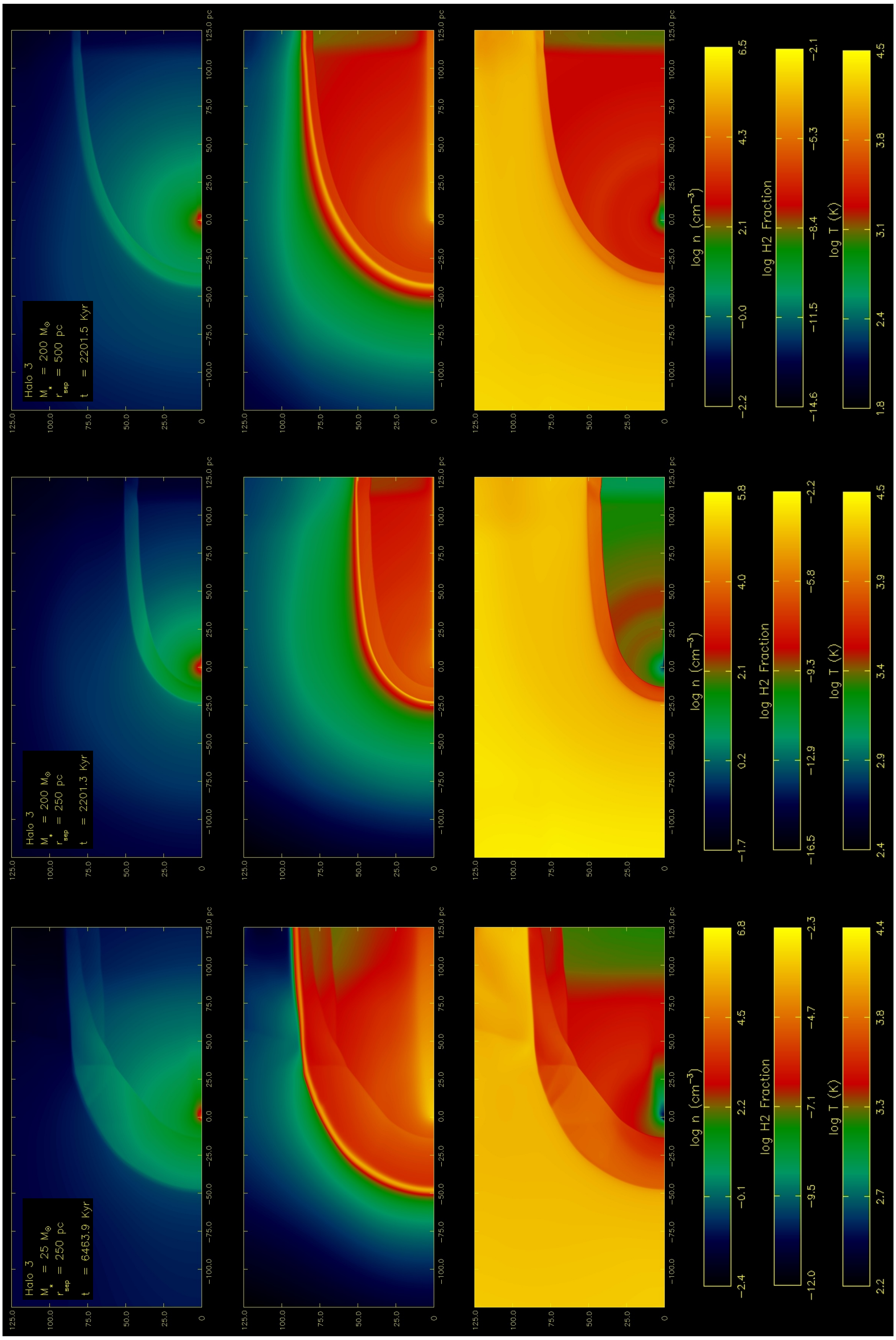

Figure 10.4: From left to right: state of halo 3 at around the time when the star dies for all three combinations of stellar mass and distance from the halo center. The $25\,M_\odot$ dies after 6.46 Myr, the $200\,M_\odot$ star after 2.2 Myr. From top to bottom: density, H_2 mass fractions and temperature with their respective colorbar at the bottom of each column.

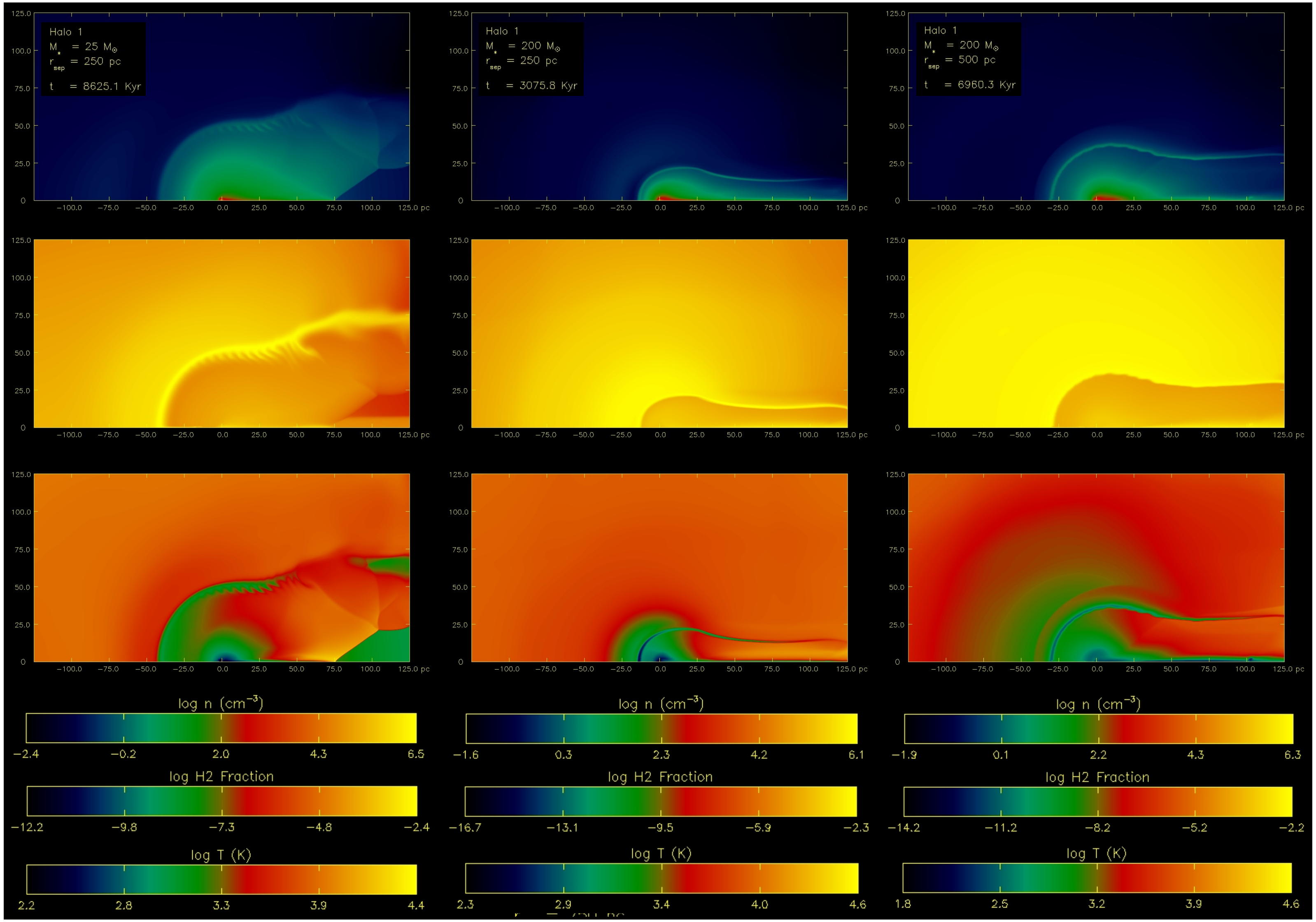

Figure 10.5: From left to right: state of halo 1 at the end of 2D ZEUS-MP halo photoevaporation simulations for all three combinations of stellar mass and distance from the halo center.

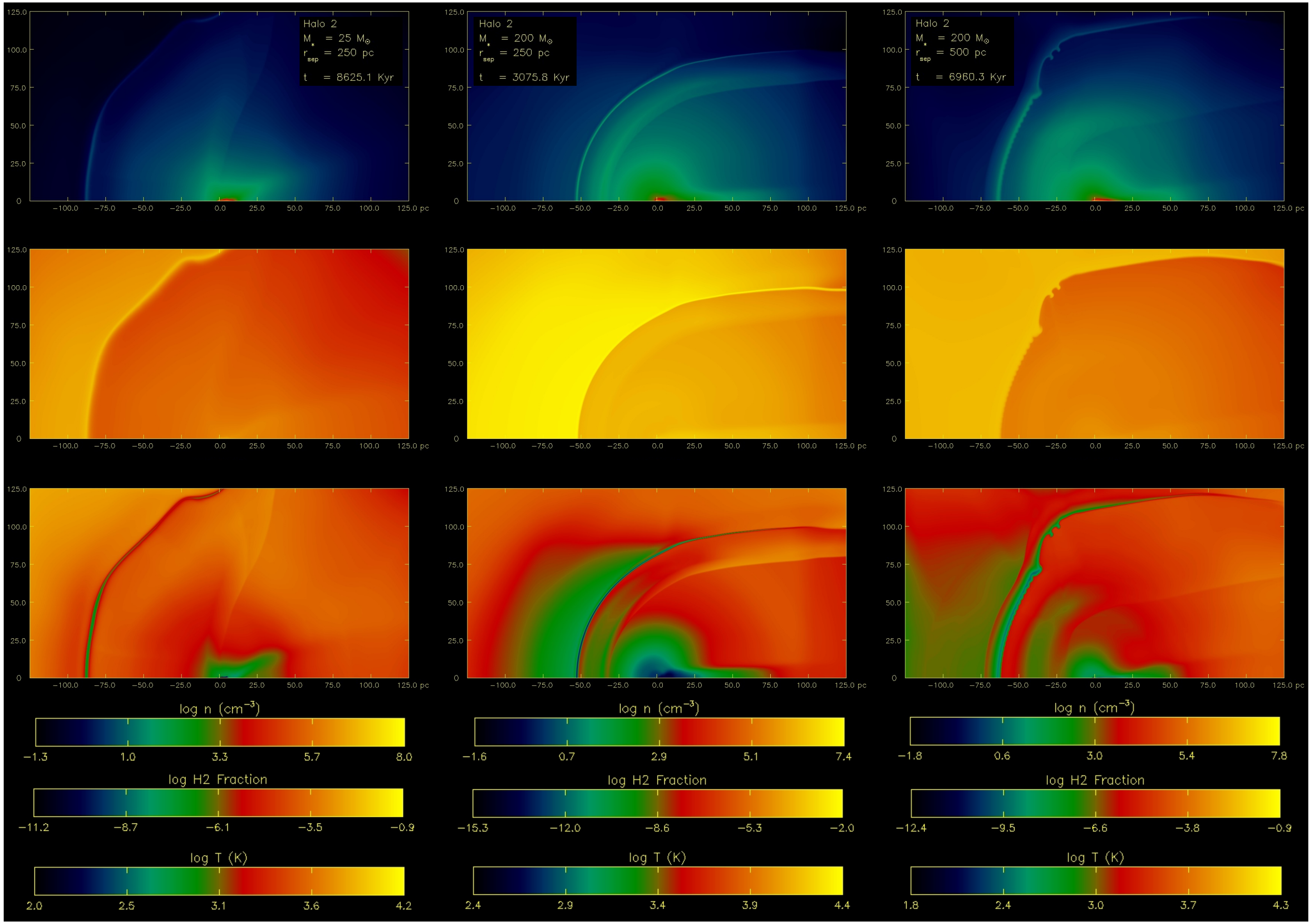

Figure 10.6: From left to right: state of halo 2 at the end of 2D ZEUS-MP halo photoevaporation simulations for all three combinations of stellar mass and distance from the halo center.

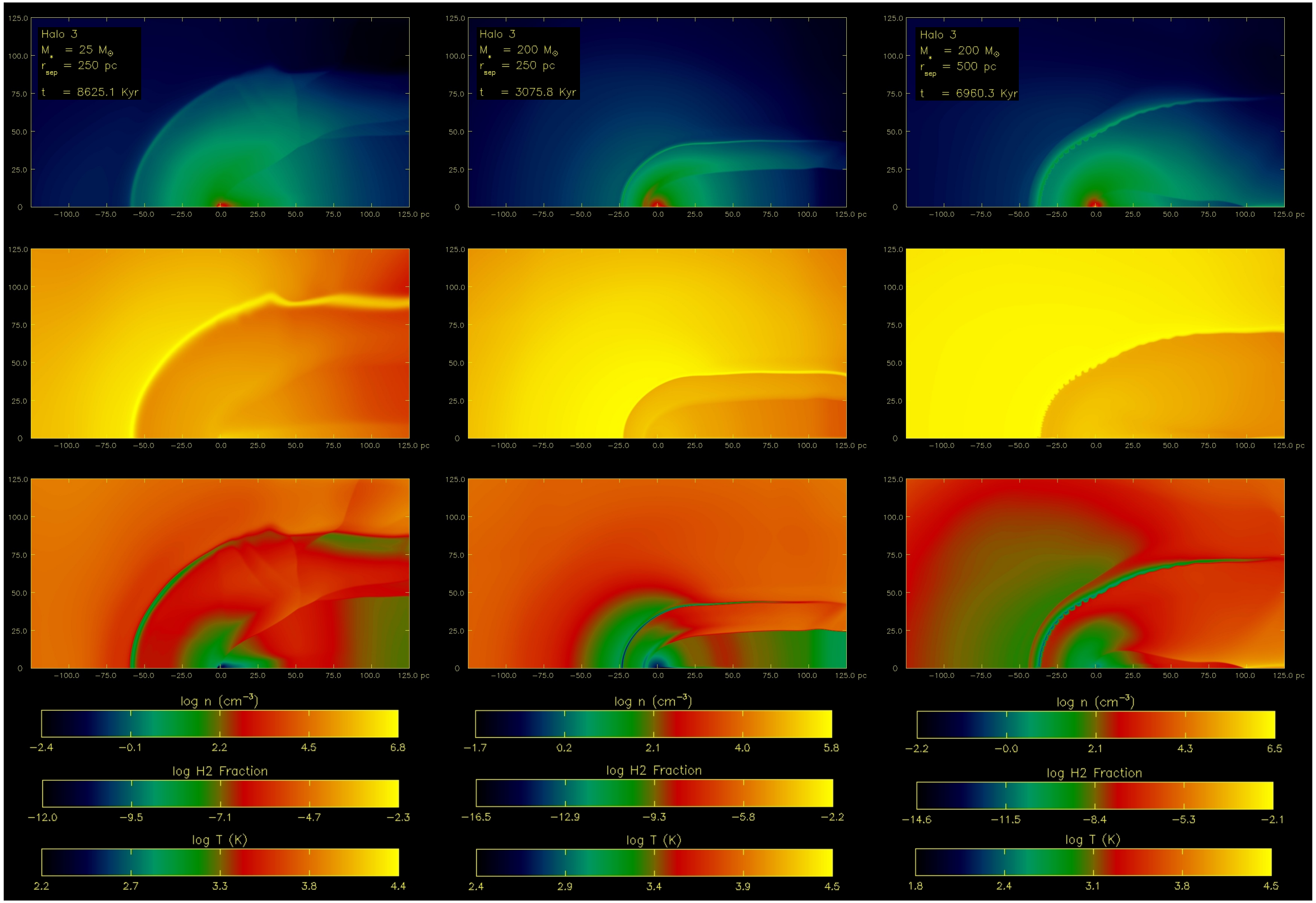

Figure 10.7: From left to right: state of halo 3 at the end of 2D ZEUS-MP halo photoevaporation simulations for all three combinations of stellar mass and distance from the halo center.

10.2 Additional material: the fragmentation behavior of Population III protostellar disks

10.2.1 Additional figures

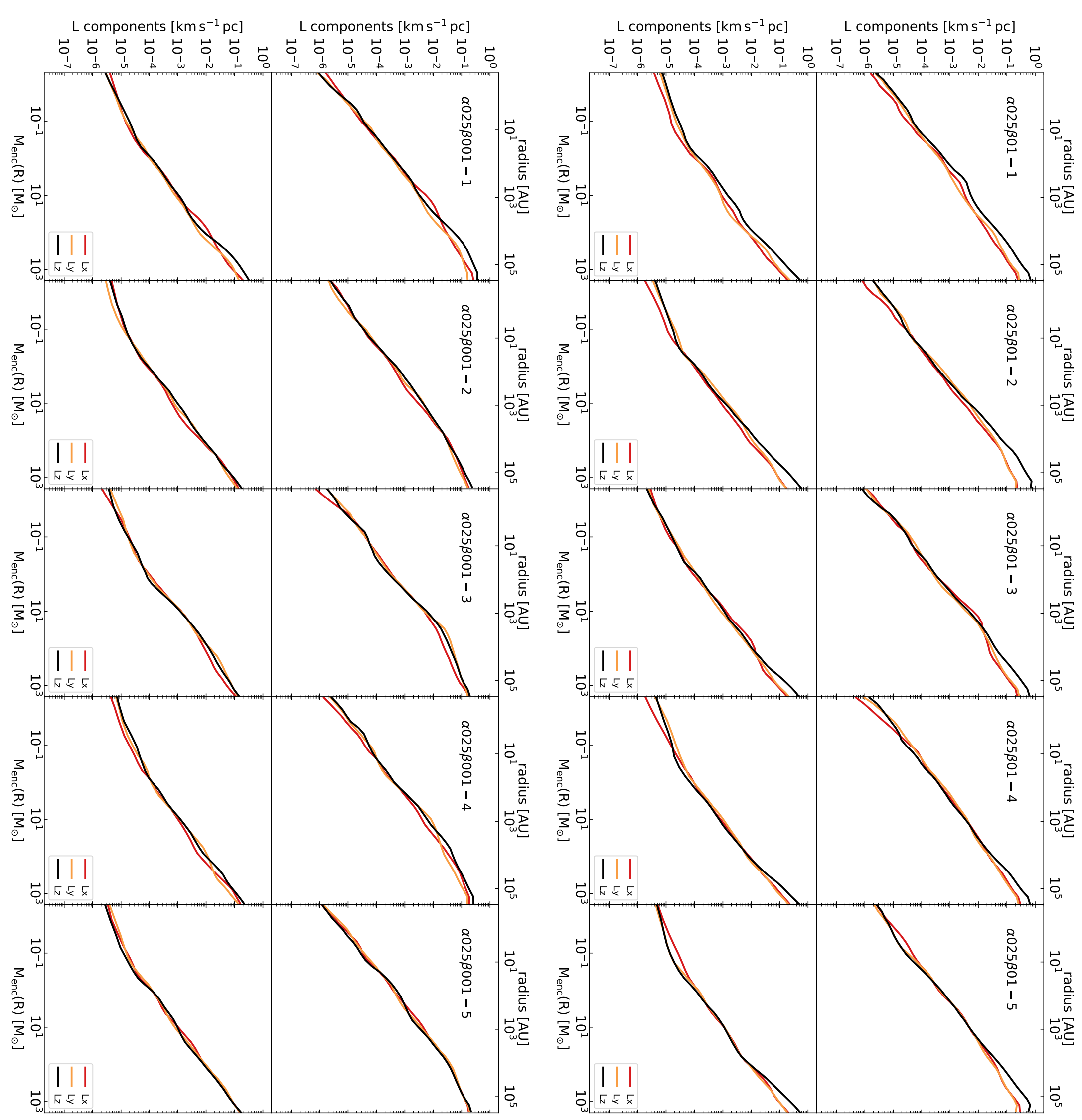

Figure 10.8: Behavior of the L_x, L_y and L_z component of the specific angular momentum vector computed with respect to the densest gas cell versus radius (top panels) and enclosed mass (bottom panels). The values are mass-weighted averages in spherical shells centered on the densest cell just before first sink formation using logarithmic binning with 40 bins. The name of the realization is indicated.

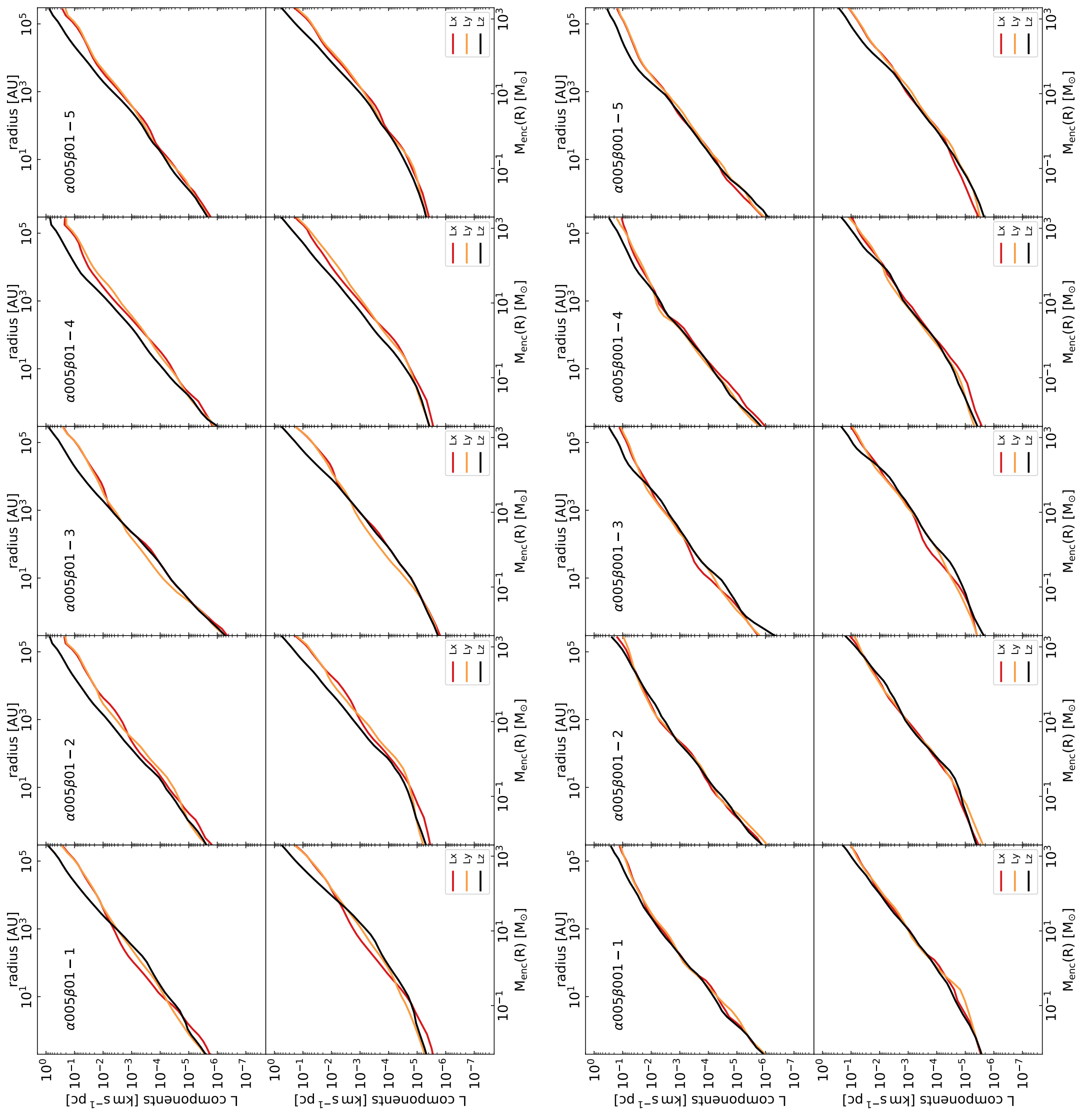

Figure 10.9: Same as in Fig. 10.8, but for further mixed realizations.

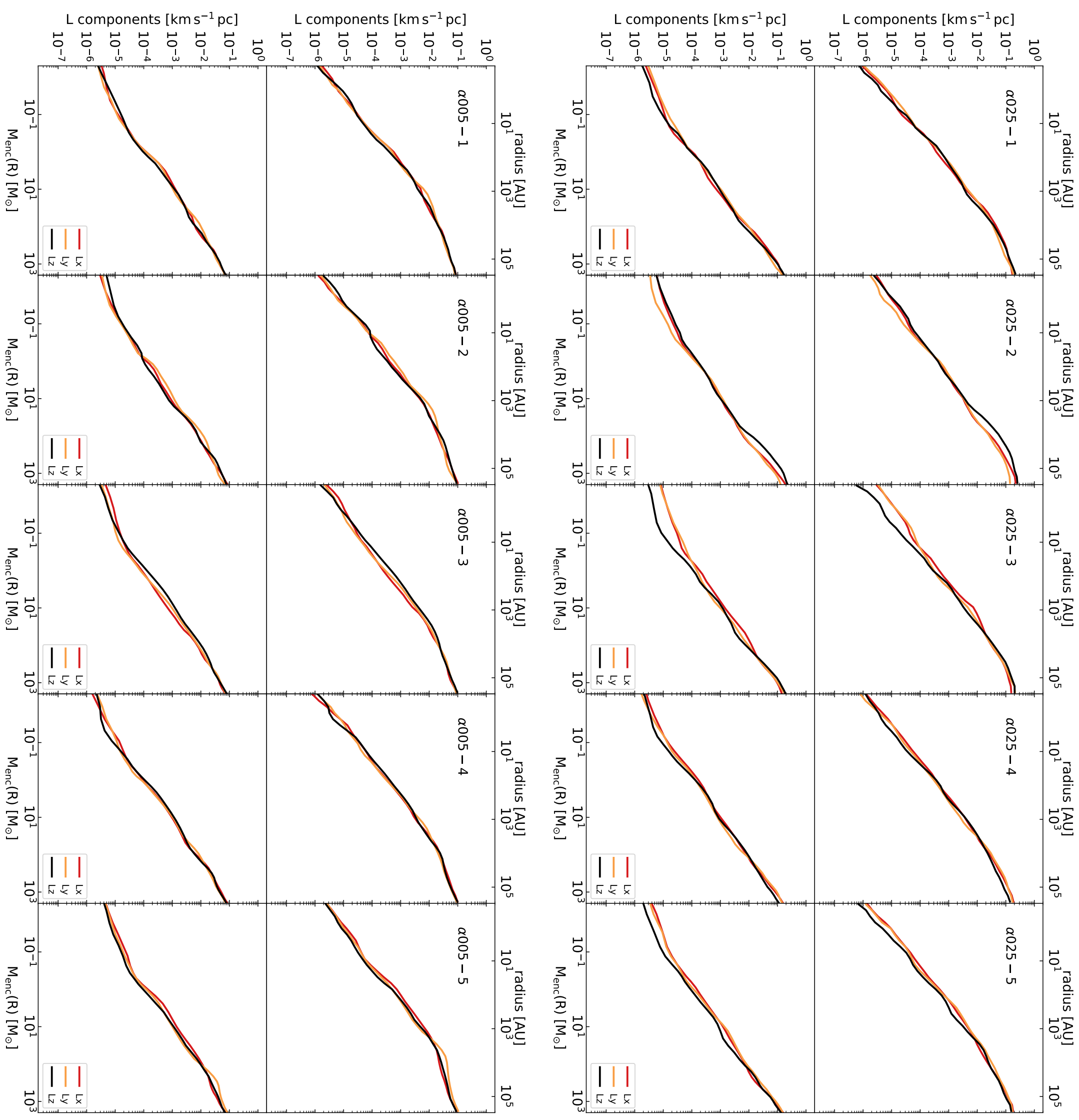

Figure 10.10: Same as in Fig. 10.8, but for the purely turbulent realizations.

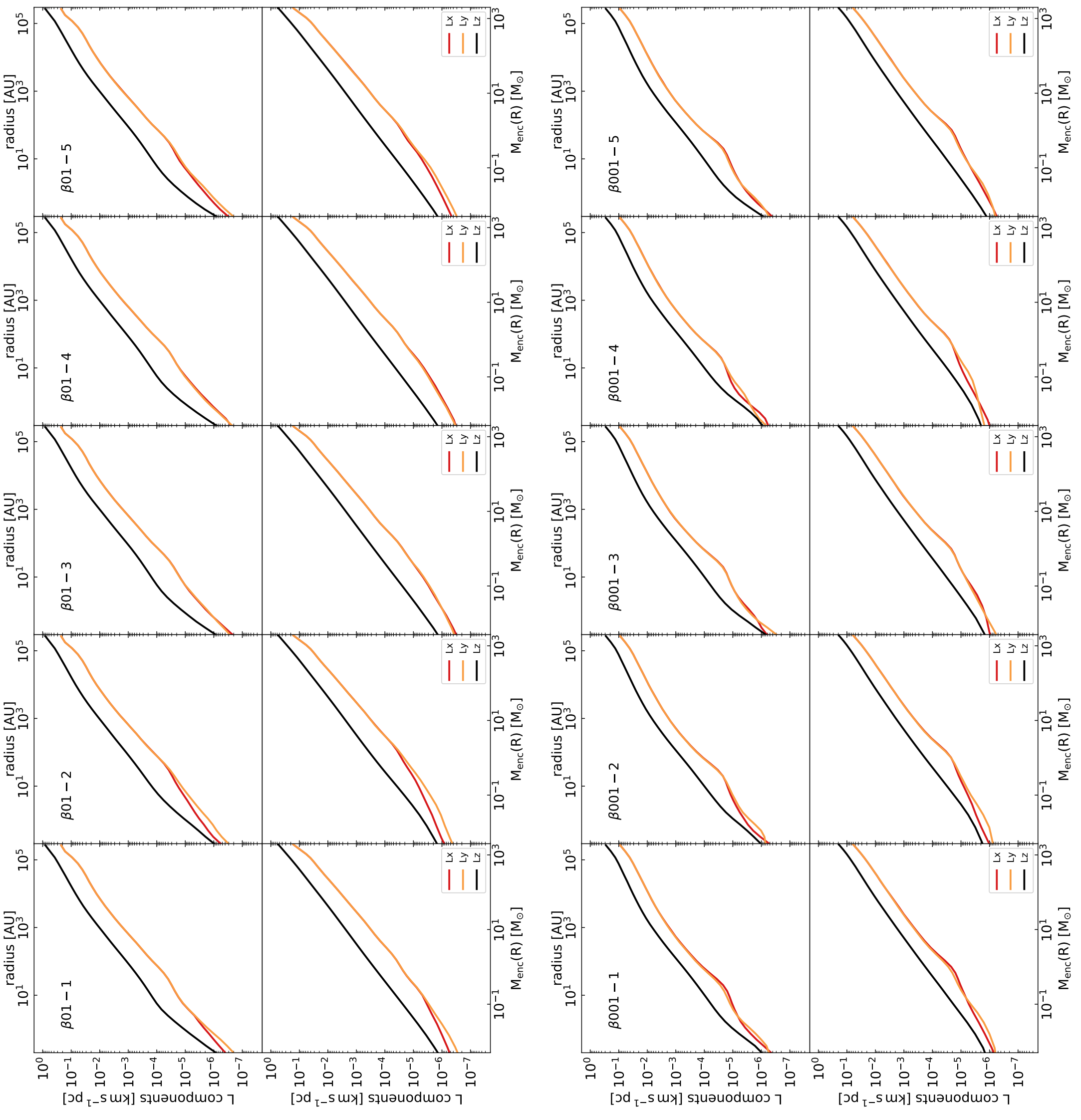

Figure 10.11: Same as in Fig. 10.8, but for the purely rotational realizations.

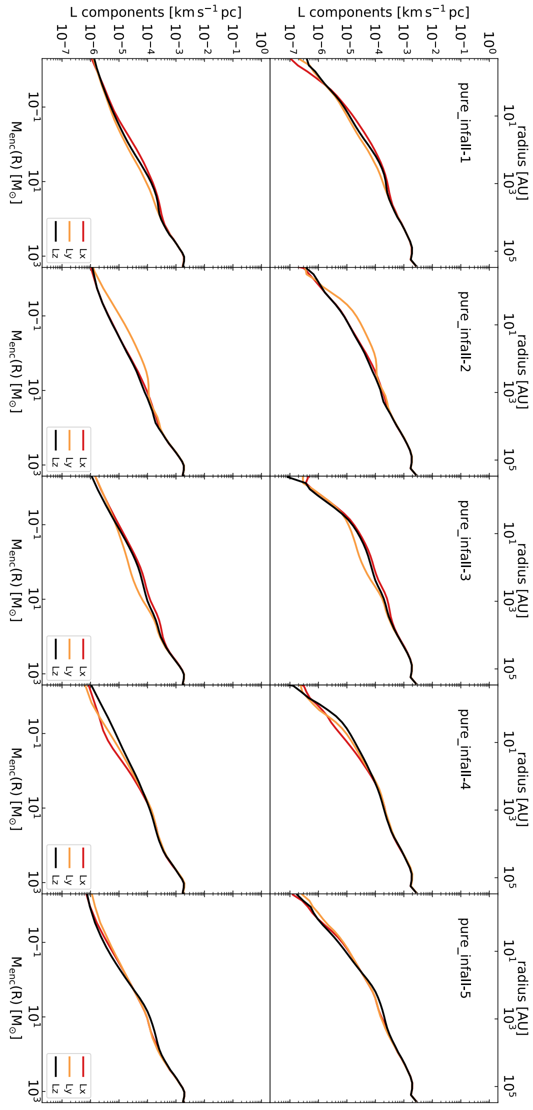

Figure 10.12: Same as in Fig. 10.8, but for the *pure infall* realizations.

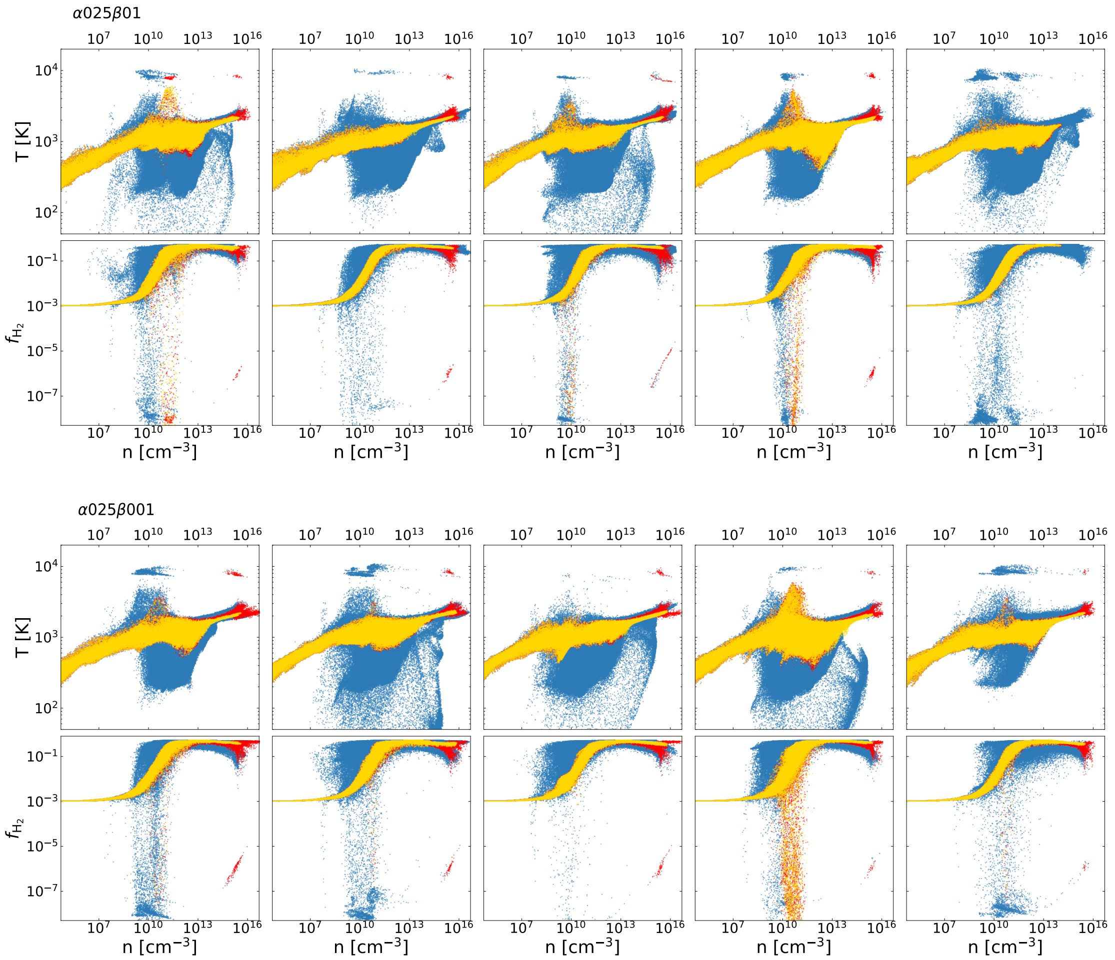

Figure 10.13: Phase plots of temperature and molecular fraction as a function of number density. Three different stages of the gas cloud evolution are shown: just prior to sink formation (yellow), just after first sink formation (red), and 1000 yr later (blue). From left to right, realization 1 to 5 are given.

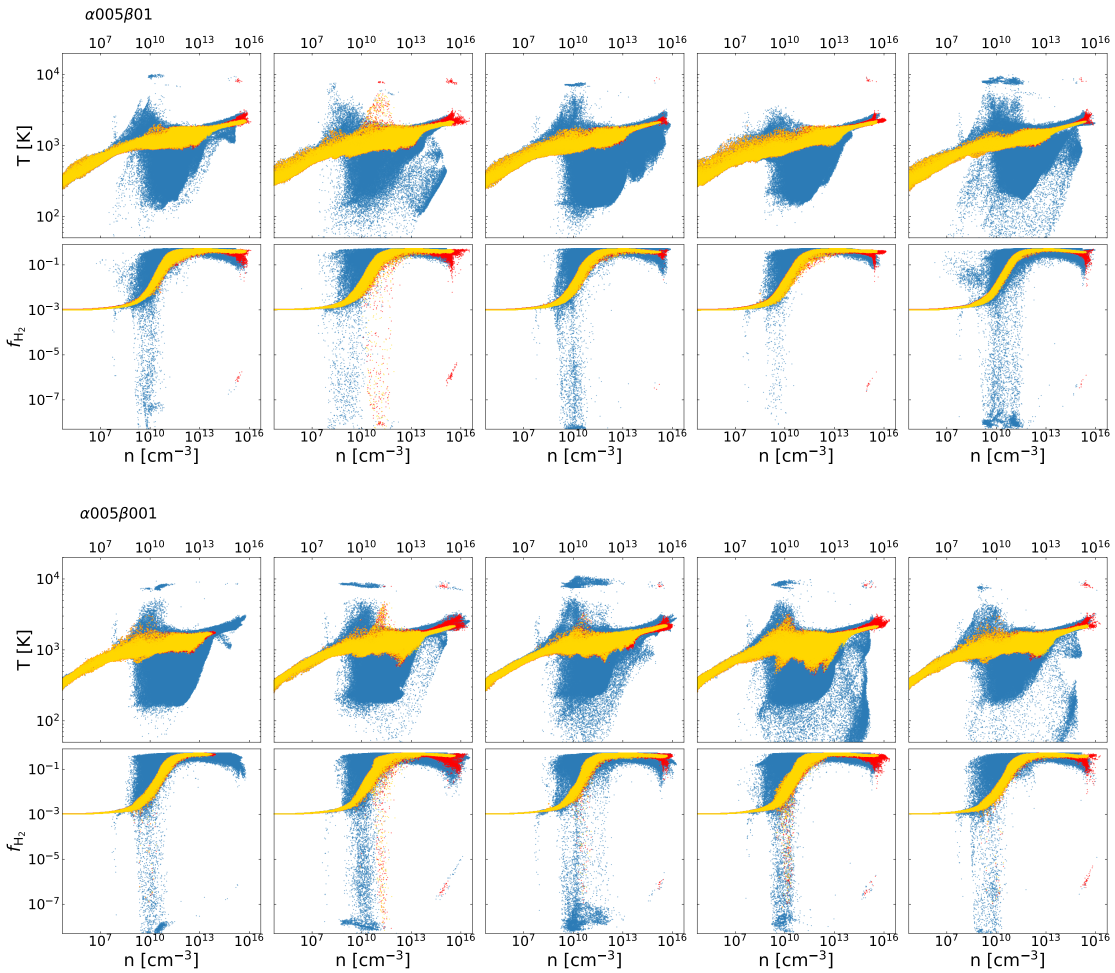

Figure 10.14: Same as Fig. 10.13, but for further mixed realizations.

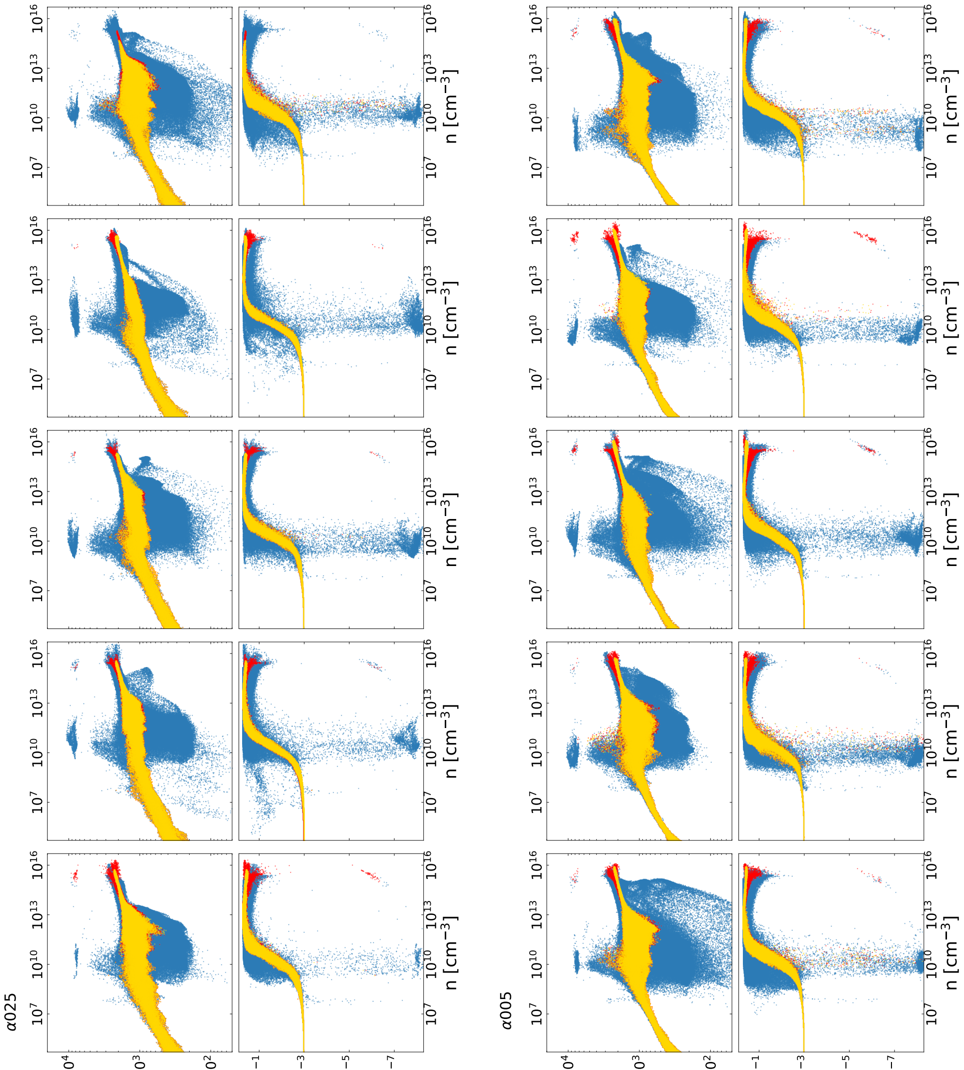

Figure 10.15: Same as Fig. 10.13, but for the purely turbulent realizations.

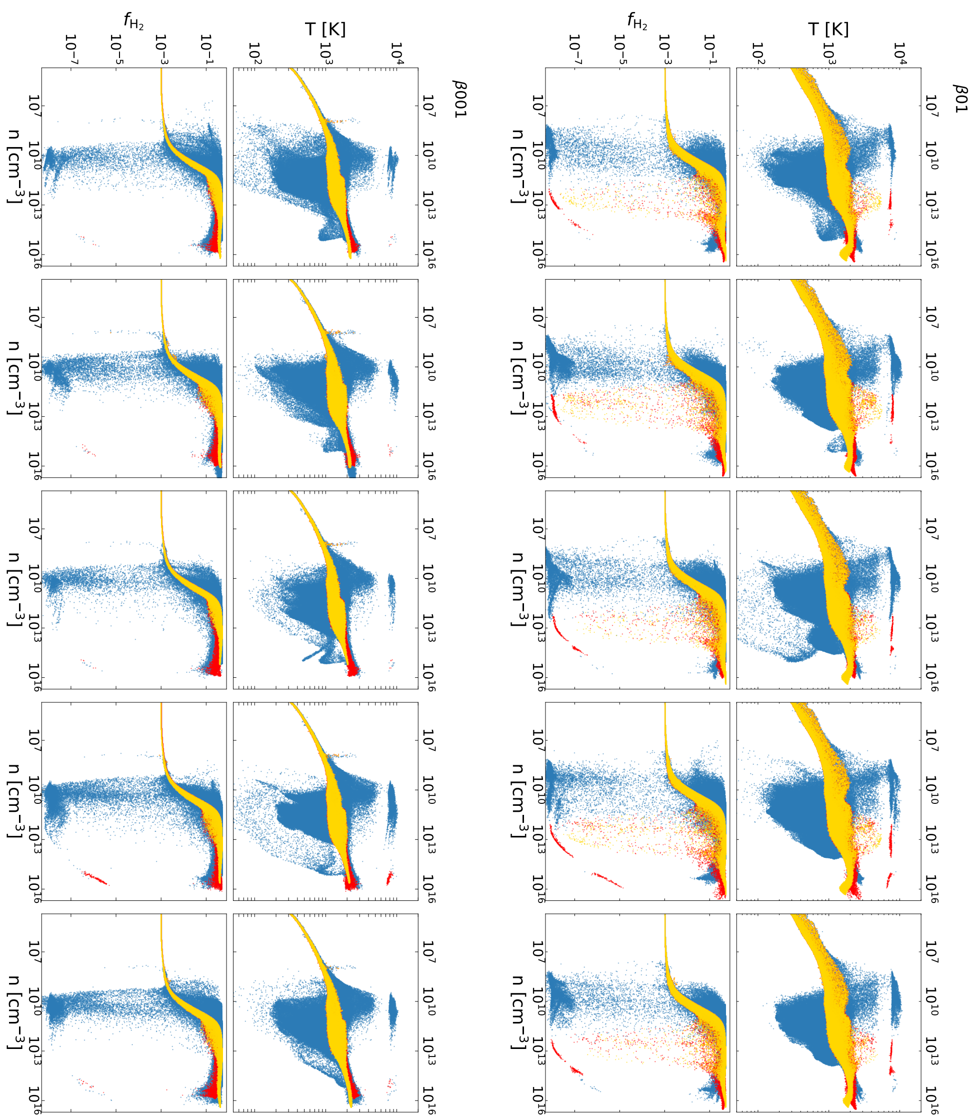

Figure 10.16: Same as Fig. 10.13, but for the purely rotational realizations.

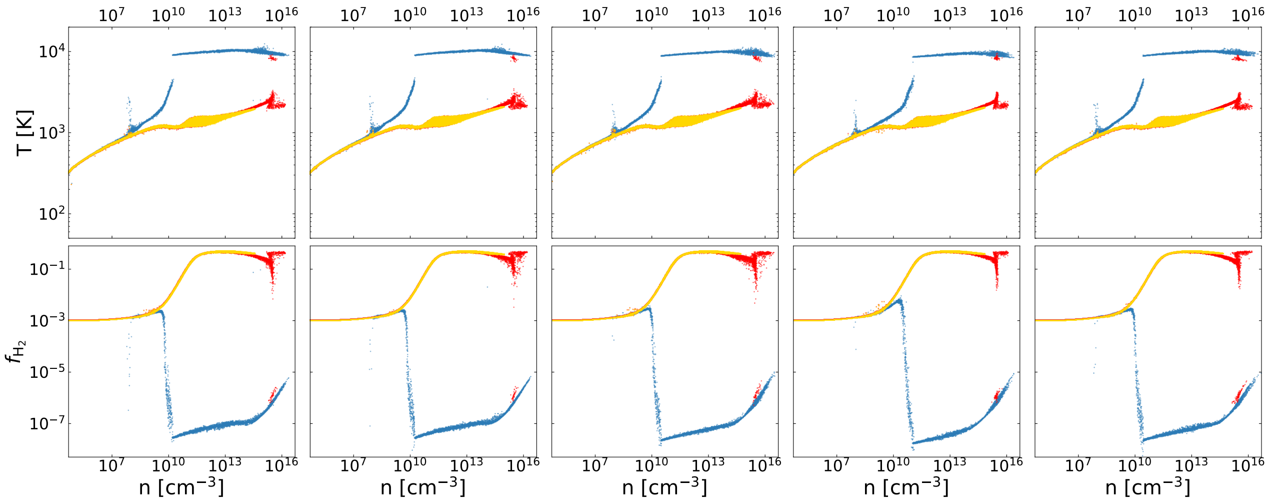

Figure 10.17: Same as Fig. 10.13, but for the *pure infall* realizations. The phase plots at the final output time show a high temperature of $T \sim 10^4$ K and a related low molecular fraction of $f_{\mathrm{H}_2} \sim 10^{-7} - 10^{-3}$ over a wide range of densities. This is due to the accretion luminosity feedback that is nearly isotropically emitted from the single protostar.

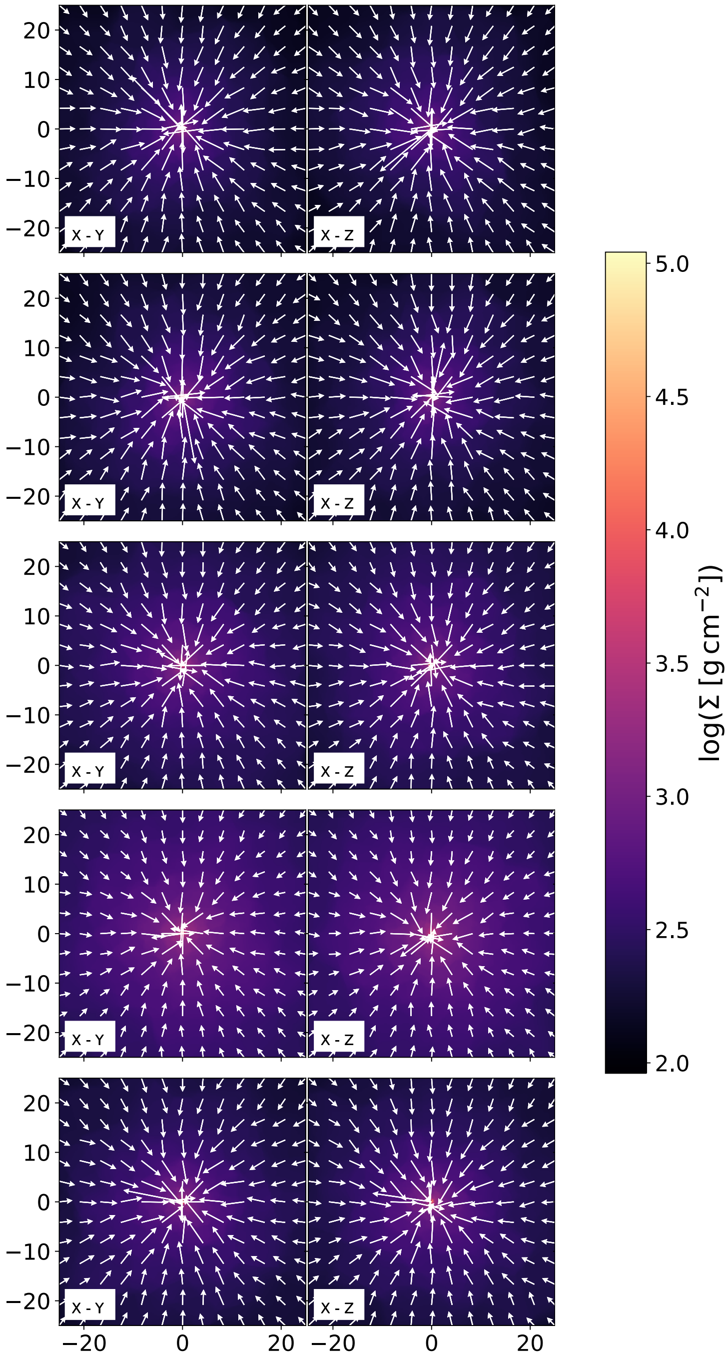

Figure 10.18: Column density projections of the *pure infall* realizations (top to bottom: model 1 to 5) at the last output time as noted in Table 10.1. Even after several hundred years of accretion, no rotationally-supported disk has formed but the accretion onto the protostar occurs in a spherical fashion. The projections have a thickness of 100 AU.

10.2.2 Additional tables

Table 10.1: Time at which the data of the various profile plots in Chapter 5 is extracted from the simulation. Time values are given in years with respect to the formation of the first sink particle.

Realization	$t_{\mathrm{before\,SF}}$ [yr]	t_{SF} [yr]	t_{final} [yr]
pure infall - 1	- 1.8	1.3	989
pure infall - 2	- 1.1	1.0	948
pure infall - 3	- 1.6	1.5	699
pure infall - 4	- 1.3	0.7	443
pure infall - 5	- 1.5	1.6	735
$\beta01-1$	- 0.6	0.4	1002
$\beta01-2$	- 0.4	0.6	1001
$\beta01-3$	- 0.6	0.4	1003
$\beta01-4$	- 0.9	0.1	1003
$\beta01-5$	- 0.6	0.4	1005
$\beta001-1$	- 0.4	0.6	1002
$\beta001-2$	- 0.5	0.5	1003
$\beta001-3$	- 0.5	0.6	1003
$\beta001-4$	- 0.9	0.1	1003
$\beta001-5$	- 0.3	0.7	1004
$\alpha025-1$	- 0.9	1.1	995
$\alpha025-2$	- 1.1	0.86	992
$\alpha025-3$	- 1.5	0.59	1008
$\alpha025-4$	- 0.9	1.1	1011
$\alpha025-5$	- 0.9	1.2	1008
$\alpha005-1$	- 0.7	1.5	1003
$\alpha005-2$	- 0.9	1.0	1002
$\alpha005-3$	- 0.6	1.4	1005
$\alpha005-4$	- 0.6	1.5	1002
$\alpha005-5$	- 0.8	1.1	1007
$\alpha025\beta01-1$	- 1.5	0.6	1007
$\alpha025\beta01-2$	- 1.2	0.9	1012
$\alpha025\beta01-3$	- 1.4	0.7	1008
$\alpha025\beta01-4$	- 1.6	0.5	1000
$\alpha025\beta01-5$	- 1.4	0.6	1002
$\alpha025\beta001-1$	- 1.4	0.7	1000
$\alpha025\beta001-2$	- 0.7	1.3	1000
$\alpha025\beta001-3$	- 1.2	0.8	1031
$\alpha025\beta001-4$	- 1.1	1.0	1008
$\alpha025\beta001-5$	- 1.0	1.1	1010
$\alpha005\beta01-1$	- 1.4	0.5	1007
$\alpha005\beta01-2$	- 1.2	0.8	1013
$\alpha005\beta01-3$	- 1.6	0.5	1004
$\alpha005\beta01-4$	- 1.2	0.7	1009
$\alpha005\beta01-5$	- 1.5	0.6	1007
$\alpha005\beta001-1$	- 1.1	1.0	1010
$\alpha005\beta001-2$	- 1.1	1.0	1006
$\alpha005\beta001-3$	- 1.1	0.9	1013
$\alpha005\beta001-4$	- 1.0	0.9	1005
$\alpha005\beta001-5$	- 1.0	1.1	1007

Table 10.2: Snapshot output times at $\sim 50yr$ after first sink formation used for Fig. fig:vrot-later.

Realization	$t_{\mathrm{SF+50\,yr}}$ [yr]
$\beta01-1$	56
$\beta01-2$	53
$\beta01-3$	67
$\beta01-4$	60
$\beta01-5$	61
$\alpha005-1$	52
$\alpha005-2$	51
$\alpha005-3$	51
$\alpha005-4$	50
$\alpha005-5$	54
$\alpha025\beta01-1$	51
$\alpha025\beta01-2$	57
$\alpha025\beta01-3$	50
$\alpha025\beta01-4$	52
$\alpha025\beta01-5$	52

Table 10.3: List of minimum cell masses and minimum Jeans masses, $\mathrm{M_J}$, for all our runs in which fragmentation happens. The masses are derived within a spherical shell of radius 100 AU around the first sink particle. For the derivation of the Jeans mass, we employed as additional constraint that only gas with $n > 10^{12}\,\mathrm{cm}^{-3}$ is included in our computation. With this we try to make sure that we consider gas of the disk that has high enough densities to form a sink. We remark that for the final values with have also run a test with an extended radius of 10000 AU around the first sink. We find comparable values of $\mathrm{M_{J,final}}$ and comparable or smaller values of $\mathrm{M_{cell,final}}$. We find that at this stage the minimum cell mass is of the order $\lesssim 10^{-6}\,\mathrm{M_\odot}$. This is three orders of magnitude smaller than the minimum mass value that appears in our mass function. The minimum cell mass decreases further later on in our simulations as the Voronoi mesh continues to refine according to the Jeans refinement criterion. Thus our effective mass resolution is fine enough to resolve the smallest fragment masses and the cut-off at $10^{-3}\,\mathrm{M_\odot}$ in our mass functions is physical given by the local Jeans mass in our disk.

Realization	$\mathrm{M_{cell,SF}}$ $[\mathrm{M_\odot}]$	$\mathrm{M_{cell,final}}$ $[\mathrm{M_\odot}]$	$\mathrm{M_{J,SF}}$ $[\mathrm{M_\odot}]$	$\mathrm{M_{J,final}}$ $[\mathrm{M_\odot}]$	$\mathrm{t_{SF}}$ [yr]	$\mathrm{t_{final}}$ [yr]
$\beta01-1$	7.3e-7	2.8e-8	8.2e-3	1.6e-2	0.38	1002
$\beta01-2$	4.2e-7	1.4e-9	7.7e-3	2.5e-2	0.59	1001
$\beta01-3$	4.0e-7	1.8e-9	1.2e-2	2.9e-2	0.41	1003
$\beta01-4$	4.2e-7	4.7e-10	4.6e-3	1.7e-2	0.14	1003
$\beta01-5$	4.0e-7	8.5e-10	8.0e-3	1.7e-2	0.41	1005
$\beta001-1$	1.5e-6	2.1e-8	1.2e-2	2.1e-2	0.59	1002
$\beta001-2$	5.4e-7	8.0e-10	7.8e-3	1.5e-2	0.52	1003
$\beta001-3$	1.5e-6	1.1e-8	1.2e-2	1.3e-2	0.60	1003
$\beta001-4$	8.3e-7	1.6e-8	7.5e-3	3.4e-2	0.12	1003
$\beta001-5$	5.6e-7	4.2e-9	1.6e-2	7.9e-3	0.70	1004
$\alpha025-1$	9.1e-7	2.8e-9	8.4e-3	2.3e-2	1.1	995
$\alpha025-2$	7.7e-7	3.4e-9	1.3e-2	4.9e-3	0.86	992
$\alpha025-3$	2.2e-6	1.1e-9	1.1e-2	3.6e-2	0.59	1008
$\alpha025-4$	2.5e-6	3.6e-9	1.1e-2	1.4e-2	1.1	1011
$\alpha025-5$	4.0e-7	6.8e-10	8.5e-3	8.1e-3	1.2	1008
$\alpha005-1$	8.9e-7	1.3e-9	1.0e-2	2.9e-2	1.5	1003
$\alpha005-2$	8.3e-7	2.0e-9	1.0e-2	3.1e-2	1.0	1002
$\alpha005-3$	5.0e-7	1.7e-9	6.3e-3	5.0e-3	1.4	1005
$\alpha005-4$	8.0e-7	1.3e-9	6.0e-3	2.3e-2	1.5	1002
$\alpha005-5$	8.2e-7	3.3e-9	1.2e-2	8.3e-2	1.1	1007
$\alpha025\beta01-1$	8.2e-7	1.5e-9	1.1e-2	1.3e-3	0.61	1007
$\alpha025\beta01-2$	5.5e-7	1.4e-9	1.1e-2	8.0e-3	0.85	1012
$\alpha025\beta01-3$	8.3e-7	3.8e-9	8.3e-3	9.3e-3	0.72	1008
$\alpha025\beta01-4$	5.1e-7	3.5e-9	1.0e-2	2.2e-2	0.53	1000
$\alpha025\beta01-5$	1.1e-6	5.8e-10	1.1e-2	3.2e-2	0.58	1002
$\alpha025\beta001-1$	3.9e-7	7.1e-10	3.6e-3	8.4e-3	0.68	1000
$\alpha025\beta001-2$	1.0e-6	2.1e-10	6.3e-3	2.2e-2	1.3	1000
$\alpha025\beta001-3$	6.7e-7	3.7e-9	5.1e-3	1.2e-2	0.76	1031
$\alpha025\beta001-4$	7.3e-7	5.9e-9	1.0e-2	1.5e-2	0.96	1008
$\alpha025\beta001-5$	5.6e-7	5.8e-9	1.1e-2	1.3e-2	1.1	1010
$\alpha005\beta01-1$	7.4e-7	2.6e-9	1.1e-2	2.3e-2	0.53	1007
$\alpha005\beta01-2$	1.2e-7	7.6e-11	6.3e-3	5.6e-4	0.84	1013
$\alpha005\beta01-3$	8.5e-7	7.4e-10	1.4e-2	1.1e-2	0.46	1004
$\alpha005\beta01-4$	1.1e-6	1.5e-9	1.3e-2	2.5e-2	0.71	1009
$\alpha005\beta01-5$	1.2e-6	6.6e-10	1.0e-2	1.2e-2	0.64	1007
$\alpha005\beta001-1$	6.6e-7	1.6e-9	8.9e-3	1.2e-2	0.96	1010
$\alpha005\beta001-2$	6.5e-7	3.8e-10	6.3e-3	7.1e-3	1.0	1006
$\alpha005\beta001-3$	8.9e-7	9.7e-10	1.1e-2	8.9e-3	0.87	1013
$\alpha005\beta001-4$	1.1e-6	6.8e-9	1.1e-2	2.3e-2	0.93	1005
$\alpha005\beta001-5$	4.2e-7	3.4e-9	9.9e-3	2.8e-2	1.1	1007

Table 10.4: Kolmogorov-Smirnov (KS) statistic of the combined sink mass functions (MF). The first line in every field is the KS statistic value and the second line the p-value. A small KS statistic value or a high p-values (> 0.01, i.e. > 1%) indicates that the combined MF distributions of the two compared setups are the same.

	$\beta 01$	$\beta 001$	$\alpha 025$	$\alpha 005$	$\alpha 025 \beta 01$	$\alpha 025 \beta 001$	$\alpha 005 \beta 01$	$\alpha 005 \beta 001$	32-$\alpha 005 \beta 001$
$\beta 01$	0.00 1.00e+00	0.18 4.19e-03	0.28 1.58e-08	0.12 5.76e-02	0.19 2.00e-03	0.20 4.33e-04	0.11 2.16e-01	0.18 1.80e-03	0.16 6.48e-03
$\beta 001$	0.18 4.19e-03	0.00 1.00e+00	0.27 2.18e-07	0.22 7.42e-05	0.20 1.41e-03	0.21 3.29e-04	0.11 2.35e-01	0.23 5.35e-05	0.18 4.16e-03
$\alpha 025$	0.28 1.58e-08	0.27 2.18e-07	0.00 1.00e+00	0.18 1.21e-04	0.12 5.58e-02	0.14 1.20e-02	0.21 2.25e-04	0.13 1.85e-02	0.15 4.66e-03
$\alpha 005$	0.12 5.76e-02	0.22 7.42e-05	0.18 1.21e-04	0.00 1.00e+00	0.10 2.01e-01	0.10 1.45e-01	0.11 1.53e-01	0.08 3.23e-01	0.08 3.47e-01
$\alpha 025 \beta 01$	0.19 2.00e-03	0.20 1.41e-03	0.12 5.58e-02	0.10 2.01e-01	0.00 1.00e+00	0.06 7.53e-01	0.12 1.91e-01	0.06 7.69e-01	0.07 7.34e-01
$\alpha 025 \beta 001$	0.20 4.33e-04	0.21 3.29e-04	0.14 1.20e-02	0.10 1.45e-01	0.06 7.53e-01	0.00 1.00e+00	0.13 8.49e-02	0.07 5.02e-01	0.06 7.45e-01
$\alpha 005 \beta 01$	0.11 2.16e-01	0.11 2.35e-01	0.21 2.25e-04	0.11 1.53e-01	0.12 1.91e-01	0.13 8.49e-02	0.00 1.00e+00	0.14 5.67e-02	0.10 3.00e-01
$\alpha 005 \beta 001$	0.18 1.80e-03	0.23 5.35e-05	0.13 1.85e-02	0.08 3.23e-01	0.06 7.69e-01	0.07 5.02e-01	0.14 5.67e-02	0.00 1.00e+00	0.09 3.22e-01
32-$\alpha 005 \beta 001$	0.16 6.48e-03	0.18 4.16e-03	0.15 4.66e-03	0.08 3.47e-01	0.07 7.34e-01	0.06 7.45e-01	0.10 3.00e-01	0.09 3.22e-01	0.00 1.00e+00

Table 10.5: Details of the touching-radii scenario. Number of encounters between protostars within the same, $N_{\rm ii}$, or different mass ranges, $N_{\rm ij}$; here index i and j indicate either low-mass protostars (index 's'; $\leq 0.8\,{\rm M}_\odot$), medium-mass protostars (index 'm'; $0.8 < M \leq 5\,{\rm M}_\odot$), or high-mass protostars (index 'l'; $> 5\,{\rm M}_\odot$). In addition, the $N_{\rm ii}$ or $N_{\rm ij}$ per total number of measured close encounters in this scenario, i.e. $N_{\rm merge,tot} = N_{\rm ss} + N_{\rm sm} + N_{\rm sl} + N_{\rm mm} + N_{\rm ml} + N_{\rm ll}$, is given.

Model	$N_{\rm ss}$	$N_{\rm ss}$ $/N_{\rm merge,tot}$	$N_{\rm sm}$	$N_{\rm sm}$ $/N_{\rm merge,tot}$	$N_{\rm sl}$	$N_{\rm sl}$ $/N_{\rm merge,tot}$	$N_{\rm mm}$	$N_{\rm mm}$ $/N_{\rm merge,tot}$	$N_{\rm ml}$	$N_{\rm ml}$ $/N_{\rm merge,tot}$	$N_{\rm ll}$	$N_{\rm ll}$ $/N_{\rm merge,tot}$
$\beta01-1$	11	0.7333	4	0.2667	0	0.0000	0	0.0000	0	0.0000	0	0.0000
$\beta01-2$	0	0.0000	4	0.8000	0	0.0000	1	0.2000	0	0.0000	0	0.0000
$\beta01-3$	0	0.0000	2	0.4000	0	0.0000	3	0.6000	0	0.0000	0	0.0000
$\beta01-4$	2	0.5000	1	0.2500	0	0.0000	1	0.2500	0	0.0000	0	0.0000
$\beta01-5$	0	0.0000	2	0.5000	0	0.0000	2	0.5000	0	0.0000	0	0.0000
$\beta001-1$	0	0.0000	2	0.2000	0	0.0000	6	0.6000	2	0.2000	0	0.0000
$\beta001-2$	0	0.0000	2	0.3333	0	0.0000	3	0.5000	1	0.1667	0	0.0000
$\beta001-3$	0	0.0000	2	0.2500	0	0.0000	5	0.6250	1	0.1250	0	0.0000
$\beta001-4$	3	0.3000	1	0.2000	0	0.0000	4	0.4000	1	0.1000	0	0.0000
$\beta001-5$	4	0.4444	1	0.1111	0	0.0000	4	0.4444	0	0.0000	0	0.0000
$\alpha005-1$	0	0.0000	0	0.0000	2	0.2000	3	0.3000	4	0.4000	1	0.1000
$\alpha005-2$	2	0.2222	3	0.3333	0	0.0000	2	0.2222	1	0.1111	1	0.1111
$\alpha005-3$	0	0.0000	2	0.4000	2	0.4000	0	0.0000	1	0.2000	0	0.0000
$\alpha005-4$	0	0.0000	0	0.0000	2	0.3333	0	0.0000	4	0.6667	0	0.0000
$\alpha005-5$	0	0.0000	2	0.2500	0	0.0000	6	0.7500	0	0.0000	0	0.0000
$\alpha025-1$	0	0.0000	3	0.3750	3	0.3750	1	0.1250	1	0.1250	0	0.0000
$\alpha025-2$	2	0.4000	1	0.2000	0	0.0000	0	0.0000	1	0.2000	1	0.2000
$\alpha025-3$	0	0.0000	6	0.4286	0	0.0000	4	0.2857	4	0.2857	0	0.0000
$\alpha025-4$	0	0.0000	0	0.0000	2	0.4000	0	0.0000	3	0.6000	0	0.0000
$\alpha025-5$	1	0.1000	1	0.1000	4	0.4000	0	0.0000	3	0.3000	1	0.1000
$\alpha025\beta01-1$	1	0.0769	6	0.4615	0	0.0000	5	0.3846	1	0.0769	0	0.0000
$\alpha025\beta01-2$	0	0.0000	0	0.0000	0	0.0000	1	0.5000	1	0.5000	0	0.0000
$\alpha025\beta01-3$	0	0.0000	0	0.0000	1	1.0000	0	0.0000	0	0.0000	0	0.0000
$\alpha025\beta01-4$	1	0.1250	1	0.1250	4	0.5000	1	0.1250	1	0.1250	0	0.0000
$\alpha025\beta01-5$	0	0.0000	2	0.5000	0	0.0000	0	0.0000	2	0.5000	0	0.0000
$\alpha025\beta001-1$	1	0.1429	1	0.1429	0	0.0000	4	0.5714	1	0.1429	0	0.0000
$\alpha025\beta001-2$	0	0.0000	1	0.0833	3	0.2500	4	0.3333	3	0.2500	1	0.0833
$\alpha025\beta001-3$	0	0.0000	1	0.2500	0	0.0000	1	0.2500	2	0.5000	0	0.0000
$\alpha025\beta001-4$	2	0.2222	1	0.1111	1	0.1111	1	0.1111	2	0.2222	2	0.2222
$\alpha025\beta001-5$	0	0.0000	0	0.0000	5	0.8333	0	0.0000	1	0.1667	0	0.0000
$\alpha005\beta01-1$	1	0.1429	2	0.2857	0	0.0000	3	0.4286	1	0.1429	0	0.0000
$\alpha005\beta01-2$	0	0.0000	2	0.5000	0	0.0000	2	0.5000	0	0.0000	0	0.0000
$\alpha005\beta01-3$	1	0.1250	2	0.2500	0	0.0000	5	0.6250	0	0.0000	0	0.0000
$\alpha005\beta01-4$	0	0.0000	2	1.0000	0	0.0000	0	0.0000	0	0.0000	0	0.0000
$\alpha005\beta01-5$	0	0.0000	2	0.4000	1	0.2000	2	0.4000	0	0.0000	0	0.0000
$\alpha005\beta001-1$	2	0.5000	0	0.0000	0	0.0000	1	0.2500	1	0.2500	0	0.0000
$\alpha005\beta001-2$	0	0.0000	2	0.3333	0	0.0000	0	0.0000	4	0.6667	0	0.0000
$\alpha005\beta001-3$	0	0.0000	2	0.1818	6	0.5455	0	0.0000	3	0.2727	0	0.0000
$\alpha005\beta001-4$	0	0.0000	0	0.0000	3	0.2727	4	0.3636	2	0.1818	2	0.1818
$\alpha005\beta001-5$	1	0.2000	0	0.0000	3	0.6000	0	0.0000	1	0.2000	0	0.0000

Table 10.6: Details of the tidal-radius scenario. Number of encounters between protostars within the same, N_{ii}, or different mass ranges, N_{ij}; here index i and j indicate either low-mass protostars (index 's'; $\leq 0.8\,\mathrm{M}_{\odot}$), medium-mass protostars (index 'm'; $0.8 < M \leq 5\,\mathrm{M}_{\odot}$), or high-mass protostars (index 'l'; $> 5\,\mathrm{M}_{\odot}$). In addition, the N_{ii} or N_{ij} per total number of measured close encounters in this scenario, i.e. $N_{\mathrm{merge,tot}} = N_{\mathrm{ss}} + N_{\mathrm{sm}} + N_{\mathrm{sl}} + N_{\mathrm{mm}} + N_{\mathrm{ml}} + N_{\mathrm{ll}}$, is given.

Model	N_{ss}	N_{ss} $/N_{\mathrm{merge,tot}}$	N_{sm}	N_{sm} $/N_{\mathrm{merge,tot}}$	N_{sl}	N_{sl} $/N_{\mathrm{merge,tot}}$	N_{mm}	N_{mm} $/N_{\mathrm{merge,tot}}$	N_{ml}	N_{ml} $/N_{\mathrm{merge,tot}}$	N_{ll}	N_{ll} $/N_{\mathrm{merge,tot}}$
$\beta01-1$	18	0.6207	10	0.3448	0	0.0000	1	0.0345	0	0.0000	0	0.0000
$\beta01-2$	2	0.1538	8	0.6154	0	0.0000	3	0.2308	0	0.0000	0	0.0000
$\beta01-3$	6	0.3750	5	0.3125	0	0.0000	5	0.3125	0	0.0000	0	0.0000
$\beta01-4$	3	0.2500	7	0.5833	0	0.0000	2	0.1667	0	0.0000	0	0.0000
$\beta01-5$	4	0.4000	4	0.4000	0	0.0000	2	0.2000	0	0.0000	0	0.0000
$\beta001-1$	2	0.1176	4	0.2353	1	0.0588	8	0.4706	2	0.1176	0	0.0000
$\beta001-2$	0	0.0000	5	0.4167	1	0.0833	4	0.3333	2	0.1667	0	0.0000
$\beta001-3$	1	0.0625	5	0.3125	2	0.1250	6	0.3750	2	0.1250	0	0.0000
$\beta001-4$	6	0.2857	7	0.3333	2	0.0952	5	0.2381	1	0.0476	0	0.0000
$\beta001-5$	7	0.3889	4	0.2222	0	0.0000	7	0.3889	0	0.0000	0	0.0000
$\alpha005-1$	1	0.0417	4	0.1667	8	0.3333	5	0.2083	5	0.2083	1	0.0417
$\alpha005-2$	3	0.1304	9	0.3913	3	0.1304	6	0.2609	1	0.0435	1	0.0435
$\alpha005-3$	1	0.0526	6	0.3158	9	0.4737	1	0.0526	2	0.1053	0	0.0000
$\alpha005-4$	2	0.1176	0	0.0000	11	0.6471	0	0.0000	4	0.2353	0	0.0000
$\alpha005-5$	1	0.0588	5	0.2941	0	0.0000	9	0.5294	2	0.1176	0	0.0000
$\alpha025-1$	0	0.0000	7	0.2917	15	0.6250	1	0.0417	1	0.0417	0	0.0000
$\alpha025-2$	3	0.1875	2	0.1250	8	0.5000	0	0.0000	2	0.1250	1	0.0625
$\alpha025-3$	2	0.0769	11	0.4231	0	0.0000	9	0.3462	4	0.1538	0	0.0000
$\alpha025-4$	1	0.0909	3	0.2727	3	0.2727	0	0.0000	4	0.3636	0	0.0000
$\alpha025-5$	1	0.0323	4	0.1290	20	0.6452	1	0.0323	4	0.1290	1	0.0323
$\alpha025\beta01-1$	4	0.1739	11	0.4783	0	0.0000	7	0.3043	1	0.0435	0	0.0000
$\alpha025\beta01-2$	0	0.0000	2	0.4000	0	0.0000	1	0.2000	2	0.4000	0	0.0000
$\alpha025\beta01-3$	0	0.0000	3	0.5000	2	0.3333	0	0.0000	0	0.0000	1	0.1667
$\alpha025\beta01-4$	1	0.0625	2	0.1250	9	0.5625	1	0.0625	3	0.1875	0	0.0000
$\alpha025\beta01-5$	0	0.0000	10	0.5000	6	0.3000	0	0.0000	4	0.2000	0	0.0000
$\alpha025\beta001-1$	2	0.1176	5	0.2941	3	0.1765	6	0.3529	1	0.0588	0	0.0000
$\alpha025\beta001-2$	1	0.0323	7	0.2258	12	0.3871	7	0.2258	3	0.0968	1	0.0323
$\alpha025\beta001-3$	2	0.1000	4	0.2000	3	0.1500	5	0.2500	6	0.3000	0	0.0000
$\alpha025\beta001-4$	2	0.0952	3	0.1429	9	0.4286	1	0.0476	4	0.1905	2	0.0952
$\alpha025\beta001-5$	0	0.0000	2	0.0952	18	0.8571	0	0.0000	1	0.0476	0	0.0000
$\alpha005\beta01-1$	2	0.1429	5	0.3571	0	0.0000	6	0.4286	1	0.0714	0	0.0000
$\alpha005\beta01-2$	0	0.0000	5	0.5000	0	0.0000	5	0.5000	0	0.0000	0	0.0000
$\alpha005\beta01-3$	2	0.1818	4	0.3636	0	0.0000	5	0.4545	0	0.0000	0	0.0000
$\alpha005\beta01-4$	0	0.0000	5	1.0000	0	0.0000	0	0.0000	0	0.0000	0	0.0000
$\alpha005\beta01-5$	1	0.0909	4	0.3636	1	0.0909	4	0.3636	1	0.0909	0	0.0000
$\alpha005\beta001-1$	5	0.4167	5	0.4167	0	0.0000	1	0.0833	1	0.0833	0	0.0000
$\alpha005\beta001-2$	1	0.0667	5	0.3333	3	0.2000	1	0.0667	5	0.3333	0	0.0000
$\alpha005\beta001-3$	0	0.0000	4	0.1905	11	0.5238	1	0.0476	5	0.2381	0	0.0000
$\alpha005\beta001-4$	0	0.0000	5	0.2174	4	0.1739	7	0.3043	5	0.2174	2	0.0870
$\alpha005\beta001-5$	3	0.2308	0	0.0000	6	0.4615	0	0.0000	4	0.3077	0	0.0000

Table 10.7: Details of the sink ejection study. Overview of all ejected sinks, i.e. all sinks that fulfill the criterion $v_{\mathrm{rad}}/v_{\mathrm{esc}} > 1$ and that have $v_{\mathrm{rad}} > 0$. Total number of such ejections, $N_{\mathrm{ejec,tot}}$, and this number subdivided in ejected objects with small mass $N_{\mathrm{ejec,s}}$ ($\leq 0.8\,\mathrm{M}_{\odot}$), medium mass $N_{\mathrm{ejec,m}}$ ($0.8 < M \leq 5\,\mathrm{M}_{\odot}$), and high mass $N_{\mathrm{ejec,l}}$ ($> 5\,\mathrm{M}_{\odot}$). Furthermore, we give ratios of these quantities with the total number of sinks, N_{tot}, and the total number of ejections, $N_{\mathrm{ejec,tot}}$.

Realization	N_{ejec}	$N_{\mathrm{ejec,tot}}$ $/N_{\mathrm{tot}}$	$N_{\mathrm{ejec,s}}$	$N_{\mathrm{ejec,s}}$ $/N_{\mathrm{tot}}$	$N_{\mathrm{ejec,s}}$ $/N_{\mathrm{ejec,tot}}$	$N_{\mathrm{ejec,m}}$	$N_{\mathrm{ejec,m}}$ $/N_{\mathrm{tot}}$	$N_{\mathrm{ejec,m}}$ $/N_{\mathrm{ejec,tot}}$	$N_{\mathrm{ejec,l}}$	$N_{\mathrm{ejec,l}}$ $/N_{\mathrm{tot}}$	$N_{\mathrm{ejec,l}}$ $/N_{\mathrm{ejec,tot}}$
$\beta01-1$	11	22.4	7	14.3	63.6	4	8.2	36.4	0	0.0	0.0
$\beta01-2$	14	45.2	8	25.8	57.1	6	19.4	42.9	0	0.0	0.0
$\beta01-3$	15	35.7	11	26.2	73.3	4	9.5	26.7	0	0.0	0.0
$\beta01-4$	8	29.6	4	14.8	50.0	4	14.8	50.0	0	0.0	0.0
$\beta01-5$	9	20.0	4	8.9	44.4	5	11.1	55.6	0	0.0	0.0
$\beta001-1$	9	32.1	5	17.9	55.6	2	7.1	22.2	2	7.1	22.2
$\beta001-2$	7	26.9	5	19.2	71.4	1	3.8	14.3	1	3.8	14.3
$\beta001-3$	10	27.0	5	13.5	50.0	5	13.5	50.0	0	0.0	0.0
$\beta001-4$	15	34.9	12	27.9	80.0	1	2.3	6.7	2	4.7	13.3
$\beta001-5$	14	40.0	10	28.6	71.4	3	8.6	21.4	1	2.9	7.1
$\alpha025-1$	45	62.5	41	56.9	91.1	4	5.6	8.8	0	0.0	0.0
$\alpha025-2$	18	45.0	15	37.5	83.3	2	5.0	11.1	1	2.5	5.6
$\alpha025-3$	10	22.2	6	13.3	60.0	3	6.7	30.0	1	2.2	10.0
$\alpha025-4$	8	42.1	6	31.6	75.0	1	5.3	12.5	1	5.3	12.5
$\alpha025-5$	71	60.2	70	59.3	98.6	0	0.0	0.0	1	0.847	1.41
$\alpha005-1$	25	41.0	18	29.5	72.0	5	8.2	20.0	2	3.3	8.0
$\alpha005-2$	14	24.6	12	21.1	85.7	1	1.8	7.1	1	1.8	7.1
$\alpha005-3$	27	42.9	23	36.5	85.2	3	4.8	11.1	1	1.6	3.7
$\alpha005-4$	23	45.1	21	41.1	91.3	2	3.9	8.7	0	0.0	0.0
$\alpha005-5$	9	23.1	5	12.8	55.6	4	10.3	44.4	0	0.0	0.0
$\alpha025\beta01-1$	14	34.1	11	26.8	78.6	3	7.3	21.4	0	0.0	0.0
$\alpha025\beta01-2$	15	46.9	13	40.6	86.7	2	6.3	13.3	0	0.0	0.0
$\alpha025\beta01-3$	4	19.0	3	14.3	75.0	0	0.0	0.0	1	4.8	25.0
$\alpha025\beta01-4$	30	56.6	29	54.7	96.7	0	0.0	0.0	1	1.9	3.3
$\alpha025\beta01-5$	14	34.1	9	22.0	64.3	5	12.2	35.7	0	0.0	0.0
$\alpha025\beta001-1$	13	38.2	10	29.4	76.9	3	8.8	23.1	0	0.0	0.0
$\alpha025\beta001-2$	25	45.5	19	34.5	76.0	4	7.3	16.0	2	3.6	8.0
$\alpha025\beta001-3$	9	17.3	6	11.5	66.7	3	5.8	33.3	0	0.0	0.0
$\alpha025\beta001-4$	22	36.1	19	31.1	86.4	0	0.0	0.0	3	4.9	13.6
$\alpha025\beta001-5$	30	68.2	29	65.9	96.7	1	2.3	3.33	0	0.0	0.0
$\alpha005\beta01-1$	8	23.5	5	14.7	62.5	2	5.9	25.0	1	2.9	12.5
$\alpha005\beta01-2$	14	40.0	9	30.0	64.3	3	10.0	21.4	0	0.0	0.0
$\alpha005\beta01-3$	11	28.2	10	25.6	90.9	1	2.6	9.1	0	0.0	0.0
$\alpha005\beta01-4$	4	26.7	4	26.7	100.0	0	0.0	0.0	0	0.0	0.0
$\alpha005\beta01-5$	8	25.0	6	18.8	75.0	1	3.1	12.5	1	3.1	12.5
$\alpha005\beta001-1$	13	32.5	11	27.5	84.6	1	2.5	7.7	1	2.5	7.7
$\alpha005\beta001-2$	18	34.0	15	28.3	83.3	3	5.7	16.7	0	0.0	0.0
$\alpha005\beta001-3$	18	40.0	15	33.3	83.3	3	6.7	16.7	0	0.0	0.0
$\alpha005\beta001-4$	30	37.0	26	32.1	86.7	3	3.7	10.0	1	1.2	3.3
$\alpha005\beta001-5$	14	43.8	11	34.4	78.6	2	6.3	14.3	1	3.1	7.1

10.3 Additional material: resolution study

In Fig. 10.19, we show radial mass-weighted averages of gas cloud properties at about 2 yr before first sink formation. The minor divergence of the black line of realization *2AUracc* from the other two profiles only occurs in close surrounding of the densest cell where the sink is about to form, i.e. at radii $< 10\,\mathrm{AU}$ or $\mathrm{M_{enc}} < 1\,\mathrm{M_\odot}$. As this region is highly dynamical at that time, the exact behavior of the gas may slightly vary from run to run.

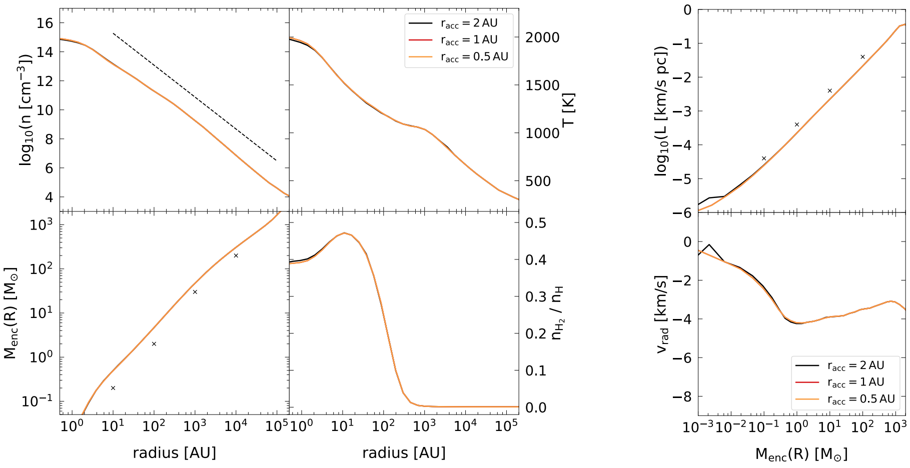

Figure 10.19: Left subplot: radial, mass-weighted averages of cloud properties just prior to first sink formation. From top left to bottom right: number density, n, temperature, T, mass enclosed within radius R, M_{enc}, molecular hydrogen fraction, $n_{\mathrm{H_2}}/n_{\mathrm{H}}$. Right subplot: mass-weighted averages of the total specific angular momentum, L, and the radial velocity, v_{rad}, within in the cloud. The properties are plotted against the enclosed mass. In both subplots, the averages are derived within spherical shells centered on the densest gas cells just before first sink formation.

In Table 10.8, we list the time in the simulation at which profiles of gas cloud or disk properties are plotted for different runs in the resolution study.

Table 10.8: Simulation time of output dumps used for gas cloud and disk property profiles in Fig.10.19, 6.2, 6.7, and 6.9.

Setup	t/yr just prior SF	t/yr just after SF
8Jeans	-2.3	2.7
16Jeans	-2.8	1.2
32Jeans	-2.7	1.2
0.5AUracc	-2.3	2.7
1AUracc	-2.3	2.8
2AUracc	-2.2	2.7

Bibliography

Abel, T., Bryan, G. L., & Norman, M. L. 2002, Science, 295, 93

Abel, T., Wise, J. H., & Bryan, G. L. 2007, ApJ, 659, L87

Alizadeh, E., & Hirata, C. M. 2011, Phys. Rev. D, 84, 083011

Almgren, A. S., Beckner, V. E., Bell, J. B., et al. 2010, ApJ, 715, 1221

Alvarez, M. A., Bromm, V., & Shapiro, P. R. 2006, ApJ, 639, 621

Alves, J. F., Lada, C. J., & Lada, E. A. 2001, Nature, 409, 159

André, P., Bouwman, J., Belloche, A., & Hennebelle, P. 2004, Ap&SS, 292, 325

Anninos, P., Zhang, Y., Abel, T., & Norman, M. L. 1997, New Astronomy, 2, 209

Aoki, W., Tominaga, N., Beers, T. C., Honda, S., & Lee, Y. S. 2014, Science, 345, 912

Arshakian, T. G., Beck, R., Krause, M., & Sokoloff, D. 2009, A&A, 494, 21

Balbus, S. A., & Hawley, J. F. 1991, ApJ, 376, 214

—. 1998, Reviews of Modern Physics, 70, 1

Banerjee, R., & Pudritz, R. E. 2006, ApJ, 641, 949

Banerjee, R., Pudritz, R. E., & Holmes, L. 2004, MNRAS, 355, 248

Bardeen, J. M., Bond, J. R., Kaiser, N., & Szalay, A. S. 1986, ApJ, 304, 15

Barkana, R., & Loeb, A. 2001, Phys. Rep., 349, 125

Bate, M. R., Bonnell, I. A., & Bromm, V. 2003, MNRAS, 339, 577

Bate, M. R., Bonnell, I. A., & Price, N. M. 1995, MNRAS, 277, 362

Bate, M. R., & Burkert, A. 1997, MNRAS, 288, 1060

Baumgardt, H., & Klessen, R. S. 2011, MNRAS, 413, 1810

Beck, R. 2015, A&A Rev., 24, 4

Beers, T. C., & Christlieb, N. 2005, ARA&A, 43, 531

Belczynski, K., Ryu, T., Perna, R., et al. 2017, MNRAS, 471, 4702

Biermann, L. 1950, Zeitschrift Naturforschung Teil A, 5, 65

Blandford, R. D., & Payne, D. G. 1982, MNRAS, 199, 883

Bondi, H. 1952, MNRAS, 112, 195

Bondi, H., & Hoyle, F. 1944, MNRAS, 104, 273

Bonnor, W. B. 1956, MNRAS, 116, 351

Bovino, S., Schleicher, D. R. G., & Grassi, T. 2014, A&A, 561, A13

Brandenburg, A., & Subramanian, K. 2005, Phys. Rep., 417, 1

Bromm, V. 2013, Reports on Progress in Physics, 76, 112901

Bromm, V., Coppi, P. S., & Larson, R. B. 2002, ApJ, 564, 23

Bromm, V., Ferrara, A., Coppi, P. S., & Larson, R. B. 2001a, MNRAS, 328, 969

Bromm, V., Kudritzki, R. P., & Loeb, A. 2001b, ApJ, 552, 464

Bromm, V., & Larson, R. B. 2004, ARA&A, 42, 79

Bromm, V., & Loeb, A. 2006, ApJ, 642, 382

Bromm, V., Yoshida, N., & Hernquist, L. 2003, ApJ, 596, L135

Bryan, G. L., Norman, M. L., O'Shea, B. W., et al. 2014, ApJS, 211, 19

Caffau, E., Bonifacio, P., François, P., et al. 2012, A&A, 542, A51

Caffau, E., Bonifacio, P., Sbordone, L., et al. 2013, A&A, 560, A71

Caselli, P., Benson, P. J., Myers, P. C., & Tafalla, M. 2002, ApJ, 572, 238

Cen, R., & Riquelme, M. A. 2008, Astrophys.J., 674, 644

Chatzopoulos, E., & Wheeler, J. C. 2012, ApJ, 748, 42

Chen, K.-J., Whalen, D. J., Wollenberg, K. M. J., Glover, S. C. O., & Klessen, R. S. 2017, ApJ, 844, 111

Chiaki, G., Yoshida, N., & Kitayama, T. 2013, ApJ, 762, 50

Ciardi, B., & Ferrara, A. 2005, Space Sci. Rev., 116, 625

Clark, P. C., Glover, S. C. O., & Klessen, R. S. 2008, ApJ, 672, 757

Clark, P. C., Glover, S. C. O., Klessen, R. S., & Bromm, V. 2011a, ApJ, 727, 110

Clark, P. C., Glover, S. C. O., Smith, R. J., et al. 2011b, Science, 331, 1040

Commerçon, B., Hennebelle, P., & Henning, T. 2011, ApJ, 742, L9

Crutcher, R. M. 2009, in Revista Mexicana de Astronomia y Astrofisica Conference Series, Vol. 36, Revista Mexicana de Astronomia y Astrofisica Conference Series, 107–112

Cyburt, R. H., Fields, B. D., & Olive, K. A. 2008, JCAP, 11, 012

Darwish, M., & Moukalled, F. 2003, International Journal of Heat and Mass Transfer, 46, 599

de Souza, R. S., Ciardi, B., Maio, U., & Ferrara, A. 2013, MNRAS, 428, 2109

Dedner, A., Kemm, F., Kröner, D., et al. 2002, Journal of Computational Physics, 175, 645

Draine, B. T., & Bertoldi, F. 1996, ApJ, 468, 269

Duffin, D. F., & Pudritz, R. E. 2009, ApJ, 706, L46

Ebert, R. 1955, ZAp, 37, 217

Elmegreen, B. G., & Burkert, A. 2010, ApJ, 712, 294

Emden, R. 1907, Gaskugeln: Anwendungen der mechanischen WŁrmetheorie auf kosmologische und meteorologische Probleme (B. Teubner)

Evans, C. R., & Hawley, J. F. 1988, ApJ, 332, 659

Federrath, C., Chabrier, G., Schober, J., et al. 2011a, Phys. Rev. Lett., 107, 114504

Federrath, C., Sur, S., Schleicher, D. R. G., Banerjee, R., & Klessen, R. S. 2011b, ApJ, 731, 62

Fialkov, A., Barkana, R., Tseliakhovich, D., & Hirata, C. M. 2012, MNRAS, 424, 1335

Field, G. B., Somerville, W. B., & Dressler, K. 1966, ARA&A, 4, 207

Flower, D. R., & Harris, G. J. 2007, MNRAS, 377, 705

Forrey, R. C. 2013, ApJ, 773, L25

Frebel, A., Johnson, J. L., & Bromm, V. 2008, in IAU Symposium, Vol. 255, Low-Metallicity Star Formation: From the First Stars to Dwarf Galaxies, ed. L. K. Hunt, S. C. Madden, & R. Schneider, 336–340

Frebel, A., Johnson, J. L., & Bromm, V. 2009, MNRAS, 392, L50

Frebel, A., & Norris, J. E. 2015, ARA&A, 53, 631

Frebel, A., Simon, J. D., & Kirby, E. N. 2014, ApJ, 786, 74

Frebel, A., Aoki, W., Christlieb, N., et al. 2005, Nature, 434, 871

Galli, D., & Palla, F. 1998, A&A, 335, 403

Galli, D., & Shu, F. H. 1993a, ApJ, 417, 220

—. 1993b, ApJ, 417, 243

Gammie, C. F. 2001, ApJ, 553, 174

Gardiner, T. A., & Stone, J. M. 2005, Journal of Computational Physics, 205, 509

Girart, J. M., Beltrán, M. T., Zhang, Q., Rao, R., & Estalella, R. 2009, Science, 324, 1408

Girart, J. M., Rao, R., & Marrone, D. P. 2006, Science, 313, 812

Girichidis, P., Federrath, C., Banerjee, R., & Klessen, R. S. 2012, MNRAS, 420, 613

Glover, S. 2005, Space Sci. Rev., 117, 445

Glover, S. 2008, in American Institute of Physics Conference Series, Vol. 990, First Stars III, ed. B. W. O'Shea & A. Heger, 25–29

Glover, S. 2013, in Astrophysics and Space Science Library, Vol. 396, The First Galaxies, ed. T. Wiklind, B. Mobasher, & V. Bromm, 103

Glover, S. C. O., & Abel, T. 2008, MNRAS, 388, 1627

Glover, S. C. O., & Brand, P. W. J. L. 2001, MNRAS, 321, 385

—. 2003, MNRAS, 340, 210

Glover, S. C. O., & Jappsen, A.-K. 2007, ApJ, 666, 1

Glover, S. C. O., & Savin, D. W. 2009, MNRAS, 393, 911

Gnedin, N. Y. 2000, ApJ, 542, 535

Gnedin, N. Y., & Hollon, N. 2012, ApJS, 202, 13

Gnedin, N. Y., & Hui, L. 1998, MNRAS, 296, 44

Goodman, A. A., Benson, P. J., Fuller, G. A., & Myers, P. C. 1993, ApJ, 406, 528

Goodwin, S. P., Whitworth, A. P., & Ward-Thompson, D. 2004a, A&A, 414, 633

—. 2004b, A&A, 423, 169

Gould, R. J., & Salpeter, E. E. 1963, ApJ, 138, 393

Gray, W. J., & Scannapieco, E. 2011, ApJ, 733, 88

Greif, T., Springel, V., White, S., et al. 2011, ApJ, 737, 75

Greif, T. H. 2014, MNRAS, 444, 1566

Greif, T. H., Bromm, V., Clark, P. C., et al. 2012, MNRAS, 424, 399

Greif, T. H., Johnson, J. L., Bromm, V., & Klessen, R. S. 2007, ApJ, 670, 1

Greif, T. H., Johnson, J. L., Klessen, R. S., & Bromm, V. 2008, MNRAS, 387, 1021

Haehnelt, M. G. 1995, MNRAS, 273, 249

Haemmerlé, L., Woods, T. E., Klessen, R. S., Heger, A., & Whalen, D. J. 2018, MNRAS, 474, 2757

Haiman, Z., Rees, M. J., & Loeb, A. 1997, ApJ, 476, 458

Haiman, Z., Thoul, A. A., & Loeb, A. 1996, ApJ, 464, 523

Hartwig, T., Bromm, V., Klessen, R. S., & Glover, S. C. O. 2015a, MNRAS, 447, 3892

Hartwig, T., Clark, P. C., Glover, S. C. O., Klessen, R. S., & Sasaki, M. 2015b, ApJ, 799, 114

Hartwig, T., Volonteri, M., Bromm, V., et al. 2016, arXiv:, arXiv:1603.05655

Hasegawa, K., Umemura, M., & Susa, H. 2009, MNRAS, 395, 1280

Hayes, J. C., Norman, M. L., Fiedler, R. A., et al. 2006, ApJS, 165, 188

Heger, A., & Woosley, S. E. 2002, ApJ, 567, 532

Hennebelle, P., & Ciardi, A. 2009, A&A, 506, L29

Hennebelle, P., Commerçon, B., Joos, M., et al. 2011, A&A, 528, A72

Hennebelle, P., & Teyssier, R. 2008, A&A, 477, 25

Hirano, S., Hosokawa, T., Yoshida, N., Omukai, K., & Yorke, H. W. 2015, MNRAS, 448, 568

Hirano, S., Hosokawa, T., Yoshida, N., et al. 2014, ApJ, 781, 60

Hollenbach, D., Johnstone, D., Lizano, S., & Shu, F. 1994, ApJ, 428, 654

Hosking, J. G., & Whitworth, A. P. 2004, MNRAS, 347, 1001

Hosokawa, T., Hirano, S., Kuiper, R., et al. 2016, ApJ, 824, 119

Hosokawa, T., & Omukai, K. 2009, ApJ, 691, 823

Hosokawa, T., Omukai, K., Yoshida, N., & Yorke, H. W. 2011, Science, 334, 1250

Hosokawa, T., Yorke, H. W., & Omukai, K. 2010, ApJ, 721, 478

Hosokawa, T., Yoshida, N., Omukai, K., & Yorke, H. W. 2012, ApJ, 760, L37

Hoyle, F. 1953, ApJ, 118, 513

Hummel, J. A., Stacy, A., & Bromm, V. 2016, MNRAS, 460, 2432

Hummel, J. A., Stacy, A., Jeon, M., Oliveri, A., & Bromm, V. 2015, MNRAS, 453, 4136

Ishiyama, T., Sudo, K., Yokoi, S., et al. 2016, ApJ, 826, 9

Jaura, O., Glover, S. C. O., Klessen, R. S., & Paardekooper, J.-P. 2018, MNRAS, 475, 2822

Jeans, J. H. 1902, Philosophical Transactions of the Royal Society of London Series A, 199, 1

Joggerst, C. C., Almgren, A., Bell, J., et al. 2010, ApJ, 709, 11

Johnson, J. L., & Bromm, V. 2006, MNRAS, 366, 247

Johnson, J. L., Greif, T. H., & Bromm, V. 2007, ApJ, 665, 85

Karlsson, T., Bromm, V., & Bland-Hawthorn, J. 2013, Reviews of Modern Physics, 85, 809

Karlsson, T., Johnson, J. L., & Bromm, V. 2008, ApJ, 679, 6

Kazantsev, A. P. 1968, Soviet Physics-JETP, 26, 1031

Keller, S. C., Bessell, M. S., Frebel, A., et al. 2014, Nature, 506, 463

Kim, W.-T., & Ostriker, E. C. 2001, ApJ, 559, 70

Kippenhahn, R., Weigert, A., & Weiss, A. 2012, Stellar Structure and Evolution (Springer-Verlag Berlin Heidelberg), doi:10.1007/978-3-642-30304-3

Kirby, E. N., Lanfranchi, G. A., Simon, J. D., Cohen, J. G., & Guhathakurta, P. 2011, ApJ, 727, 78

Kitayama, T., Yoshida, N., Susa, H., & Umemura, M. 2004, ApJ, 613, 631

Klassen, M., Pudritz, R. E., Kuiper, R., Peters, T., & Banerjee, R. 2016, ApJ, 823, 28

Klessen, R. S., Glover, S. C. O., & Clark, P. C. 2012, MNRAS, 421, 3217

Klessen, R. S., & Hennebelle, P. 2010, A&A, 520, A17

Kolmogorov, A. 1941, Akademiia Nauk SSSR Doklady, 30, 301

Komiya, Y., Suda, T., & Fujimoto, M. Y. 2015, ApJ, 808, L47

Konigl, A., & Pudritz, R. E. 2000, Protostars and Planets IV, 759

Kroupa, P. 2001, MNRAS, 322, 231

Krumholz, M. R., Klein, R. I., McKee, C. F., Offner, S. S. R., & Cunningham, A. J. 2009, Science, 323, 754

Krumholz, M. R., McKee, C. F., & Klein, R. I. 2005, ApJ, 618, L33

Kuiper, R., Klahr, H., Beuther, H., & Henning, T. 2010, ApJ, 722, 1556

—. 2011, ApJ, 732, 20

Kuiper, R., & Yorke, H. W. 2013, ApJ, 763, 104

Kuiper, R., Yorke, H. W., & Turner, N. J. 2015, ApJ, 800, 86

Kulsrud, R. M., Cen, R., Ostriker, J. P., & Ryu, D. 1997, ApJ, 480, 481

Lada, C. J., Alves, J. F., & Lombardi, M. 2007, Protostars and Planets V, 3

Lane, H. J. 1870, American Journal of Science, 50, 57, series 2

Larson, R. B. 1969, MNRAS, 145, 271

Latif, M. A., & Schleicher, D. R. G. 2015, MNRAS, 449, 77

—. 2016, A&A, 585, A151

Leer, B. V. 1977, Journal of Computational Physics, 23, 276

Lequeux, J. 2005, The Interstellar Medium (Berlin: Springer), doi:10.1007/b137959

Lodato, G. 2007, Nuovo Cimento Rivista Serie, 30, arXiv:0801.3848

Loeb, A., & Furlanetto, S. R. 2013, The First Galaxies in the Universe (Princeton University Press)

Lynden-Bell, D. 1966, The Observatory, 86, 57

Lynden-Bell, D., & Pringle, J. E. 1974, MNRAS, 168, 603

Machida, M. N., & Doi, K. 2013, MNRAS, 435, 3283

Machida, M. N., Matsumoto, T., Hanawa, T., & Tomisaka, K. 2005, MNRAS, 362, 382

Machida, M. N., Matsumoto, T., & Inutsuka, S.-i. 2008a, ApJ, 685, 690

Machida, M. N., Omukai, K., Matsumoto, T., & Inutsuka, S.-i. 2006, ApJ, 647, L1

—. 2008b, ApJ, 677, 813

Mackey, J., Bromm, V., & Hernquist, L. 2003, ApJ, 586, 1

Madau, P., Ferrara, A., & Rees, M. J. 2001, ApJ, 555, 92

Maeder, A., & Meynet, G. 2012, Reviews of Modern Physics, 84, 25

Magg, M., Hartwig, T., Agarwal, B., et al. 2018, MNRAS, 473, 5308

Maki, H., & Susa, H. 2004, ApJ, 609, 467

—. 2007, PASJ, 59, 787

Mayer, M., & Duschl, W. J. 2005, MNRAS, 358, 614

McKee, C. F., & Tan, J. C. 2008, ApJ, 681, 771

Mellon, R. R., & Li, Z.-Y. 2008, ApJ, 681, 1356

—. 2009, ApJ, 698, 922

Miyoshi, T., & Kusano, K. 2005, Journal of Computational Physics, 208, 315

Mizusawa, H., Omukai, K., & Nishi, R. 2005, PASJ, 57, 951

Mocz, P., Pakmor, R., Springel, V., et al. 2016, MNRAS, 463, 477

Mocz, P., Vogelsberger, M., & Hernquist, L. 2014, MNRAS, 442, 43

Mocz, P., Vogelsberger, M., Pakmor, R., et al. 2015, MNRAS, 452, 3853

Moeckel, N., & Clarke, C. J. 2011, MNRAS, 410, 2799

Mouschovias, T. C., & Paleologou, E. V. 1979, ApJ, 230, 204

Mouschovias, T. C., & Spitzer, Jr., L. 1976, ApJ, 210, 326

Nagakura, T., & Omukai, K. 2005, MNRAS, 364, 1378

Naoz, S., & Barkana, R. 2007, MNRAS, 377, 667

Neufeld, D. A., & Kaufman, M. J. 1993, ApJ, 418, 263

Norman, M. L. 1980, PhD thesis, Lawrence Livermore National Lab., CA.

Norman, M. L. 2000, in Revista Mexicana de Astronomia y Astrofisica, vol. 27, Vol. 9, Revista Mexicana de Astronomia y Astrofisica Conference Series, ed. S. J. Arthur, N. S. Brickhouse, & J. Franco, 66–71

Norman, M. L., & Winkler, K.-H. A. 1986, in NATO Advanced Science Institutes (ASI) Series C, Vol. 188, NATO Advanced Science Institutes (ASI) Series C, ed. K.-H. A. Winkler & M. L. Norman, 187

Oh, S. P., & Haiman, Z. 2002, ApJ, 569, 558

Omukai, K., & Nishi, R. 1998, ApJ, 508, 141

Omukai, K., Nishi, R., Uehara, H., & Susa, H. 1998, Progress of Theoretical Physics, 99, astro-ph/9809232

Omukai, K., & Palla, F. 2001, ApJ, 561, L55

—. 2003, ApJ, 589, 677

O'Shea, B. W., Abel, T., Whalen, D., & Norman, M. L. 2005, ApJ, 628, L5

Pacucci, F., Loeb, A., & Salvadori, S. 2017, MNRAS, 471, L72

Pakmor, R., Bauer, A., & Springel, V. 2011, MNRAS, 418, 1392

Pakmor, R., & Springel, V. 2013, MNRAS, 432, 176

Pakmor, R., Springel, V., Bauer, A., et al. 2016, MNRAS, 455, 1134

Palla, F., Salpeter, E. E., & Stahler, S. W. 1983, ApJ, 271, 632

Pawlik, A. H., Milosavljević, M., & Bromm, V. 2013, ApJ, 767, 59

Peacock, J. A. 1999, Cosmological Physics (Cambridge University Press), 704

Peters, T., Banerjee, R., Klessen, R. S., & Mac Low, M.-M. 2011, ApJ, 729, 72

Peters, T., Klessen, R. S., Mac Low, M.-M., & Banerjee, R. 2010, ApJ, 725, 134

Peters, T., Schleicher, D. R. G., Klessen, R. S., et al. 2012, ApJ, 760, L28

Peters, T., Schleicher, D. R. G., Smith, R. J., Schmidt, W., & Klessen, R. S. 2014, MNRAS, 442, 3112

Planck Collaboration, Akrami, Y., Arroja, F., et al. 2018a, ArXiv e-prints, arXiv:1807.06205

Planck Collaboration, Aghanim, N., Akrami, Y., et al. 2018b, ArXiv e-prints, arXiv:1807.06209

Powell, K. G., Roe, P. L., Linde, T. J., Gombosi, T. I., & De Zeeuw, D. L. 1999, Journal of Computational Physics, 154, 284

Price, D. J., & Bate, M. R. 2007, Ap&SS, 311, 75

Pudritz, R. E., & Silk, J. 1989, ApJ, 342, 650

Rees, M. J. 1976, MNRAS, 176, 483

Rees, M. J., & Ostriker, J. P. 1977, MNRAS, 179, 541

Riaz, R., Bovino, S., Vanaverbeke, S., & Schleicher, D. R. G. 2018, MNRAS, 479, 667

Richardson, M. L. A., Scannapieco, E., & Gray, W. J. 2013, ApJ, 778, 80

Ricotti, M. 2016, MNRAS, 462, 601

Ricotti, M., Gnedin, N. Y., & Shull, J. M. 2001, ApJ, 560, 580

Ripamonti, E., & Abel, T. 2004, MNRAS, 348, 1019

Ripamonti, E., Haardt, F., Ferrara, A., & Colpi, M. 2002, MNRAS, 334, 401

Ritter, J. S., Safranek-Shrader, C., Gnat, O., Milosavljevic, M., & Bromm, V. 2012, Astrophys.J., 761, 56

Ruzmaikin, A. A., Sokolov, D. D., & Shukurov, A. M., eds. 1988, Astrophysics and Space Science Library, Vol. 133, Magnetic fields of galaxies

Rydberg, C.-E., Zackrisson, E., Lundqvist, P., & Scott, P. 2013, MNRAS, 429, 3658

Safranek-Shrader, C., Milosavljević, M., & Bromm, V. 2014, MNRAS, 440, L76

Sakurai, Y., Vorobyov, E. I., Hosokawa, T., et al. 2016, MNRAS, 459, 1137

Salpeter, E. E. 1955, ApJ, 121, 161

Saslaw, W. C., & Zipoy, D. 1967, Nature, 216, 976

Schaerer, D. 2002, Astron.Astrophys., 382, 28

Schauer, A. T. P., Regan, J., Glover, S. C. O., & Klessen, R. S. 2017, MNRAS, 471, 4878

Schauer, A. T. P., Whalen, D. J., Glover, S. C. O., & Klessen, R. S. 2015, MNRAS, 454, 2441

Schekochihin, A. A., Cowley, S. C., Hammett, G. W., Maron, J. L., & McWilliams, J. C. 2002, New Journal of Physics, 4, 84

Schleicher, D. R. G., Banerjee, R., Sur, S., et al. 2010, A&A, 522, A115

Schleicher, D. R. G., Galli, D., Palla, F., et al. 2008, A&A, 490, 521

Schleicher, D. R. G., Latif, M., Schober, J., et al. 2013, Astronomische Nachrichten, 334, 531

Schneider, R., Graziani, L., Marassi, S., et al. 2017, MNRAS, 471, L105

Schneider, R., Omukai, K., Inoue, A. K., & Ferrara, A. 2006, MNRAS, 369, 1437

Schober, J., Schleicher, D., Federrath, C., et al. 2012, ApJ, 754, 99

Scrimgeour, M. I., Davis, T., Blake, C., et al. 2012, MNRAS, 425, 116

Seifried, D., Banerjee, R., Klessen, R. S., Duffin, D., & Pudritz, R. E. 2011, MNRAS, 417, 1054

Seifried, D., Banerjee, R., Pudritz, R. E., & Klessen, R. S. 2013, MNRAS, 432, 3320

Seifried, D., Pudritz, R. E., Banerjee, R., Duffin, D., & Klessen, R. S. 2012, MNRAS, 422, 347

Shakura, N. I., & Sunyaev, R. A. 1973, A&A, 24, 337

Shapiro, P. R., Giroux, M. L., & Babul, A. 1994, ApJ, 427, 25

Shen, S., Kulkarni, G., Madau, P., & Mayer, L. 2017, MNRAS, 469, 4012

Shu, F. H. 1977, ApJ, 214, 488

Sigl, G., Olinto, A. V., & Jedamzik, K. 1997, Phys. Rev. D, 55, 4582

Silk, J., & Langer, M. 2006, MNRAS, 371, 444

Smith, B. D., & Sigurdsson, S. 2007, ApJ, 661, L5

Smith, B. D., Turk, M. J., Sigurdsson, S., O'Shea, B. W., & Norman, M. L. 2009, ApJ, 691, 441

Smith, B. D., Wise, J. H., O'Shea, B. W., Norman, M. L., & Khochfar, S. 2015, MNRAS, 452, 2822

Smith, R. J., Glover, S. C. O., Clark, P. C., Greif, T., & Klessen, R. S. 2011, MNRAS, 414, 3633

Smith, R. J., Hosokawa, T., Omukai, K., Glover, S. C. O., & Klessen, R. S. 2012, MNRAS, 424, 457

Springel, V. 2005, MNRAS, 364, 1105

—. 2010, MNRAS, 401, 791

Springel, V., & Hernquist, L. 2002, MNRAS, 333, 649

Springel, V., White, S. D. M., Jenkins, A., et al. 2005, Nature, 435, 629

Stacy, A., & Bromm, V. 2013, MNRAS, 433, 1094

—. 2014, ApJ, 785, 73

Stacy, A., Bromm, V., & Lee, A. T. 2016, MNRAS, 462, 1307

Stacy, A., Greif, T. H., & Bromm, V. 2010, MNRAS, 403, 45

—. 2012, MNRAS, 422, 290

Stacy, A., Greif, T. H., Klessen, R. S., Bromm, V., & Loeb, A. 2013, MNRAS, 431, 1470

Stahler, S. W., Palla, F., & Salpeter, E. E. 1986, ApJ, 302, 590

Stecher, T. P., & Williams, D. A. 1967, ApJ, 149, L29

Steenbeck, M., & Krause, F. 1966, Zeitschrift Naturforschung Teil A, 21, 1285

Strittmatter, P. A. 1966, MNRAS, 132, 359

Subramanian, K. 1997, arXiv:, astro-ph/9708216

Sur, S., Federrath, C., Schleicher, D. R. G., Banerjee, R., & Klessen, R. S. 2012, MNRAS, 423, 3148

Sur, S., Schleicher, D. R. G., Banerjee, R., Federrath, C., & Klessen, R. S. 2010, ApJ, 721, L134

Susa, H. 2007, ApJ, 659, 908

—. 2013, ApJ, 773, 185

Susa, H., Doi, K., & Omukai, K. 2015, ApJ, 801, 13

Susa, H., Hasegawa, K., & Tominaga, N. 2014, ApJ, 792, 32

Susa, H., & Umemura, M. 2006, ApJ, 645, L93

Susa, H., Umemura, M., & Hasegawa, K. 2009, ApJ, 702, 480

Tan, J. C., & Blackman, E. G. 2004, ApJ, 603, 401

Tegmark, M., Silk, J., Rees, M. J., et al. 1997, ApJ, 474, 1

Toomre, A. 1964, ApJ, 139, 1217

Toro, E. 1997, Riemann Solvers and Numerical Methods for Fluid Dynam ic:A Practical Introduction. (Springer-Verlag Berlin Heidelberg)

Truelove, J. K., Klein, R. I., McKee, C. F., et al. 1997, ApJ, 489, L179

Tseliakhovich, D., Barkana, R., & Hirata, C. M. 2011, MNRAS, 418, 906

Tseliakhovich, D., & Hirata, C. 2010, Phys. Rev. D, 82, 083520

Turk, M. J., Abel, T., & O'Shea, B. 2009, Science, 325, 601

Turk, M. J., Clark, P., Glover, S. C. O., et al. 2011, ApJ, 726, 55

Turk, M. J., Oishi, J. S., Abel, T., & Bryan, G. 2012, ApJ, 745, 154

Turner, M. S., & Widrow, L. M. 1988, Phys. Rev. D, 37, 2743

Vainshtein, S. I., & Ruzmaikin, A. A. 1971, AZh, 48, 902

van Leer, B. 1984, SIAM Journal on Scientific and Statistical Computing, 5, 1

—. 2006, COMMUNICATIONS IN COMPUTATIONAL PHYSICS, Vol. 1, pp. 192

Vanaverbeke, S., Keppens, R., Poedts, S., & Boffin, H. 2009, Computer Physics Communications, 180, 1164

Volonteri, M. 2012, Science, 337, 544

Volonteri, M., & Rees, M. J. 2005, ApJ, 633, 624

Walch, S., Burkert, A., Whitworth, A., Naab, T., & Gritschneder, M. 2009, MNRAS, 400, 13

Wang, F. Y., Bromm, V., Greif, T. H., et al. 2012, ApJ, 760, 27

Wang, P., Li, Z.-Y., Abel, T., & Nakamura, F. 2010, ApJ, 709, 27

Whalen, D., Abel, T., & Norman, M. L. 2004, ApJ, 610, 14

Whalen, D., Hueckstaedt, R. M., & McConkie, T. O. 2010, ApJ, 712, 101

Whalen, D., & Norman, M. L. 2008a, ApJ, 673, 664

Whalen, D., O'Shea, B. W., Smidt, J., & Norman, M. L. 2008, ApJ, 679, 925

Whalen, D. J., Joggerst, C. C., Fryer, C. L., et al. 2013a, ApJ, 768, 95

Whalen, D. J., & Norman, M. L. 2006, Astrophys.J.Suppl., 162, 281

Whalen, D. J., & Norman, M. L. 2008b, ApJ, 672, 287

Whalen, D. J., Even, W., Frey, L. H., et al. 2013b, ApJ, 777, 110

Whalen, D. J., Even, W., Smidt, J., et al. 2013c, ApJ, 778, 17

Williams, R. J. R. 2002, MNRAS, 331, 693

Wise, J. H., & Abel, T. 2007, ApJ, 665, 899

—. 2008, ApJ, 685, 40

Wise, J. H., Turk, M. J., Norman, M. L., & Abel, T. 2012, ApJ, 745, 50

Wong, W. Y., Moss, A., & Scott, D. 2008, MNRAS, 386, 1023

Woods, T. E., Heger, A., Whalen, D. J., Haemmerlé, L., & Klessen, R. S. 2017, ApJ, 842, L6

Xu, H., O'Shea, B. W., Collins, D. C., et al. 2008, ApJ, 688, L57

Yoshida, N., Abel, T., Hernquist, L., & Sugiyama, N. 2003, ApJ, 592, 645

Yoshida, N., Bromm, V., & Hernquist, L. 2004, Astrophys.J., 605, 579

Yoshida, N., Oh, S. P., Kitayama, T., & Hernquist, L. 2007, ApJ, 663, 687

Yoshida, N., Omukai, K., & Hernquist, L. 2008, Science, 321, 669

Yoshida, N., Omukai, K., Hernquist, L., & Abel, T. 2006, ApJ, 652, 6

Zackrisson, E., Rydberg, C.-E., Schaerer, D., Östlin, G., & Tuli, M. 2011, ApJ, 740, 13

Zhang, W., Howell, L., Almgren, A., Burrows, A., & Bell, J. 2011, ApJS, 196, 20

Zhao, B., Li, Z.-Y., Nakamura, F., Krasnopolsky, R., & Shang, H. 2011, ApJ, 742, 10

Acknowledgements

The successful completion of this thesis would not have been possible without the support and encouragement of many people whom I would like to say thank you now. First of all, I want to thank my advisor, Simon Glover, for his continuous support over the last couple of years, his always helpful and constructive feedback, his honesty and for sharing some of his detailed knowledge about numerical methods, primordial chemistry, Population III star formation and physics in general with me. Second, I thank my advisor Ralf Klessen for offering me financial support during the main part of my PhD which made it also possible for me to present my results at several conferences. I am also very grateful to him as well as to the Heidelberg School of Fundamental Physics (HGSFP) and the International Max Planck Research School for Astronomy & Cosmic Physics (IMPRS) at the University of Heidelberg for providing extended funding during the last year of my PhD. This extension made it possible for me to switch to AREPO and to finally successfully perform and gain the main results of this thesis as presented in Chapter 5, 6 as well as in Chapter 8, after a painful, desparate and hopeless odyssey with the FLASH code. Thank you for giving me this chance!

At this point, I want to thank Volker Springel for being a member of my thesis committee, for his commitment and support, and for the opportunity to use AREPO for my project. A big thank you goes also to Volker's AREPO development group, specifcally Rüdiger Pakmor and Rainer Weinberger, and to the ITA AREPO group, in particular Robin Gopala Tress, Ondrej Jaura, Thomas Greif, and Mattis Magg, who helped me getting started with the code and the analysis tools and were ready to discuss whenever I had a question.

I would like to express my gratitude to my collaborators over the years: Volker Bromm for his continuous support, guidance, his creative ideas, enthusiasm and encouragement. Ke-Jung "Ken" Chen for his tireless commitment in getting our paper published, his kindness and encourangement. Philipp Girichidis for becoming an active collaborator in my work with FLASH, for being always friendly, patient, and creative in helping me debugging the code. Luigi Iapichino for his tireless, always friendly and enthusiastic effort in providing me the best solution when using SuperMUC. Daniel Whalen for the good supervision in the first half year of my PhD. Finally, Jennifer Schober for giving me an insight into primordial magnetic fields and the small-scale dynamo, and Paul Clark and Rowan Smith for their advise during my ideal MHD study in AREPO.

Furthermore, I want to thank many other colleagues and friends for the enjoyable time together: Erik Bertram, Bhaskar Agarwal, Dimitrios Gouliermis, Diane Cormier, Kiwan Park, Sam Geen, Mattia Sormani, Daniel Rahner, Todor Veltchev, Michael Küffmeier, Adriana Pohl, Clio Bertelli Motta, Roxana Chira, Sara Rezaei Khoshb-

hakht, and several more that I have met over the years. Vielen Dank an Stella und Luigi von Divinos für die leckere Verpflegung und ausgezeichnete Bewirtung in den vergangenen Jahren.

I am happy to have Lena, Julian, Alexis, Holli, Jens, Martin, Jonathan, Günter, Nicky, Björn, Claudia, and Marco in my life, who lent me an ear when I needed one, and who brought lots of interesting conversations, laughther, good food, meditative moments, new inspirations, and in general lots of good and happy times in my life. Thanks as well to all the writers, musicians and other artists of the world that gave me inspiration and strength.

Ich danke meiner Familie für ihre Unterstützung in den vergangenen Jahren, für die Momente, in denen ich ihnen mein Fach näherbringen durfte, für einen Rückzugsort zum Zusammenschreiben und viel gutes Essen.

I am deeply grateful for the support and commitment offered by Guido Thimm. Guido, you not only made me smile when we began talking about our common interest, movies, you also helped me finding my smile and courage again. Thank you!

I am very grateful for María Jesús Jiménez Donaire, Sacha Hony, Carla Bernhardt, Katharina Winkler, Kris Coester und Nina Gausmann whose geniality, humor, helpfulness and advise which I deeply appreciate.

At last, I want to thank Jan for his friendship and love, for his endless support and encouragement.

Eidesstattliche Erklärung:

Ich versichere, dass ich diese Arbeit selbstständig verfasst habe und keine anderen als die angegebenen Quellen und Hilfsmittel benutzt habe.

Heidelberg, den 03.11.2018

Katharina Wollenberg